Microscopic calculation of line tensions

Von der Fakultät für Mathematik und Physik der Universtität Stuttgart zur Erlangung der Würde eines Doktors der Naturwissenschaften (Dr. rer. nat.) genehmigte Abhandlung

Vorgelegt von

Rolf-Jürgen Christian Merath

aus Esslingen am Neckar

Hauptberichter:	Prof. Dr. S. Dietrich
Mitberichter:	Prof. Dr. U. Seifert

Tag der Einreichung:	9. September 2008
Tag der mündlichen Prüfung:	16. Oktober 2008

Institut für Theoretische und Angewandte Physik
Universität Stuttgart

und

Max-Planck-Institut für Metallforschung
Stuttgart

2008

Contents

List of figures

Achknowledgement

To many people I am grateful for supporting me. I thank ...

... Prof. Dr. S. Dietrich for the opportunity to perform my doctoral studies at his department at the Max-Planck-Insitut für Metallforschung in Stuttgart. His guiding comments are always precious. Whenever in any way possible, he took some time for me. I am thankfull for having granted me a lot of freedom at work, e. g., for pursuing my interest in membrane fluctuations.

... Prof. Dr. U. Seifert for kindly co-reviewing this thesis. Furthermore I thank him for the fruitful cooperation on the field of membrane fluctuations even after my diploma studies.

... Dr. Roland Roth for supervising my work at Prof. Dietrich's department. Especially I thank him for having introduced me rapidly into practical aspects of density functional theory, for valuable pieces of advice, hints and for his good sense of humor.

... Dr. Markus Bier, who has become a close friend in the first semester and who by chance shared the room with me for almost two years. I thank him for his countless pieces of advice in many fields.

... all the other colleagues at Prof. Dietrich's department for the nice working atmosphere, useful scientific discussions and pleasurable conversations during lunch.

... the colleagues at the computer department of the institute for their competent maintenance of the computer equipment.

... Prof. Dr. M. Napiórkowski and Prof. Dr. J. O. Indekeu for fruitful discussions.

... my parents, Rolf-Peter and Dagmar Merath, for their great support during my physics studies.

... my grandmother Erna Schwarz (now at the age of 94), who brought me down to earth again, when she regarded some formulae of my work as "Gekritzel" (doodle).

1 Introduction

1.1 Motivation

Macroscopic material properties are based on interactions of the constitutive particles on a microscopic level. An attractive interaction among particles favors them to agglomerate. Therefore from the energetic point of view a liquid, in which the particles are close to each other, but not regularly positioned like in a crystal, is more favorable than a gas, in which the interparticle distance is much larger and hence the mean particle density is much lower. On the other hand the freedom of movement of the particles decreases, if they are densely packed. This means that from the entropic point of view a gas is more favorable than a liquid. Consequently the actual arrangement of the particles as a liquid or a gas results from an interplay of energy and entropy.

A fluid does not always exhibit a liquid and a gas phase. If the temperature is sufficiently high, solely one fluid phase can be observed. The critical point describes the state in which two phases — here the liquid and the gas phase — become indistinguishable. For temperatures below the critical temperature the liquid and the gas phase can coexist in equilibrium, i. e., they are both thermodynamically stable and suitable boundary conditions ensure the presence of both phases at a time. The spatial region where two or more phases are in contact is called *interface*. An example of a system with three phases in contact is given in Fig. 1.1.

Usually the fluid in an interfacial region, e. g., a solid–gas, solid–liquid, or liquid–gas interface, behave differently than in a "bulk" system, i. e., a system without any interfaces or boundaries. The influence of an interface may reach far from the interface position, which can be defined with some degree of arbitrariness. The inhomogeneous distribution of particles at an interface gives rise to an extra free energy contribution called surface tension or — more general — interfacial tension. On a microscopic length scale the structure of an interface can be very complicated and is not simply given by two bulk systems glued together unchanged: The particle density usually varies continuously from one bulk density to the other, and it may even exhibit density oscillations indicating packing effects, i. e., the particles tend to form layers there.

A particular kind of inhomogeneity is formed, if a planar liquid–gas interface is brought into contact with a planar substrate, e. g., a glass plate. On a macroscopic scale a *liquid*

Fig. 1.1: Droplet on a superhydrophobic surface [1]. The substrate is covered by aligned, coated nanofibres. Here a droplet with a diameter of 2 mm resides on the tips of the fibres. The diameter and length of these fibres can be varied between 10–40 nm and 70–360 nm, respectively. The property of the surface can range between superhydrophobic and superhydrophilic depending on the type of coating.

wedge resting on a substrate may form. The contact angle describes the inclination of the liquid–gas interface with respect to the substrate surface. The line where the three involved phases (gas, liquid, and solid substrate) are in contact is — in a macroscopic picture — called contact line. However, the structure of the three-phase contact region is much richer on a microscopic scale. The spatial distribution of the fluid particles in such a wedge geometry is analyzed theoretically in this work.

The system of a sessile liquid wedge is inspired by *sessile droplets* (see Fig. 1.1). The contact angle θ of a sessile liquid droplet is described by *Young's law* [2],

$$\cos\theta = \frac{\sigma_{\mathrm{sg}} - \sigma_{\mathrm{sl}}}{\sigma_{\mathrm{lg}}}. \tag{1.1}$$

σ_{sg}, σ_{sl}, and σ_{lg} are the interfacial tensions of solid–gas, solid–liquid, and liquid–gas interfaces, respectively. An interfacial tension describes the energy that is necessary to create an interface. Young's equation can be illustrated by a lateral force balance at the contact line:

$$\sigma_{\mathrm{sg}} = \sigma_{\mathrm{sl}} + \sigma_{\mathrm{lg}} \cos\theta. \tag{1.2}$$

However, for sessile droplets smaller than approximately one micrometer deviations from this law occur. They are attributed to some extend to the influcence of a so-called *line tension*. This is, roughly speaking, the free energy contribution (per unit length) associated with the contact line. The line tension of a sessile liquid wedge is related to the sessile droplet line tension and therefore is an important quantity both for a thorough theoretical understanding and for technological applications comprising small amounts of liquid.

Up to now theoretical studies of phenomenological model systems did not take the microscopic spatial structure of the fluid into account. In the present work microscopic details of the particle–particle interactions as well as microscopic details of the fluid structure are taken into account. Consequently this *fully microscopic approach* enables one to calculate the line tension of a sessile liquid wedge in an unprecedented realistic way.

1.2 Outline

The present chapter introduces the topic of line tensions. The line tension was mentioned already in the previous Sec. 1.1 in the context of sessile droplets smaller than approximately 1 μm, for which the line tension helps to explain deviations of the contact angle from Young's law. In the following Sec. 1.3 the subject of this study and its aims are specified. The general definition of a line tension applies to many, sometimes very different systems. They are categorized into classes of line tensions in Sec. 1.4. Some technological applications of such systems with relevant line tensions are highlighted in Sec. 1.5. The present work is embedded into the research field of line tensions of sessile liquid wedges or droplets in Sec. 1.6. For completeness the research on line tensions for substrate-free three-phase coexistence is reviewed in Sec. 1.7.

After the introduction in the present chapter the method applied in this work, classical density functional theory (DFT), is introduced in Chapter 2. Fluid interfaces are considered thereafter, especially from the point of view of DFT, in Chapter 3. Chapter 4 is dedicated to sessile droplets, the definition of a line tension for that system, and the connection between the line tensions of a sessile liquid droplet or wedge, respectively. Other line excess quantities, besides the line tension of a sessile liquid wedge or droplet,

are described in Chapter 5. The model system studied here, a liquid wedge on a substrate, is described in Chapter 6 in more detail than in the present chapter. The same system has been analyzed using the so-called "sharp-kink approximation". This approach is described and extended in Chapter 7. Thus in Chapter 8 the results of the fully microscopic approach can be compared to those obtained from the semi-microscopic sharp-kink calculations. The perspectives arising from this work are sketched in Chapter 9. Finally, a summary is given in Chapter 10.

1.3 Formulation of the scientific problem

The model system analyzed in this study is described briefly in Sec. 1.3.1. Moreover the definition of a line tension in general and of the liquid wedge line tension in particular are given in Sec. 1.3.2. Then the status of this work is assessed in Sec. 1.3.3.

1.3.1 Subject: line tension of a sessile liquid wedge

The system under consideration is a liquid wedge residing on a planar substrate. Such a sessile liquid wedge can be regarded as a part of a macroscopicly large sessile droplet. Thermodynamic equilibrium, for which the liquid coexists with its gas phase, is presumed.

In this study the theoretical model of actual fluids is a one-component fluid the intermolecular interactions of which are modeled either by a short-ranged square-well potential or by a long-ranged Lennard-Jones (12–6) potential, respectively. The homogeneous, flat, chemically inert substrate is represented by a Lennard-Jones (9–3) potential and varieties thereof. The model is described in more detail in Chapter 6.

The method to calculate the structure of the three-phase contact region and the line tension for the present model system is a density functional calculation of the effectively two-dimensional equilibrium particle number density distribution $\varrho(x, z)$. These technical terms are explained in the following chapter.

1.3.2 Definition of a line tension

Shortcomings of macroscopic line tension definitions:
If theoretical calculations based on a macroscopic scale utilize the line tension (e. g., colloids at a liquid–gas interface or a liquid ridge on a substrate), the line tension is typically considered as an external parameter, the value of which has to be inserted by hand. Typically in macroscopic approaches the total free energy of the studied system is unknown and approximatively described, for instance, by contributions known for simpler geometries or by assigning values to individual quantities.

Macroscopic calculations of line tensions rest upon a coarse grained definition. E. g., in an interface displacement model the line tension exclusively depends on the position of a liquid–gas interface. The line tension is well-defined there, however, the connection to its microscopic origin is kept only in a crude way.

Microscopic definition of a liquid wedge line tension:
A "microscopic" approach resolves molecular details of the involved particles, i. e., the spatial distribution of particles on a molecular length scale and characteristics of the particle–particle interactions. From a microscopic perspective the line tension of the considered system, a liquid wedge resting on a substrate, is defined as follows. Within

the grand canonical ensemble the natural thermodynamic potential is the grand potential $\Omega = \Omega(T, V, \mu)$ with temperature T, volume V, and chemical potential μ.

A "microscopic calculation" yields the value of the grand potential of a microscopic model system. This is in contrast to macroscopic approaches, in which the precise value of Ω remains unspecified. The microscopicly obtained value of Ω is decomposed into terms (a) proportional to the volume V of the fluid, (b) proportional to the surface areas A_{sg}, A_{sl}, and A_{lg} of the solid–gas, solid–liquid, and liquid–gas interfaces, respectively, and (c) proportional to the length L of the contact line. The contact line is the curve where the substrate, the liquid region, and the gaseous region are in contact. From a microscopic point of view the line tension τ is defined as the coefficient of the contribution to the grand potential which is proportional to the length L of the contact line,

$$\Omega \;=\; -\,p\,V \;+\; \sigma_{\mathrm{sg}}\,A_{\mathrm{sg}} \;+\; \sigma_{\mathrm{sl}}\,A_{\mathrm{sl}} \;+\; \sigma_{\mathrm{lg}}\,A_{\mathrm{lg}} \;+\; \tau\,L. \tag{1.3}$$

σ_{sg}, σ_{sl}, and σ_{lg} are the interfacial tensions of solid–gas, solid–liquid, and liquid–gas interfaces, respectively, which are discussed in more detail in Sec. 3.1. If the pressure and the interfacial tensions are calculated consistently (i. e., for the same interactions and physical parameters), the above decomposition determines the value of the line tension. Note that the values of the solid–gas and solid–liquid interfacial tensions, σ_{sg} and σ_{sl}, depend on the choice of the interface position (cf. Sec. 3.3.2). Hence the value of the liquid wedge line tension depends on this choice as well [Eq. (6.4)].

General line tension defnition:
In short, a line tension is a one-dimensional analogue of the surface tension. Gibbs introduced the concept of a "linear tension" in 1878, when he suggested that a line formed by three phases should be treated entirely analogously to interfaces [3].

In general, a line tension is related to a free energy that scales with the length of a linear structure (e. g., a line) of the considered system. It describes the excess in free energy due to this linear structure, in addition to volume ("bulk"), surface, and — possibly — point contributions. Precisely, the line tension is the coefficient of the line excess contribution in a decomposition of the "natural" thermodynamic potential of the system into volume, surface, linear, and point terms.

1.3.3 Aims and status of this work

The main task of this study is to calculate line tension values for different model systems in different wetting scenarios (cf. Subsecs. 1.6.1 and 3.3.5). In order to obtain a line tension value via the presently applied method, the microscopic structure of the three-phase contact region, where the three phases (solid substrate, liquid, and gas) are in contact, has to be calculated. In doing so a continuous particle density is taken into account. This means that the particle density is not piecewise constant but is free to vary smoothly. Moreover effects due to details of the interaction between a fluid particle and another fluid particle or a substrate particle are resolved in the theoretical description as well. Consequently, since microscopic details both of the molecular interactions and of the particle distribution are taken into account, the approach presented here can be regarded as "fully microscopic".

Previous studies of similar, phenomenological model systems treated the solid–fluid and liquid–gas interfaces in a crude, so-called sharp-kink approximation. The fluid in a certain phase is regarded to be homogeneous right up to the interface position, where the density changes discontinuously. Hence the intrinsic interfacial structure is neglected. Solid–liquid interfaces, for instance, can exhibit strong density oscillations due to packing effects

(i. e., the liquid tends to form layers in the vicinity of the substrate surface). Hence a comparison between the fully microscopic approach and the sharp-kink theory should reveal the quality of the sharp-kink approximation in the context of liquid wedge line tensions.

This theoretical model study renders the line tension of a rather realistic model system more accurately than in previous studies. It is a step towards a complete understanding of the shape of very small droplets, i. e., droplets with diameters below the micrometer range. The liquid wedge line tension is related to the line tension of a sessile droplet by a computationally simple transformation [4]. Furthermore a proposal is given how axisymmetric sessile droplets could be described efficiently at the same level of accuracy.

1.4 Classes of line tensions

Although the line energy contribution is usually much smaller than the surface energy contribution, it plays an important role in various physical systems [5]. One can distinguish between the following (and even more [6]) classes of line tensions:

1. Three-dimensional, simple fluid systems:

   (a) Line tension (or contact line tension) of a *sessile liquid droplet*:

   - A liquid droplet sitting on a planar, homogeneous substrate and coexisting with its vapor phase, a so-called sessile droplet, exhibits a three-phase contact region. Macroscopicly this region can be regarded as a circular contact line. Its line tension affects the equilibrium droplet shape, if the droplet diameter is well below the micrometer range. This situation represents a constrained equilibrium, since the solid phase is not thermodynamically coexisting with the other two phases. Fig. 1.1 shows a nearly perfect dewetting scenario, where a sessile droplet is barely touching the solid surface.
   - For advancing (e. g., spreading) or receding small droplets on a substrate the shape of the moving contact line is influenced by the line tension. Surface inhomogeneities can disort an otherwise moving contact line, on the spot, which is called "pinning" of the contact line [7]. The spreading dynamics is influenced by the line tension for droplet sizes in the micro-/nanometer range [8].
   - The line tension plays an important role in heterogeneous droplet nucleation and growth [9]. In this context nucleation means the onset of condensation, i. e., droplets emerge in a saturated vapor phase. For heterogeneous nucleation this happens preferentially at nucleation sites (on a surface or inside the fluid). For sessile droplets such condensation nuclei can be composed of chemical impurities or geometrical defects. Volatile dust particles, for instance, can serve as condensation nuclei for free (i. e., not sessile) liquid droplets. This line tension has to be distinguished from the line tension for surface crystal nucleation, which will be discussed below.

   (b) Line tension (or contact line tension) of a *sessile liquid wedge*:
   In the limiting case of a macroscopicly large sessile droplet the three-phase contact region resembles a sessile liquid wedge. Its liquid–gas interface is planar, and the contact line is straight. Since this system is effectively two-dimensional, it is perfectly suited as a model system to study its line tension, the wedge line tension. There is a computationally simple relation between the line tensions of a sessile wedge and of a sessile droplet, which will be explained in Chapter 4.

(c) Line tension of a *sessile bubble*:
The inverse scenario to a sessile liquid droplet alludes to a gas bubble that resides on a substrate and is surrounded by liquid. An example are the bubbles that form in a glass of sparkling water and stay at the glass–water interface. A line tension assigned to the three-phase contact line (or region) can be defined like in the case of a sessile liquid droplet.

(d) Line tension of a three-phase contact region for full *three-phase equilibrium*:
In a system of three coexisting phases (i. e., in an unconstrained equilibrium) that form a common contact line, the morphology of this contact line is governed by the line tension. Analogously to a sessile droplet and a wedge, one can distinguish between a *macroscopicly large* lense and a lense of *limited volume* immersed in an interface of two other phases. The macroscopicly large lense corresponds to bulk coexistence (i. e., a planar interface formed by any two of the three phases is thermodynamically stable), so that each of the three phases fills a macroscopicly large spatial region. The lense of finite volume is in coexistence with the other two phases due to an increased pressure in the inside, the so-called Laplace pressure. In the case of bulk coexistence (or a macroscopicly large lense) the three angles between the individual interfaces are described by the Neumann equation. The Young equation represents a special case thereof. However, the angles related to a lense of finite volume are modified by the line tension. The phase of the fluid lense merely needs to be different from the other two phases, it is not restricted to the case of a liquid lense (i. e., a liquid droplet at the interface) or a gas lense (i. e., a gas bubble at the interface). This means that one or several of the three phases could be solid. For a one-component simple fluid the three phases can merely be gas, liquid, and solid; for a binary (or multi-component) simple fluid also three (or more) fluid phases are possible.

(e) *Boundary (line) tension*:
In certain fluid systems with a planar *substrate* and in a state on the prewetting line near a first-order wetting transition, the coexistence between two surface phases with different film thicknesses is possible. The system has a small film thickness, say on the left-hand side, a large film thickness on the right-hand side, and a straight interface between both parts. Then the boundary region is attributed a boundary line tension, shortly named "boundary tension".
Like any liquid–gas interfacial tension also the boundary tension has to be positive for stability reasons. For a negative boundary tension infinitely many interfaces between the two kinds of surface phases would occur in order to reduce the total free energy. Exactly at the wetting transition (cf. Sec. 3.3.5) the boundary tension equals the wedge line tension (cf. Sec. 5.2.1). At the prewetting critical point the two surface phases become identical and consequently the boundary tension vanishes [10].

A boundary tension may be defined analogously for *interfacial wetting* instead of wetting of a solid substrate [10]. Here another fluid phase plays the role of the substrate.

(f) *Substrate boundary line tension*:
Consider a fluid on a geometrically or chemically structured substrate. If there is a line separating one substrate region from the other (e. g., an edge, a wedge, or a chemical step), the associated excess free energy can be regarded as the line tension of such a substrate boundary [11]. Clearly, more complex substrate structures (like geometrical steps of finite height or subsequent chemical stripes [12]) can be studied as well, and the corresponding line tension obtains a size dependence (i. e., it depends on the step height or the stripe width).

(g) Line tension for *droplets on or near particles*:
The interaction of gas bubbles with solid inclusions in a melt or with aqueous drops involves three phases in contact as well. A similar situation exists in emulsions or foams which are stabilized by fine particles. Here the "substrate" consists of spherical or, in general, irregularly shaped and (more or less) hard particles. Furthermore droplets residing on larger solid spheres [13, 14, 15] or cylinders [16] are examples for regularly shaped, but curved "substrates".

(h) Line tension for *surface nucleation at freezing*:
The freezing of a liquid into a solid phase (e. g., a crystal) can either start in the liquid bulk region (homogeneous nucleation) or at an interface with another phase (heterogeneous nucleation). Heterogeneous nucleation can occur, for instance, at an interface with a gas surface, a substrate or an impurity (e. g., in a hard sphere crystal [17, 18]). In the case of surface nucleation at a liquid–gas interface a roughly lense-shaped solid-like nucleus (embryo) emerges. The work to form such a nucleus with a certain number of atoms contains a term related to the perimeter of the lense. Hence this line tension influences the shape of the nucleus and the freezing process [19, 20], particularly since freezing preferably occurs in the three-phase contact region [21].

The freezing lense scenario is similar to the three coexisting phases (with a lense) or the sessile liquid droplet discussed above. For freezing near a gas phase, however, the gas does not have to coexist with the solid and liquid phases, if the number of gas particles is fixed. The case of freezing near a substrate corresponds to a sessile liquid droplet, where now the droplet is solid and the surrounding is liquid.

2. Three-dimensional, complex fluid systems: In this category an example of a line tension is the boundary tension between *lamellar phases*. In systems containing oil, water, and surfactant amphiphilic layers in a lamellar phase can form between water and oil regions for suitable concentrations. Phases with different stack thicknesses can coexist, and boundary line tensions are attributed to the boundaries between them [22]. Thus the situation is in principle comparable to the case of membrane domains (see below). Smectic liquid-crystal multilayers can exhibit coexisting domains with different thicknesses as well, and a line tension is associated with the domain boundaries [23].

3. Quasi-two-dimensional systems:
"Quasi-two-dimensionality" means that one spatial extension of a genuinely three-dimensional physical system is very small, such that it appears to be two-dimensional at first glance. This notion has to be distinguished from "effective two-dimensionality", where the system extended considerably in all three spatial directions contains translational symmetry and can therefore be described by solely two coordinates.

(a) Two kinds of line tensions of a fluid *membrane*:
Line tension also plays an important role in systems which are merely distantly related to liquid drops. The fusion of fluid membranes (i. e., lipid bilayer membranes) is vital in many cell-biological processes. The rate of membrane fusion depends on the line tension of a *hole* (pore) formed in the membrane [24]. The membrane hole line tension has to be positive in order to prevent the membrane from dissolving.
Another line tension related to fluid membranes arises at boundaries of membrane *domains* (so-called "lipid rafts") [25, 26, 27, 28, 29]. The thermal fluctuations of domain boundaries are related to the line tension and can be analyzed by means of flicker spectroscopy [30, 31]. Like surfactants can reduce a surface tension, a class of molecules ("linactants") can reduce this membrane domain boundary line tension [32].

(b) Thin fluid *films*:
A thin fluid film can, e. g., consist of a liquid film on a substrate or a soap film. A soap film represents the symmetrical film case, where either a (surfactant-stabilized) water-film exists between two identical gas phases or an oil film exists between two identical aqueous phases. Viewed in reflected white light against a black background, films becoming gradually thinner loose their white appearance and finally appear black. They are called common black films or Newton black films, if their thickness is either sensitive or not very sensitive on parameter changes.
A line tension can be related to the perimeter of a finite thin film [33, 34]. Very thin films tend to form domains, i. e., finite spatial regions exhibiting a constant film thickness. The curve limiting such a film domain can be attributed a line tension as well, which is called interphase line tension [35].

Since systems containing thin membranes or thin liquid films are quasi-two-dimensional, their line tensions cannot be compared to the line tensions in three-dimensional systems like droplets or liquid lenses.

Among the listed line tensions exclusively the boundary line tension and the membrane hole line tension have to be positive to ensure thermodynamic stability. Hence solely these two line tensions can be regarded as true one-dimensional analogues of the surface tension, if for the latter one has in mind a liquid–gas interfacial tension.

1.5 Technological applications of systems exhibiting a line tension

Possible applications of the physical systems and effects described in the previous section are positioned in the research fields of nanofluidics and surface material science. Fast technological progress in these fields has promoted corresponding fundamental and applied research activities. The general trend towards miniaturization of technical devices also affects devices that handle small amounts of fluids. Shrinking system sizes increase the relevance of line tension effects for the system properties. Some technological applications of the mentioned simple-fluid systems involving line tension effects, especially small sessile droplets, are listed in the following.

1. Lab on a chip: Micro- and nanofluidics deals with the manipulation of small amounts of liquid, which can occur, for instance, in biotechnology, chemistry, and pharmacy. Analogously to the development of micro- and nanoelectronics one aims at very small devices ("lab on a chip"), that accomplish tasks like guided transport, mixing, separation, and controlled chemical reactions of fluids.

2. Coatings: A branch of surface material science is concerned with solid–fluid interfaces. A solid–fluid interface is the "borderland" between a solid phase and an adjacent fluid (liquid or gas). Detailed knowledge about the behavior of such interfaces is relevant for the controlled manipulation of surface-related material properties. Solid–fluid interfaces exist in coatings, easy-to-clean, or self-cleaning surfaces, adhesion, gluing and corrosion due to humidity. Large public interest has been attracted by the effect of *superhydrophobicity*, commonly known as "lotus effect". A rough surface formed by a hydrophobic material can attain very large contact angles, so that (small) sessile

droplets are almost spherical (see Fig. 1.1). The field of applications of superhydrophobic coatings is large and covers, e. g., conservation of buildings and cars, sanitary facilities, housekeeping products, and textiles.

3. Ink applications: In typical ink applications, e. g., in an ink printer, a newspaper printing machine, or when writing with a pen or biro, a paper surface is covered with small amounts of liquid. The shape of the boundary of an ink droplet is crucial for the sharpness of the printing product. Hence to extend the knowledge about the microscopic structure of ink droplets is helpful in order to improve printing technologies.

4. Flotation: Flotation is a widely applied method to concentrate or purify sulphide minerals (like copper, lead, and zinc) or to recycle paper. Air is pumped into an aqueous suspension of ore or used paper, respectively, such that air bubbles form. The difference in wettability of the desired material (metal or paper) and inclusions (minerals or ink remains) is exploited. The air bubbles are intended to carry the inclusions to the surface, where they are removed. The interplay between air bubbles, water, metal/paper, and inclusion particles determines the functioning of the flotation process.

   Undesired inclusions (e. g., silica) in an iron or steel melt can be removed by flotation as well [36]. In order to avoid oxidation, here typically argon instead of air is pumped through the melt. This process depends on the microscopic interplay of liquid metal, inclusions, and argon bubbles.

5. Particle-stabilized emulsions and foams: Emulsions (i. e., a mixture of at least two immiscible liquids, e. g., milk, mayonnaise, or cosmetics) tend to phase-separate (demix) in many cases. The prevailing procedure to stabilize an emulsion employs tensides (emulsifiers). However, also small solid particles can stabilize an emulsion. The microscopic structure and the line tension of the three-phase contact region on the surface of such a particle is responsible for the emulsion stability. Similar thoughts hold for particle-stabilized foams, i. e., small gas bubbles bordered by thin liquid or solid walls.

1.6 Current state of research on substrate-related line tensions

A line tension can be defined for various systems where an excess free energy is attributed to a linear structure. The current state of research on line tensions of systems involving simple fluids is presented in this and the following section, Sec. 1.7. These systems either comprise an inert phase (so do, for instance, sessile liquid wedges, sessile droplets, or two coexisting surface phases) or contain three thermodynamically coexisting phases. For simplicity here the case of an inert third phase is considered as containing a "substrate", while the case of three coexisting phases is considered as containing no substrate.

A broader review of theoretical and experimental line tension studies can be found in Ref. [37]. Theoretically determined line tension values are of the order of 10^{-12} to 10^{-10} N, whereas experimental values span a wide range from 10^{-12} to 10^{-6} N [37, 38].

First, there are fluid systems which involve a substrate and for which a line tension can be identified. The case of deformable substrates giving rise to an effective line tension [5, 6, 39] is not discussed here. The second case of three coexisting phases (i. e., without a "substrate") is discussed in Sec. 1.7.

1.6.1 Sessile liquid wedge

Experiments on sessile liquid wedges are — strictly speaking — impossible to arrange, since an infinitely long, straight three-phase contact region cannot exist in reality. This situation exists merely approximately in the three-phase contact region of a very large sessile droplet. Gravity has to be taken into account for the overall shape of a large droplets. But counterintuitively Young's law still holds in the presence of gravity [40, 41]. (Other experimental and theoretical studies claim a non-trivial relation between the droplet size and its contact angle due to gravity [42], thus the topic is still controversal.)

For sessile liquid droplets a local contact angle can be introduced in addition to the macroscopic contact angle given by Young's law. For this purpose a spherical cap is fitted to the top of the droplet, and the local contact angle is defined as the inclination of the spherical cap at the substrate surface. However, there is no generally accepted way to define a local contact angle of a sessile liquid wedge, hence merely the macroscopic contact angle is an observable here.

Theoretical work on the wedge geometry offers a convenient way to treat the sessile wedge under idealized conditions, e. g., without substrate inhomogeneities, with a perfectly straight contact line, and with perfectly planar interfaces. There is a connection between the line tension of a sessile wedge and that of a sessile droplet (cf. Chapter 4).

In 1981 Tarazona and Navascués presented the first theory of wedge line tension based on statistical mechanics [43]. Their choice of the system volume corresponds to a cylinder around the three-phase contact region. The particle density distribution was assumed to be formed by the macroscopic step-like profiles of the three participating planar interfaces (solid–gas, solid–liquid, and liquid–gas) plus a function which decays exponentially in the direction perpendicular to the substrate and depends on the lateral coordinate. Both the circular shape of the cross-section of the system and the crude approximation of the actual density profile are questionable and limit the quantitative validity of their results.

In 1992 Indekeu analyzed the behavior of the wedge line tension close to wetting in an interface displacement model (IDM) [44, 45]. An IDM is a simple kind of effective interface Hamiltonian, which accounts for the effective interface potential $\omega(l)$ and an increase of the liquid–gas interfacial area due to a non-horizontal contour $l(x)$. The asymptotic behavior of the line tension is expected to display universal features that are independent of details of the model system. Hence the IDM is a helpful tool, even though molecular details are not resolved. The asymptotic behavior of the wedge line tension upon approaching a wetting transition was predicted (cf. Sec. 3.3.5). Depending on the range of the interactions and the order of the wetting transition, four wetting scenarios can be distinguished:

- **Short-ranged** forces (i. e., short-ranged fluid–fluid interactions as well as short-ranged substrate–fluid interactions):
  - **First-order** wetting transition:

$$\tau \simeq \tau_{\text{wetting}} + c_1\,\theta\,\ln\theta + c_2\,\theta + \mathcal{O}\left(\theta^2\right) \tag{1.4}$$

$$\rightarrow \tau_{\text{wetting}} \quad \text{for} \quad T \nearrow T_{\text{w}} \tag{1.5}$$

    with $0 < \tau_{\text{wetting}} < \infty$ and the contact angle θ expressed as radian measure. Hence τ reaches a *positive, finite* value at the wetting transition temperature T_{w} and approaches it from below. The wedge contour $l(x)$ at T_{w} behaves as

$$l(x) \sim \ln x \tag{1.6}$$

    for large values of x.

– **Critical** wetting (second-order wetting transition):

$$\tau \sim -\theta \to 0 \quad \text{for} \quad T \nearrow T_\mathrm{w} \tag{1.7}$$

The *vanishing* limiting value at T_w is reached from below as well. The contour $l(x)$ reaches its asymptote, i. e., a planar solid–gas interface far from the three-phase contact region on the gas side and a planar liquid–gas interface far from the contact region on the liquid side, from above. In other words, the kink of the asymptote at the contact line is smeared out.

- **Long-ranged** forces (i. e., long-ranged fluid–fluid interactions or/and long-ranged substrate–fluid interactions): Here unretarded van der Waals forces are assumed.

  – **First-order** wetting transition: Upon approaching T_w the line tension obeys

$$\tau \sim -\ln\theta \to +\infty \quad \text{for} \quad T \nearrow T_\mathrm{w}. \tag{1.8}$$

The line tension changes sign from negative to positive values upon approaching T_w and finally *diverges* at wetting. The contact angle θ vanishes as

$$\theta \sim t^{1/2} \to 0 \quad \text{for} \quad t \searrow 0 \tag{1.9}$$

with the reduced temperature $t := (T_\mathrm{w} - T)/T_\mathrm{w}$, that corresponds to the relative temperature deviation from the wetting temperature. The contour profile $l(x)$ at T_w is given by

$$l(x) \sim \left(x - x_\mathrm{tp}\right)^{1/2} \tag{1.10}$$

with a (diverging) turning point $x_\mathrm{tp} \sim t^{-1}$. Close to T_w the actual contour corresponds to an interpolation between the above function (for relativeley small values of l) and the planar wedge boundary condition (for large values of l). The cross-over point x_cp, up to which the approximation by the above function is valid, also diverges. Since $x_\mathrm{cp} - x_\mathrm{tp}$ diverges as well, the square-root-like profile in Eq. (1.10) can evolve at wetting. τ approaches its singularity continuously, while the film thickness diverges abruptly.

  – **Critical** wetting: The line tension close to T_w can be described by

$$\tau \sim -\theta^{1/3} \to 0 \quad \text{for} \quad T \nearrow T_\mathrm{w}. \tag{1.11}$$

The line tension is negative close to wetting and finally *vanishes* at wetting. The contact angle θ vanishes as

$$\theta \sim t^{3/2} \to 0 \quad \text{for} \quad t \searrow 0. \tag{1.12}$$

Qualitatively the contour $l(x)$ behaves like in the case of critical wetting with short-ranged forces, i. e., it reaches its asymptote from above for small as well as for large values of the x coordinate. Upon approaching T_w the film thickness l_0 diverges here like

$$l_0 \sim t^{-1}. \tag{1.13}$$

Indekeu's IDM employs a square-gradient approximation for the expression of the interfacial area. To incorporate the full, unapproximated expression for this area neither complicates the calculation much nor does it change the asymptotic behavior of the line tension (and boundary tension) [46].

Numerical line tension calculations are restricted to finite system sizes. The influence of a macroscopic, but finite system size on the leading order behavior of a wedge line tension was analyzed with scaling arguments by Indekeu and Dobbs for an interface displacement model [47]. For long-ranged, van-der-Waals–like interactions (decaying as

r^{-6} in leading order) the line tension at first-order wetting diverges logarithmically with increasing (vertical) system size. For short-ranged interactions the finite size correction to the line tension at first-order wetting vanishes exponentially with increasing (vertical) system size. The slope of the line tension as a function of the contact angle diverges (to $-\infty$) linearly in the (vertical) system size $L_\perp$, i. e., $\mathrm{d}\tau/\mathrm{d}\theta|_{\theta=0^\circ} \sim -L_\perp$, both for first-order and critical wetting.

In 1995 Perković, Blokhuis and Han [48] presented the first (numerically) exact calculations of the wedge line tension (and the boundary tension) for a continuous model system (i. e., not a lattice model). This model system is not related to realistic fluid–fluid interactions. By fitting expressions containing the value at T_w and the first two correction terms to the obtained line tension (and boundary tension) data, they found excellent agreement with preditions by Indekeu [44] and Blokhuis [49]. The employed free-energy functional corresponds to a square-gradient approximation, i. e., the free energy density depends locally on the density and its gradient. Several further assumptions on the specific form of the involved functions are made, basically in order to obtain coexistence of two fluid phases and a partial wetting scenario.

Within a density functional theory the morphology of the three-phase contact region and the line tension of a sessile liquid wedge was analyzed on a semi-microscopic level by Getta and Dietrich [50, 51] as well as Bauer and Dietrich [11, 52] in the late 1990s. The microscopic details of the fluid–fluid and substrate–fluid interactions were taken into account. However, the continuous particle density distribution function was replaced by a piecewise constant sharp-kink distribution. This sharp-kink theory represents the first line tension calculations for a phenomenological model system. This sharp-kink theory is reviewed and partially extended in Chapter 7, since it serves as comparison for the fully microscopic approach presented in this work.

In 1999 Dobbs applied Indekeu's IDM theory to a phenomenological interface potential [53]. This was the first calculation of the (wedge) line tension for parameter values of a specific, actual system, even though molecular details were merely taken into account via a coarse-grained IDM description. The results for the line tension (and the boundary tension) upon approaching T_w are in agreement with Indekeu's predictions.

Fluctuations of the contact line and the liquid–gas interface were addressed in a phenomenological model by Clarke in 1992 [54]. The influence of the line tension on the mean square fluctuation magnitude was analyzed. It was found that a positive line tension value modifies the fluctuations near a wetting transition. For a vanshing line tension value the contact line fluctuations are larger than for a liquid–gas interface. For negative line tension values, however, the model breaks down.

1.6.2 Sessile liquid droplet

In a macroscopic picture the shape of an axisymmetric sessile droplet results from the minimization of the the free energy expression for the system under the constraint of a certain fixed amount of liquid in the droplet (e. g., a certain droplet volume, if the liquid is incompressible). The corresponding Euler-Lagrange equation for this variational problem is called shape equation or Young-Laplace equation,

$$\Delta p \; + \; \varrho_\mathrm{m}\, g\, h(r) \;=\; 2\,\sigma_\mathrm{lg}\, H(r). \tag{1.14}$$

Here Δp is the Laplace pressure (i. e., the pressure difference between inside and outside the drop), ϱ_m the (bulk) liquid mass density, g the gravitational acceleration, $h(r)$ the droplet surface, σ_lg the liquid–gas interfacial tension, and $H(r)$ the mean curvature of the surface h at the point r of the drop base area.

Gravity can be neglected for sufficiently small droplets, i. e., if the droplet is small compared to the *capillary length*

$$l \;=\; \sqrt{\frac{\sigma_{\mathrm{lg}}}{\varrho_{\mathrm{m}}\, g}}. \tag{1.15}$$

For water under ambient conditions one finds $l \simeq 2.6$ mm, thus water droplets with a diameter below approximately 1 mm can be regarded as free from gravitational influences. In this case the solution of the shape equation gives a *spherical cap*.

A small sessile droplet with a radius below 1 mm, but above approximately 1 μm, macroscopicly resembles a spherical cap. This shape is governed by the surface free energy alone. Minimizing the surface free energy with respect to the base radius and the droplet height, again keeping the volume constant, leads to Young's law for the contact angle.

However, for very small sessile droplets below the micrometer scale deviations of the intrinsic contact angle θ (i. e., the equilibrium contact angle on a planar, homogeneous, inert substrate) from the value θ_0 predicted by the Young equation occur. These deviations have been attributed for decades to the line tension almost exclusively via the *modified Young equation* [55],

$$\cos\theta \;=\; \cos\theta_0 \;-\; \frac{\tau}{\sigma_{\mathrm{lg}}\, r}, \tag{1.16}$$

which was proposed by Boruvka and Neumann in 1976. Here, r denotes the radius of the circular droplet base and the line tension τ is regarded as a constant which is independent of the droplet size. Based on this equation positive or negative values of the line tension are commonly interpreted as follows: A positive line tension value increases the contact angle, thus the droplet tends to shrink its perimeter. Analogously a negative line tension value decreases the contact angle, and the droplet perimeter is expanded.

In 1997 Marmur [56] pointed out difficulties in interpreting experimental results and questioned the connection between the physical line tension and the value obtained from the modified Young equation. He claimed the line tension to depend on the contact angle and suggested an approximative correction of the modified Young equation. Further improvements of the modified Young equation were proposed [57]. Very recently Schimmele, Napiórkowski, and Dietrich [4] introduced an equation for the contact angle of a sessile liquid droplet — which is called *"corrected modified Young equation"* in the present work — that involves additional quantities which are comparable to the line tension term. Thus, in view of the above mentioned corrected modified Young equation, most experimental results did not determine the bare line tension, but a sum of the line tension and several other terms.

The earliest *molecular dynamics (MD) simulations* of a sessile droplet were carried out in the early 1990s [58]. In the recent years large improvements of the MD techniques were made. E. g., a droplet consisting of a Lennard-Jones fluid sitting on a homogeneous Lennard-Jones (9–3) substrate (cf. Sec. 3.3.1) was studied [59, 60]. Besides a homogeneous LJ substrate also a crystal (fcc lattice) was investigated [61]. Further examples are MD simulations of water molecules on polymer surfaces [62] or on amorphous silica [63]. MD simulations represent an alternative to a density functional theory (DFT) approach in order to obtain the equilibrium particle density distribution. The line tension could be determined from this density distribution by means of the corrected modified Young equation mentioned above. The number of particles in a MD simulation is limited: In the LJ fluid simulations mentioned above the droplet contained at most around 120 [61], 18000 [59] or 70000 [60] particles, respectively. The water simulations mentioned contained up to 600 water molecules [63] or few thousands [62], respectively. Hence, in order to reach

the limiting case of large droplets and to substantiate the MD results, one is still obliged to use other techniques like DFT for axisymmetric systems (cf. Sec. 9.3).

For a broader overview of the methods to address fluid properties some other — mainly numerical — methods applicable to fluids should be mentioned as well: Results from *Monte Carlo (MC) simulations* are regarded as quasi-exact, since they emerge from a sort of "computer experiment". A system with an effectively two-dimensional equilibrium particle distribution function $\varrho(x, z)$ has to be simulated in three dimensions nevertheless, in order to capture all fluctuations. In 2001 Milchev and Milchev presented results from a MC study on sessile droplets consisting of a polymer melt [64]. For nanodroplets they observed strong distortions of the spherical droplet shape.
A lattice model based on the Ising model offers an analytical way (using cluster expansion techniques) to address the line tension of a sessile droplet [65]. However, the handling of this very crude model system is very sophisticated and does not open the way towards a more realistic description.
Integral equation theories [66] originate mainly from the 1960s and yield approximative analytical results in many cases. Nevertheless in general the results have to be obtained numerically. This is an alternative route to obtain fluid properties, but to my knowledge sessile droplets or wedges have not yet been analyzed with this method.
Density functional calculations presumably offer the most direct and numerically efficient access to the morphology of the three-phase contact region and the line tension value. This is the reason, why in this work DFT has been chosen as method of calculation.

Experiments on line tensions of sessile liquid droplets or sessile liquid wedges (as parts of a larger droplet) mainly rest upon contact angle measurements and an interpretation via the modified Young equation. As mentioned above this approach implies that not the bare line tension value is extracted. Furthermore nanoscale substrate inhomogeneities play an important role for the sessile droplet shape and limit the quantitative accuracy in all substrate-related line tension measurements [67].

Scanning force microscopy (SFM), a variant of atomic force microscopy (AFM), is frequently used to determine liquid surface topographies with a high resolution of a few nanometers [68]. Pompe and Herminghaus evaluated the line tension from measured contour profiles $l(x)$ on the basis of the sharp-kink line tension theory (cf. Chapter 7) [68, 69]. This approach directly yields (wedge) line tension values and does not suffer from the shortcomings of the modified Young equation. The quantitative agreement with the sharp-kink theory is reasonable. For a first-order wetting transition line tension values ranging from -200 pN for large contact angles (around 55°) up to $+25$ pN for small contact angles (around 5°) were found [69]. A predicted line tension divergence could not be observed, either since such small contact angles were not obtained or since a short-ranged interaction might have dominated and possibly leads to a finite positive value [69]. In order to minimize the perturbation of the droplet exerted by the AFM tip, recently AFM experiments in *noncontact* mode were performed by Checco and coworkers [70].

The most widespread experimental technique to analyze the shape of microscopic sessile droplets is light interferometry, a variant of optical microscopy. An experimental setup is described in Ref. [71]. From the interference patterns the drop shape can be reconstructed (as described, e. g., in Ref. [72]). The contact angle is obtained by fitting a spherical cap to the top of the droplet and is usually interpreted in terms of the modified Young equation.

Electron micriscopy represents another method to detect the shape of sessile droplets with a high resolution [73]. Once the shape profile of a small droplet is obtained, the (microscopic) contact angle θ can be obtained by fitting a spherical cap to the data points. For larger droplets, above a base diameter of approximatively a micrometer, gravity plays

a role and the contact angle has to be determined in a more evolved fashion [74, 75].

The droplet material does not have to be liquid at room temperature; metals, for instance, can form sessile liquid droplets at high enough temperatures as well (e. g., gold on alumina [76] or graphite [77] at 1100° C).

A widely applied experimental technique to manipulate droplets is based on the phenomenon called *electrowetting*. A review on this topic can be found in Ref. [78]. The basic setup contains an electrode as substrate, a sessile liquid droplet consisting of electrically polar particles and a second electrode in contact with the droplet. The role of the second/upper electrode is usually played by a needle immersed into the liquid or by the ceiling in a closed nano-/microfluidic device which touches the droplet. If a voltage is applied between the two electrodes, the charged fluid particles are exposed to an external electrical field, which changes the droplet shape and may even lead to wetting, i. e., the wetting temperature becomes voltage dependent. The voltage dependence of the contact angle (determined as the contact angle of a spherical cap fitted to the top of the droplet) is prevalently described by the Young-Lippmann equation,

$$\cos\big(\theta(U)\big) \;=\; \cos\big(\theta(U=0)\big) \;+\; \tfrac{\varepsilon_\mathrm{r}\,\varepsilon_0}{2\,\sigma_\mathrm{lg}\,d}\,U^2, \tag{1.17}$$

where U is the voltage, d the thickness of the insulating layer between the substrate electrode and the droplet, ε_0 the dielectric susceptibility of vacuum, ε_r the relative permittivity of the dielectric layer, and σ_lg the liquid–gas interfacial tension. There are other extensions of Young's law due to different aspects of electro-wetting systems, such as an ionic layer (acting as a capacitor), a dielectric liquid, or a finite liquid resistance (which is considered to be responsible for contact angle saturation at high voltages) [79]. If the voltage is switched off, the system tends to restore the initial configuration (apart from hysteresis and non-equilibrium effects). The local contact angle (measured microscopicly in the three-phase contact region), however, resembles the angle given by Young's law, i. e., the local contact angle is independent of the applied voltage [80, 81, 82].
The electrowetting effect can be exploited experimentally or technologically in order to discontinuously switch or gradually control the wetting behavior of the fluid simply by changing the applied voltage. Moving the immersed electrode needle or using a patterned electrode with different individually addressable areas is a method to steer the droplet on the substrate (e. g., in a microfluidic device) [83] or to move single particles within a droplet [84].
Contributions to the line tension stemming from substrate/fluid charges or external electric fields have been been addressed on a mechanical or local thermodynamic level in recent years [85, 86]. However, a microscopic treatment seems to be out of reach yet.

Certainly droplet *dynamics* is a broad and interesting field of research as well. Even though dynamics is beyond the scope of this work, some issues emerging there are briefly mentioned. For a spreading small droplet intertia seem to influence the kinetics in the first few milliseconds [87]. A sliding droplet (e. g., due to gravity on an inclined substrate) contains an advancing front and a receding back part. The contact angles in these parts, the advancing and receding contact angle, are usually quite different (called "contact angle hysteresis"), and the equilibrium contact angle attains values between them. Furthermore advancing and receding contact angles change (relax) slowly with time [88]. An advancing or receding droplet front is also present for condensing or evaporating droplets, respectively. Sliding drops on an inclined substrate can be investigated by Lattice-Boltzmann simulations [89, 90, 91]. Lattice-Boltzmann methods constitute an efficient way to simulate dynamic behavior of fluids. The fluid dynamics is split into propagation and collision processes on a discrete lattice. These methods form a simulation counterpart to analytical hydrodynamic calculations (typically based on the Navier-Stokes equation) or their

numerical implementations (which yield numerical solutions of the hydrodynamic equations and not simulation results).
Substrate inhomogeneities lead to a threshold angle for the substrate inclination. For angles smaller than this threshold angle the droplet base does not move (and solely the upper droplet part bends). An advancing contact line might be stopped by geometric or chemical obstacles, which is called "contact line pinning". It is a matter of interest how the contact line interacts with defects and to what extent the line tension is changed thereby.

Coalescence of droplets or conversely rupture of large droplets into smaller ones raises the question of *stability* of droplets [92] or certain liquid structures. The line tension is important for these processes. The dynamics of droplets in micro-/nanofluidic channels — which can be open (like railway tracks) or closed (like tubes) — is another, lively field of research. (For the topic of stability and micro-/nanofluidics see the comments and references in Sec. 9.2.3 around page 132.) Droplets on a vibrating substrate [93] and bouncing droplets (e. g., on a microstructured superhydrophobic substrate [94]) represent further topics within the research on droplet dynamics.

Stationary shapes of liquid droplets in hydrodynamic flow and localized by optical tweezers yield an effective line tension, which results from a competition of the bare line tension with dipole and hydrodynamic forces [95]. The shape of the droplet reacts on external manipulations, which brings the elasticity of the three-phase contact line into play [96].

1.6.3 Surface phase coexistence in a prewetting scenario

In a prewetting scenario (cf. Sec. 3.3.5) two surface phases of a fluid on a substrate can coexist. The thickness of the liquid-like film forming near the substrate is different for the two surface phases. In the case of a straight interfacial region between two of these phase regions, a *boundary (line) tension* can be introduced (cf. Sec. 5.2.1 for details of the definition and the reference system). At the wetting transition the boundary tension is expected to equal the line tension [Eq. (5.7)].

In 1995 Perković, Blokhuis, and Han calculated the boundary tension of a model system numerically exact [48]. In 2005 the boundary tension τ_b was obtained by Monte Carlo simulations [97].

1.6.4 Structured substrates

Furthermore geometrically or chemically structured substrates can give rise to a linear free energy excess as well. This free energy per unit length of the structural line is called *"substrate boundary line tension"*. The simplest case is a sharp geometrical change of the otherwise planar substrate substrate (i. e., a substrate composed of a solid edge or wedge) or a chemical "step", i. e., a sharp straight line (or plane) separating two chemically different substrate regions. The substrate boundary line tension is described in more detail in Sec. 5.2.2. For the distantly related system of an electrolyte on an electrode substrate with a step-like shape, the line tension of this step (called "step line tension") has already been evaluated (by solving the Poisson-Boltzmann equation) [98].

1.7 Current state of research on line tensions in substrate-free systems

Besides line tensions in systems containing a substrate, a line tension can arise in systems without an inert substrate, i. e., in unconstrained three-phase coexistence. Such a situation exists, e. g., in a system containing a *liquid lense* at a liquid–gas interface. If the three phases α, β, and γ are at bulk coexistence, the interfaces formed by pairs of them are planar far away from the three-phase contact region. The angles between the three planes set up by the dividing interfaces far away from the contact line and the involved interfacial tensions are related by a force balance in the Neumann triangle,

$$\sigma_{\alpha\gamma} \;=\; \sigma_{\alpha\beta}\cos(\pi-\alpha_0) \;+\; \sigma_{\beta\gamma}\cos(\pi-\gamma_0), \tag{1.18}$$

that ensures mechanical equilibrium. From this expression the *Neumann equation* follows:

$$\sigma_{\alpha\gamma} \;+\; \sigma_{\alpha\beta}\;\cos\alpha_0 \;+\; \sigma_{\beta\gamma}\cos\gamma_0 \;=\; 0. \tag{1.19}$$

However, if a liquid lense of finite size (with radius r) is considered, deviations from the above equation occur. Traditionally this difference is assigned to the line tension by means of the *modified Neumann equation* [55],

$$\sigma_{\alpha\gamma} \;+\; \sigma_{\alpha\beta}\;\cos\alpha \;+\; \sigma_{\beta\gamma}\cos\gamma \;=\; \frac{\tau}{r}. \tag{1.20}$$

For a macroscopicly large liquid lense (i. e., $r \to \infty$) the situation of three planar interfaces intersecting at the contact line is recovered and the angles between the planes of dividing interfaces are not changed by the line tension. Very recently it has been found by Schimmele, Napiórkowski, and Dietrich [4] that the modified Neumann equation should be extended towards an equation, which is called *"corrected modified Neumann equation"* in the present work. This equation distinguishes between the role of the line tension and additional quantities, which are comparable to the line tension term and therefore cannot be neglected. Coexistence of three fluid phases is not possible for a one-component simple fluid, however a binary mixture would form the simplest model system suited for this purpose.

Up to now line tension experiments in unconstrained three-phase coexistence used the modified Neumann equation in order to attribute deviations from the Neumann equation to the line tension term appearing in that equation. However, in view of the above mentioned corrected modified Neumann equation, the experimental results did not determine the bare line tension.

In 1992 Szleifer and Widom [99] studied the line tension behavior of a two-component fluid model system upon approaching a wetting transition. In this substrate-free system wetting means that one of the angles between two adjacent phases vanishes. The two density profiles are described by approximate functions. The model free-energy functional is based on a square-gradient approximation (i. e., it depends locally on the densities and their gradients).

Recently Koga and Widom studied the line tension in unconstrained three-phase coexistence [100, 101]. The line tension and the boundary tension were analyzed for a model system that exhibits a first-order wetting transition [100]. The line tension upon approaching critical wetting was feasible within a closely related model system [101]. The specific form of the free energy expressions in these two studies allows to exploit a known formula (namely the Kerins-Boiteux integral), in order to calculate the line tension in a convenient way. An advantage of these model systems is to be able to study the line tension behavior close to wetting. There is strong numerical evidence that the predictions

from Indekeu's IDM for the line tension behavior upon approaching a wetting transition are valid also for these model systems.

In 2005 Djikaev performed a Monte Carlo simulation of a rather simple ternary mixture model system in the three-phase contact region in order to evaluate the line tension [102].

Experimentally obtained line tension values for liquid lenses are typically smaller than those for sessile droplets [38]. The setup without a substrate has the advantage that the otherwise strong influence of substrate inhomogeneities is not present. An oil lense at an otherwise planar air–water interface was studied by Takata and co-workers in 2005 [103]. They obtained experimental line tension values for different surfactant concentrations in water. Seven such values are reported, which vary between -138 pN and $+24$ pN. However, the dependence on lense size and the experimental errors were not discussed.

Fluctuations of the contact line and the three interfaces were investigated by Clarke [104]. This analysis represents an extension of the fluctuation model for a sessile liquid wedge [54] [see Subsec 1.6.1].

2 Classical density functional theory

Density functional theory (DFT) was first invented for studying the ground state (at temperature $T = 0$) of quantum mechanical (electronic) systems. The fundamental principles were developed by Hohenberg and Kohn [105] in 1964 and by Kohn and Sham [106] in 1965.
In the same year 1965 Mermin [107] studied electronic DFT for non-zero temperatures and derived a variational principle for the probability distribution function in the grand canonical ensemble. This work facilitated the transfer of the ideas of electronic DFT to fluid systems. Reviews of classical DFT are given, e. g., in Refs. [108], [109], and [110].

Many interactions among fluids are based on quantum mechanical effects. Masking this background, DFT for fluids treats particle interactions as classical potentials which, e. g., might depend on the interparticle distance, their orientation and their charge. In order to distinguish between the DFT for quantum mechanical systems and the DFT for fluids, the latter is called "classical" DFT.

2.1 Basic principles of classical DFT

2.1.1 Equilibrium density distribution ϱ

The central quantity in classical DFT is the equilibrium one-particle density ϱ. In a homogeneous system this function is a constant, while in an inhomogeneous systems it depends on the position, i. e., $\varrho = \varrho(\mathbf{r}) \equiv \varrho(x, y, z)$. The density ϱ is usually treated in the grand canonical ensemble. This means that the natural variables of the fluid system, temperature T, volume V, and chemical potential μ, are fixed, while their conjugate counterparts, entropy S, pressure p, and number of particles N are functions of T, V, and μ.

2.1.2 Theorems of classical DFT

Classical DFT deals with the relation between the density ϱ and an external potential $V_{\text{ext}}(\mathbf{r})$. It can be shown [108] that the external potential $V_{\text{ext}}(\mathbf{r})$ uniquely follows from a equilibrium density $\varrho_{\text{eq}}(\mathbf{r})$. The inverse statement, that the equilibrium density follows from the external potential, also holds, except for a system in a state of phase-coexistence. (For a quantum mechanical system such a state corresponds to a degenerate ground-state.)

Classical DFT rests on two theorems: First, there is a functional $\Omega[\varrho]$ of the density function $\varrho(\mathbf{r})$, which equals the grand potential Ω_{eq}, if the *equilibrium* density distribution $\varrho_{\text{eq}}(\mathbf{r})$ is inserted,

$$\Omega_{\text{eq}} \;=\; \Omega[\varrho_{\text{eq}}]. \tag{2.1}$$

Second, this density functional obeys a variational principle. For a non-equilibrium distribution $\varrho(\mathbf{r})$ the value of the functional is larger than the grand potential,

$$\Omega[\varrho] \;>\; \Omega[\varrho_{\text{eq}}] \;=\; \Omega_{\text{eq}}. \tag{2.2}$$

However, the exact density functional $\Omega[\varrho]$ is unknown in most cases. Hence a suitable approximation for the functional has to be constructed.

2.1.3 Density functional $\Omega[\varrho]$

The density functional can be separated into

$$\Omega[\varrho] \;=\; \mathcal{F}[\varrho] + \int_{\mathbb{R}^3} \mathrm{d}\mathbf{r}\; \varrho(\mathbf{r})\; (V_{\mathrm{ext}}(\mathbf{r}) - \mu) \tag{2.3}$$

with an "intrinsic" free energy functional $\mathcal{F}[\varrho]$. $\mathcal{F}[\varrho_{\mathrm{eq}}]$ is the "intrinsic" free energy, since the free energy contribution from an external field is left out here. Keeping this in mind, the functional $\mathcal{F}$ is simply called free energy functional.

The free energy functional is divided into an ideal gas contribution and an excess part,

$$\mathcal{F}[\varrho] \;=\; \mathcal{F}_{\mathrm{id}}[\varrho] \;+\; \mathcal{F}_{\mathrm{ex}}[\varrho]. \tag{2.4}$$

The intrinsic free energy functional of an ideal gas, which consists of point-particles with a mass m and without any interactions, is exactly known as

$$\mathcal{F}_{\mathrm{id}}[\varrho] \;=\; \mathrm{k_B}T \int_{\mathbb{R}^3} \mathrm{d}\mathbf{r}\; \varrho(\mathbf{r}) \left(\ln\left[\lambda^3 \varrho(\mathbf{r})\right] - 1 \right) \tag{2.5}$$

with the thermal de Broglie wavelength $\lambda = h/\sqrt{2\pi m\, \mathrm{k_B}T}$ and the Planck constant h. However, the density functional $\Omega[\varrho]$ does not depend on λ [Eq. (2.17)] and therefore not on the mass m of the particles.

The interaction among the fluid particles is reflected by the excess free energy functional $\mathcal{F}_{\mathrm{ex}}[\varrho]$. The fluid–fluid pair interaction potential $\phi_{\mathrm{ff}}(r)$ with a distance r between two interacting particles can be separated into an attractive and a repulsive part,

$$\phi_{\mathrm{ff}}(r) \;=\; \phi_{\mathrm{ff}}^{\mathrm{rep}}(r) \;+\; \phi_{\mathrm{ff}}^{\mathrm{att}}(r). \tag{2.6}$$

The excess free energy functional can be decomposed as well,

$$\mathcal{F}_{\mathrm{ex}}[\varrho] \;=\; \mathcal{F}_{\mathrm{ex}}^{\mathrm{rep}}[\varrho] \;+\; \mathcal{F}_{\mathrm{ex}}^{\mathrm{att}}[\varrho]. \tag{2.7}$$

The functionals $\mathcal{F}_{\mathrm{ex}}^{\mathrm{rep}}[\varrho]$ and $\mathcal{F}_{\mathrm{ex}}^{\mathrm{att}}[\varrho]$ depend on the total interaction potential $\phi_{\mathrm{ff}}(r)$ in general. Widely used approximations [cf. Eq. (2.52)], however, allow to regard $\mathcal{F}_{\mathrm{ex}}^{\mathrm{rep}}[\varrho]$ as determined solely by $\phi_{\mathrm{ff}}^{\mathrm{rep}}(r)$ and $\mathcal{F}_{\mathrm{ex}}^{\mathrm{att}}[\varrho]$ as determined solely by $\phi_{\mathrm{ff}}^{\mathrm{att}}(r)$.

The repulsive potential is usually approximated by a hard-sphere (HS) potential. Thus the repulsive excess free energy functional is replaced by a hard-sphere excess free energy functional,

$$\mathcal{F}_{\mathrm{ex}}^{\mathrm{rep}}[\varrho] \;\simeq\; \mathcal{F}_{\mathrm{ex}}^{\mathrm{HS}}[\varrho]. \tag{2.8}$$

The excess free energy functional of a HS fluid is well described by a microscopicly based theory, the fundamental measure theory (cf. Sec. 2.2). The attractive part is treated by perturbation theory (cf. Sec. 2.3).

2.1.4 Euler-Lagrange equation

General form of the Euler-Lagrange equation:
In order to find the equilibrium density distribution for a given functional, the variational principle, Eq. (2.2), is applied. The functional derivative has to vanish for the equilibrium density profile,

$$\left.\frac{\delta\Omega}{\delta\varrho(\mathbf{r})}\right|_{\varrho(\mathbf{r})=\varrho_{\mathrm{eq}}(\mathbf{r})} \;\stackrel{!}{=}\; 0. \tag{2.9}$$

This equation is called Euler-Lagrange equation. From here on the index "eq", indicating an equilibrium particle density distribution, is suppressed and $\varrho(\mathbf{r})$ is — depending on the

context — used both for an arbitrary density profile and the solution of the Euler-Lagrange equation. For the density functional at hand [Eqs. (2.3) and (2.4)] the Euler-Lagrange equation reads

$$\frac{\delta\Omega}{\delta\varrho(\mathbf{r})} \;=\; \frac{\delta\mathcal{F}_{\mathrm{id}}[\varrho]}{\delta\varrho(\mathbf{r})} + \frac{\delta\mathcal{F}_{\mathrm{ex}}[\varrho]}{\delta\varrho(\mathbf{r})} + V_{\mathrm{ext}}(\mathbf{r}) - \mu \;\stackrel{!}{=}\; 0. \tag{2.10}$$

Chemical potential μ:
In the canonical ensemble, where the free energy is the appropriate thermodynamic potential, for a homogeneous system with constant density ϱ_0 (and volume V and number of particles, N) the differential relation

$$\mathrm{d}F \;=\; -S\,\mathrm{d}T - p\,\mathrm{d}V + \mu\,\mathrm{d}N \tag{2.11}$$

holds. The *chemical potential* μ is given by

$$\mu \;=\; \left.\frac{\partial F}{\partial N}\right|_{T,V} \;=\; \left.\frac{\partial f}{\partial \varrho}\right|_{T,V;\,\varrho=\varrho_0} \;=\; \left.\frac{\delta\mathcal{F}}{\delta\varrho(\mathbf{r})}\right|_{\varrho(\mathbf{r})=\varrho_0}. \tag{2.12}$$

Since the free energy density f can be decomposed into two contributions, f_{id} and f_{ex}, the chemical potential is also separable into the chemical potential of an ideal gas and an excess chemical potential,

$$\mu \;=\; \mu_{\mathrm{id}} + \mu_{\mathrm{ex}} \;=\; \left.\frac{\partial f_{\mathrm{id}}}{\partial \varrho}\right|_{T,V} + \left.\frac{\partial f_{\mathrm{ex}}}{\partial \varrho}\right|_{T,V}. \tag{2.13}$$

For an ideal gas with constant density $\varrho(\mathbf{r}) = \varrho_0$ the chemical potential μ_{id} follows from Eqs. (2.5) and (2.13),

$$\mu_{\mathrm{id}} \;=\; \mathrm{k_B}T\,\ln(\lambda^3\varrho_0). \tag{2.14}$$

This means that the density ϱ_0 is related to the ideal gas chemical potential via $\varrho_0 \;=\; e^{\beta\mu_{\mathrm{id}}}/\lambda^3$.

Rearranged Euler-Lagrange equation:
The functional derivative $\delta\mathcal{F}_{\mathrm{id}}[\varrho]/\delta\varrho(\mathbf{r})$ can be obtained from Eq. (2.5) as well,

$$\frac{\delta\mathcal{F}_{\mathrm{id}}[\varrho]}{\delta\varrho(\mathbf{r})} \;=\; \mathrm{k_B}T\,\ln\bigl(\lambda^3\varrho(\mathbf{r})\bigr). \tag{2.15}$$

The Euler-Lagrange equation, Eq. (2.10), can be rearranged as

$$\varrho(\mathbf{r}) = \varrho_0\,\exp\left\{-\beta V_{\mathrm{ext}}(\mathbf{r}) + \beta\mu_{\mathrm{ex}} - \frac{\delta\beta\mathcal{F}_{\mathrm{ex}}[\varrho]}{\delta\varrho(\mathbf{r})}\right\}. \tag{2.16}$$

The Euler-Lagrange equation [Eq. (2.10) or (2.16)] is solved for non-trivial cases by a numerical iteration procedure, e. g., a Picard iteration scheme (cf. Sec. 6.2.4.1).

Rearranged density functional:
Employing Eqs. (2.5) and (2.14) for the ideal gas terms $\mathcal{F}_{\mathrm{id}}[\varrho]$ and μ_{id}, respectively, the density functional from Eq. (2.3) can be expressed as

$$\beta\Omega[\varrho] \;=\; \beta\mathcal{F}_{\mathrm{ex}}[\varrho] + \int_{\mathbb{R}^3}\mathrm{d}\mathbf{r}\;\varrho(\mathbf{r})\,\left\{\ln\left(\frac{\varrho(\mathbf{r})}{\varrho_0}\right) - 1 + \beta V_{\mathrm{ext}}(\mathbf{r}) - \beta\mu_{\mathrm{ex}}\right\}. \tag{2.17}$$

Here the thermal de Broglie wavelength does not enter. This equation is applied to calculate the grand potential for a given density distribution.

2.2 Hard-sphere fluid: fundamental measure theory

Realistic intermolecular interactions exhibit a repulsion at short distances. The simplest model comprising a repulsive fluid–fluid interaction is a hard-sphere fluid. It is formed by an ideal gas plus the condition that the spherical particles may not penetrate each other. The hard-sphere fluid was addressed for a one-dimensional system (hard rods on a line) analytically with exact results [111] and for the three-dimensional case within density functional theory [112]. In 1989 Rosenfeld presented his density functional approach to a hard-sphere fluid [113]. It is called fundamental measure theory (FMT).

2.2.1 Geometric fundament of FMT

The exact expression for the excess free energy of a one-component hard-sphere fluid for almost vanishing densities (low-density limit) contains a Θ function to account for the impenetrability of the hard spheres (with radius R and diameter $d := 2\,R$) [66],

$$\lim_{\varrho\to 0} \beta\mathcal{F}_{\text{ex}}[\varrho] = -\frac{1}{2}\int_{\mathbb{R}^3}\mathrm{d}\mathbf{r}\int_{\mathbb{R}^3}\mathrm{d}\mathbf{r}'\,\varrho(\mathbf{r})\,\varrho(\mathbf{r}')\;f\left(|\mathbf{r}-\mathbf{r}'|\right) \tag{2.18}$$

$$= \frac{1}{2}\int_{\mathbb{R}^3}\mathrm{d}\mathbf{r}\int_{\mathbb{R}^3}\mathrm{d}\mathbf{r}'\,\varrho(\mathbf{r})\,\varrho(\mathbf{r}')\;\Theta\left(d-|\mathbf{r}-\mathbf{r}'|\right). \tag{2.19}$$

The Mayer f function for a fluid–fluid interaction potential $\phi_{\text{ff}}(r)$ is defined as

$$f(r) := e^{-\beta\phi_{\text{ff}}(r)} - 1. \tag{2.20}$$

Thus for hard-spheres with

$$\beta\phi_{\text{HS}}(r) = \begin{cases} \infty & \text{for } r < d \\ 0 & \text{for } r \geq d \end{cases} \tag{2.21}$$

the Mayer f function is $f_{\text{HS}}(r) = -\Theta(d-r)$.

Rosenfeld decomposed the Θ function exactly into a sum of convolutions of weight functions. The original work of Rosenfeld is valid for mixtures. However, since in the present work exclusively a single species with hard-sphere radius R is employed, the formulae are given for this special case.

The *convolution* of two (either scalar or vectorial) functions $g_1(\mathbf{r})$ and $g_2(\mathbf{r})$ can be defined by

$$(g_1 \otimes g_2)(\mathbf{r}) := \int_{\mathbb{R}^3}\mathrm{d}\mathbf{r}'\;g_1(\mathbf{r}-\mathbf{r}')\,g_2(\mathbf{r}'). \tag{2.22}$$

Rosenfeld introduced six *weight functions* $w_\alpha(\mathbf{r})$, where the index α labels the four scalar weight functions w_3, w_2, w_1, and w_0 as well as the vectorial weight functions $\mathbf{w}_2$ and $\mathbf{w}_1$.

For a one-component hard-sphere fluid with hard-sphere radius R the weight functions are given as

$$w_3(\mathbf{r}) = \Theta(R-|\mathbf{r}|)\;, \tag{2.23}$$

$$w_2(\mathbf{r}) = \delta(R-|\mathbf{r}|)\;, \tag{2.24}$$

$$w_1(\mathbf{r}) = \frac{w_2(\mathbf{r})}{4\pi R} = \frac{\delta(R-|\mathbf{r}|)}{4\pi R}\;, \tag{2.25}$$

$$w_0(\mathbf{r}) = \frac{w_2(\mathbf{r})}{4\pi R^2} = \frac{\delta(R-|\mathbf{r}|)}{4\pi R^2}\;, \tag{2.26}$$

$$\mathbf{w}_2(\mathbf{r}) = \frac{\mathbf{r}}{|\mathbf{r}|}\,\delta(R-|\mathbf{r}|)\;, \tag{2.27}$$

$$\mathbf{w}_1(\mathbf{r}) = \frac{\mathbf{w}_2(\mathbf{r})}{4\pi R} = \frac{1}{4\pi R}\,\frac{\mathbf{r}}{|\mathbf{r}|}\,\delta(R-|\mathbf{r}|). \tag{2.28}$$

The decomposition of the Θ function then reads

$$\begin{aligned}\Theta\left(2R-|\mathbf{r}|\right) &= (w_0\otimes w_3)(\mathbf{r}) + (w_3\otimes w_0)(\mathbf{r}) + (w_1\otimes w_2)(\mathbf{r}) \\ &\quad + (w_2\otimes w_1)(\mathbf{r}) + (\mathbf{w}_1\otimes \mathbf{w}_2)(\mathbf{r}) + (\mathbf{w}_2\otimes \mathbf{w}_1)(\mathbf{r}).\end{aligned} \tag{2.29}$$

For a constant density ϱ the volume integrals over the two vectoral weight functions vanish, whereas the corresponding integrals over the four scalar weight functions yield

$$\int_{\mathbb{R}^3} \mathrm{d}\mathbf{r}\; w_\alpha(\mathbf{r}) = \frac{4}{3}\pi R^3,\; 4\pi R^2,\; R,\; 1 \quad \text{for } \alpha = 3,\, 2,\, 1,\, 0. \tag{2.30}$$

These values recover the fundamental measures (volume, surface area, radius, and Euler characteristics) of a sphere. This was the motivation for the name "fundamental measure theory".

2.2.2 Excess free energy in FMT

The six weight functions [Eqs. (2.23) to (2.28)] are used to construct four scalar and two vectorial *weighted densities* $n_\alpha(\mathbf{r})$ by convolutions with the density,

$$n_\alpha(\mathbf{r}) := (\varrho\otimes w_\alpha)(\mathbf{r}). \tag{2.31}$$

For a constant density ϱ the weighted density n_3 corresponds to the packing fraction

$$\eta := \varrho\,\frac{4}{3}\pi R^3. \tag{2.32}$$

FMT consists of two features. First, the above definitions of the weight functions and the corresponding weighted densities. Second, it is assumed that the excess free energy functional $\mathcal{F}_{\mathrm{ex}}[\varrho]$ can be written as

$$\beta\mathcal{F}_{\mathrm{ex}}[\varrho] = \int_{\mathbb{R}^3} \mathrm{d}\mathbf{r}\; \Phi\left(\{n_\alpha(\mathbf{r})\}\right). \tag{2.33}$$

The function $\Phi(\{n_\alpha\})$ corresponds to a dimensionless excess free energy density, and its form is not predefined by FMT. Rosenfeld introduced a certain functional, the so-called Rosenfeld functional. In 2002 the White Bear functional was derived [114] and refined in 2006 [115]. All these functionals are constructed for the low-density limit ($\varrho \to 0$) and then extrapolated to higher densities. Fortunately even for higher densities the agreement with the structure and thermodynamic quantities obtained from Monte Carlo simulations of a hard-sphere fluid is very good.

All versions of FMT have the following characteristic properties in common: First, the density functionals are non-local in the density. Second, the weight functions are geometrically based and thus better justified than in an ordinary weighted density approximation (WDA). Third, the low-density limit ($\varrho \to 0$) is correctly reproduced by construction. Fourth, algorithms based on FMT are relatively efficient (cf. Sec. 6.2.2). Fifth, FMT is applicable to mixtures of hard-spheres with different radii as well.

2.2.3 Rosenfeld functional

Rosenfeld proposed a certain choice for the function $\Phi\left(\{n_\alpha(\mathbf{r})\}\right)$,

$$\begin{aligned}\Phi^{\mathrm{RF}}\left(\{n_\alpha(\mathbf{r})\}\right) &:= -n_0\ln(1-n_3) + \frac{n_1\,n_2 - \mathbf{n}_1\cdot\mathbf{n}_2}{1-n_3} \\ &\quad + \frac{(n_2)^3 - 3\,n_2\,(\mathbf{n}_2\cdot\mathbf{n}_2)}{24\,\pi\,(1-n_3)^2}.\end{aligned} \tag{2.34}$$

The excess free energy functional [Eq. (2.33)] that employs this function is called the Rosenfeld (RF) functional.

Rosenfeld derived the function Φ^{RF} using scaled particle theory (SPT) [116, 117]. SPT states that in the limit of an infinitely large hard-sphere radius R the chemical potential μ equals the work $p\,V$ that has to be performed against the pressure, if a spherical particle with radius R_{test} is inserted and then scaled up. Then one has the SPT equation

$$\lim_{R_{\mathrm{test}}\to\infty} \frac{\mu}{V} \;=\; p. \tag{2.35}$$

The Rosenfeld functional recovers the Percus-Yevick (PY) equation of state (EOS) [118, 119, 120] for a hard sphere fluid,

$$\beta p_{\mathrm{PY}} \;=\; \varrho\,\frac{1+\eta+\eta^2}{(1-\eta)^3}. \tag{2.36}$$

In 1990 Kierlik and Rosinberg introduced a free energy functional for the inhomogeneous hard-sphere fluid [121], which involves solely scalar weight functions and no vector contributions. However, instead of the vectorial weight functions here weight functions come into play, which contain first and second derivatives of Dirac's δ function. The Kierlik-Rosinberg functional and the Rosenfeld functional are equivalent [122].

2.2.4 White Bear functional

The White Bear (WB) functional is related to the more accurate Carnahan-Starling (CS) EOS [123] for a hard-sphere fluid,

$$\boxed{\beta p_{\mathrm{CS}} \;=\; \varrho\,\frac{1+\eta+\eta^2-\eta^3}{(1-\eta)^3},} \tag{2.37}$$

instead of the PY EOS. A generalization of the CS EOS to a hard-sphere mixture is called the Boublík-Mansoori-Carnahan-Starling-Leland (BMCSL) EOS [124, 125]. There the pressure depends not on the total packing fraction but on the four scalar weighted densities for mixtures. The BMCSL EOS serves as an input for the derivation of the WB functional.

The function $\Phi\left(\{n_\alpha(\mathbf{r})\}\right)$ [Eq. (2.33)] for the WB functional can be expressed as

$$\begin{aligned}\Phi^{\mathrm{WB}}\left(\{n_\alpha(\mathbf{r})\}\right) \;&:=\; -n_0\ln(1-n_3) \;+\; \frac{n_1\,n_2-\mathbf{n}_1\cdot\mathbf{n}_2}{1-n_3}\\ &+\; \frac{(n_2)^3-3\,n_2\,(\mathbf{n}_2\cdot\mathbf{n}_2)}{24\,\pi\,(1-n_3)^2}\times\frac{2}{3}\,\frac{n_3+(1-n_3)^2\ln(1-n_3)}{(n_3)^2}.\end{aligned} \tag{2.38}$$

The last factor (after the $\times$ symbol) goes to 1 for vanishing n_3, that corresponds to the packing fraction η in regions with constant density. Thus for small densities the WB functional resembles the RF functional. Consequently the WB version also recovers the correct low-density limit. The WB functional contains a slight inconsistency between the pressure calculated from the SPT equation and the pressure from the underlying equation of state.

Recently a modified version of the WB functional was presented, called the White Bear mark II functional [115]. Here the above mentioned inconsistency is overcome for a one-component hard-sphere fluid. The WBII functional is based on another generalization of the CS EOS to mixtures [126]. Density distributions $\varrho(\mathbf{r})$ resulting from the WB and the WBII functional differ very little [115]. These tiny differences are much below the level of

accuracy aimed at in this work. The computer program is slowed down by approximately 10 percent due to more elaborate array initializations, if the WBII version is applied instead of the WB functional. Therefore for this work exclusively the WB functional is used.

2.2.5 Functional derivate $\delta\mathcal{F}_{\mathrm{ex}}/\delta\varrho(\mathbf{r})$ within FMT

In order to solve the Euler-Lagrange equation, Eq. (2.16), or to calculate the grand potential, Eq. (2.17), it is necessary to calculate the functional derivative of the excess free energy functional, $\delta\beta\mathcal{F}_{\mathrm{ex}}[\varrho]/\delta\varrho(\mathbf{r})$. The functional $\mathcal{F}_{\mathrm{ex}}$ is approximated by a hard-spheres term and an attractive term [Eqs. (2.7) and (2.8)]. So the functional derivative of $\mathcal{F}_{\mathrm{ex}}$ contains two parts,

$$\frac{\delta\mathcal{F}_{\mathrm{ex}}[\varrho]}{\delta\varrho(\mathbf{r})} \simeq \frac{\delta\mathcal{F}_{\mathrm{ex}}^{\mathrm{HS}}[\varrho]}{\delta\varrho(\mathbf{r})} + \frac{\delta\mathcal{F}_{\mathrm{ex}}^{\mathrm{att}}[\varrho]}{\delta\varrho(\mathbf{r})}. \tag{2.39}$$

The functional derivative $\delta\mathcal{F}_{\mathrm{ex}}^{\mathrm{att}}/\delta\varrho(\mathbf{r})$, that belongs to the attractive part of the fluid–fluid interaction, is discussed in Sec. 2.3.1.

If the hard-sphere repulsion is accounted for by FMT, the functional derivative of the excess free energy functional for hard-spheres can be simplified to convolutions (convolution integrals): First, from Eq. (2.33) follows

$$\frac{\delta\beta\mathcal{F}_{\mathrm{ex}}^{\mathrm{HS}}[\varrho]}{\delta\varrho(\mathbf{r})} = \sum_{\alpha}\int_{\mathbb{R}^3}\mathrm{d}\mathbf{r}'\,\frac{\partial\Phi}{\partial n_\alpha[\varrho(\mathbf{r}')]}\,\frac{\delta n_\alpha[\varrho(\mathbf{r}')]}{\delta\varrho(\mathbf{r})}, \tag{2.40}$$

where again α labels the six weight functions (see Sec. 2.2.1). Second, from Eq. (2.31) one finds

$$\frac{\delta n_\alpha[\varrho(\mathbf{r}')]}{\delta\varrho(\mathbf{r})} = w_\alpha(\mathbf{r}'-\mathbf{r}) = (\pm)_\alpha\, w_\alpha(\mathbf{r}-\mathbf{r}') \tag{2.41}$$

with a "sign factor",

$$(\pm)_\alpha := \begin{cases} +1 & \text{for scalar weight functions} \\ -1 & \text{for vectorial weight functions} \end{cases}, \tag{2.42}$$

i. e., depending on whether the weight function w_α is even or odd. Altogether the functional derivative for the hard-spheres part reads

$$\frac{\delta\beta\mathcal{F}_{\mathrm{ex}}^{\mathrm{HS}}[\varrho]}{\delta\varrho(\mathbf{r})} = \sum_{\alpha}(\pm)_\alpha\left(\frac{\partial\Phi}{\partial n_\alpha}\otimes w_\alpha\right)(\mathbf{r}). \tag{2.43}$$

For concrete calculations this general expression has to be adapted to the employed coordinate system (cf. Sec. 2.4) and evaluated for the employed functional (see Subsecs. 2.2.3 and 2.2.4).

2.2.6 Thermodynamic quantities of a hard-sphere fluid

In this section the thermodynamic quantities of a one-component hard-sphere fluid — like pressure, excess free energy density, and chemical potential — are considered. In order to emphasize that solely a hard-sphere fluid is considered here and any attraction is absent, the thermodynamic quantities are labeled by "HS". In order to account for attractive parts of the fluid–fluid interaction as well, the above formulae for the thermodynamic quantities for a hard-sphere fluid are extended in Sec. 2.3.2.

Pressure p^{HS}:
As mentioned before, Rosenfeld's functional corresponds to the Percus-Yevick equation of state (PY EOS), Eq. (2.36), while the White Bear functional (in the standard and the mark II version) corresponds to the Carnahan-Starling equation of state (CS EOS), Eq. (2.37).

Chemical potential:
In general, the chemical potential μ can be calculated from the free energy density f via the definition $\mu = \partial f/\partial \varrho$. Since f can be split into an ideal gas part and an excess contribution, also the chemical potential can be split analogously [Eq. (2.13)]. For a hard-sphere fluid this means

$$\mu^{\mathrm{HS}} \;=\; \mu_{\mathrm{id}} \,+\, \mu_{\mathrm{ex}}^{\mathrm{HS}} \;=\; \frac{\partial f_{\mathrm{id}}}{\partial \varrho} \,+\, \frac{\partial f_{\mathrm{ex}}^{\mathrm{HS}}}{\partial \varrho}. \tag{2.44}$$

The excess chemical potential $\mu_{\mathrm{ex}}^{\mathrm{HS}}$ of a hard-sphere fluid reads

$$\beta\mu_{\mathrm{ex}}^{\mathrm{PY}} \;=\; -\ln(1-\eta) + \frac{7\eta - \frac{13}{2}\eta^2 + \frac{5}{2}\eta^3}{(1-\eta)^3}. \tag{2.45}$$

for the PY EOS and

$$\boxed{\beta\mu_{\mathrm{ex}}^{\mathrm{CS}} \;=\; \frac{3\eta^2 - 9\eta + 8}{(1-\eta)^3}} \tag{2.46}$$

for the CS EOS.

The chemical potential μ^{HS} additonally contains the ideal gas chemical potential $\beta\mu_{\mathrm{id}} = \ln(\lambda^3\varrho) = \ln(\lambda^3) + \ln\varrho$. However, the value of the thermal de Broglie wavelength λ is irrelevant for the thermodynamical properties of the system [Eq. (2.17)]. Furthermore λ merely enters as an additive constant on both sides of the conditional equation for phase-coexistence, Eq. (2.59). If the chemical potential is shifted suitably,

$$\beta\tilde{\mu}_{\mathrm{id}} \;:=\; \beta\mu_{\mathrm{id}} - \ln\left(\lambda^3/(\tfrac{4}{3}\pi R^3)\right), \tag{2.47}$$

and the tilde symbol is suppressed, the ideal gas chemical potential obtains a simple form,

$$\beta\mu_{\mathrm{id}} = \ln\eta. \tag{2.48}$$

This shift in the ideal gas part of the chemical potential is tacitly presumed in the following.

2.3 Attractive interactions: perturbation theory

The interaction potential between two fluid particles is separated into a repulsive and an attractive part. The repulsive part is approximated by a hard-sphere interaction potential. The attractive part can be taken into account approximatively by a (first-order) perturbation theory.

2.3.1 Perturbation theory/random phase approximation (RPA)

According to Eq. (2.18) the low-density limit expression of the excess free energy functional involves the Mayer f function [Eq. (2.20)],

$$\beta\mathcal{F}_{\mathrm{ex}}[\varrho] \;\simeq\; -\frac{1}{2}\int_{\mathbb{R}^3}\mathrm{d}\mathbf{r}\int_{\mathbb{R}^3}\mathrm{d}\mathbf{r}'\,\varrho(\mathbf{r})\,\varrho(\mathbf{r}')\;f\left(|\mathbf{r}-\mathbf{r}'|\right),\quad \varrho\to 0. \tag{2.49}$$

In other words, here f corresponds to the low-density limit of the direct correlation function $c^{(2)}$ however this is not a mean-field approximation.

The fluid–fluid interaction potential is separated into a repulsive and an attractive part [Eq. (2.6)]. The repulsive part of the interaction potential equals a hard-sphere potential in the case of a square-well fluid (cf. Sec. 2.3.5) or can be approximated by such a hard-sphere potential in the case of a Lennard-Jones fluid (cf. Sec. 2.3.4),

$$\phi_{\mathrm{ff}}(r) \;=\; \phi_{\mathrm{ff}}^{\mathrm{rep}}(r) \;+\; \phi_{\mathrm{ff}}^{\mathrm{att}}(r) \;\simeq\; \phi_{\mathrm{HS}}(r) \;+\; \phi_{\mathrm{ff}}^{\mathrm{att}}(r) \quad . \tag{2.50}$$

Within *random phase approximation (RPA)* the direct correlation function $c^{(2)}$ is approximated by

$$\boxed{c^{(2)} \;\simeq\; c_{\mathrm{HS}}^{(2)} \;-\; \beta\phi_{\mathrm{ff}}^{\mathrm{att}},} \tag{2.51}$$

where $c_{\mathrm{HS}}^{(2)}$ is the direct correlation function of the hard-sphere reference system and the attractive part of the interaction potential constitutes a perturbation [66]. RPA is a mean-field-like approximation.

This approximation is also refered to as a "first-order perturbation theory", since the perturbation of the HS reference system corresponds approximately to a first-order expansion (in the attractive potential) of the Mayer f function.

Thus the excess free energy functional can be expressed as the sum of the (extrapolated) excess free energy of a hard-sphere fluid and a term containing the attractive part of the interaction,

$$\begin{aligned} \mathcal{F}_{\mathrm{ex}}[\varrho] \;&=\; \mathcal{F}_{\mathrm{ex}}^{\mathrm{rep}}[\varrho] \;+\; \mathcal{F}_{\mathrm{ex}}^{\mathrm{att}}[\varrho] \\ &\simeq\; \mathcal{F}_{\mathrm{ex}}^{\mathrm{HS}}[\varrho] \;+\; \frac{1}{2}\int_{\mathbb{R}^3}\mathrm{d}\mathbf{r}\int_{\mathbb{R}^3}\mathrm{d}\mathbf{r}'\;\varrho(\mathbf{r})\,\varrho(\mathbf{r}')\;\phi_{\mathrm{ff}}^{\mathrm{att}}(|\mathbf{r}-\mathbf{r}'|). \end{aligned} \tag{2.52}$$

The functional derivative of the attractive excess free energy, Eq. (2.39), is specified for the RPA (first-order perturbation theory),

$$\frac{\delta\beta\mathcal{F}_{\mathrm{ex}}^{\mathrm{att}}[\varrho]}{\delta\varrho(\mathbf{r})} \;\simeq\; \int_{\mathbb{R}^3}\mathrm{d}\mathbf{r}\;\varrho(\mathbf{r}')\;\beta\phi_{\mathrm{att}}(|\mathbf{r}-\mathbf{r}'|) \;=\; \left(\varrho\otimes\beta\phi_{\mathrm{ff}}^{\mathrm{att}}\right)(\mathbf{r}) \tag{2.53}$$

$$=:\; \left(\varrho\otimes w_{\mathrm{ff}}\right)(\mathbf{r}) \;=:\; n_{\mathrm{ff}}(\mathbf{r}). \tag{2.54}$$

Like a weighted density n_α is a convolution of the density ϱ and a weight function w_α, the functional derivative of $\beta\mathcal{F}_{\mathrm{ex}}^{\mathrm{att}}$ is a convolution of ϱ and a function w_{ff}. In an effectively three-dimensional system w_{ff} is identical to the dimensionless attractive part of the interaction potential. However, in effectively lowered dimensions (cf. Sec. 2.4) the corresponding function is either called "weight function" as well, if its role in a convolution with ϱ shall be emphasized, or "integrated potential" in order to stress its origin. Due to the analogy with weighted densities the convolution product is also regarded as a weighted density, called n_{ff}.

2.3.2 Thermodynamic quantities

Thermodynamic quantities — like pressure, (excess) free energy density, and (excess) chemical potential — of a hard-sphere fluid have been discussed in Sec. 2.2.6. Now these quantities associated to a fluid with additional attractive fluid–fluid interaction are presented.

Excess free energy density $f_{\mathrm{ex}}(\varrho)$:
According to the (approximative) excess free energy functional in Eq. (2.52) the bulk

excess free energy density $f_{\mathrm{ex}}(\varrho)$ can be decomposed into the sum of a hard-sphere term and a contribution from the attractive part of the interaction. The integral over this attractive part,

$$\alpha \;:=\; \int_{\mathbb{R}^3} \mathrm{d}\mathbf{r}\; \phi_{\mathrm{ff}}^{\mathrm{att}}(|\mathbf{r}|), \tag{2.55}$$

is called the *integrated strength* of the attractive potential. Then one has

$$f_{\mathrm{ex}} \;=\; f_{\mathrm{ex}}^{\mathrm{rep}} \;+\; f_{\mathrm{ex}}^{\mathrm{att}} \;\simeq\; f_{\mathrm{ex}}^{\mathrm{HS}} \;+\; \frac{1}{2}\varrho^2\,\alpha. \tag{2.56}$$

This equation determines the excess chemical potential and the excess pressure.

Excess chemical potential:
The excess chemical potential follows from Eqs. (2.13) and (2.56),

$$\mu_{\mathrm{ex}} \;=\; \frac{\partial f_{\mathrm{ex}}}{\partial \varrho} \;=\; \frac{\partial f_{\mathrm{ex}}^{\mathrm{rep}}}{\partial \varrho} \;+\; \frac{\partial f_{\mathrm{ex}}^{\mathrm{att}}}{\partial \varrho} \;\simeq\; \mu_{\mathrm{ex}}^{\mathrm{HS}} \;+\; \varrho\,\alpha. \tag{2.57}$$

Pressure p:
In general, the free energy density and the chemical potential are related to the pressure via $p = -\,(f - \mu\,\varrho)$. Hence the hard-sphere pressure is given by

$$p \;\simeq\; p^{\mathrm{HS}} \;+\; \frac{1}{2}\varrho^2\,\alpha. \tag{2.58}$$

2.3.3 Bulk phase diagram

A "*bulk*" system is a fictitious infinitely large system (i. e., without boundaries) without any external fields. A *phase diagram* is a graph that illustrates for which values of physical parameters (like temperature, pressure, chemical potential, and packing fraction or particle density) which thermodynamic phase is present in equilibrium. A bulk phase diagram displays the different phases of a bulk system. The lines which separate regions (in parameter space) of different phases are called binodal lines or binodals. However, since meta-stable states (e. g., a supercooled/undercooled liquid or a superheated liquid) could exist, also the spinodal lines or spinodals are interesting, since they tell where a phase-transition must take place at the latest.

In contrast, a surface phase diagram can contain additional information about surface-related phenomena, e. g., the wetting temperature and the course of a prewetting line (if they exist).

In a grand canonical ensemble the conditions for coexistence between fluid phases (in thermodynamic equilibrium) are the following: For a given temperature T below the critical temperature T_{c} the chemical potential and the grand potential have to be the same for the coexisting phases. In a bulk system $\Omega = -pV$ holds, and the pressure has to be identical in the coexisting bulk phases.

Hence for liquid–gas phase coexistence, the case relevant for this work, the conditions of bulk phase coexistence read

$$p_{\mathrm{l}} \;\stackrel{!}{=}\; p_{\mathrm{g}} \quad \text{and} \quad \mu_{\mathrm{l}} \;\stackrel{!}{=}\; \mu_{\mathrm{g}}, \tag{2.59}$$

where the indices l and g refer to the liquid and the gas phase, respectively. These two conditions represent a coupled system of non-linear equations. The packing fractions η_{l} and η_{g} or, equivalently, the bulk densities ϱ_{l} and ϱ_{g} of the coexisting liquid and gas phases have to be obtained numerically.

Within RPA and for a certain HS EOS the phase diagrams for all intermolecular interactions collaps to a master curve, if the temperature is scaled accordingly. This is due to the fact that within RPA the phase diagram merely depends on the integrated strength α of the interaction potential [Eq. (2.55)].

From the condition $\partial p/\partial \varrho \stackrel{!}{=} 0$ the spinodals,

$$\mathrm{k_B}T_{\mathrm{spinodal}} \;=\; -\,\alpha\,\varrho\,\frac{(1-\eta)^4}{1+4\,\eta+4\,\eta^2-4\,\eta^3+\eta^4}, \tag{2.60}$$

are obtained for a fluid described by RPA and the CS EOS. Likewise for such a system the conditions $\partial p/\partial \varrho \stackrel{!}{=} 0$ and $\partial^2 p/\partial \varrho^2 \stackrel{!}{=} 0$ lead to

$$\eta_{\mathrm{c}}^5 - 5\,\eta_{\mathrm{c}}^4 + 4\,\eta_{\mathrm{c}}^3 + 20\,\eta_{\mathrm{c}}^2 + 5\,\eta_{\mathrm{c}} - 1 \;=\; 0 \tag{2.61}$$

for the packing fraction at the critical point, η_{c}. Hence this critical packing fraction is $\eta_{\mathrm{c}} \simeq 0.130444$, and the critical temperature follows as

$$\mathrm{k_B}T_{\mathrm{c}} \;\simeq\; -\,0.047164\;\frac{1}{\frac{4}{3}\pi\,R^3}\,\alpha. \tag{2.62}$$

The bulk phase diagram for a fluid described by RPA and the CS EOS is shown in Fig. 2.1 for the case of a so-called WCA-LJ fluid (see Sec. 2.3.4 for details).

2.3.4 Lennard-Jones potential

Liquid–gas coexistence is required for studying the liquid wedge system in thermodynamic equilibrium. Hard-spheres do not exhibit a fluid–fluid phase transition. The simplest possible fluid exhibiting a liquid–gas phase transition is a square-well (SW) fluid, which will be described in Sec. 2.3.5.

A phenomenological interparticle interaction potential widely used in physics and chemistry is the Lennard-Jones (LJ) potential. The famous LJ (12–6) potential is a phenomenological fluid–fluid interaction potential, which contains both a long-ranged attraction and a short-ranged repulsion. It resembles the tail of a van der Waals potential, i. e., $\phi_{\mathrm{LJ}}(r \to \infty) \sim -r^{-6}$. The LJ (12–6) potential is defined as

$$\phi_{\mathrm{LJ}}(r) \;:=\; 4\,\varepsilon_{\mathrm{LJ}}\left[\left(\frac{\sigma_{\mathrm{LJ}}}{r}\right)^{12} - \left(\frac{\sigma_{\mathrm{LJ}}}{r}\right)^{6}\right] \tag{2.63}$$

with an energy parameter $\varepsilon_{\mathrm{LJ}} > 0$ (that corresponds to the depth of the potential) and a length parameter σ_{LJ}. The LJ potential crosses zero for $r = \sigma_{\mathrm{LJ}}$ and attains its minimum for $r = r_{\min} := \sqrt[6]{2}\,\sigma_{\mathrm{LJ}}$.

The original interaction potential is decomposed exactly [Eq. (2.6)] into a repulsive and an attractive part,

$$\phi_{\mathrm{LJ}}(r) \;=\; \phi_{\mathrm{LJ}}^{\mathrm{rep}}(r) \;+\; \phi_{\mathrm{LJ}}^{\mathrm{att}}(r). \tag{2.64}$$

The attractive part is tackled by perturbation theory, while the repulsive part is approximated by a hard-sphere potential,

$$\phi_{\mathrm{LJ}}(r) \;\simeq\; \phi_{\mathrm{HS}}(r) \;+\; \phi_{\mathrm{LJ}}^{\mathrm{att}}(r). \tag{2.65}$$

There are two commonly used separation schemes:

Weeks-Chandler-Andersen (WCA) separation scheme:
The decomposition method employed in this work goes back to Weeks, Chandler, and Andersen [127]. The LJ potential is repulsive for $r < r_{\min} = \sqrt[6]{2}\,\sigma_{\mathrm{LJ}}$ and attractive for

$r > r_{\min}$. The attractive part of the potential, $\phi^{\text{att}}_{\text{LJ}}(r)$, is constructed by this attractive contribution and extrapolating it into the core by a constant,

$$\phi^{\text{att}}_{\text{WCA}-\text{LJ}}(r) \;:=\; -\varepsilon_{\text{LJ}}\,\Theta\big(\sqrt[6]{2}\,\sigma_{\text{LJ}} - r\big) + \phi_{\text{LJ}}(r)\,\Theta\big(r - \sqrt[6]{2}\,\sigma_{\text{LJ}}\big). \tag{2.66}$$

Consequently the repulsive part reads

$$\phi^{\text{rep}}_{\text{WCA}-\text{LJ}}(r) \;:=\; \big(\phi_{\text{LJ}}(r) + \varepsilon_{\text{LJ}}\big)\,\Theta\big(\sqrt[6]{2}\,\sigma_{\text{LJ}} - r\big). \tag{2.67}$$

Barker-Henderson (BH) separation scheme:
An also widely applied procedure to split the potential into two parts was invented by Barker and Henderson [128]. Here the positive and negative parts of the potential are separated, i. e.,

$$\phi^{\text{att}}_{\text{BH}-\text{LJ}}(r) \;:=\; \phi_{\text{LJ}}(r)\,\Theta\big(r - \sigma_{\text{LJ}}\big) \tag{2.68}$$

and

$$\phi^{\text{rep}}_{\text{BH}-\text{LJ}}(r) \;:=\; \phi_{\text{LJ}}(r)\,\Theta\big(\sigma_{\text{LJ}} - r\big). \tag{2.69}$$

Effective hard-sphere diameter $d_{\text{eff}}(T_{\text{LJ}})$ for WCA and BH:
In both the BH and the WCA scheme a part of the interaction potential is approximated by a hard-sphere potential with radius R and diameter $d \equiv 2\,R$. A temperature dependent choice of an effective hard-sphere diameter $d_{\text{eff}}(T)$ has been suggested by Barker and Henderson [128].

In this work the Lennard-Jones parameter σ_{LJ} is directly employed as hard-sphere diameter,

$$2\,R \;\equiv\; d \;:=\; \sigma_{\text{LJ}}. \tag{2.70}$$

Nevertheless, the temperature dependent epxressions are presented for completeness: The effective hard-sphere diameter reads

$$d^{\text{BH}}_{\text{eff}}(T_{\text{LJ}}) \;:=\; \int_{r=0}^{\sigma_{\text{LJ}}} \mathrm{d}r\,\Big\{1 - e^{-\beta\,\phi_{\text{LJ}}(r)}\Big\} \tag{2.71}$$

for a BH-LJ fluid and

$$d^{\text{WCA}}_{\text{eff}}(T_{\text{LJ}}) \;:=\; \int_{r=0}^{\sqrt[6]{2}\,\sigma_{\text{LJ}}} \mathrm{d}r\,\Big\{1 - e^{-\beta\,[\phi_{\text{LJ}}(r) + \varepsilon_{\text{LJ}}]}\Big\} \tag{2.72}$$

for a WCA-LJ fluid.

Integrated strength α:
The integrated strength [Eq. (2.55)] of the attractive part of the WCA-LJ potential is

$$\begin{aligned}\alpha_{\text{WCA}-\text{LJ}} \;&\equiv\; \int_{\mathbb{R}^3} \mathrm{d}\mathbf{r}\;\phi^{\text{att}}_{\text{WCA}-\text{LJ}}(|\mathbf{r}|) \;=\; -\frac{32}{9}\,\sqrt{2}\,\pi\,\sigma^3_{\text{LJ}}\,\varepsilon_{\text{LJ}} \\ &\overset{(2.70)}{=}\; -\frac{4}{3}\pi\,(3\,R)^3\,\varepsilon_{\text{LJ}} \times \frac{64}{81}\sqrt{2}.\end{aligned} \tag{2.73}$$

For a BH separation α is

$$\alpha_{\text{BH}-\text{LJ}} \;\equiv\; \int_{\mathbb{R}^3} \mathrm{d}\mathbf{r}\;\phi^{\text{att}}_{\text{BH}-\text{LJ}}(|\mathbf{r}|) \;=\; -\frac{32}{9}\,\pi\,\sigma^3_{\text{LJ}}\,\varepsilon_{\text{LJ}} \;=\; \alpha_{\text{WCA}-\text{LJ}}/\sqrt{2}. \tag{2.74}$$

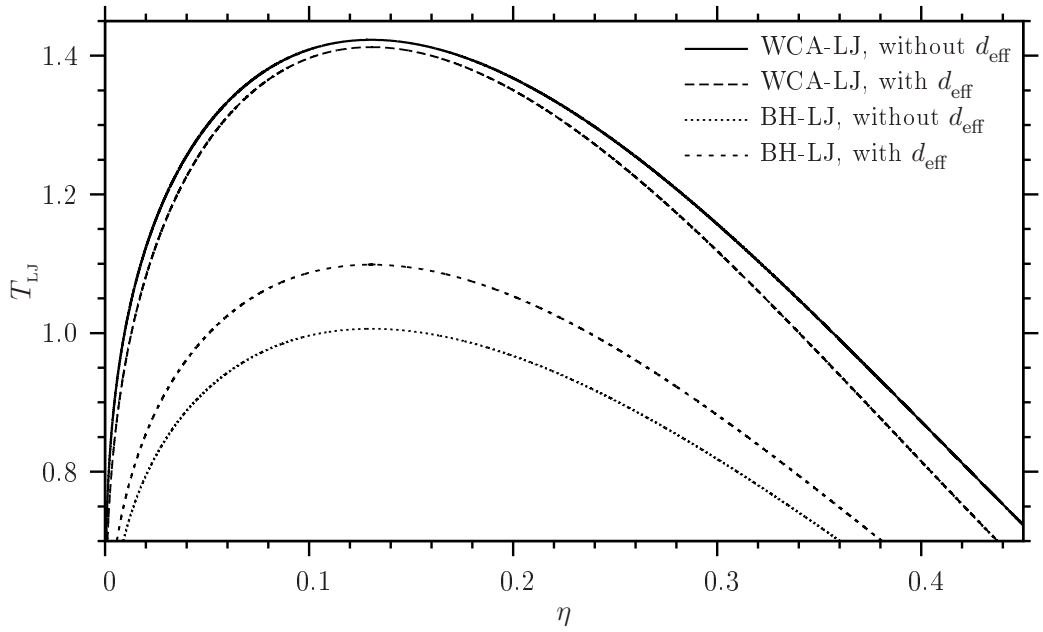

Fig. 2.1: Bulk phase diagrams for several models for a Lennard-Jones (9–3) fluid. The effective temperature $T_{\text{LJ}} = 1/(\beta\varepsilon_{\text{LJ}})$ is plotted versus the packing fraction η. The phase diagrams are determined within the random phase approximation (first-order perturbation theory) for the Weeks-Chandler-Anderson (WCA) and the Barker-Henderson (BH) separation scheme. Both the WCA-LJ and the BH-LJ fluid are analyzed with and without the effective hard-sphere diameter d_{eff}. In the situations without d_{eff} the LJ parameter σ_{LJ} is chosen as the corresponding hard-sphere diameter. A WCA-LJ fluid without d_{eff} is employed in the DFT calculations for this work. In this case the critical point is situated at $\eta_{\text{c}} \simeq 0.130444$ and $T_{\text{LJ,c}} \simeq 1.422933$. The temperature of the triple point of a LJ fluid is $T_{\text{LJ}} \simeq 0.75$ [129]. However, for the *WCA*-LJ fluid with a relatively high critical temperature ($\sqrt{2}$ times as large as for the BH-LJ fluid, each considered without d_{eff}) the triple point temperature for a WCA-LJ fluid is expected to be situated in the effective temperature range between 0.75 and $\sqrt{2} \times 0.75 \simeq 1.06$.

This relation between α for BH and WCA, respectively, illustrates the difference between these separation schemes. However, if a reduced temperature $t := T_{\text{LJ}}/T_{\text{LJ,c}}$ with a critical effective temperature $T_{\text{LJ,c}}$ is considered, the apparent difference between BH and WCA becomes much smaller, and the two phase diagrams within RPA even match exactly.

Bulk phase diagram of a (WCA-)LJ fluid:
The bulk phase diagram of a WCA-LJ fluid calculated within RPA (or "first-order" perturbation theory) and the CS EOS for the hard spheres is shown in Fig. 2.1. The spinodals and binodals are plotted in the plane formed by the effective temperature

$$T_{\text{LJ}} \;:=\; \frac{1}{\beta\varepsilon_{\text{LJ}}} \tag{2.75}$$

and the packing fraction η.

Weight functions:
The weight function $w_{\text{ff}}(\mathbf{r})$ [Eq. (2.54)] for the WCA decomposition of a LJ interaction is given by

$$w_{\text{LJ}}(\mathbf{r}) \;=\; \beta\phi^{\text{att}}_{\text{WCA-LJ}}(|\mathbf{r}|). \tag{2.76}$$

The corresponding one- and two-dimensional versions $w_{\text{LJ}}(z)$ and $w_{\text{LJ}}(x,z)$ are presented in Sec. 2.4.2 [Eqs. (2.94) and (2.110)].

2.3.5 Square-well potential

A SW fluid represents a short-ranged, theoretical model system, which is widely used (for overviews see, e. g., Refs. [130] and [131]). The SW potential is defined as

$$\phi_{\mathrm{SW}}(r) \;:=\; \begin{cases} \infty & \text{for } r < \sigma \\ -\varepsilon_{\mathrm{SW}} & \text{for } \sigma \le r \le \sigma_{\mathrm{SW}} \\ 0 & \text{for } r > \sigma_{\mathrm{SW}}, \end{cases} \tag{2.77}$$

where $d \equiv 2\,R$ is the hard-sphere diameter and the energy parameter $\varepsilon_{\mathrm{SW}} > 0$ describes the depth of the potential well. Throughout this work

$$\sigma_{\mathrm{SW}} \;:=\; \frac{3}{2}\,d \;\equiv\; 3\,R \tag{2.78}$$

is chosen. For the inverse case of a negative value of the well depth parameter ε the fluid is called square-shoulder fluid [132].

The SW potential is well suited for a (first-order) perturbation theoretical treatment. It can be decomposed into a hard-sphere potential and an attractive potential. Since the potential is infinitely large for small distances anyway, one is free to chose the attractive part arbitrarily for small distances $r < d$. An intuitive choice is to extrapolate the constant $-\varepsilon_{\mathrm{SW}}$ into the core of the hard-spheres. Then the attractive part of the interaction potential as a function of the interparticle distance r reads

$$\phi_{\mathrm{SW}}^{\mathrm{att}}(r) \;=\; -\,\varepsilon_{\mathrm{SW}}\,\Theta\left(\sigma_{\mathrm{SW}} - r\right) \;\overset{(2.78)}{=}\; -\,\varepsilon_{\mathrm{SW}}\,\Theta\left(3\,R - r\right). \tag{2.79}$$

The integrated strength [Eq. (2.55)] of the attractive part of the SW potential is

$$\alpha_{\mathrm{SW}} \;\equiv\; \int_{\mathbb{R}^3} \mathrm{d}\mathbf{r}\; \phi_{\mathrm{SW}}^{\mathrm{att}}(|\mathbf{r}|) \;=\; -\,\frac{4}{3}\pi\,\sigma_{\mathrm{SW}}^3\,\varepsilon_{\mathrm{SW}} \;\overset{(2.78)}{=}\; -\left(\tfrac{4}{3}\pi\,R^3\right) \times 27\,\varepsilon_{\mathrm{SW}}. \tag{2.80}$$

This quantity determines the bulk phase behavior [Eqs. (2.57) and (2.58) and Sec. 2.3.3].

As mentioned before (in Sec. 2.3.3), the phase diagram within RPA (and for a certain HS EOS) is the same for all fluids. Thus the phase diagram calculated for a WCA-LJ fluid (see Fig. 2.1 in Sec. 2.3.4) can readily be used for the SW fluid as well, if the axis of the effective temperature is scaled properly. The integrated strengths of the attractive parts of the SW and the WCA-LJ potential are identical for

$$\varepsilon_{\mathrm{SW}} \;=\; \frac{64}{81}\sqrt{2}\;\varepsilon_{\mathrm{LJ}} \;\simeq\; 1.117403\;\varepsilon_{\mathrm{LJ}} \tag{2.81}$$

or, equivalently, for

$$T_{\mathrm{SW}} \;:=\; \frac{1}{\beta\varepsilon_{\mathrm{SW}}} \;=\; \frac{1}{\frac{64}{81}\sqrt{2}}\;\frac{1}{\beta\varepsilon_{\mathrm{LJ}}} \;\equiv\; \frac{1}{\frac{64}{81}\sqrt{2}}\;T_{\mathrm{LJ}} \;\simeq\; 0.894932\;T_{\mathrm{LJ}}. \tag{2.82}$$

The weight function $w_{\mathrm{ff}}(\mathbf{r})$ employed in perturbation theory [Eq. (2.54)] in the SW case is given by its attractive interaction part,

$$w_{\mathrm{SW}}(\mathbf{r}) \;=\; \beta\,\phi_{\mathrm{SW}}^{\mathrm{att}}(|\mathbf{r}|). \tag{2.83}$$

For effectively one- and two-dimensional Cartesian systems the corresponding weight functions $w_{\mathrm{SW}}(z)$ and $w_{\mathrm{SW}}(x,z)$ are displayed in Sec. 2.4.2 [Eqs. (2.93) and (2.109)].

2.4 Effectively one- and two-dimensional Cartesian systems

2.4.1 Exploiting symmetries in three-dimensional systems

If one considers a three-dimensional liquid or gas in contact to a planar, homogeneous wall, the corresponding density profile ϱ exclusively depends on the (Cartesian) coordinate z perpendicular to the wall, i. e., $\varrho(\mathbf{r}) \equiv \varrho(x, y, z) = \varrho(z)$, if the interaction is isotropic and no spontaneous symmetry breaking (e. g., crystallization) occurs. In the case of coexistence between the liquid and the gas phase, the density profile may vary in more directions, depending on the boundary conditions and external fields. A liquid wedge on a substrate has a density profile that is translationally invariant in one lateral direction, say the y-direction. The density profile solely depends on the other lateral coordinate x and the vertical coordinate z, $\varrho(\mathbf{r}) = \varrho(x, z)$.

If the coordinate dependency of ϱ is restricted to one (z) or two (x and z) coordinates, crystallization — where the density dramatically varies in all three spatial directions — cannot be covered. In other words, the configuration space has been reduced. This procedure remains reasonable for temperatures above the triple point. Also the possible effect of pre-crystallization at a wall (i. e., crystallization at a density slightly below the density where crystallization takes place in a bulk system) is not considered here. However, if a lattice-like structure arises in the effectively two-dimensional density $\varrho(x, z)$, this is at least a sign that crystallization could take place, if the dependency on the third dimension was released.

Another example of an effectively one-dimensional system is a fluid around a larger spherical particle, e. g., a single colloid. Here above the melting temperature the density solely depends on the distance from the center of the particle.

2.4.2 Weighted densities

The coordinate dependency of the density profile ϱ is crucial for concrete calculations. It depends strongly on the type of coordinate system (Cartesian, polar etc.) and on the number of "active" coordinates, i. e., the number of coordinates the density profile really depends on. The convolution integrals and the associated weight functions w_α in the basic version of FMT are written in three Cartesian dimensions. If one uses another type of coordinate system or less than three coordinates, the weight functions have to be expressed in the new coordinate system such that they lead to the same weighted densities as in the Cartesian case.

In the following Rosenfeld's weight functions w_α, the square-well weight function w_{SW}, and the Lennard-Jones weight function w_{LJ} are adapted to effectively one- and two-dimensional systems.

2.4.2.1 Effectively one-dimensional Cartesian systems

Let the particle density in the three-dimensional space be translationally invariant in two Cartesian directions, so that it exclusively depends on a single direction, say the z-direction,

$$\varrho(\mathbf{r}) = \varrho(z). \tag{2.84}$$

Then the weighted densities $n_\alpha(\mathbf{r})$ also depend on solely one Cartesian coordinate and can be written as [Eq. (2.31)]

$$\begin{aligned} n_\alpha(z) &= n_\alpha(\mathbf{r}) \equiv \int_{\mathbb{R}^3} \mathrm{d}\mathbf{r}'\, \varrho(\mathbf{r}-\mathbf{r}')\, w_\alpha(\mathbf{r}') \\ &= \int_{\mathbb{R}} \mathrm{d}z'\, \varrho(z-z')\, w_\alpha(z') \equiv (\varrho \otimes w_\alpha)(z) \end{aligned} \tag{2.85}$$

with one-dimensional weight functions (or more precisely: weight functions with a one-dimensional argument),

$$w_\alpha(z) := \int_{x=-\infty}^{\infty} \mathrm{d}x \int_{y=-\infty}^{\infty} \mathrm{d}y\; w_\alpha(\mathbf{r}), \tag{2.86}$$

and one-dimensional convolutions.

The one-dimensional weight functions for FMT are determined from the three-dimensional ones. Merely three of them are independent,

$$w_3(z) = \pi(R^2 - z^2)\,\Theta(R-|z|) \quad , \tag{2.87}$$

$$w_2(z) = 2\pi R\,\Theta(R-|z|) \quad , \tag{2.88}$$

$$(\mathbf{w}_2)_z(z) = 2\pi z\,\Theta(R-|z|), \tag{2.89}$$

where the x and y components of the vectorial weight function $\mathbf{w}_2(z)$ vanish. The other three weight functions are related to them via a constant prefactor,

$$w_1(z) = \frac{w_2(z)}{4\pi R}, \quad w_0(z) = \frac{w_2(z)}{4\pi R^2}, \quad \text{and} \quad \mathbf{w}_1(z) = \frac{\mathbf{w}_2(z)}{4\pi R}. \tag{2.90}$$

The functional derivative of the excess free energy functional of a hard-sphere fluid [Eq. (2.43)] can also be expressed in terms of the one-dimensional weight functions and one-dimensional convolutions,

$$\frac{\delta\beta\mathcal{F}_{\mathrm{ex}}^{\mathrm{HS}}[\varrho]}{\delta\varrho(\mathbf{r})} = \sum_\alpha (\pm)_\alpha \left(\frac{\partial\Phi}{\partial n_\alpha} \otimes w_\alpha\right)(z). \tag{2.91}$$

The perturbation theoretical treatment of the attractive part of the intermolecular interaction is specified for the case of an effectively one-dimensional density $\varrho(z)$ as follows: Equation (2.54) is valid for a one-dimensional convolution as well, and the corresponding effectively one-dimensional weight function $w_{\mathrm{ff}}(z)$ with

$$w_{\mathrm{ff}}(z) := \int_{x=-\infty}^{\infty} \mathrm{d}x \int_{y=-\infty}^{\infty} \mathrm{d}y\; w_{\mathrm{ff}}(\mathbf{r}) \tag{2.92}$$

can be determined for both the square-well and the Lennard-Jones potential: First, the weight function for the SW fluid reads

$$w_{\mathrm{SW}}(z) = -\pi\beta\varepsilon_{\mathrm{SW}}\left(\sigma_{\mathrm{SW}}^2 - z^2\right)\,\Theta\left(\sigma_{\mathrm{SW}} - |z|\right). \tag{2.93}$$

Second, the weight function for the LJ potential (using the WCA separation) is

$$\begin{aligned} w_{\mathrm{LJ}}(z) &= -\pi\beta\varepsilon_{\mathrm{LJ}}\left(\frac{9}{5}\big(\sqrt[6]{2}\,\sigma_{\mathrm{LJ}}\big)^2 - z^2\right)\,\Theta\big(\sqrt[6]{2}\,\sigma_{\mathrm{LJ}} - |z|\big) \\ &\quad -\pi\beta\varepsilon_{\mathrm{LJ}}\left(-\frac{4}{5}\frac{\sigma_{\mathrm{LJ}}^{12}}{z^{10}} + 2\frac{\sigma_{\mathrm{LJ}}^6}{z^4}\right)\,\Theta\big(|z| - \sigma_{\mathrm{LJ}}\big). \end{aligned} \tag{2.94}$$

2.4.2.2 Effectively two-dimensional Cartesian systems

Analogously, a three-dimensional density distribution may now depend on two Cartesian coordinates x and z, but not on the y coordinate,

$$\varrho(\mathbf{r}) = \varrho(x,z). \tag{2.95}$$

The weighted densities for this case involve two-dimensional weight functions $w_\alpha(x,z)$ and two-dimensional convolutions:

$$\begin{aligned} n_\alpha(x,z) &= n_\alpha(\mathbf{r}) \equiv \int_{\mathbb{R}^3} \mathrm{d}\mathbf{r}'\, \varrho(\mathbf{r}-\mathbf{r}')\, w_\alpha(\mathbf{r}') \\ &= \int_{\mathbb{R}} \mathrm{d}z' \int_{\mathbb{R}} \mathrm{d}z'\, \varrho(x-x', z-z')\, w_\alpha(x',z') \equiv (\varrho \otimes w_\alpha)(x,z). \end{aligned} \tag{2.96}$$

The two-dimensional weight functions

$$w_\alpha(x,z) := \int_{y=-\infty}^{\infty} \mathrm{d}y\; w_\alpha(\mathbf{r}) \tag{2.97}$$

within FMT are given as

$$w_3(x,z) = 2\sqrt{R^2-(x^2+z^2)}\,\Theta(R-\sqrt{x^2+z^2}) \;, \tag{2.98}$$

$$w_2(x,z) = \frac{2R}{\sqrt{R^2-(x^2+z^2)}}\,\Theta(R-\sqrt{x^2+z^2}) \;, \tag{2.99}$$

$$(\mathbf{w}_2)_x(x,z) = \frac{2x}{\sqrt{R^2-(x^2+z^2)}}\,\Theta(R-\sqrt{x^2+z^2}) \;, \tag{2.100}$$

$$(\mathbf{w}_2)_z(x,z) = \frac{2z}{\sqrt{R^2-(x^2+z^2)}}\,\Theta(R-\sqrt{x^2+z^2}) \;, \tag{2.101}$$

$$(\mathbf{w}_2)_y(x,z) = 0, \tag{2.102}$$

and

$$w_1(z) = \frac{w_2(z)}{4\pi R}, \quad w_0(z) = \frac{w_2(z)}{4\pi R^2}, \quad \text{and} \quad \mathbf{w}_1(z) = \frac{\mathbf{w}_2(z)}{4\pi R}. \tag{2.103}$$

Numerically it is difficult to calculate the weighted densities $n_2(x,z)$ and $\mathbf{n}_2(x,z)$ [and their dependent weighted densities $n_1(x,z)$, $n_0(x,z)$, and $\mathbf{n}_1(x,z)$] by a convolution of $\varrho(x,z)$ with the corresponding weight function $w_2(x,z)$ or $\mathbf{w}_2(x,z)$, since they diverge at the border of the Θ function. In order to circumvent this difficulty, *relations between the weight functions* are used: The weight functions w_2 and $\mathbf{w}_2$ are related to the weight function w_3 via

$$w_2 = \frac{\partial}{\partial R} w_3 \quad \text{and} \quad \mathbf{w}_2 = -\nabla w_3, \tag{2.104}$$

respectively. These relations hold independently of the effective dimension of a three-dimensional system, i. e., for $w_3(\mathbf{r})$, $w_3(x,z)$, and $w_3(z)$. They translate to relations between the weighted densites,

$$n_2 = \varrho \otimes w_2 = \varrho \otimes \frac{\partial}{\partial R} w_3 = \frac{\partial}{\partial R}\,(\varrho \otimes w_3) = \frac{\partial}{\partial R}\, n_3 \tag{2.105}$$

and

$$\mathbf{n}_2 = \varrho \otimes \mathbf{w}_2 = \varrho \otimes (-\nabla w_3) = -\nabla\,(\varrho \otimes w_3)\,, \tag{2.106}$$

since here integrations and differentiations permute. Consequently the weighted density n_3 evaluated for two or three different HS radii is sufficient to determine the other weighted densities as well. Details of the numerical implementation are mentioned in Sec. 6.2.2.3.

The functional derivative of the excess free energy functional of a hard-sphere fluid in the case of a two-dimensional density $\varrho(x,z)$ can be expressed as a sum of two-dimensional convolutions,

$$\frac{\delta\beta\mathcal{F}_{\mathrm{ex}}^{\mathrm{HS}}[\varrho]}{\delta\varrho(\mathbf{r})} \;=\; \sum_{\alpha}(\pm)_{\alpha}\left(\frac{\partial\Phi}{\partial n_{\alpha}}\otimes w_{\alpha}\right)(x,z). \tag{2.107}$$

The perturbation theoretical treatment of an attractive interaction part is specified for the case of an effectively two-dimensional density $\varrho(x,z)$ as follows: The weight function $w_{\mathrm{ff}}(x,z)$ for an effectively two-dimensional system reads

$$w_{\mathrm{ff}}(x,z) \;:=\; \int_{y=-\infty}^{\infty}\mathrm{d}y\; w_{\mathrm{ff}}(\mathbf{r}) \tag{2.108}$$

in general and

$$w_{\mathrm{SW}}(x,z) \;=\; -2\beta\varepsilon_{\mathrm{SW}}\sqrt{\sigma_{\mathrm{SW}}^2-(x^2+z^2)}\;\Theta\big(\sigma_{\mathrm{SW}}-\sqrt{x^2+z^2}\big) \tag{2.109}$$

for a SW fluid.

Furthermore I calculated the weight function $w_{\mathrm{LJ}}(x,z)$ for a WCA-LJ fluid analytically. It depends merely on the distance from the origin in the xz plane, $c:=\sqrt{x^2+z^2}$. Except at the origin the weight function can be expressed as

$$\begin{aligned} w_{\mathrm{LJ}}(x,z) \;&\equiv\; w_{\mathrm{LJ}}(c)\\ &=\; \beta\varepsilon_{\mathrm{LJ}}\sigma_{\mathrm{LJ}}\Bigg\{\left[\frac{63}{64}\,\pi\,\left(\frac{\sigma_{\mathrm{LJ}}}{c}\right)^{11}-\frac{3}{2}\,\pi\,\left(\frac{\sigma_{\mathrm{LJ}}}{c}\right)^{5}\right]\Theta\Big(c-\sqrt[6]{2}\,\sigma_{\mathrm{LJ}}\Big)\\ &\qquad +\; f_{\mathrm{LJ}}\Big(\frac{c}{\sigma_{\mathrm{LJ}}}\Big)\;\Theta\Big(\sqrt[6]{2}\,\sigma_{\mathrm{LJ}}-c\Big)\Bigg\} \end{aligned} \tag{2.110}$$

with an auxiliary function

$$\begin{aligned} f_{\mathrm{LJ}}(s) \;:=\;& \tfrac{63}{32}\;s^{-11}\;\arctan\Big(s/\sqrt{2^{1/3}-s^2}\Big) \;-\; \tfrac{63}{32}\,\tfrac{1}{2^{1/3}}\;s^{-10}\,\sqrt{2^{1/3}-s^2}\\ &-\tfrac{21}{32}\,2^{1/3}\;s^{-8}\,\sqrt{2^{1/3}-s^2} \;-\; \tfrac{21}{40}\;s^{-6}\,\sqrt{2^{1/3}-s^2}\\ &-3\;s^{-5}\;\arctan\Big(s/\sqrt{2^{1/3}-s^2}\Big) \;+\; \tfrac{51}{20}\,\tfrac{1}{2^{1/3}}\;s^{-4}\,\sqrt{2^{1/3}-s^2}\\ &+\tfrac{4}{5}\,2^{1/3}\;s^{-2}\,\sqrt{2^{1/3}-s^2} \;-\; 2\,\sqrt{2^{1/3}-s^2}. \end{aligned} \tag{2.111}$$

At the origin the weight function is described by

$$w_{\mathrm{LJ}}(x=0,z=0) \;=\; -\frac{144}{55}\,\sqrt[6]{2}\;\beta\varepsilon_{\mathrm{LJ}}\sigma_{\mathrm{LJ}}. \tag{2.112}$$

For numerical implementations an expansion of $w_{\mathrm{LJ}}(c)$ for small values of c is useful. It is reported in Appendix A on page 144.

3 Planar fluid interfaces

The density profiles of three planar interfaces, namely a solid–gas (s–g), a solid–liquid (s–l), and a liquid–gas (l–g) interface, serve as boundary conditions for the sessile liquid wedge system. In this work the crystal structure of the substrate is neglected and the substrate particles are assumed to be smeared out to an unstructured, homogeneous continuum. Thus effectively one-dimensional s–g, s–l, and l–g interfacial density profiles $\varrho(z)$ are ingredients for the liquid wedge program.

General aspects of fluid interfaces, like the concept of surface tension and (Gibbs) dividing interface, are introduced in the following section. Then the cases of a liquid–gas interface (cf. Sec. 3.2) and a solid–fluid interface (cf. Sec. 3.3) are discussed.

3.1 Surface tension and dividing interfaces

Infinitely large homogeneous systems ("bulk" systems) are an idealization, actual systems are always surrounded by bounderies. Boundary conditions often influence system properties not only in these border regions but also further away from them, deep inside the system. An interface is formed where two phases are in contact. A surface is a certain kind of interface at which one side is filled with air.

An interface usually changes the energy of the system in comparison to bulk systems. The surface excess free energy or the surface excess contribution to the grand potential,

$$\sigma A \;=\; \Omega \;+\; p V, \tag{3.1}$$

scales with the interfacial area A (for an almost infinitely large system and a volume V of the fluid). The associated prefactor is called *surface tension* or *interfacial tension* σ.

Excess quantities (like surface tensions and line tension) are calculated on the basis of a reference system, which consists of imaginary regions of bulk density. Such a region is confined by at least one *dividing interface*, which is the imaginary sharp interface separating two adjacent regions containing different thermodynamic phases. The dividing interface of a liquid–gas interface is discussed in Sec. 3.2.1, whereas solid–liquid and solid–gas interfaces are considered in Sec. 3.3.2.

3.2 Liquid–gas interfaces

3.2.1 Liquid–gas dividing interface

In a situation where a liquid and a gas phase can thermodynamically coexist a *planar* liquid–gas interface actually develops only under the influence of a weak external field, e. g., gravity. For most theoretical descriptions this field can be chosen arbitrarily weak and thus be neglected [133].

At a liquid–gas interface the density distribution varies smoothly over several or many atomic radii. Thus it is not obvious where exactly to locate the dividing interface. In principle the l–g dividing interface can be chosen arbitrarily, and there are several reasonable ways to do so:

First, the plane $z = z_0$ with a density corresponding to the arithmetic average of the bulk liquid and bulk gas densities,

$$\varrho(z = z_0) \;\stackrel{!}{=}\; \frac{1}{2}\left(\varrho_\mathrm{l} \;+\; \varrho_\mathrm{g}\right), \tag{3.2}$$

is an intuitive choice of the dividing interface of a planar l–g interface. This definition has been employed in the present work.

Second, the equimolar dividing interface of a planar l–g interface [assuming $\lim_{z\to-\infty}\varrho(z)=\varrho_\mathrm{l}$ and $\lim_{z\to\infty}\varrho(z)=\varrho_\mathrm{g}$ without loss of generality] is defined by

$$\int_{z=-\infty}^{z_0}\mathrm{d}z\ \left[\varrho_\mathrm{l}-\varrho(z)\right]\ \stackrel{!}{=}\ \int_{z=z_0}^{\infty}\mathrm{d}z\ \left[\varrho(z)-\varrho_\mathrm{g}\right]. \tag{3.3}$$

This definition arranges the dividing interface plane $z=z_0$ such that on each side there is the same amount of particles "missing" in comparison to the bulk liquid density or "too much" in comparison to the bulk gas density, respectively. In other words, the particle deficit on the liquid side and the particle excess on the gas side of the equimolar dividing interface are balanced. For the sharp-kink approximation (cf. Chapter 7) of a liquid–gas interfacial profile this second definition recovers the first definition.

The liquid–gas surface tension σ_lg is *independent* of the choice of the dividing interface for a planar liquid–gas interface. This can be understood by considering the following definition for the l–g surface tension σ_lg, which is more rigorous than the general one in Eq. (3.1):

$$\begin{aligned}\sigma_\mathrm{lg}\ &:=\ \lim_{V_\mathrm{l},V_\mathrm{g}\to\infty}\frac{\Omega\ -\ V_\mathrm{l}\omega_\mathrm{l}\ -\ V_\mathrm{g}\omega_\mathrm{g}}{A_\mathrm{lg}}\ =\ \lim_{V_\mathrm{l},V_\mathrm{g}\to\infty}\frac{\Omega\ +\ p\,V_\mathrm{l}\ +\ p\,V_\mathrm{g}}{A_\mathrm{lg}}\\ &=\ \lim_{V_\mathrm{l},V_\mathrm{g}\to\infty}\frac{\Omega\ +\ p\,V}{A_\mathrm{lg}}.\end{aligned} \tag{3.4}$$

The grand canonical free energy densities $\omega_\mathrm{l}=-p$ and $\omega_\mathrm{g}=-p$ of the liquid phase and of the gas phase, respectively, are equal in thermodynamic equilibrium. For a shifted dividing interface the volumina of each of the two phases changes, but the overall volume $V\equiv V_\mathrm{l}+V_\mathrm{g}$ remains constant. Several analytic approaches to calculate the liquid–gas interfacial tension of a LJ fluid have been made (see, e. g., Ref. [134] and references therein).

Besides the macroscopic thermodynamic description, which ignores the molecular composition of simple fluids, and the statistical mechanical picture, which takes the interactions among molecules into account (on the basis of a partition function or a DFT), another level of description of a l–g interface exists, namely the mechanical (or local thermodynamic) description. From the condition of local mechanical equilibrium an expression for the liquid–gas interfacial tension follows [133],

$$\sigma_\mathrm{lg}\ =\ \int_{z=-\infty}^{\infty}\mathrm{d}z\ \left[p_\mathrm{n}-p_\mathrm{t}(z)\right], \tag{3.5}$$

where p_n is the normal and $p_\mathrm{t}(z)$ the transversal pressure. However, the definition of the latter is not unique and thus makes the approach problematic. This is due to the fact that the forces within the fluid act between molecules and the above expression is based on continuum mechanics [133].

3.2.2 Liquid–gas interfacial density profiles

The asymptotic structure of a planar interface reflects the asymptotic decay of correlations in the corresponding bulk fluid [135]. Here planar liquid–gas interfaces of a LJ and a SW fluid are considered. Let z be the coordinate perpendicular to the interface, which is zero at the interface, positive for the gas region and negative for the liquid region.

A *LJ fluid* comprises long-ranged interactions among the particles. For such a fluid–fluid interaction the density distribution far away from a planar liquid–gas interface reaches the bulk gas or bulk liquid density obeying inverse power laws, which are called "van der Waals tails". The dominant term behaves as z^{-3} [135, 136, 137, 138]. Therefore the asymptotic behavior of the l–g interfacial density profile can be described by

$$\varrho(z) - \varrho_\mathrm{l} \sim -|z|^{-3} \quad \text{for } z \to -\infty \,, \tag{3.6}$$

$$\varrho(z) - \varrho_\mathrm{g} \sim z^{-3} \quad \text{for } z \to \infty. \tag{3.7}$$

Also oscillatory behavior may occur for small or intermediate distances from the interface, see Fig. 3.1.

A *SW fluid* represents a model fluid with short-ranged interactions among the fluid particles. For short-ranged interactions the asymptotic convergence of the density $\varrho(z)$ towards the liquid or gas bulk density exhibits either a monotonic, exponential decay or exponentially damped oscillations, depending on which of the two cases applies to the decay of correlations in the corresponding bulk fluid. A cross-over between the two scenarios occurs at the Fisher-Widom (FW) line in the phase diagram [139]. Typically the FW line reaches the binodals on the liquid side of the phase diagram. For temperatures above the temperature of that point in the phase diagram the density decays exponentially on both sides of a l–g interface. Below that temperature solely the density on the gas side of a l–g interface decays purely exponentially, while the density on the liquid side attains its bulk value in an exponentially damped oscillatory fashion. Examples of density distributions of a SW fluid at liquid–gas interfaces are given in Fig. 3.1.

3.3 Solid–fluid interfaces

Solid surfaces could exhibit arbitrarily many shapes and structures, which likewise affect the shape of an interface between this solid and a fluid phase. Here the substrate molecules are assumed to be homogeneously smeared out, thus the actual crystal structure is neglected. The solid–fluid interface for a planar, unstructured continuum substrate is effectively one-dimensional, if a one-component simple fluid and isotropic interactions are assumed and spontaneous symmetry breaking is excluded. In this case the density distribution exclusively depends on the distance from the substrate surface, i. e., $\varrho = \varrho(z)$.

3.3.1 Substrate potentials

A commonly used description of the interaction between a fluid particle and a planar, laterally translationally invariant (i. e., laterally smeared out, but possibly inhomogeneous in the direction perpendicular to the surface) solid substrate is an expansion of the substrate potential in terms of $1/z$, where z is the distance from the substrate. If one has a substrate composed of acutal molecules in mind, the plane $z = 0$ corresponds here to a plane through the centers of the topmost layer of substrate molecules. The long-ranged behavior is given by a $1/z^3$ term. Thus the substrate potential can be written as

$$V(z > 0) \equiv -\sum_{i \geq 3} \frac{u_i}{z^i}, \tag{3.8}$$

with constant coefficients u_i. Clearly, merely a fraction of all imaginable substrate potentials can be described that way; however, this class of substrate potentials is particularly suited to analyze long-ranged solid–fluid interactions systematically.

A steric interaction (repulsion) between the substrate and the fluid is taken into account by the substrate–fluid potential. An excluded volume (cf. Sec. 3.3.3) can be assigned

to the narrow zone near the substrate surface which is almost free of (centers of) fluid particles, in order to construct the external potential $V_{\text{ext}}(z)$ that is employed in the numerical calculations.

LJ (10–4), (9–3), and (9–4–3) potentials:
A special case of the above mentioned class of substrate potentials is the one which arises from a standard Lennard-Jones (12–6) potential [Eq. (2.63)],

$$\phi_{\text{sf}}(r) \;:=\; 4\,\varepsilon_{\text{w}} \left[\left(\frac{\sigma_{\text{w}}}{r}\right)^{12} - \left(\frac{\sigma_{\text{w}}}{r}\right)^{6} \right], \tag{3.9}$$

between a fluid particle and a substrate particle at distance r. In general, the substrate potential is defined as

$$V_{\text{sf}}(\mathbf{r}) \;:=\; \int_{\mathbb{R}^3} \mathrm{d}\mathbf{r}'\; \varrho_{\text{w}}(\mathbf{r}')\; \phi_{\text{sf}}(|\mathbf{r}-\mathbf{r}'|) \tag{3.10}$$

with the density $\varrho_{\text{w}}(\mathbf{r}')$ of the substrate (wall) particles, which in the present cases is constant (ϱ_{w}) in the substrate region and zero outside. Note that the substrate is assumed to be smeared out and thus homogeneous even on a microscopic level, consequently its potential solely depends on the vertical distance z from the surface.

If the substrate occupies a half space, the resulting potential contains a z^{-9} and a z^{-3} term and is called Lennard-Jones (9–3) potential,

$$\begin{aligned} V_{9-3}(z) \;&:=\; \int_{V_{\text{w}}} \mathrm{d}\mathbf{r}'\; \varrho_{\text{w}}(\mathbf{r}')\; \phi_{\text{sf}}(|\mathbf{r}-\mathbf{r}'|) \;=\; \int_{\mathbb{R}^3} \mathrm{d}\mathbf{r}'\; \varrho_{\text{w}}\,\Theta(-z')\; \phi_{\text{sf}}(|\mathbf{r}-\mathbf{r}'|) \\ &=\; \frac{2}{3}\pi\,\varrho_{\text{w}}\,\sigma_{\text{w}}^3\,\varepsilon_{\text{w}} \left[\frac{2}{15}\left(\frac{\sigma_{\text{w}}}{z}\right)^{9} - \left(\frac{\sigma_{\text{w}}}{z}\right)^{3} \right]. \end{aligned} \tag{3.11}$$

In this work the density of substrate particles is set to

$$\varrho_{\text{w}} \;:=\; \sigma_{\text{w}}^{-3}. \tag{3.12}$$

Likewise in the case of a LJ fluid for the parameter σ_{w} the corresponding parameter of the fluid is chosen, i. e.,

$$\sigma_{\text{w}} \;:=\; \sigma_{\text{LJ}}. \tag{3.13}$$

(For easier comparison also in the case of a square-well fluid the parameters of the external potential are denoted that way.) These two choices are done without loss of generality, since the potential strength can still be adjusted by ε_{w}. A given external potential can be expressed by another substrate density and another value for σ_{w} as well, if the parameter ε_{w} is rescaled accordingly. Thus the solid–fluid interaction parameters and the coefficients from Eq. (3.8) are related via

$$u_3 \;=\; \frac{2}{3}\pi\,\varrho_{\text{w}}\,\sigma_{\text{w}}^6\,\varepsilon_{\text{w}} \;=\; \frac{2}{3}\pi\,\sigma_{\text{LJ}}^3\,\varepsilon_{\text{w}} \tag{3.14}$$

$$u_9 \;=\; -\frac{4}{45}\pi\,\varrho_{\text{w}}\,\sigma_{\text{w}}^{12}\,\varepsilon_{\text{w}} \;=\; -\frac{4}{45}\pi\,\sigma_{\text{LJ}}^9\,\varepsilon_{\text{w}}. \tag{3.15}$$

Note that a positive coefficient u_i corresponds to an attractive contribution.

A monolayer of substrate particles leads to a substrate potential which contains a z^{-10} and a z^{-4} term and is therefore called Lennard-Jones (10–4) potential,

$$\begin{aligned} V_{10-4}(z) \;&:=\; \int_{\mathbb{R}^3} \mathrm{d}\mathbf{r}'\; \varrho_{\text{w,A}}\,\delta(z')\; \phi_{\text{sf}}(|\mathbf{r}-\mathbf{r}'|) \\ &=\; 2\pi\,\varrho_{\text{w,A}}\,\sigma_{\text{w}}^2\,\varepsilon_{\text{w}} \left[\frac{2}{5}\left(\frac{\sigma_{\text{w}}}{z}\right)^{10} - \left(\frac{\sigma_{\text{w}}}{z}\right)^{4} \right], \end{aligned} \tag{3.16}$$

with $\varrho_{\mathrm{w,A}}$ as the number of substrate particles per surface area. The coefficients u_4 and u_{10} can be read off.

If the substrate contains a surface layer different from the substrate structure underneath (e. g., an oxyde layer), the substrate potential contains a z^{-4} term in addition to a LJ (9–3) potential and is abbreviated as Lennard-Jones (9–4–3) potential. This z^{-4} term in addition to a LJ (9–3) potential can exert a large influence on the wetting behavior (cf. Sec. 3.3.5). For convenience let the dimensionless parameter

$$b_4 \;:=\; \frac{u_4}{u_3\,\sigma_{\mathrm{LJ}}} \tag{3.17}$$

describe the relative strength of the z^{-4} term compared to the z^{-3} term.

Clearly, if the substrate is not homogeneous in the z-direction (but still translationally invariant in the lateral directions), many of the coefficients u_i in Eq. (3.8) could be non-zero.

One has to distinguish between the coordinate origin (here $z = 0$ corresponds to the plane through the centers of the topmost layer of substrate molecules), the definition of the dividing interface (cf. Sec. 3.3.2), and the steric interaction between substrate and fluid particles (cf. Sec. 3.3.3).

3.3.2 Solid–fluid dividing interface

The solid–fluid surface tension can be determined for any packing fraction (i. e., for any bulk density) corresponding to a point on or outside the meta-/instability region of the phase diagram. The surface tension involving a substrate and a fluid, liquid, or gas phase is regarded as solid–fluid interfacial tension.

Different choices of a substrate–fluid dividing interface are possible. In the situation of a wedge or droplet on a substrate, where both solid–gas (s–g) and solid–liquid (s–l) interfaces are present at the same time, it is convenient to use a common plane for both the s–g and the s–l interface and regard it as solid–fluid dividing interface. Throughout this work the plane $z = 0$ constitutes the solid–fluid dividing interface.

Sometimes the substrate is treated as a part of the system, sometimes merely the fluid is considered as the system, on which an external potential acts. In Eq. (1.3) the substrate was not included in the system. Since in this section the dividing interface between the substrate and the fluid is focused on and different choices for this plane are allowed, the substrate is treated as a part of the system here. Then analogously to Eq. (3.4) the solid–fluid interfacial tension is defined as

$$\sigma_{\mathrm{sf}} \;:=\; \lim_{V_{\mathrm{s}},V_{\mathrm{f}}\to\infty} \frac{\Omega \;-\; V_{\mathrm{s}}\omega_{\mathrm{s}} \;-\; V_{\mathrm{f}}\omega_{\mathrm{f}}}{A_{\mathrm{sf}}}, \tag{3.18}$$

where ω_{s} and $\omega_{\mathrm{f}} = -p$ denote the grand canonical free energy density of the substrate and the fluid, respectively.

A parallel shift of the dividing interface plane by δh changes the volumina, $V_{\mathrm{s}}^{(2)} = V_{\mathrm{s}}^{(1)} + \delta h\, A_{\mathrm{sf}}$ and $V_{\mathrm{f}}^{(2)} = V_{\mathrm{s}}^{(1)} - \delta h\, A_{\mathrm{sf}}$. Consequently also the value of the surface tension changes,

$$\sigma_{\mathrm{sf}}^{(2)} \;=\; \sigma_{\mathrm{sf}}^{(1)} \;+\; (\omega_{\mathrm{f}} - \omega_{\mathrm{s}})\,\delta h, \tag{3.19}$$

since in general solid and fluid energy densities are different. This difference is due to a constrained equilibrium, where merely the liquid and gas phases thermodynamically coexist and the substrate is regarded as chemically inert. Thus the value of the surface tension of a solid–fluid interface depends on the definition of the s–f dividing interface.

3.3.3 Excluded volume

The steric repulsion between the substrate and fluid particles close to the substrate leads to an (almost) empty region near the substrate surface. In the sharp-kink approximation (cf. Chapter 7) an important parameter is the width d_{w} of this *excluded volume*, since there the fluid density jumps from zero to a finite value. This means that the density does not automatically adjust to values compatible with the external potential, but it is chosen by hand. In numerical, fully microscopic DFT calculations the external potential would be enough to account for steric repulsion. Nevertheless, such a parameter d_{w} can be introduced as an approximation, if the particle density almost vanishes for distances $z \lesssim d_{\mathrm{w}}$.

The substrate–fluid potential is assumed to be a LJ potential in most cases analyzed in this work. Within the WCA or BH separation of a LJ fluid the fluid particles are assigned a hard core of radius R, i. e., a hard-spherical contribution to the interaction potential. Hence it is plausible to perform a similar approximation for the substrate–fluid interaction as well. While in the approximation of the fluid–fluid interaction the distance between two particles cannot be smaller than two atomic radii, here the fluid particles are allowed to approach the substrate surface $z = 0$ up to a distance R. Consequently the region between $z = 0$ and $z = R$ is absolutely free from any particle centers. This choice corresponds to a value

$$d_{\mathrm{w}} \;=\; R \tag{3.20}$$

of the widh of the excluded zone.

The choice $d_{\mathrm{w}} = R$ directly translates into a hard-wall (HW) potential

$$\beta V_{\mathrm{HW}}(z) \;:=\; \begin{cases} \infty & \text{for } z < R \\ 0 & \text{for } z \geq R. \end{cases} \tag{3.21}$$

As a consequence, in this work the external potential $V_{\mathrm{ext}}(z)$ entering Eq. (2.3) shall contain a hard-wall potential,

$$V_{\mathrm{ext}}(z) \;:=\; V_{\mathrm{HW}}(z) \;+\; V(z). \tag{3.22}$$

3.3.4 Solid–fluid interfacial density profiles

3.3.4.1 Sum rules

The equilibrium particle density distribution $\varrho(\mathbf{r})$ of a solid-fluid interface obeys thermodynamic consistency relations called "sum rules". Especially for effectively one-dimensional interfaces, i. e,. a planar solid surfaces with a homogeneous substrate potential, the sum rules are of practical importance as check of the resulting $\varrho(z)$. In the present case two sum rules hold:

Wall theorem or contact value theorem:
The fluid density profile near a substrate fulfills an integral condition over the whole fluid region. Henderson, Blum, and Lebowitz [140] have shown that such a *wall theorem* for an external potential according to Eq. (3.22) and a density $\varrho(z)$ reads

$$\beta p \;=\; \varrho(R^+) \;-\; \int\limits_{z=R^+}^{\infty} \mathrm{d}z \; \frac{\mathrm{d}\beta V(z)}{\mathrm{d}z} \, \varrho(z). \tag{3.23}$$

In the special case of a hard wall the wall theorem above becomes a *contact value theorem*, i. e., it involves merely the density at the closest possible position, $z = R$, of a molecule (with a hard-sphere radius R) at the wall,

$$\beta p \;=\; \varrho(R^+). \tag{3.24}$$

Gibbs' adsorption theorem:
Another useful relation involves the excess adsorption Γ at a planar solid–fluid interface. Γ describes the additional (with respect to a fluid with constant density ϱ_0 up to the excluded volume near the substrate) amount of particles per surface area,

$$\Gamma \;:=\; \frac{1}{A_{\mathrm{sf}}} \int_V \mathrm{d}\mathbf{r} \, \big[\varrho(\mathbf{r}) - \varrho_0\big]. \tag{3.25}$$

Then the Gibbs' adsorption theorem

$$\Gamma \;=\; -\left.\frac{\partial \sigma_{\mathrm{sf}}}{\partial \mu}\right|_{T,V} \tag{3.26}$$

follows from the Gibbs-Duhem relation. For practical purposes the right-hand side is rephrased:

$$\Gamma \;=\; -\frac{\partial \beta\sigma_{\mathrm{sf}}}{\partial \eta} \Big/ \frac{\partial \beta\mu}{\partial \eta}. \tag{3.27}$$

The first factor is accessible numerically, the second factor can be calculated analytically for first-order perturbation theory and the chemical potential belonging to the PY or CS EOS for hard spheres [Eqs. (2.57), (2.44) to (2.46), and (2.48)].

3.3.4.2 Solid–fluid interfacial density profiles

The asymptotic behavior of solid–fluid interfacial density profiles is expected to depend merely on bulk fluid correlations and not on details of the external potential [135]. Hence the statements on liquid–gas interfaces in Sec. 3.2.2 translate directly to solid–fluid interfaces.

A gas in a thermodynamic state of coexistence with its liquid phase can possibly wet a substrate (cf. the next subsection, Sec. 3.3.5). Then the solid–gas interfacial structure recovers the corresponding solid–liquid profile and particularly the asymptotic decay towards the liquid bulk density. In a partial wetting situation the asymptotic decay of a solid–gas interfacial density is still predicted by the Fisher-Widom line, even though density oscillations close to the substrate surface might occur.

Similarly to the liquid–gas interface the density distribution of a LJ fluid at a substrate asymptotically attains the bulk density via a power law with z^{-3} as the dominant term [137, 138],

$$\varrho(z) - \varrho_{\mathrm{f}} \;\sim\; z^{-3} \qquad \text{for } z \to \infty. \tag{3.28}$$

Solid–fluid interfaces comprising LJ or SW fluids, respectively, are displayed in Fig. 3.1.

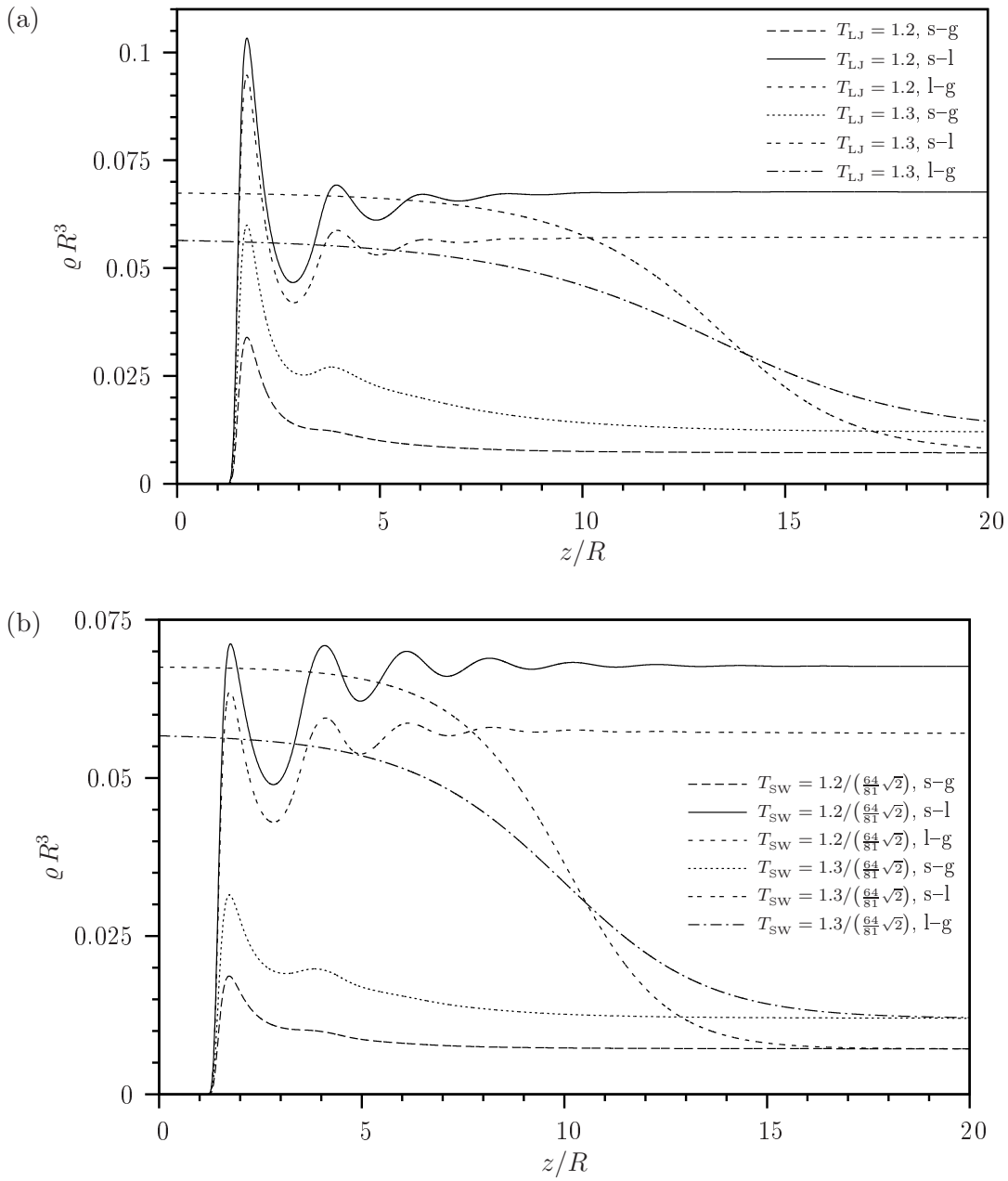

Fig. 3.1: Solid–gas, solid–liquid, and liquid–gas interfacial profiles for (a) LJ and (b) SW fluids. The substrate–fluid interaction is given by a LJ (9–3) potential in both cases, whose strength is described by $\beta\varepsilon_{\mathrm{w}} = 0.6707$ for the LJ fluid in (a) and $\beta\varepsilon_{\mathrm{w}} = 0.45$ for the SW fluid in (b). The LJ fluid is treated within the WCA separation scheme, and the interaction is truncated at an interparticle distance of 10 hard-sphere radii. Hence the physical parameters in (a) and (b) correspond to the wedge line tension calculations in Sec. 8.1.1.1 and 8.1.1.2, respectively. The SW and LJ interfacial profiles are displayed each for two temperatures. The distance from the substrate surface is displayed as abscissa for the s–g and s–l interface, however, the l–g interfacial profiles are shifted suitably such that the interfacial position lies in the plotted range.

3.3.5 Wetting

Wetting and drying transitions:
If the gaseous phase of a suitable fluid is in contact with a sufficiently attractive substrate, a liquid-like film forms on the substrate surface. For suitable parameters (temperature, substrate attractivity, fluid–fluid interaction potential) at liquid–gas coexistence this layer attains a macroscopic thickness, i. e., the film thickness diverges. The transition from a finite to an infite film thickness is called wetting transition or shortly *wetting*. The minimal temperature at which wetting can occur is called wetting temperature T_w.

If the liquid phase of a suitable fluid is in contact with a sufficiently repulsive substrate, a gas-like film forms on the substrate surface. For suitable parameters the film thickness diverges. This analogous effect is called *drying*. Solely the case of wetting with liquid is of interest in the following.

Types of wetting transitions:
If the liquid–gas coexistence line in the phase diagram is approached from the gas side (i. e., $\varrho \nearrow \varrho_\mathrm{g}$ and $\mu \nearrow \mu_\mathrm{coex}$) for a temperature above the wetting temperature ($T > T_\mathrm{w}$), the film thickness (e. g., expressed by the excess adsorption Γ) diverges continuously. One speaks about *complete wetting*.

If for a gas at liquid–gas coexistence ($\varrho = \varrho_\mathrm{g}$ and $\mu = \mu_\mathrm{coex}$) the wetting temperature is approached from below, $T \nearrow T_\mathrm{w}$, two scenarios are possible: Either the film thickness diverges continuously during this process, which is called *critical wetting (or second-order wetting)*, or the film thickness discontinuously changes from finite to infinite at T_w, which is called *first-order wetting*.

Both complete wetting and critical wetting transitions belong to the category of *continuous* wetting transitions, since the layer thickness diverges continuously.

A system of a fluid near a substrate that features a first-order wetting transition displays another phenomenon called *prewetting* (or analogously predrying). Upon approaching coexistence above the wetting temperature (but below the temperature of the prewetting critical point), the film thickness first performs a finite jump (still off coexistence) and then jumps to infinity at $T = T_\mathrm{w}$. The prewetting line in the phase diagram displays the parameters where this finite jump occurs. The prewetting line meets the coexistence line at the wetting transition point, whereas a prewetting critical point constitutes its other end.

Wetting as a phase transition:
A wetting transition represents a surface phase transition (for reviews see Refs. [141] and [142]). In general, a *first-order phase transition* is characterized by a jump in a first partial derivative of a thermodynamic potential, and a *second-order or continuous phase transition* exhibits a non-analyticity (jump or divergence) in a second partial derivative of a thermodynamic potential.

The argumentation, why the above definition of a phase transition is fulfilled for complete, critical, and first-order wetting, is summarized in Appendix C on page 146.

Critical point wetting:
A critical point is a point in the phase diagram where two coexisting phase become indistinguishable. At the critical point of a fluid system any difference between the liquid phase and the coexisting gaseous phase vanishes and merely a fluid phase remains.

In 1977 Cahn [143] presented a conjecture, that complete wetting should always occur close to a critical point. His substantiation for *critical point wetting* is called Cahn's

argument. An illustrative plausibility consideration refers to Young's law and brings to mind the fact that the difference between liquid and gas vanishes at the critical point and that consequently the liquid–gas surface tension vanishes there as well, i. e.,

$$\lim_{T \nearrow T_c} \sigma_{lg} = 0. \tag{3.29}$$

In order to satisfy Young's equation even for vanishing liquid–gas interfacial tension, $\cos\theta$ has to attain the largest possible value, namely 1. As a consequence the contact angle θ vanishes near a critical point, i. e.,

$$\lim_{T \nearrow T_c} \theta = 0, \tag{3.30}$$

which is related to a wetting transition. However, exceptions to Cahn's conjecture have been found in experiments and theory [144], where partial wetting persists even near the critical point.

Effective interface potential:
A useful tool to study wetting properties of a fluid at a solid surface is the *effective interface potential* ω. It is the grand canonical free energy which is necessary to establish an interface between a liquid-like film and the gas phase at a certain, finite distance from the surface instead of forming it infinitely far from the surface. For a planar, homogeneous substrate ω is a function of the film thickness l, which is the distance of the liquid–gas dividing interface from the surface. Thus one can write $\omega = \omega(l)$. Clearly, from the definition one can easily recognize $\omega(l \to \infty) = 0$. The equilibrium film thickness corresponds to the global minimum of the effective interface potential, i. e.,

$$l_0 = \min_l \omega(l). \tag{3.31}$$

A first- or second-order wetting transition as well as prewetting can be understood in this picture as follows. Consider a finite film thickness l_0 and let the temperature increase towards the wetting temperature.
At a first-order wetting transition the position of the minimum jumps from a finite value to infinity. This scenario is related to a negative minimum below the wetting temperature and an energy barrier comprising positive ω values. Upon approaching T_w the depth of the minimum decreases, and finally at T_w the global minimum is degenerate, i. e., $\omega(l_0) = 0 = \omega(l \to \infty)$, and for an infinitesimal temperature increase the equilibrium film thickness diverges.
For critical wetting (i. e., a second-order wetting transition) $\omega(l)$ does not exhibit a positive energy barrier between the finite l_0 [with $\omega(l_0) < 0$] and infinity slightly below the wetting temperature. Upon approaching the wetting transition the minimum becomes less negative and its position is shifted towards large l values. Hence the film thickness diverges continuously with increasing temperature.

Upon approaching the liquid–gas coexistence curve in the phase diagram at a temperature above the wetting temperature prewetting occurs, if the wetting transition on coexistence (approaching the wetting temperature from below) is of first order. Here the jump of the position of the global minimum of ω does not reach an infinite film thickness directly. Rather another minimum at an intermediate l value is accessed before. Therefore the effective interface potential in this case exhibits two (positive-valued) energy barriers, which separate the first and second minimum as well as the second minimum and the third position situated at infinity.

4 Excursion I: sessile droplets and their connection to liquid wedges

In the present study the line tension is deduced from numerical computations of the grand canonical free energy of sessile liquid wedges. However, in order to find observable consequences resulting from the existence of a line tension, object like sessile liquid droplets have to be studied. Locally a sessile droplet can be regarded as a sessile wedge. Moreover in the limit of an infinitely large sessile liquid droplet the structure of the three-phase contact region should resemble the one of a sessile liquid wedge. Thus the two systems, a sessile droplet and a sessile wedge, are closely related.

However, as described in a recent paper by Schimmele, Napiórkowski, and Dietrich [4], very much care is necessary, in order to decompose the grand canonical free energy of a drop into volume, interfacial and line contributions. The problem arises, because a number of contributions to the grand canonical free energy of the drop scale with a linear system dimension and some contributions may be attributed either to the three-phase contact line or alternatively to an interface in terms of appropriate corrections to the interfacial tension. Therefore, when basing the definition of the line tension on a decomposition of the grand canonical free energy of a liquid drop, the mentioned degree of freedom leads to two alternative sensible definitions of a line tension.
In case of the first definition the line tension τ turns out to be *independent* of the position of the Gibbs dividing interfaces separating two adjacent phases; the positions of the Gibbs dividing interfaces are arbitrary to some extent. In this chapter the symbol τ is employed for the first definition of the droplet line tension, whereas in the other chapters it denotes the wedge line tension.
In case of the second definition, the respective line tension denoted $\tau^{(\mathrm{wedge})}$ in the following *does depend* on the choice of the Gibbs dividing interfaces. As the notation indicates, $\tau^{(\mathrm{wedge})}$ agrees with the line tension deduced from the numerical studies of a sessile liquid wedge on a substrate presented later on. The two line tensions τ and $\tau^{(\mathrm{wedge})}$ are connected by a simple relation deduced in Ref. [4]. This relation will be given in Sec. 4.6.

In a further step a modified Young equation, expressing the dependence of the contact angle of a drop on its size (base radius) in terms of the interfacial tensions, the line tension, and other material parameters has to be established. As shown in Ref. [4], in addition to the line tension two further stiffness coefficients have to be attributed to the three-phase contact line, in order to arrive at a description which is free of internal inconsistencies.

The main ideas and results of Ref. [4] are reviewed in the following. Although numerical results presented in this work exclusively refer to wedge systems, in Sec. 9.3.1 an outlook is given, how axisymmetric sessile droplets could be addressed in a fully microscopic approach efficiently.

4.1 Line tension of a sessile droplet

Line tension with or without subdominant terms:
The word "line tension" has to be used with care, since many (more or less precise) definitions are in use. The grand potential of a sessile droplet contains a contribution attributable to the contact line and scaling with the length L of the three-phase contact line. The line tension of a sessile droplet, τ_∞, can be defined as the leading order contribution

of the grand potential line contribution divided by the length of the contact line [4],

$$\left\{\Omega - \sum_{i=\mathrm{s,l,g}} V_i\omega_i - \sum_{i=\mathrm{sg,sl,lg}} A_i\sigma_i\right\}\Big/ L \;=:\; \tau_{_L} \;=:\; \tau_\infty + \text{subleading terms.} \tag{4.1}$$

Here ω_s, ω_l, and ω_g denote the grand canonical free energy densities of a homogeneous solid, liquid, and gas system, respectively. V_i, $i \in \{s, l, g\}$, is the volume of the phase i in the droplet scenario. A_i and σ_i denote the interfacial areas and tensions, respectively. The length of the three-phase contact line is L.

For finite droplet sizes $\tau_{_L}$ as defined via Eq. (4.1) also contains subdominant terms. However, subdominant contributions to the line tension will be disregarded consistently in what follows. In the same spirit contributions to the modified Young equation beyond the order of the line tension term are consistently truncated. By definition the subleading terms vanish for a infinitely long contact line,

$$\lim_{L\to\infty} \tau_{_L} \;=\; \tau_\infty. \tag{4.2}$$

Definition of the reference system:
A reference system has to be defined, with respect to which the line tension of a sessile droplet represents an excess quantity. The consideration is limited to droplets of micrometer size or below. Gravity does not play a role for such small droplets. Consequently in this size regime a sessile droplet has the same shape as, e. g., a pendant droplet or a droplet near a vertical wall. Since a micrometer-sized droplet macroscopicly looks like a spherical cap, the liquid–gas dividing interface is chosen to be a spherical cap, which is fitted to the upper part of the droplet and extrapolated into the three-phase contact region. Hence for this description the droplet has to be sufficiently large such that its shape far from the contact line resembles a spherical cap.

Simple geometric considerations (see, e. g., Ref. [76]) for spherical caps reveal relationships between the contact angle and extension parameters. The contact angle θ, for instance, is related to the heigth h and the radius r of the contact circle via

$$\tan(\theta/2) \;=\; h/r \tag{4.3}$$

and related to the heigth h and the radius $\tilde{R}$ of the sphere, which forms the cap, via

$$\cos\theta \;=\; 1 - h/\tilde{R}. \tag{4.4}$$

The contact angle for partial dewetting (i. e., $90° < \theta < 180°$) and vertical observation cannot be obtained from Eq. (4.3), since r is inaccessible in that case. However, it can be determined from Eq. (4.4), since $\tilde{R}$ can be measured that way.

The solid–gas and solid–liquid dividing interfaces are chosen to lie in the same plane, thus they can be combined to a single solid–fluid interface. The three-phase contact line is defined by the intersection of the spherical cap with this plane. Hence the contact line serves as a "dividing line" [145]. Then the line tension $\tau_{_L}$ is defined by the decomposition of the grand potential [4],

$$\begin{aligned}\Omega \;=\;& -(p+\Delta p)\,V_\mathrm{l} \;-\; p\,V_\mathrm{g} \;+\; \omega_\mathrm{s}\,V_\mathrm{s} \\ & + A_\mathrm{lg}\,\sigma_\mathrm{lg}(R) \;+\; \pi r^2\,\sigma_\mathrm{sl} \;+\; (A-\pi r^2)\,\sigma_\mathrm{sg} \;+\; 2\pi r\,\tau_{_L}\end{aligned} \tag{4.5}$$

with the radius r of the circular base and the radius R of the sphere forming the spherical cap. The contact angle θ is defined as the angle between the solid–fluid dividing interface and the tangent to the spherical cap at the three-phase contact line. The Laplace pressure, i. e., the difference between the pressure inside the droplet ($p_\mathrm{l} = p + \Delta p$) and the pressure

in the gas region ($p_\mathrm{g} = p$), has to be taken into account. Therefore the liquid and gas phases are slightly off bulk coexistence. $\sigma_\mathrm{lg}(R)$ is the surface tension of a free spherical drop surrounded by gas. For infinitely large droplets it recovers the surface tension of a free planar liquid–gas interface,

$$\lim_{R\to\infty} \sigma_\mathrm{lg}(R) \;=\; \sigma_\mathrm{lg}. \tag{4.6}$$

The surface tensions σ_sg and σ_sl are evaluated at the pressure p. Another choice, to evaluate σ_sl at the increased pressure $p + \Delta p$, is reasonable as well and will be discussed in Sec. 4.6.

4.2 Notional invariance

The grand potential Ω is a physical quantity and does not depend on the actual choice of the dividing interfaces. Hence a variation of the dividing interfaces has to leave Ω unchanged. The physical droplet and hence the particle density distribution $\varrho(\mathbf{r})$ remain the same during this variation. Shifts of the dividing interfaces are called *notional shifts* [4]. The property that Ω remains constant under these shifts is called notional invariance. It is applied to derive an equation for the contact angle θ, a (corrected) modified Young equation (cf. Sec. 4.4).

Changes of thermodynamic variables (like surface tension or line tension) induced by a notional shift are described by notional derivatives, which are indicated in Ref. [4] by square brackets enclosing the derivative. $\left[\frac{\mathrm{d}\tau}{\mathrm{d}\theta}\right]$, for instance, is the notional derivative of the line tension with respect to a notional change of θ.

The line tension $\tau = \tau_\infty$, defined via Eq. (4.5) ($L \to \infty$) with the surface tensions σ_sg and σ_sl both taken at the pressure p, is *independent* of the choice of the solid–fluid dividing interface. Notional invariance of τ is a remarkable result, since the line tension $\tau^{(\mathrm{wedge})}$ as well as σ_sg and σ_sl do depend on the position of the solid–fluid interface.

4.3 Variation under constraint of fixed volume

Variations of the droplet shape under the constraint of fixed volume involve non-equilibrium configurations close to equilibrium. The corresponding grand potential is minimized in order to find an equilibrium droplet shape. During this variation procedure the physical system is changed. This contrasts the notional variation in Sec. 4.2.

The derivative of thermodynamic quantities under this variation is indicated by a vertical bar on the right-hand side of the derivative. To call such a quantity "derivative" might lead to misconceptions, since the corresponding infinitesimal change of the system leads the system a little bit away from thermal equilibrium. $\frac{\partial\tau}{\partial R}\big|$, for instance, refers to an equilibrium configuration with radius R and a non-equilibrium configuration with radius $R + \mathrm{d}R$ and the same other physical parameters. These "derivatives" cannot be perceived as usual physical derivatives, that connect equilibrium states, and should rather be regarded as "stiffness coefficients" [4].

The notional derivatives and the constrained variational derivatives (i. e., the stiffness coefficients) of the line tension,

$$\frac{\mathrm{d}\tau}{\mathrm{d}\theta}\bigg| \;=\; \left[\frac{\mathrm{d}\tau}{\mathrm{d}\theta}\right] \quad\text{and}\quad \frac{\mathrm{d}\tau}{\mathrm{d}r}\bigg| \;=\; \left[\frac{\mathrm{d}\tau}{\mathrm{d}r}\right], \tag{4.7}$$

are equal. However, these stiffness coefficients (or notional derivatives) do depend on the choice of the dividing interfaces [4].

4.4 Corrected modified Young equation

Both variational procedures, the notional variation and the constrained variation, lead to the same corrected modified Young equation [4],

$$\sigma_{\mathrm{lg}}(R)\,\cos\theta \,+\, \sigma_{\mathrm{sl}} \,-\, \sigma_{\mathrm{sg}} \;=\; -\,\frac{\tau_\infty}{r} \,-\, \left.\frac{\mathrm{d}\tau}{\mathrm{d}r}\right| \,-\, \frac{\sin\theta\,\cos\theta}{r}\,\left.\frac{\mathrm{d}\tau}{\mathrm{d}\theta}\right|, \tag{4.8}$$

which relates the contact angle θ to the three involved surface tensions, the line tension, and derivatives of the line tension with respect to the droplet base radius r and the contact angle. These two derivatives can be regarded as stiffness coefficients attributed to the contact line. Note that $\sigma_{\mathrm{lg}}(R)$ is the surface tension of a spherical liquid drop (with radius R of the dividing interface) in a gaseous environment [146]. The Tolman length is defined via the first coefficient in an expansion of the surface tension in terms of the inverse curvature $1/R$ [133, 147, 148, 149],

$$\sigma_{\mathrm{lg}}(R) \;=\; \sigma_{\mathrm{lg}}^{\infty}\left(1 \,-\, \frac{2\,\delta_{\mathrm{lg}}^{\mathrm{T}}}{R} \,+\, \ldots\right), \tag{4.9}$$

where $\sigma_{\mathrm{lg}}^{\infty} = \sigma_{\mathrm{lg}}(R \to \infty)$ is the liquid–gas surface tension of a planar interface. The macroscopic contact angle θ_0 is well-known according to Young's equation. The geometric relation $\sin\theta = \frac{r}{R}$ connects the radius R and the base radius r of a spherical cap.

In order to resemble the left-hand side of the standard modified Young equation, Eq. (1.16), the corrected modified Young equation can be expressed as [4]

$$\boxed{\begin{aligned}\cos\theta \;=\; \cos\theta_0 - \frac{\tau_\infty}{r\,\sigma_{\mathrm{lg}}^{\infty}} \,+\, \left(2\,\delta_{\mathrm{lg}}^{\mathrm{T}} - \frac{1}{r\,\sigma_{\mathrm{lg}}^{\infty}}\,\left.\frac{\mathrm{d}\tau}{\mathrm{d}\theta}\right|\right)\,\sin\theta_0\cos\theta_0 \\ -\,\frac{1}{\sigma_{\mathrm{lg}}^{\infty}}\,\left.\frac{\mathrm{d}\tau}{\mathrm{d}r}\right| \,+\, \mathcal{O}\left(\tfrac{\ln r}{r^2}\right).\end{aligned}} \tag{4.10}$$

The curvature dependent surface tension enters here via the surface tension for a planar interface and the Tolman length. Each of the four terms on the right-hand side contributes with comparable magnitude to the difference between the contact angle θ of the considered small droplet and the contact angle θ_0 of a macrsocopic drop. Consequently reported experimental values for the line tension of a droplet do not represent the quantity which should be called line tension. In fact, the experimental line tension values subsume four different contributions from which merely one is the line tension.

4.5 Interpretation of Young's law as a force balance

Young's law, which is valid for macroscopicly large droplets, can be interpreted as a lateral force balance at the contact line. This force balance acts as a boundary condition for the droplet shape. In this macroscopic picture solely translations (and not curvature) of the droplet surface contribute to the surface energy, hence a kink in the droplet surface is not related to a cost in energy and thus a non-vanishing contact angle is possible [150]. The boundary conditions for systems with derivatives in the surface Hamiltonian contain other quantities as well which are related to interface derivatives [150]. The energy of an adhering vesicle, for instance, is sensitive to surface curvature; therefore the contact angle vanishes and the bending rigidity enters the boundary condition [151, 152]. For the microscopic version of Young's law, i. e., the corrected modified Young equation, the interpretation as a lateral force balance is possible as well, even though the additional ingredients [i. e., the four additional terms on the right-hand side of Eq. (4.10)] are not obvious from the beginning.

4.6 Connection between a wedge and a droplet

The line tension of a sessile liquid wedge and the line tension τ defined in Sec. 4.1 for a sessile liquid droplet are closely related. If in Eq. (4.5) the solid–liquid surface tension σ_{sl} is evaluated at the pressure $p + \Delta p$ inside the drop, one obtains another definition of the line tension This alternatively defined sessile droplet line tension is called $\tau_L^{(\mathrm{wedge})}$. The leading term,

$$\tau_\infty^{(\mathrm{wedge})} := \lim_{L\to\infty} \tau_L^{(\mathrm{wedge})} \tag{4.11}$$

equals the line tension of a liquid wedge on a substrate [4]. The reason for this equality is, that the modification of the solid–liquid interfacial tension due to the presence of the Laplace pressure is now explicitly taken care of via the pressure dependent solid–liquid interfacial tension and thus taken out from the definition of a line tension. Therefore, $\tau_L^{(\mathrm{wedge})}$ is the "clean" line tension. On the other hand the equation for the contact angle becomes simpler in terms of τ. Moreover $\tau_\infty^{(\mathrm{wedge})}$, i. e., the alternative droplet line tension or the wedge line tension, depends on the choice of the solid–fluid dividing interface.

The difference in the surface tensions evaluated at different pressures is reflected in the relation between τ and $\tau^{(\mathrm{wedge})}$ [4],

$$\tau \;=\; \tau^{(\mathrm{wedge})} \;+\; \frac{r}{2}\big[\sigma_{\mathrm{sl}}(p+\Delta p) - \sigma_{\mathrm{sl}}(p)\big]. \tag{4.12}$$

Expanding the surface tension $\sigma_{\mathrm{sl}}(p + \Delta p)$ around p yields

$$\begin{aligned} \sigma_{\mathrm{sl}}(p+\Delta p) \;&\simeq\; \sigma_{\mathrm{sl}}(p) \;+\; \frac{\partial\sigma_{\mathrm{sl}}}{\partial\mu}\,\frac{\partial\mu}{\partial p}\,\Delta p \\ &=\; \sigma_{\mathrm{sl}}(p) \;+\; (-\Gamma_{\mathrm{sl}}) \times \frac{1}{\varrho_{\mathrm{l}}} \times \frac{2}{r}\sigma_{\mathrm{lg}}(p)\sin\theta_0 \end{aligned} \tag{4.13}$$

with the excess adsorption Γ_{sl} [Eq. (3.25)] and the bulk liquid density ϱ_{l}.

Hence the transformation law between the two line tensions (focusing merely on the leading terms) reads [4]

$$\boxed{\tau_\infty \;=\; \tau_\infty^{(\mathrm{wedge})} \;-\; \frac{\Gamma_{\mathrm{sl}}}{\varrho_{\mathrm{l}}}\,\sigma_{\mathrm{lg}}(p)\,\sin\theta_0.} \tag{4.14}$$

The quantities Γ_{sl}, $\sigma_{\mathrm{lg}}(p)$, and the macroscopic contact angle θ_0 can be calculated in an effectively one-dimensional geometry, and ϱ_{l} is known from the bulk phase diagram. Consequently line tension calculations for the wedge model providing values of $\tau_\infty^{(\mathrm{wedge})}$ are sufficient to determine the line tension τ_∞ of a sessile droplet.

5 Excursion II: other line excess quantities

The concept of *line excess quantities* reaches beyond the line tension. A line excess quantity represents a coefficient of a line term in a decomposition of a certain quantity into volume, surface, line, and point contributions. Relevant decomposable quantities in the one-component, simple, electrically uncharged fluid systems considered in this work are the grand potential and the average (excess) number of adsorbed particles. The name of a line excess quantity in an energetical decomposition contains the word "tension" (e. g., line tension, boundary line tension or substrate boundary line tension), whereas the line excess quantity in an *excess particle number decomposition* is called *line adsorption* Λ. Both the line tension and the line adsorption can be calculated from a givend density distribution $\varrho(x, z)$ and values of the corresponding surface tensions and excess adsorptions, respectively.

Clearly, for a multi-component system the excess particle number of each species can be decomposed accordingly, leading to a line adsorption for each species. In an electrically charged system one could decompose the equilibrium mean charge distribution into volume, surface, line, and point contributions as well.

The main question which arises on discussing excess quantities is, what the (virtual) *reference system* is, with respect to which the excess (in energy, particle number, or whatever) is counted. In the following the line adsoprtion for a liquid wedge and the line tensions for a few other systems are considered briefly. Even though these quantities are not calculated explicitly in this study, the conceptual aspects addressed here serve to perceive the subject of wedge line tensions from a more general point of view.

5.1 Line adsorption of a liquid wedge

The line adsorption Λ of a fluid system describes the amount of particles, which is accumulated at a certain structural line in addition to the particles present in the corresponding bulk fluid systems and in addition to the excess adsorption at participating interfaces. Such a structural line can be formed by the contact line of a sessile droplet or liquid wedge or by the line of a chemical substrate boundary or a geometrical edge or wedge in the shape of the substrate surface.

The definition of the line adsorption Λ of a sessile liquid wedge proceeds analogously to the definition of the wedge line tension [Eqs. (1.3) and (6.1)], i. e.,

$$\langle N \rangle := \int_{\mathbb{R}^3} \mathrm{d}\mathbf{r}\, \varrho(\mathbf{r}) =: -\varrho_{\mathrm{bulk}}\, V_{\mathrm{fluid}} + \Gamma_{\mathrm{sg}}\, A_{\mathrm{sg}} + \Gamma_{\mathrm{sl}}\, A_{\mathrm{sl}} + \Gamma_{\mathrm{lg}}\, A_{\mathrm{lg}} + \Lambda\, L. \quad (5.1)$$

The value of the line adsorption of a sessile liquid wedge depends on the position of the substrate–fluid dividing interface like the line tension does. Furthermore the line adsorption depends on the choice of the liquid–gas dividing interface. This is a major difference to the wedge line tension, which does not depend on it. The reason for this difference is the fact that the grand canonical free energy densities are identical for coexisting liquid and gas phases, however, the bulk liquid and bulk gas particle number densities are not identical.

In order to enable the comparison of values for Λ, which correspond to different choices of both the liquid–gas and the solid–fluid dividing interface, the transformation laws for Λ are presented here. They are derived in the spirit of the derivation of the transformation rule for the wedge line tension (cf. Appendix B on page 144).

First, a shift δh of the solid–fluid dividing interface is related to a change in the line adsorption value according to

$$\Lambda^{(2)} - \Lambda^{(1)} \;=\; \frac{\delta h}{\tan\theta}\left(\Gamma_{\mathrm{sl}}^{(1)} - \Gamma_{\mathrm{sg}}^{(1)} + \frac{1}{\cos\theta}\,\Gamma_{\mathrm{lg}}\right) \;+\; \frac{1}{2}\,\frac{(\delta h)^2}{\tan\theta}\,\left(\varrho_{\mathrm{l}} - \varrho_{\mathrm{g}}\right). \tag{5.2}$$

Here $\Gamma_{\mathrm{sg}}^{(1)}$, $\Gamma_{\mathrm{sl}}^{(1)}$, and Γ_{lg} denote the excess adsorption of a planar solid–gas, solid–liquid, or liquid–gas interface, θ is the contact angle, and ϱ_{l} and ϱ_{g} are the bulk liquid and bulk gas densities, respectively.

Second, a shift Δz_{lg} of the liquid–gas dividing interface (such that the liquid volume is enlarged at the expense of the gas volume) gives rise to the following change:

$$\Lambda^{(2)} - \Lambda^{(1)} \;=\; \frac{\Delta z_{\mathrm{lg}}}{\sin\theta}\,\left(\Gamma_{\mathrm{sg}} - \Gamma_{\mathrm{sl}}\right) \;+\; \frac{1}{2}\,\frac{\left(\Delta z_{\mathrm{lg}}\right)^2}{\tan\theta}\,\left(\varrho_{\mathrm{l}} - \varrho_{\mathrm{g}}\right). \tag{5.3}$$

A liquid wedge corresponds to a constrained three-phase equilibrium, and so it represents the special case of one angle of 180° in a Neumann triangle. The Neumann triangle consists of the three dividing interfaces between three phases α, β, and γ and three angles (with the same names) between them. Let μ_i be the chemical potential of species $i \in \{1, 2, \ldots, c\}$ in a c-component system. A change in the line tension value is related to changes in temperature, chemical potentials, and angles via the (modified) linear adsorption equation [153],

$$\mathrm{d}\tau \;=\; \sum_{i=1}^{c}\left(-s_{\mathrm{line}}^{i}\,\mathrm{d}T \;-\; \Lambda_i\,\mathrm{d}\mu_i\right) \;+\; \sum_{\zeta=\alpha,\beta,\gamma} c_\zeta\,\mathrm{d}\zeta. \tag{5.4}$$

Here s_{line}^{i} is the line entropy of species i. The last term of this expression accounts for the change of the angles on changing the chemical potentials. In the special case of a one-component sessile wedge the above linear adsorption equation simplifies to

$$\mathrm{d}\tau \;=\; -\,s_{\mathrm{line}}\,\mathrm{d}T \;-\; \Lambda\,\mathrm{d}\mu \;+\; c_\theta\,\mathrm{d}\theta, \tag{5.5}$$

where one of the three angles is the contact angle θ.

The concept of line adsorption, described above exemplarily for the sessile wedge system, can be applied to other systems as well, e. g., the ones discussed in the following section.

5.2 A closer look at other line tensions

Line tensions, i. e., energetical line excess quantities, can arise in different systems (see Sec. 1.4). The line tension of a sessile liquid droplet and its relationship with the wedge line tension have already been discussed in Chapter 4.

Now the boundary line tension and the line tensions due to geometric or chemical substrate boundaries shall be considered from the microscopic point of view. Special attention is turned to the definition of an appropriate reference system for each case.

5.2.1 Surface phase coexistence for prewetting: boundary tension

Assume a solid–fluid interface in a prewetting scenario, i. e., the thermodynamic state corresponds to a point on the prewetting line in the phase diagram. Then two surface phases can coexist. They exhibit different heights of a liquid-like film formed on the substrate.

The two surface tensions, associated with one of the two phases on a planar substrate, are equal at coexistence. The reason for this is, that coexistence between both surface phases requires a lateral shift of the interface between both surface phases not to cost any energy. Since the bulk grand canonical free energy density and the surface tension are identical for both phases at coexistence, the value of the boundary tension is independent from the position of the dividing interface between the two substrate regions.

If the two coexisting surface phases form to a straight linear interface, a boundary line tension is attributed to this contact line. It is defined via a decomposition of the grand potential Ω_b for this prewetting scenario,

$$\Omega_\mathrm{b} \;=:\; -p\,V + \sigma_\mathrm{sf}\,(A_\mathrm{thin} + A_\mathrm{thick}) + \tau_\mathrm{b}\,L, \tag{5.6}$$

where A_thin and A_thick are the interfacial areas of the two surface phases exhibiting a thin or thick liquid-like film, respectively. Hence the reference system for the boundary tension scenario consists of two adjacent regions comprising a planar interface between the substrate and the first or second surface phase, respectively. Then the boundary tension is the excess grand canonical free energy per unit length of the straight contact line between the two coexisting surface phases.

At the wetting transition the boundary line tension and the wedge line tension are expected to be equal [44],

$$\lim_{T \to T_\mathrm{W}} \tau_\mathrm{b} \;=\; \tau. \tag{5.7}$$

The above statement can be proven for the microscopic DFT approach, the described reference systems for the wedge line tension and the boundary tension and for the choice of a trapezoidal shape of the finite system (cf. Sec. 6.1) as follows: The grand potential for the wedge scenario is given in Eq. (1.3). Young's law for the wetting transition ($\theta \to 0$) gives $\sigma_\mathrm{sg} \;=\; \sigma_\mathrm{sl} + \sigma_\mathrm{lg}$. If the solid–liquid and the liquid–gas interfacial areas are chosen to be equal,

$$A_\mathrm{sl} \;=\; A_\mathrm{lg}, \tag{5.8}$$

the wedge energy decomposition can be expressed as

$$\Omega \;=\; -p\,V + \sigma_\mathrm{sg}\left(A_\mathrm{sg} + A_\mathrm{sl}\right) + \tau\,L. \tag{5.9}$$

Equation (5.8) holds (even for all contact angles) for the trapezoidal shape of the finite region for which Ω is obtained. At the wetting transition the solid–fluid surface tension

σ_{sf} is given by the solid–gas surface tension. The values of the grand potential are the same at the wetting transition ($T = T_{\mathrm{w}}$), no matter whether this point in the phase diagram was reached on the prewetting line (from $T > T_{\mathrm{w}}$) or on the coexistence line (from $T < T_{\mathrm{w}}$). Clearly, the sums $A_{\mathrm{thin}} + A_{\mathrm{thick}}$ and $A_{\mathrm{sg}} + A_{\mathrm{sl}}$ both equal the area A of the solid surface. Consequently the values of the line and boundary tension are indeed identical at the wetting temperature.

5.2.2 Chemically structured substrate: substrate boundary line tension

In fluid systems with chemically structured substrates a grand potential contribution scaling with a length can arise as well. This is the case, e. g., if there is a planar substrate consisting of two different materials meeting at a plane perpendicular to their substrate–fluid surfaces [154]. Then they expose a boundary line that is translationally invariant in the y direction towards the fluid phase. Line excess quantities for the decomposition (with respect to volume, surface, and line contributions) of the grand potential and the excess particle number can be defined. They are denoted as "substrate boundary line tension" and "substrate boundary line adsorption", respectively. The reference system contains a planar solid–fluid dividing interface, where the substrate is split into two parts. The decomposition of the grand potential,

$$\Omega \;=:\; -p\,V \;+\; \sigma_{\mathrm{sf}\,1}\,A_{\mathrm{sf}\,1} \;+\; \sigma_{\mathrm{sf}\,2}\,A_{\mathrm{sf}\,2} \;+\; \tau_{\text{chem. step}}\,L, \tag{5.10}$$

defines the substrate boundary line tension (or chemical step line tension). Note that the value of the line tension for this system depends not only on the choice of the solid–fluid dividing interface, but also on the lateral position of the substrate boundary line, which separates the two adjacent kinds of substrate material.

In this context of chemically structured substrates it is inevitable to mention *Cassie's law* from 1944 [155, 156], which proposes a droplet contact angle for a binary composite substrate,

$$\cos\theta_{\mathrm{C}} \;=\; f_1\,\cos\theta_1 \;+\; (1-f_1)\,\cos\theta_2, \tag{5.11}$$

where f_1 denotes the fractional area of species 1, while the contact angle for a pure substrate of species 1 or 2 is given by θ_1 and θ_2, respectively.
Cassie's law gives an illustrative explanation of superhydrophobicity for rough, hydrophobic surfaces: If the liquid does not fill the air pockets on the surface (a so-called Cassie-Baxter state [155]), the situation represents a composite wetting state with the substrate material as species 1 and air as species 2. Liquid on air has a contact angle of 180°, so the above general expression simplifies to

$$\cos\theta_{\mathrm{C}} \;=\; f_1\,\cos\theta_1 \;+\; f_1 - 1 \;=\; -1 \;+\; f_1\,(1 + \cos\theta_1)\,. \tag{5.12}$$

Consequently the composite structure leads to a larger contact angle than for the pure, planar solid.

Based on a free energy minimization of a droplet residing on a rough or/and chemically inhomogeneous substrate, generalizations of Cassie's and Wenzel's law were obtained, which in limiting cases yield these two equations [157]. Besides gravity and line tension influences are detected. It has been found meanwhile [158, 159], that for a system with a contorted (i. e., not parallel) contact line Cassie's law requires a correction which involves the contact line and therewith the line tension. However the modified equations discussed there do not include the stiffness coefficients of the contact line [4] (see Chapter 4). Very recently was claimed [160], that contact lines and not contact areas (which enter Cassie's law) influence the wetting behavior of structured substrates.

5.2.3 Geometrically structured substrates

A simple case of a linear, geometrical substrate structure is a wedge- or edge-shaped substrate, not necessarily with a right angle. In general, the angle between two planar semi-infinite solid–fluid interfaces could vary between 0° and 360°. A substrate wedge corresponds to an edge-shaped fluid region and vice versa. The reference system shall consist of bulk fluid extrapolated up to the solid–fluid interface, which is sharp bent at the edge/wedge line. The surface tension for this bent solid–fluid interface is taken from a planar interface. Thus the edge or wedge line tension, τ_{edge} or τ_{wedge}, respectively, is defined via the following decomposition of the grand potential,

$$\Omega \;=:\; -p\,V \;+\; \sigma_{\text{sf}}\,A_{\text{sf}} \;+\; \tau_{\text{edge/wedge}}\,L. \tag{5.13}$$

Another example is a *geometrical step* in the substrate, which consists of a rectangular substrate edge followed by a rectangular substrate wedge. This step can be conceived as a unified structure and attributed a line tension and a line adsorption (called step line tension or step line adsorption, respectively). A reference system for this case can be defined as a step-shaped fluid region consisting of bulk fluid (with its bulk density). The solid–fluid interfaces — also in the possibly short part between the edge and the wedge — are taken into account by the correspdonding surface tension for a planar substrate. For a very large step heigth H the step line tension is simply the sum of a substrate wedge line tension and a substrate edge line tension. For an intermediate step height H the step line tension depends on H, and for vanishing step heigth the step line tension obviously has to vanish.

Wenzel's law [161],

$$\cos\theta_{\text{w}} \;=\; r_{\text{m}}\,\cos\theta_0, \tag{5.14}$$

describes the effect of surface roughness on the contact angle. The corresponding planar substrate gives rise to a contact angle θ_0. The roughness factor r_{m} is defined as the ratio of the total surface area (including the sides and base of the roughness elements) to the projected surface area (not including the sides of the roughness elements). For Wenzel's law the droplet is assumed to be in a Wenzel state, i. e., the droplet covers its base surface area intimately and does not leave air pockets. Drelich modified Wenzel's equation by taking the line tension into account [159]. To include rough substrates into DFT calculations is a matter of long-standing interest [162, 163, 164, 165].

6 Model system: a liquid wedge on a substrate

6.1 Details of the model system

As mentioned briefly in Sec. 1.3, a sessile liquid wedge coexisting with its gas phase is considered in an effectively two-dimensional, Cartesian coordinate system. y denotes the direction of the straight contact line (in which the density distribution is translationally invariant); x and z label the remaining lateral and vertical directions. In comparision to a finite sessile droplet the advantages of a liquid wedge are twofold: (i) The contact line is straight, and (ii) the liquid–gas interface is asymptotically planar.

The fluid consists of particles interacting via a (truncated) Lennard-Jones (12–6) potential (see Sec. 2.3.4) or a short-ranged square-well potential (see Sec. 2.3.5). The LJ potential is untruncated in the y-direction, since this direction is integrated out analytically. However, in x- and z-direction a cut-off is introduced in a radial symmetric fashion. The interaction is set to zero for a particle distance $\sqrt{x^2 + z^2}$ in the xz plane of more than $\mathrm{cut}_{\mathrm{LJ}}$. Note that auxiliary, effectively one-dimensional density distributions $\varrho(z)$ do not comprise a cut-off in the x-direction, since also this direction was integrated out analytically. Thus, strictly speaking, for a LJ fluid $\varrho(z)$ and $\varrho(x, z)$ refer to slightly different model systems. Differences between the discrete, effectively one- and two-dimensional LJ fluid systems arise both from this different cut-offs and different discretization errors. Contrarily the SW fluid systems exhibit merely slightly differnt discretization errors in effectively one and two dimensions. The cut LJ potential is regarded as an approximation of the untruncated LJ, i. e., the integrated strength from the untruncated LJ potential is employed. This is the reason, why the phase diagram for the LJ fluid is apparently independent of the cut-off. Technical aspects of the cut-off and a compensation of numerical integration errors are mentioned in Sec. 6.2.3.

The LJ fluid was treated in the WCA separation scheme (see Sec. 2.3.4). The attractive parts of the LJ or SW fluid–fluid interaction are taken into account by the RPA (see Sec. 2.3.1). An effective hard-sphere diameter [Eq. (2.72)] for the WCA-LJ fluid was not applied here. Instead the hard-sphere diameter is set equal to the LJ length parameter σ_{LJ}.

The liquid wedge is residing on a homogeneous, planar substrate. It is described by a LJ (9–4–3) potential (see Sec. 3.3.1), a cut and shifted LJ (9–3) potential (cf. Sec. 8.1.3) or a tailored potential (cf. Sec. 8.2).

Definition of the wedge contour:
The *contour* of an object is called the connected surface which characterizes its shape, and it is obtained from the continuous density distribution. The contour of a liquid wedge can be described reasonably by the non-planar liquid–gas dividing interface $c(x, z)$. There are several possibilities for such a dividing interface (see Sec. 3.2.1), here an "arithmetic average" dividing interface is employed.

Contours based on this definition are accessible both in the fully microscopic calculations (cf. Chapter 8) and in the sharp-kink calculations (cf. Sec. 7.3). For sharp contact angles, $\theta < 90°$, the contour is a function $l(x)$ for the sharp-kink approach. However, in the fully microscopic approach packing effects typically lead to more than one contour point for a certain lateral position x, hence contour within the fully microscopic approach is a function of x and z.

Rigorous definition of the line tension of a sessile liquid wedge:
The definition of the line tension of a liquid wedge on a substrate follows the definition for a sessile droplet [Eq. (4.1)] for an infinitely large contact line length L,

$$\Omega^{(\text{with substrate})} =: \sum_{i=\text{s,l,g}} V_i\,\omega_i + \sum_{i=\text{sg,sl,lg}} A_i\,\sigma_i + \tau\,L \tag{6.1}$$

with grand canonical free energy densities ω_i, $i \in \{s, l, g\}$, and the three involved surface tensions σ_i of planar interfaces. So the reference system is defined as a virtual liquid wedge with sharp solid–fluid and liquid–gas interfaces where a planar l–g interface approaches the substrate under the macroscopic contact angle θ. The particle density in the solid, liquid, or gas region of the reference system equals the respective bulk density. The line tension corresponds to an excess free energy with respect to this reference system.

For a certain choice of the solid–fluid dividing interface the substrate contribution to the grand potential of the whole system can be ignored and one can concentrate on the fluid subsystem,

$$\Omega := \Omega^{(\text{with substrate})} - V_\text{s}\,\omega_\text{s}. \tag{6.2}$$

Hence with $\omega_\text{l} = \omega_\text{g} = -p$ and the fluid volume $V := V_\text{l} + V_\text{g}$ the line tension definition from Eq. (1.3) is recovered,

$$\Omega = -p\,V + A_\text{sg}\,\sigma_\text{sg} + A_\text{sl}\,\sigma_\text{sl} + A_\text{lg}\,\sigma_\text{lg} + \tau\,L. \tag{6.3}$$

Transformation law for a different solid–fluid dividing interface:
The value of the line tension τ of a liquid wedge depends on the choice of the dividing interface for the solid–fluid interface. In other words, a differently chosen solid–fluid dividing interface causes a different value of the liquid wedge line tension. A shift δh of the s–f dividing interface in positive z-direction is accompagnied by changes of the area of the planar and sharp interfaces of the reference system. Since the substrate volume changes through the shift process, it is not sufficient to consider exclusively the fluid subsystem [Eq. (6.3)], but the substrate has to be included as well [Eq. (6.1)].

The derivation of the transformation law for the line tension of a sessile liquid wedge is performed in Appendix B on page 144. The result reads [Eq. (B.18)]

$$\tau^{(2)} - \tau^{(1)} = \frac{\sigma_\text{lg} + \left(\sigma_\text{sl}^{(1)} - \sigma_\text{sg}^{(1)}\right)\cos\theta}{\sin\theta}\,\delta h. \tag{6.4}$$

Consequently in order to make wedge line tension values comparable, besides the bare values also the employed definition of the substrate surface has to be mentioned.

6.2 Aspects of the numerical implementation

Some details of the numerical, fully microscopic calculation of the structure of the three-phase contact region and the corresponding wedge line tension are presented here.

The fluid density $\varrho(x, z)$ is desbribed by a two-dimensional, discrete array. The discretization is realized as follows: A distance corresponding to the hard-sphere radius R is split into N grid points. The effectively one-dimensional calculations discretize merely the z coordinate, whereas the effectively one-dimensional calculations discretize both the x and z coordinate such that a unit cell is a square with side length

$$\Delta := \frac{R}{N}. \tag{6.5}$$

If not stated differently, $N = 15$ was used throughout this work.

6.2.1 Boundary profiles and initialization of the ϱ-array

The calculation of the wedge density distribution $\varrho(x, z)$ has to be performed in a finite region of the xz plane and simultaneously has to mimic a fluid halfspace.

Boundary profiles:
The three-phase contact region of a liquid wedge on a substrate is formed by the contact of three interfaces, namely a solid–gas, a solid–liquid, and a liquid–gas interface. Far from this contact region the unperturbed interfacial profiles are recovered. This fact determines the boundary conditions of the necessarily finite system serving for numerical calculations. Beyond the region where the iteration procedure for solving the Euler-Lagrange equation is performed the three interfacial profiles are kept fixed. These "boundary profiles" have to govern whole stripes (and not only single rows), since the range of the fluid–fluid interaction has to be respected. For a square-well fluid the distance between the iteration region and the end of the boundary region has to be $\sigma_{\mathrm{sw}} = 3\,R$; for a Lennard-Jones fluid this distance has to be, in principle, infinitely large, therefore a cut-off has to be introduced. Typical cut-offs used in the performed calculations are of the order of 10 to $20\,R$ in effectively one- and two-dimensional cases or sometimes even up to hundreds of molecular radii R in effectively one-dimensional cases.

The boundary profiles are effectively one-dimensional. However, the effectively one-dimensional results serve as an input for the two-dimensional program, where the x coordinate is discretized as well and not integrated out analytically. Hence the 2D program runs to a slightly different convergence point than the 1D program. Particularly the wetting temperatures in effectively 1D and 2D deviate slightly (cf. Chapter 8). Such refined 2D boundary profiles are employed for all line tension calculations performed for this work
.

The liquid–gas interface profile is rotated by the contact angle θ in order to serve as a boundary profile for the wedge. However, the grid of the wedge system is Cartesian and consequently there is a grid mismatch. Hence the grid points in the liquid–gas boundary region have to be filled by an interpolation of the liquid–gas profile. For this purpose a linear interpolation is established such that for the density initialization at a certain distance from the l-g dividing interface of the wedge the two neighboring data points which are closest to this distance from the interface are employed.

Initialization of the ϱ-array besides the boundary profiles:
Besides the boundary profiles mentioned above, the remaining region of the two-dimensional array representing the density distribution $\varrho(x, z)$ has to be initialized somehow. Since the fluid particle density is zero inside the substrate and since Fourier transforms of the density array presume periodic boundary conditions, a strip of zeros has to be introduced to the density array for large values of z. Similarly for $0 \leq z < R$ the density is zero as well due to the hard cores of the fluid particles and the substrate. For the remaining region it would be sufficient, in principle, to initialize with a constant particle density value. In order to optimize the convergence speed of the iteration process the initial density distribution is recommended to be chosen as similar to the expected equilibrium density distribution as possible with reasonable effort. Consequently in the regions near the substrate either a solid–liquid or a solid–gas interfacial profile is employed and the region of the liquid–gas interface is initialized with a liquid–gas interface for the actual parameter values. In other words, the boundary profiles are extrapolated up to the contact line. In order to decide for at each point which interface profile should be applied here the bisecting lines of the contact angle θ and the complementary angle (i. e., $180° - \theta$) are taken as a reference, decomposing the fluid halfspace into a solid–gas, a solid–liquid,

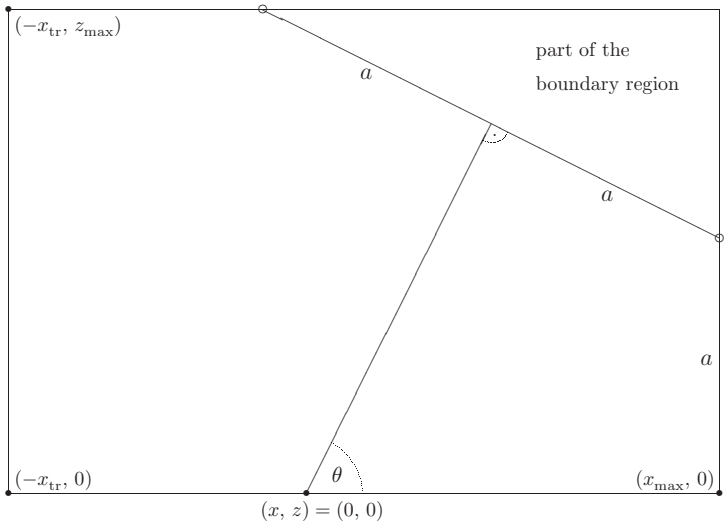

Fig. 6.1: Sketch of the finite system. The trapezoidal iteration region is displayed, in which the Picard iteration is performed. Additionally the rectangular $\varrho(x, z)$-array contains boundary regions, which serve to establish planar s–g, s–l, and l–g interfacial profiles far away from the three-phase contact region. Depending on the range of the fluid–fluid interaction the size of the whole array may be much larger than the iteration region. The two points in the xz plane that are marked by empty circles are at least a distance a away from both the liquid–gas and the solid–fluid dividing interface. A sufficiently large value of a ensures that artificial line tension contributions can be neglected.

and a liquid–gas initialization region. An exception is made: The region near the substrate surface is dominated by the substrate influence, and therefore only solid–gas and solid–liquid interfacial profiles are used there. Otherwise near the triple line large changes during the first iteration steps might occur (which decreases the maximum possible value of the mixing parameter).

Iteration region and integration region:
The iteration region, i. e., the region where the values of the ϱ-array are subject to changes in the course of the iteration process, corresponds to a trapeze, see Fig. 6.1. It omits the boundary regions, where the boundary profiles are kept untouched, and the zero-stripes for large (and small) values of the z coordinate. Such a trapezoidal shape of the integration area was used before [48].

Young's law determines the contact angle θ, which is attained far away from the three-phase contact region. Hence the (for sharp contact angles) top-right, inclined boundary of the trapeze is perpendicular to the asymptotic contour profile, which is a straight line from this boundary to the substrate surface $z = 0$, which it touches at $x = 0$. (This is in contrast to the definition in the sharp-kink theory, where $x = 0$ describes the intersection of the asymptotic liquid–gas interface curve and the equilibrium film thickness l_0.)

The mismatch of the liquid–gas boundary profile, due to the profile inclination and the accompanied interpolation, leads to very small artefacts in the density distribution $\varrho(x, z)$. However, this effect is limited to that part of the iteration region which is situated very close to the liquid–gas boundary region. Consequently artefacts in the quantities calculated from the density distribution $\varrho(x, z)$ can be avoided, if a small stripe of the iteration region near the liquid–gas boundary is omitted in integrations. In other words, the integration region is a little bit smaller than the iteration region.

The lateral and vertical system size is described by the trapezoidal iteration (or integration) region. Within this trapeze one has $x \in [0, x_{\max}]$ and $z \in [0, z_{\max}]$. The parameters $x_{\max}$ and $z_{\max}$ are determined by three conditions:

(i) The distance between the point where the inclined boundary line to the l–g boundary profile intersects the ($x = x_{\max}$)-axis and the substrate surface is a. The calculations performed in this study employed $a/R = 30$ throughout, except in the analysis of numerical errors.

(ii) The contour asymptote [starting at $(x, z) = (0, 0)$] separates the inclined boundary (adjacent to the l–g boundary profile) into two equally long parts of length a.

(iii) The triple point is located at a distance $x_{\rm tr} := 1.5\, a$ from the gas (or liquid) boundary profile for a sharp (or obtuse) contact angle.

These conditions ensure for given memory space a largest possible distance of the two points where the inclined boundary line intersects the boundary lines $x = x_{\max}$ and $z = z_{\max}$ from the liquid–gas and the solid–fluid dividing interfaces. Consequently these two points are almost situated in bulk regions, where they cannot give rise to artificial line tension contributions.

6.2.2 Evaluating convolutions efficiently

6.2.2.1 Convolutions treated in Fourier space

In fundamental measure theory (see Sec. 2.2) and first-order perturbation theory (see Sec. 2.3) several convolution integrals have to be evaluated in every iteration step [Eqs. (2.31), (2.43), and (2.53)]. The necessary number of iteration steps to obtain numerical convergence is of the order of 10^5 (depending on the system size and the interaction range). So the typical number of convolutions during the calculation of a wedge density profile is 10^6. In real space these integrations on approximately 5 to 10 million grid points cannot be performed within a reasonable period of time.

Therefore one is urged to perform the convolutions on a less time-consuming way: The convolution of two functions $f_1(\mathbf{r})$ and $f_2(\mathbf{r})$ can be expressed by means of the convolution theorem as

$$(f_1 \otimes f_2)(\mathbf{r}) \;=\; \mathcal{F}^{-1}\left\{\mathcal{F}\left(f_1(\mathbf{r})\right) \cdot \mathcal{F}\left(f_2(\mathbf{r})\right)\right\}. \tag{6.6}$$

Here the Fourier transform (FT) of a function $f(\mathbf{r})$ is defined as

$$\widehat{f}(\mathbf{k}) \;:=\; \mathcal{F}\left(f(\mathbf{r})\right) \;:=\; \int_{\mathbb{R}^3} \mathrm{d}\mathbf{r}\; e^{-i\mathbf{k}\cdot\mathbf{r}}\, f(\mathbf{r}), \tag{6.7}$$

and $\mathcal{F}^{-1}$ indicates the corresponding backwards transform. On a grid a discrete FT is attainable efficiently by a fast Fourier transform (FFT) [166].

A prerequisite for the use of FFT is a Cartesian grid. For axisymmetric systems this is not the case (since the system indeed is effectively two-dimensional but merely in cylindrical coordinates), what makes the numerical treatment difficult (cf. Sec. 9.3).

6.2.2.2 Fourier transforms of Rosenfeld's weight functions $w_\alpha(x,z)$

The weight functions $w_2(x,z)$ and $\mathbf{w}_2(x,z)$, which are used for an effectively two-demensional system with density $\varrho(x,z)$, are diverging at the border of the since they diverge at the border of the involved Θ function [Eqs. (2.99) to (2.101)]. It is possible to Fourier transform these weight functions analytically. These Fourier transforms are not diverging. One might try to use them in order to initialize the FFT of the weight functions on a computer.

However, short-wavelength oscillations in the density distribution occur, such that the whole iteration process becomes instable. Most likely the mathematical reason for this numerical instability is the fact that there is a difference between first discretizing and then discretely Fourier transforming (real-space initialization) and first (continuously) Fourier transforming and then discretizing (reciprocal-space initialization). Consequently the way of numerical differentiations (cf. Sec. 6.2.2.3) is much more convenient than using the problematic weight functions.

For completeness the Fourier transforms of Rosenfeld's independent weight functions [Eqs. (2.98) to (2.103)] are displayed:

$$\widehat{w}_2(k) \;\equiv\; \widehat{w}_2(k_x,k_z) \;=\; 4\pi R^2\,\frac{\sin(kR)}{kR} \tag{6.8}$$

with $\lim\limits_{k\to 0}\widehat{w}_2(k) = 4\pi R^2$,

$$\widehat{w}_3(k) \;\equiv\; \widehat{w}_3(k_x,k_z) \;=\; 4\pi R^3\left(\frac{\sin(kR)}{(kR)^3}-\frac{\cos(kR)}{(kR)^2}\right) \tag{6.9}$$

with $\lim\limits_{k\to 0}\widehat{w}_3(k) = \frac{4}{3}\pi R^3$,

$$\left(\widehat{\mathbf{w}}_2\right)_x(k_x,k_z) \;=\; 4\pi R^2\; i\,\frac{k_x}{k}\left(\frac{\sin(kR)}{(kR)^2}-\frac{\cos(kR)}{kR}\right), \tag{6.10}$$

and

$$\left(\widehat{\mathbf{w}}_2\right)_z(k_x,k_z) \;=\; 4\pi R^2\; i\,\frac{k_z}{k}\left(\frac{\sin(kR)}{(kR)^2}-\frac{\cos(kR)}{kR}\right) \tag{6.11}$$

with $\lim\limits_{k\to 0}\widehat{\mathbf{w}}_2(k_x,k_z) = \mathbf{0}$.

6.2.2.3 Numerical differentiations of $n_3(x,z)$

In the calculations of the effectively two-dimensional density distribution $\varrho(x,z)$ numerical differentiations are performed in order to construct weighted densities from a radius dependent weighted density $n_3 = n_3(x,z;R)$ (see Sec. 2.4.2.2). The symmetrical scheme

$$n_2(x,z) \;=\; \frac{n_3(x,z;R+\Delta R)-n_3(x,z;R-\Delta R)}{2\,\Delta R}+\mathcal{O}\left((\Delta R)^2\right), \tag{6.12}$$

is employed. The small constant $\Delta R \ll R$ needs to be chosen suitably depending on the grid spacings Δ_x and Δ_z. For equal grid spacings in both directions, $\Delta_x = \Delta_z = \Delta$ [Eq. (6.5)], the choice

$$\Delta R \;=\; 0.36\,\Delta \tag{6.13}$$

has turned out to be quite optimal, in the sense that it leads to very good agreement with a corresponding effectively one-dimensional density profile $\varrho(z)$, for which a numerical differentiation is not necessary.

The numerical differentiations with respect to the coordinates x or z, respectively, are performed analogously. The x component of the vectorial weighted density $\mathbf{n}_2(x,z)$, e. g., reads

$$(\mathbf{n}_2)_x(x,z) = -\frac{\partial}{\partial x} n_3(x,z) = -\frac{n_3(x+\Delta x,z) - n_3(x-\Delta x,z)}{2\,\Delta x} + \mathcal{O}\left((\Delta x)^2\right). \quad (6.14)$$

6.2.3 Partially cut and shifted Lennard-Jones potential

For a LJ fluid the fluid–fluid interaction is truncated in order to be numerically accessible (see Sec. 6.1). The phase diagram is obtained for an infinitely long-ranged LJ potential, i. e., the integrated strength of the untruncated potential is used. Technically this cut-off is reflected in a cut-off of the weight functions $w_{\mathrm{LJ}}(z)$ and $w_{\mathrm{LJ}}(x,z)$. A shift of the weight function is established by calibrating the zero-component of its fast Fourier transform, which equals the integrated potential strength, to the analytically available value of the complete, uncut potential. Such a tiny shift is also applied to the weight functions $w_{\mathrm{SW}}(z)$ and $w_{\mathrm{SW}}(x,z)$ of the SW fluid, in order to obtain the exact, analytically calculated integrated potential strength in the numerical integration as well.

6.2.4 Convergence of the iteration process

6.2.4.1 Picard iteration and mixing parameter

The Euler-Lagrange equation, Eq. (2.16), is rearranged into a fixed-point equation

$$\varrho(\mathbf{r}) = \varrho_0 \exp\left\{-\beta V_{\mathrm{ext}}(\mathbf{r}) + \beta\mu_{\mathrm{ex}} - \frac{\delta\beta\mathcal{F}_{\mathrm{ex}}[\varrho]}{\delta\varrho(\mathbf{r})}\right\}, \quad (6.15)$$

which can be solved by *Picard iteration*. In order to improve its convergence properties, the right-hand side of Eq. (6.15) is mixed with the profile of the previous step. The quality of convergence can be checked by inserting the converged profile into the Euler-Lagrange equation,

$$\frac{\delta\beta\Omega[\varrho]}{\delta\varrho(\mathbf{r})} = \frac{\delta\beta\mathcal{F}_{\mathrm{ex}}[\varrho]}{\delta\varrho(\mathbf{r})} + \ln\left(\frac{\varrho(\mathbf{r})}{\varrho_0}\right) + \beta V_{\mathrm{ext}}(\mathbf{r}) - \beta\mu_{\mathrm{ex}} \stackrel{!}{=} 0. \quad (6.16)$$

6.2.4.2 Activation energy for bending of the liquid–gas interface

For each iteration step the value of the density functional $\Omega[\varrho]$ in the given system volume can be calculated. If the particle density distribution was the equilibrium distribution, this quantity would equal the value of the grand potential. Similarly for each density profile one can determine the associated value of the line tension functional. The line tension functional $\tau[\varrho]$ is the quantity, which yields the line tension value for the equilibrium density distribution as an input. In an iteration procedure the value of the line tension functional can be regarded as a function of the iteration step number i, $\tau[\varrho] = \tau[\varrho_{\mathrm{i}}] =: \tau(i)$, where $\varrho_{\mathrm{i}}(\mathbf{r})$ is the result of the i-th iteration step. The line tension is obtained as limiting value of this function, $\lim_{i\to\infty}\tau(i) = \tau$.

Interestingly, the value of the function $\tau(i)$ [and likewise the value of a function $\Omega(i)$] does not decay monotonously during the iteration procedure for a sessile liquid wedge, given an initial density distribution described above (see Sec. 6.2.1). Rather the value decays rapidly at first, but then rises again, overcomes an activation barrier, decays monotonously thereafter and finally reaches the line tension value.

The analysis of the convergence behavior reveals that the rapid decay at the beginning is related to a local optimization, in which the structure of the three-phase contact region close to the substrate surface is established. The intermediate rise of the values of the two functionals $\Omega[\varrho]$ and $\tau[\varrho]$ corresponds to the bending of the liquid–gas interface. Since at later iteration steps these energy values decline to smaller values than before the barrier, this hump can be considered as an activation barrier. It has been recognized for other systems before, that a shift of an interface is related to an activation energy barrier. Thus the observation of an energy barrier for bending an interface is not surprising. Clearly, for a better choice (guess) of an initial density distribution for the iteration procedure such a barrier does not have to occur.

Exponential decay beyond the barrier:
At least for the employed initialization scheme the value of the line tension functional attains its asymptotic value in an exponential decay which sets in smoothly behind the barrier maximum. This feature is found in every of the studied cases with LJ substrate potentials, however, the necessary number of iteration steps in order to obtain convergence strongly depends on the system parameters. The exponential decay law can be employed to extrapolate the value of the line tension functional to its asymptotic value, the line tension value. Within a given computational time larger systems (or slower converging situations) can be addressed with this method, since one does not have to wait for the fully converged state. Hence smaller contact angles are accessible. Vice versa the computational time to obtain results for a given system can be approximately halfed this way. The region of data beyond the local maximum has to be sufficiently large for a good exponential fit.

6.2.5 Remarkably small numerical errors

The numerical errors of the calculated line tension values are typically less than 5 % for not too small contact angles. Since the line contribution to the total grand canonical free energy of the system is very small compared to volume or surface contributions, these very small errors are notable.

The magnitude of the numerical errors is evaluated as follows. By systematically changing the discretization or/and the system size, the line tension value for an infinitely fine grid and an infinitely large system can be estimated. Numerical errors for a wider meshed, finite system result from deviations thereof.

A necessary condition to obtain such small errors is to perform several precaution measures. The most important of these implemented actions are: First, the boundary profiles are refined from an effectively one-dimensional calculation to the effectively two-dimensional program, which is used as well to perform the calculations for the liquid wedge. Hence the solid–gas and solid–liquid boundary profiles are attained smoothly. Second, the zero-components of the Fourier transforms of the weight functions are manually calibrated to resemble the analytically obtained values of the integrated potential strength. This ensures to reach bulk densities precisely and smoothly. Third, the numerical derivatives in the effectively two-dimensional program are tuned to achieve the best possible agreement with density profiles in an effectively one-dimensional program. Fourth, the integration routine to extract the line tension value from a density profile $\varrho(x, z)$ has to account for the trapezoidal shape of the integration area. The interpolation scheme is adjusted such that a constant is integrated exactly. Fifth, the integration zone comprises a “safety stripe” in order to omit artefacts from a lattice misfit of the liquid–gas boundary profile (since the boundary orientation is tilted against the substrate surface). Sixth, efficient book-keeping reduces the computer memory requirements by 50 % and therefore from the memory point of view allows for a twice as large system size.

7 Sharp-kink line tension theory

The system of a Lennard-Jones (12–6) fluid forming a liquid wedge residing on a Lennard-Jones (9–4–3) substrate was already considered before by Getta and Dietrich [50, 51] as well as by Bauer and Dietrich [11, 52]. They applied the concept of the so-called *sharp-kink approximation* (cf. Sec. 7.1.1) to the liquid wedge scenario.

The line tension calculation presented in this work goes beyond that. A continuous (i. e., smoothly varying) density distribution $\varrho(x, z)$ is employed, and hence possible packing effects near the substrate are respected. Since this method takes the microscopic details of the interactions and of the density distribution into account, it can be regarded as "fully microscopic" — in contrast to the "semi-microscopic" sharp-kink theory, where the interaction potentials enter accurately but microscopic details of the density distribution are neglected.

The sharp-kink theory of planar interfaces and the sharp-kink theory of sessile liquid wedges are recalled. Then the sharp-kink line tension theory is extended from a crude approximation of the Lennard-Jones interaction potential to the (exact) treatment of the WCA separation (see Sec. 2.3.4) of the Lennard-Jones potential. Furthermore corresponding formulae for a square-well fluid are presented (see Sec. 2.3.5). The results from the microscopic calculations are compared to the corresponding sharp-kink results in Sec. 8.2.

7.1 Sharp-kink theory of planar interfaces

The sharp-kink (SK) theory of planar fluid interfaces rests upon two fundamental assumptions, (i) the SK approximation of the involved density profiles $\varrho(z)$ and (ii) the local density approximation (LDA) of the excess free energy of hard spheres. Assumption (ii) influences the form of the density functional, whereas assumption (i) restricts the search for solutions of the corresponding Euler-Lagrange equation to SK density profiles.

7.1.1 Sharp-kink approximation of planar fluid interfaces

At interfaces fluids usually exhibit smooth density variations (see Fig. 3.1). The sharp-kink approximation replaces the interfacial structure by a SK density profile, which is composed of regions with constant density. Consequently the range of density values is discrete. Planar fluid interfaces can be desribed by $\varrho(z)$ (see Chapter 3). The SK approximation of planar liquid–gas, solid–liquid, and solid–gas interfacial profiles is defined as follows:

1. A liquid–gas interface is represented by a step function. The density discontinuously changes from one bulk density to the other.
2. A solid–liquid interface is described by a step function

$$\varrho_{\mathrm{sl}}^{(\mathrm{SK})} \;=\; \varrho_{\mathrm{l}}\,\Theta\left(z - d_{\mathrm{w}}\right), \tag{7.1}$$

   which switches from zero close to the substrate surface to a constant bulk liquid density. The adjustable parameter d_{w}, i. e., the width of the excluded volume, is described below.
3. A solid–gas interface is approximated by a liquid-like film (with constant density) and a discontinuous change to a constant bulk gas density. The liquid-like film extends up to the film thickness l. This approximation of a s–g interface is illustrated in Fig. 7.1.

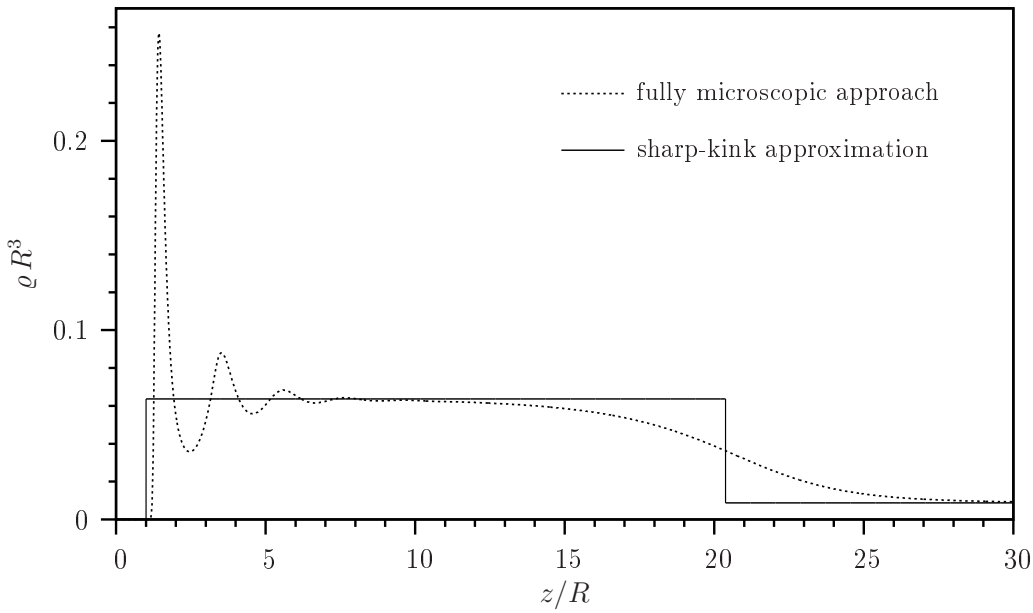

Fig. 7.1: Illustration of the sharp-kink approximation of a planar solid–gas interfacial density profile. Here the fully microscopic density $\varrho(z)$ exhibits density oscillations near the substrate surface and a smooth transition from the liquid-like film to the bulk gas density. Contrarily within the SK approximation the density distribution possesses solely three values here, namely zero (close to the surface), the bulk liquid density ϱ_l (accounting for the liquid-like film), and the bulk gas density ϱ_g. Here $d_\mathrm{w} = R$.

The *excluded volume* near the substrate surface is taken into account by the parameter d_w. The width d_w of the excluded volume near the substrate surface enters the SK calculations of solid–fluid interfaces, in contrast to fully microscopic calculations. The effect of a slight change of this quantity on the shape of the effective interface potential $\omega(l)$ can be large in the region near the substrate surface.

From a given fully microscopic density profile an optimal value of d_w can be calculated [138], however, within the SK calculation such a profile cannot be obtained. The optimal value of d_w is related to the first moment of the density distribution $\varrho(z)$ of a planar solid–liquid interface via [138]

$$d_\mathrm{w} = \int_{z=0}^{\infty} \mathrm{d}z \left(1 - \frac{\varrho(z)}{\varrho_\mathrm{l}}\right), \tag{7.2}$$

where ϱ_l is the liquid bulk density. Simple manipulations reveal a simple connection to the excess adsorption Γ [Eq. (3.25)] of the s–l interface,

$$d_\mathrm{w} = -\Gamma/\varrho_\mathrm{l}. \tag{7.3}$$

In other words, the excluded volume in the SK density profile leads to the same "deficit adsorption" (i. e., negative excess adsorption) as the fully microscopic profile.

This choice of d_w is optimal in the following sense: The analytic wetting theory presented in Ref. [138] takes density variations via Taylor expansions into account and thus goes beyond the SK theory. Expressions for the effective interface potential are derived, which contain moments of the density distribution, e. g., the right-hand side of Eq. (7.2). If this moment is identified with the parameter d_w (and if additionally a similar identification is performed), the SK expressions are recovered. This means that the apparent detour provides a way to assign a value to d_w, which was not specified by the SK theory.

7.1.2 Local density approximation (LDA)

The excess free energy functional of a hard-sphere fluid is non-local. Contrarily, in the standard SK theory the excess free energy of a hard-sphere fluid is addressed by means of the *local density approximation* (LDA). This means that the free energy density of the hard-sphere fluid at a spatial point $\mathbf{r}$ with a density $\varrho(\mathbf{r})$ is described by the free energy density of a bulk hard-sphere fluid with the same density.

Consequently within RPA [Eqs. (2.51) and (2.52)] and LDA the density functional $\Omega[\varrho]$ is

$$\begin{aligned}\Omega[\varrho] &= \int_{\mathbb{R}^3} \mathrm{d}\mathbf{r}\ \left\{ f_{\mathrm{id}}\big(\varrho(\mathbf{r})\big) + f_{\mathrm{ex}}^{HS}\big(\varrho(\mathbf{r}), T\big) \right\} \\ &\quad + \frac{1}{2} \int_{\mathbb{R}^3} \mathrm{d}\mathbf{r} \int_{\mathbb{R}^3} \mathrm{d}\mathbf{r}'\ \varrho(\mathbf{r})\, \varrho(\mathbf{r}')\ \phi_{\mathrm{ff}}^{\mathrm{att}}(|\mathbf{r}-\mathbf{r}'|) + \int_{\mathbb{R}^3} \mathrm{d}\mathbf{r}\, \varrho(\mathbf{r})\ \big(V_{\mathrm{ext}}(\mathbf{r}) - \mu\big)\,. \end{aligned} \tag{7.4}$$

Using the chemical potential of an ideal gas from Eq. (2.48), $\beta\mu_{\mathrm{id}} = \ln\eta$, the free energy density of an ideal gas can be expressed as

$$\beta f_{\mathrm{id}} = \varrho\,\big(\ln\eta - 1\big). \tag{7.5}$$

Taking the Carnahan-Starling equation of state (CS EOS) as a basis, the excess free energy density for hard-spheres, $f_{\mathrm{ex}}^{\mathrm{HS}}$, reads

$$\beta f_{\mathrm{ex}}^{\mathrm{HS}} \simeq \beta f_{\mathrm{ex}}^{\mathrm{CS}} = \varrho\,\frac{4\,\eta - 3\,\eta^2}{(1-\eta)^2}. \tag{7.6}$$

The packing fraction η and the density ϱ are connected via $\eta = \varrho\ \frac{4}{3}\pi R^3 = \varrho\ \frac{\pi}{6} d^3$ [Eq. (2.32)]. In the case of a SW fluid d is defined through the interaction potential anyway. However, if for d a BH-LJ or WCA-LJ fluid the effective hard-sphere diameter [Eq. (2.71) or (2.72)] is employed, the packing fraction becomes temperature dependent, $\eta = \eta(T)$, and the excess free energy density as well, $f_{\mathrm{ex}}^{HS} = f_{\mathrm{ex}}^{HS}\big(\varrho, T\big)$.

The bulk phase-diagram for the LDA density functional [Eq. (7.4)] is the same as for the full non-local theory (see Sec. 2.3.3), since for bulk densities the LDA resembles the non-local free energy density. Note that for a LJ fluid the bulk phase diagrams are different for (a) BH-LJ and WCA-LJ separation schemes and (b) for utilizing or not utilizing the effective hard-sphere diameter. The bulk phase diagrams of a BH-LJ or WCA-LJ fluid without usage of the effective hard-sphere diameter and that of a square-well fluid differ only by a constant prefactor.

7.2 Sharp-kink liquid wedge

Within the sharp-kink approximation a liquid wedge with a sharp contact angle (i. e., $0 \leq \theta < 90°$) is described by its contour $l(x)$. This contour represents the position of the non-planar liquid–gas interface. An ansatz for the corresponding sharp-kink density distribution reads

$$\varrho(x,z) = \Theta\big(z - d_{\mathrm{w}}\big)\ \left\{ \varrho_{\mathrm{l}}\,\Theta\big(l(x) - z\big) + \varrho_{\mathrm{g}}\,\Theta\big(z - l(x)\big) \right\}. \tag{7.7}$$

Let l_0 be the equilibrium thickness of a thin liquid-like film that might form at a solid–gas interface. The approach is only valid, if such a film is present, i. e., if l_0 is significantly larger than d_{w}, i. e., $l_0 \gg d_{\mathrm{w}}$. For obtuse contact angles ($90° \leq \theta < 180°$) the equations have to be expressed in terms of the inverse function $x(l)$ [instead of $l(x)$].

The ansatz for the density, Eq. (7.7), is inserted into the density functional, and volume, surface, and line contributions are identified. These considerations have been shown in Refs. [11, 52]. For an arbitrary interaction potential the main formulae are summarized in the next section, before they are specified for a LJ or SW fluid in the subsequent sections.

7.3 General expressions

Here general formulae — valid for all intermolecular interactions — of the sharp-kink approach to a sessile liquid wedge are presented. In Secs. 7.4 and 7.5 they are specified for an approximated BH-LJ or WCA-LJ fluid, an exact WCA-LJ fluid and a square-well fluid.

7.3.1 Effective interface potential and surface tension

Consider a solid–gas interface at liquid–gas coexistence such that a thin liquid-like film of thickness l forms at the substrate surface. Then the surface contribution (per surface area) to the grand potential within the sharp-kink approximation reads [141]

$$\Omega_{\mathrm{s}}(l) \;=\; \sigma_{\mathrm{sl}} \,+\, \sigma_{\mathrm{lg}} \,+\, \omega(l). \tag{7.8}$$

$\omega(l)$ is the effective interface potential, that corresponds to the energy which is necessary to form a finite film instead an infinitely large one. Obviously $\omega(l)$ obeys

$$\lim_{l\to\infty} \omega(l) = 0. \tag{7.9}$$

The auxiliary function

$$t(z) \;:=\; \int_{\mathbb{R}^3} \mathrm{d}\mathbf{r}' \; \Theta(z'-z)\, \phi_{\mathrm{ff}}^{\mathrm{att}}(|\mathbf{r}'|) \;=\; \int\limits_{z'=z}^{\infty} \mathrm{d}z \; \beta^{-1}\, w_{\mathrm{ff}}(z) \tag{7.10}$$

$$=:\; \sum_{i\geq 3} \frac{t_i}{z^i}, \quad z \gg R, \tag{7.11}$$

corresponds to the interaction energy of a particle interacting with a homogeneously filled halfspace at a disctance z. With its help the surface tension of a solid–fluid interface (including the special cases of a solid–liquid or a solid–gas interface),

$$\sigma_{\mathrm{sf}} \;=\; -\frac{1}{2}\,\varrho_{\mathrm{l}}^2 \int\limits_{z=0}^{\infty} \mathrm{d}z \; t(z) \;-\; d_{\mathrm{w}}\, \Omega_{\mathrm{bulk}}(\varrho_{\mathrm{l}}) \;+\; \varrho_{\mathrm{f}} \int\limits_{z=d_{\mathrm{w}}}^{\infty} \mathrm{d}z \; V_{\mathrm{ext}}(z), \tag{7.12}$$

and the interfacial tension of a liquid–gas interface,

$$\sigma_{\mathrm{lg}} \;=\; -\frac{1}{2}\,(\Delta\varrho)^2 \int\limits_{z=0}^{\infty} \mathrm{d}z \; t(z), \tag{7.13}$$

can be expressed. The difference of the bulk liquid and bulk gas densities is abbreviated as

$$\Delta\varrho \;:=\; \varrho_{\mathrm{l}} - \varrho_{\mathrm{g}}. \tag{7.14}$$

The auxiliary function $t(z)$ also plays an important role in the sharp-kink formula for the effective interface potential,

$$\omega(l) \;=\; \Delta\varrho \left(\varrho_{\mathrm{l}} \int\limits_{z=l-d_{\mathrm{w}}}^{\infty} \mathrm{d}z \; t(z) \;-\; \int\limits_{z=l}^{\infty} \mathrm{d}z \; V_{\mathrm{ext}}(z) \right) \;=:\; \sum_{i\geq 2} \frac{a_i}{l^i}. \tag{7.15}$$

This concept is most reasonable for $l \gg d_{\mathrm{w}}$. a_2 is the Hamaker constant.

The surface grand potential $\Omega_{\rm s}(l)$ is minimized by the equilibrium film thickness l_0 and then equals the solid–gas surface tension

$$\sigma_{\rm sg} \;=\; \min_l \{\Omega_{\rm s}(l)\} \equiv \Omega_{\rm s}(l_0) \;\stackrel{(7.8)}{=}\; \sigma_{\rm sl} \,+\, \sigma_{\rm lg} \,+\, \omega(l_0). \tag{7.16}$$

Inserting Young's equation, the effective interface potential ω for the equilibrium film thickness l_0 is related to the macroscopic contact angle θ,

$$\cos\theta \;\stackrel{(1.1)}{=}\; \frac{\sigma_{\rm sg} - \sigma_{\rm sl}}{\sigma_{\rm lg}} \;\stackrel{(7.16)}{=}\; 1 \,+\, \frac{\omega(l_0)}{\sigma_{\rm lg}}. \tag{7.17}$$

7.3.2 Line tension

The line tension τ of a liquid wedge can be decomposed [11, 50, 51, 52] into

$$\tau[l(x)] \;=\; \tau_a(l_0,\theta) \,+\, \tau_l[l(x)], \tag{7.18}$$

where $\tau_a(l_0,\theta)$ merely depends on the assymptote

$$a(x) \;:=\; l_0\,\Theta(-x) \,+\, (l_0 + x\,\tan\theta)\,\Theta(x) \tag{7.19}$$

with $a(0) = l_0$. Furthermore by construction τ_a is the line tension of the asymptote, i. e., $\tau[l(x) = a(x)] = \tau_a$ and $\tau_l[a(x)] = 0$.

Note that the lateral coordinate origin $x = 0$ is defined via the intersection of the wedge-like liquid–gas dividing interface with the plane $z = l_0 > 0$ in the SK theory or the substrate surface plane $z = 0$ in the fully microscopic (fm) approach, respectively. These two coordinate systems are related via $x_{\rm fm} = x_{\rm SK} + l_0/\tan\theta$.

Both line tension contributions are again split in two parts,

$$\tau_a(l_0,\theta) \;=\; \tau_{a1}(\theta) \,+\, \tau_{a2}(l_0,\theta) \tag{7.20}$$

and

$$\tau_l[l(x)] \;=\; \tau_\omega[l(x)] \,+\, \tau_{\rm i}[l(x)]. \tag{7.21}$$

The function τ_{a1} is given as

$$\tau_{a1}(\theta) \;=\; \frac{1}{2}(\Delta\varrho)^2 \left(1 - \frac{\theta}{\tan\theta}\right) \int_{x=0}^{\infty}\!\!{\rm d}x \int_{z=0}^{\infty}\!\!{\rm d}z \;\; x\,z\;\beta^{-1}\, w_{\rm ff}(x,z) \tag{7.22}$$

with the weight function $w_{\rm ff}(x,z)$ [Eq. (2.108)] and the contact angle θ expressed as radian measure. τ_{a1} is linked to the fluid–fluid interaction within the liquid wedge in addition to that within a gas wedge.

The function τ_{a2} reads

$$\tau_{a2}(l_0,\theta) \;:=\; \frac{1}{\tan\theta} \int_{l=l_0}^{\infty}\!\!{\rm d}l\;\omega(l). \tag{7.23}$$

This term is made up from energy contributions of the effective interface potential which arise from a shift of the asymptote's l–g interface from l_0 to $a(x)$, i. e., $\tau_{a2} = \int_0^\infty {\rm d}x\;\omega\,(a(x))$. Very close to a first-order wetting transition the total line tension is dominated by $\tau_{a2}(l_0,\theta)$ [51]. These two line tension contributions, $\tau_{a1}(\theta)$ and $\tau_{a2}(l_0,\theta)$, are accessible analytically for the interactions discussed in this work.

The other two line tension contributions, $\tau_\omega[l(x)]$ and $\tau_\mathrm{i}[l(x)]$, have to be calculated numerically for a given contour $l(x)$. $\tau_\omega[l(x)]$ corresponds to an integral over the effective interface potential $\omega(l)$,

$$\tau_\omega[l(x)] \;:=\; \int\limits_{x=-\infty}^{\infty} \mathrm{d}x \;\left\{\omega\big(l(x)\big) - \omega\big(a(x)\big)\right\}. \tag{7.24}$$

τ_ω describes the influence of deviations of $l(x)$ from $a(x)$ on the contributions of the effective interface potential. τ_{a2} cancels a part of this term, namely the integral from zero to infinity of the second integrand. Thus the influence of $l(x)$ on effective interface potential contributions to τ is split into the basic effect of the asymptote $a(x)$ and an additional effect due to deviations of the contour from the asymptote.

$\tau_\mathrm{i}[l(x)]$ is related to the interaction energy of the liquid–gas interface,

$$\begin{aligned}\tau_\mathrm{i}[l(x)] \;:=\; & \frac{1}{2}(\Delta\varrho)^2 \int\limits_{x=-\infty}^{\infty} \mathrm{d}x \int\limits_{x'=-\infty}^{\infty} \mathrm{d}x' \int\limits_{z=a(x)}^{l(x)} \mathrm{d}z \\ & \left(\int\limits_{z'=-\infty}^{a(x')} \mathrm{d}z' \;-\; \int\limits_{z'=l(x')}^{\infty} \mathrm{d}z' \right) \; w_\mathrm{ff}(x-x', z-z').\end{aligned} \tag{7.25}$$

τ_i is a non-local functional of $l(x)$. It can be approximated by a local functional

$$\begin{aligned}\tau_\mathrm{i}[l(x)] \;\simeq\; & \tau_\mathrm{i}^{(\mathrm{loc})}[l(x)] \\ :=\; & \sigma_\mathrm{lg} \int\limits_{x=-\infty}^{\infty} \mathrm{d}x \;\left\{ \sqrt{1+\left(\frac{\mathrm{d}l(x)}{\mathrm{d}x}\right)^2} - \sqrt{1+\left(\frac{\mathrm{d}a(x)}{\mathrm{d}x}\right)^2} \right\}.\end{aligned} \tag{7.26}$$

τ_i originates from the fluid–fluid interactions across the l–g interface and describes the excess in comparison to the asymptotic profile $a(x)$. In the local approximation the expression simplifies to an integral over the additionally created l–g interfacial area. According to Ref. [11] the line tension values and contour profiles within the non-local and the local theory differ only slightly near first-order wetting transitions and are almost indistinguishable near a critical wetting transition. These small differences even vanish upon approaching T_w.

7.3.3 Boundary value problem

In a sharp-kink wedge system the variation of the density distribution is limited to a variation of the contour profile $l(x)$. Thus the Euler-Lagrange equation here is [11, 50, 51, 52]

$$\frac{\delta\tau}{\delta l(x)} \;\stackrel{!}{=}\; 0. \tag{7.27}$$

According to Eq. (7.21) this is equivalent to

$$\frac{\delta\tau_\omega}{\delta l(x)} \;\stackrel{!}{=}\; -\frac{\delta\tau_\mathrm{i}^{(\mathrm{loc})}}{\delta l(x)} \tag{7.28}$$

in the local theory. Rewriting both sides of this equation,

$$\frac{\delta\tau_\omega}{\delta l(x)} \;\stackrel{(7.24)}{=}\; \frac{\mathrm{d}\omega(l)}{\mathrm{d}l}\Big|_{l=l(x)} \;\stackrel{(7.15)}{=}\; -\Delta\varrho\left\{\varrho_\mathrm{l}\, t\big(l(x)-d_\mathrm{w}\big) - V_\mathrm{ext}\big(l(x)\big)\right\} \tag{7.29}$$

and

$$-\frac{\delta\tau_{\mathrm{i}}^{(\mathrm{loc})}}{\delta l(x)} \;=\; \sigma_{\mathrm{lg}}\,\frac{l''(x)}{\left\{1+\left[l'(x)\right]^2\right\}^{3/2}}, \tag{7.30}$$

the Euler-Lagrange equation for the sharp-kink wedge system can be expressed as [11]

$$-\Delta\varrho\left\{\varrho_{\mathrm{l}}\,t\big(l(x)-d_{\mathrm{w}}\big)-V_{\mathrm{ext}}\big(l(x)\big)\right\} \;=\; \sigma_{\mathrm{lg}}\,\frac{l''(x)}{\left\{1+\left[l'(x)\right]^2\right\}^{3/2}}. \tag{7.31}$$

This differential equation and the wedge boundary conditions,

$$l(x\to-\infty)=l_0 \quad\text{and}\quad l'(x\to\infty)=\tan\theta, \tag{7.32}$$

constitute a boundary value problem. Its solution yields the equilibrium contour $l(x)$. Practically the boundary value problem is solved by a "shooting algorithm" [167]: A Runge-Kutta algorithm is applied for the initial value problem, which is defined by the above differential equation and the initial condition of a value l_0 and a very small slope at a starting point x_0. Then automatically the desired asymptotic shape is recovered.

7.4 Lennard-Jones fluid

The Lennard-Jones fluid can be treated within the sharp-kink approximation in different ways. First, the BH or the WCA separation scheme (see Sec. 2.3.4) can be applied to construct the attractive and repulsive parts of the interaction potential. Second, either this attractive part is used exactly or in a simplifying analytical approximation. The analytical approximations for a BH-LJ and a WCA-LJ fluid are reviewed in Sec. 7.4.1, and the general sharp-kink formalism is extended to the exact treatment of a WCA-LJ fluid in Sec. 7.4.2.

7.4.1 Approximated BH-LJ and WCA-LJ fluid

The attractive part of the LJ fluid–fluid interaction potential can be derived by the Barker-Henderson (BH) method or the Weeks-Chandler-Andersen (WCA) method [Eqs. (2.68) and (2.66)]. The analytical sharp-kink calculations are simplified, if this attractive potential is approximated by a simple expression. This approximation has been applied by Getta and Dietrich [50, 51] for the BH-LJ fluid, whereas Bauer and Dietrich [11, 52] chose the same type of function for the WCA-LJ fluid. The two approximative functions merely differ in a prefactor $\sqrt{2}$, which is due to the different value of the integrated strenght in both cases [Eqs. (2.74) and (2.73)],

$$\alpha_{\mathrm{BH-LJ}} \;=\; -\frac{32}{9}\,\pi\,\sigma_{\mathrm{LJ}}^3\,\varepsilon_{\mathrm{LJ}}\quad, \tag{7.33}$$

$$\alpha_{\mathrm{WCA-LJ}} \;=\; -\frac{32}{9}\,\sqrt{2}\,\pi\,\sigma_{\mathrm{LJ}}^3\,\varepsilon_{\mathrm{LJ}} \;=\; \sqrt{2}\times\alpha_{\mathrm{BH-LJ}}. \tag{7.34}$$

In order to address both approximative functions simultaneously, it is convenient to subsume them by the label "X-LJ", where X either stands for BH or WCA. In this notation the approximative function $\phi_{\mathrm{X-LJ}}^{\mathrm{att,app}}(r)$ is given by

$$\phi_{\mathrm{X-LJ}}^{\mathrm{att}}(r) \;\simeq\; \phi_{\mathrm{X-LJ}}^{\mathrm{att,app}}(r) \;:=\; \frac{4}{\pi^2}\,\frac{\alpha_{\mathrm{X-LJ}}}{\sigma_{\mathrm{LJ}}^3}\,\frac{1}{\left[1+\left(\frac{r}{\sigma_{\mathrm{LJ}}}\right)^2\right]^3}. \tag{7.35}$$

From this potential the corresponding auxiliary function [Eq. (7.10)] follows,

$$t^{\mathrm{app}}_{\mathrm{X-LJ}}(z) \;=\; \frac{1}{\pi}\,\alpha_{\mathrm{X-LJ}}\left(\frac{\pi}{2} - \arctan\left(z/\sigma_{\mathrm{LJ}}\right) - \frac{z/\sigma_{\mathrm{LJ}}}{1+\left(z/\sigma_{\mathrm{LJ}}\right)^2}\right). \tag{7.36}$$

Hence in the present case the liquid–gas surface tension is

$$\sigma^{\mathrm{X-LJ,app}}_{\mathrm{lg}} \;=\; -\,\frac{1}{2\,\pi}\,(\Delta\varrho)^2\,\sigma_{\mathrm{LJ}}\,\alpha_{\mathrm{X-LJ}} \;>\; 0 \tag{7.37}$$

and the effective interface potential reads

$$\begin{aligned}\omega^{\mathrm{app}}_{\mathrm{X-LJ}}(l) \;=\; \Delta\varrho\,\sigma^3_{\mathrm{LJ}}\Bigg\{ & \frac{\alpha_{\mathrm{X-LJ}}}{\pi\,\sigma^2_{\mathrm{LJ}}}\,\varrho_{\mathrm{l}}\left[1+\frac{l-d_{\mathrm{w}}}{\sigma_{\mathrm{LJ}}}\left(\arctan\left(\tfrac{l-d_{\mathrm{w}}}{\sigma_{\mathrm{LJ}}}\right)-\frac{\pi}{2}\right)\right] \\ & +\;\frac{1}{\sigma^3_{\mathrm{LJ}}}\sum_{i\geq 2}\frac{1}{i}\,\frac{u_{i+1}}{l^i}\Bigg\}\end{aligned} \tag{7.38}$$

with the coefficients u_i, $i \geq 3$, of the external potential [Eq. (3.8)].

For completeness the weight function $w_{\mathrm{ff}}(z)$ [Eq. (2.92)] for the approximative interaction is given,

$$w^{\mathrm{app}}_{\mathrm{X-LJ}}(z) \;=\; \frac{2}{\pi\,\sigma_{\mathrm{LJ}}}\,\alpha_{\mathrm{X-LJ}}\,\frac{1}{\left[1+\left(\frac{z}{\sigma_{\mathrm{LJ}}}\right)^2\right]^2}. \tag{7.39}$$

The weight function $w_{\mathrm{ff}}(x,z)$ [Eq. (2.108)] for the present case,

$$w^{\mathrm{app}}_{\mathrm{X-LJ}}(x,z) \;=\; \frac{3}{2\,\pi\,\sigma^2_{\mathrm{LJ}}}\,\alpha_{\mathrm{X-LJ}}\,\frac{1}{\left[1+\left(\frac{x}{\sigma_{\mathrm{LJ}}}\right)^2+\left(\frac{z}{\sigma_{\mathrm{LJ}}}\right)^2\right]^{5/2}}, \tag{7.40}$$

is useful to calculate the line tension contribution $\tau_{a1}(\theta)$. Thus the latter reads

$$(\tau_{a1})^{\mathrm{app}}_{\mathrm{X-LJ}}(\theta) \;=\; \frac{1}{4\,\pi}(\Delta\varrho)^2\,\sigma^2_{\mathrm{LJ}}\,\alpha_{\mathrm{X-LJ}}\left(1-\frac{\theta}{\tan\theta}\right) \tag{7.41}$$

with the contact angle θ expressed as radian measure. With the help of $\omega^{\mathrm{app}}_{\mathrm{X-LJ}}(l)$ the function $\tau_{a2}(l_0,\theta)$ can be obtained analytically,

$$\begin{aligned}(\tau_{a2})^{\mathrm{app}}_{\mathrm{X-LJ}}(l_0,\theta) \;=\; \frac{\Delta\varrho}{\tan\theta}\Bigg(\frac{1}{2\,\pi}\,\sigma^2_{\mathrm{LJ}}\,\alpha_{\mathrm{X-LJ}}\,\varrho_{\mathrm{l}}\Bigg\{ & \left[\left(\tfrac{l_0-d_{\mathrm{w}}}{\sigma_{\mathrm{LJ}}}\right)^2+1\right] \\ & \times\left[\frac{\pi}{2}-\arctan\left(\tfrac{l_0-d_{\mathrm{w}}}{\sigma_{\mathrm{LJ}}}\right)\right]\;-\;\frac{l_0-d_{\mathrm{w}}}{\sigma_{\mathrm{LJ}}}\Bigg\}\;+\;\sum_{i\geq 1}\frac{1}{i\,(i+1)}\,\frac{u_{i+2}}{l_0^i}\Bigg).\end{aligned} \tag{7.42}$$

Comment on the strength of the tail:
The following consideration is performed for the case of a an approximated WCA-LJ fluid, however, a BH-LJ fluid can be addressed analogously. The approximative potential is constructed such that it contains a r^{-6}-term, possesses a $1/(\sigma_{\mathrm{LJ}}+r^2)^3$ shape and the same integrated potential strength as the WCA-LJ potential. However, the adjusted constant in front of the potential leads to the fact that the r^{-6}-term is much stronger than in the original potential. Hence the substrate strength ε_{w} for which the Hamaker constant vanishes [cf. Eq. (8.1)] and hence critical wetting might occur is overestimated by a factor

$$\frac{32}{9}\,\sqrt{2}\,\frac{1}{\pi} \;\simeq\; 1.60056234. \tag{7.43}$$

If the shape $1/(\ldots + r^2)^3$ of an approximative potential is desired and on the other hand the critical wetting parameters should be predicted for a WCA-LJ fluid in a quantitative fashion, a solution to this problem could be to choose

$$\phi_{\mathrm{X-LJ}}^{\mathrm{att,app}}(r) \;:=\; 4\,\varepsilon_{\mathrm{LJ}}\,\frac{1}{\left[c^2+r^2\right]^3} \tag{7.44}$$

as the approximative expression. The suitably chosen constant

$$c \;:=\; \sigma_{\mathrm{LJ}}\left(\frac{9\,\pi}{32\sqrt{2}}\right)^{1/3} \tag{7.45}$$

guarantees the same integrated potential strength as for the WCA-LJ potential, and at the same time the LJ tail is maintained.

7.4.2 Exactly treated WCA-LJ fluid

The general expressions are now applied to a WCA-LJ fluid without further approximations. A WCA-LJ fluid is focused on, and a BH-LJ fluid can be treated analogously. For this model system the effective interface potential can be obtained analytically. However, the calculation of the associated line tension values requires numerical calculations.

The integrated potential α in this case is [Eq. (2.73)]

$$\alpha_{\mathrm{WCA-LJ}} \;=\; -\frac{32}{9}\,\sqrt{2}\,\pi\,\sigma_{\mathrm{LJ}}^3\,\varepsilon_{\mathrm{LJ}}, \tag{7.46}$$

the auxiliary function related to the WCA-LJ potential reads

$$t_{\mathrm{WCA-LJ}}(z) \;=\; \begin{cases} -\pi\,\varepsilon_{\mathrm{LJ}}\,\sigma_{\mathrm{LJ}}^3\left[\frac{32}{9}\sqrt{2}-\frac{4}{45}\left(\frac{\sigma_{\mathrm{LJ}}}{z}\right)^9+\frac{2}{3}\left(\frac{\sigma_{\mathrm{LJ}}}{z}\right)^3\right] & \text{for } z<-\sqrt[6]{2}\sigma_{\mathrm{LJ}} \\ -\pi\,\varepsilon_{\mathrm{LJ}}\,\sigma_{\mathrm{LJ}}^3\left[\frac{16}{9}\sqrt{2}-\frac{9}{5}\sqrt[3]{2}\,\frac{z}{\sigma_{\mathrm{LJ}}}+\frac{1}{3}\left(\frac{z}{\sigma_{\mathrm{LJ}}}\right)^3\right] & \\ \qquad\qquad \text{for } -\sqrt[6]{2}\sigma_{\mathrm{LJ}}\le z\le\sqrt[6]{2}\sigma_{\mathrm{LJ}} & \\ -\pi\,\varepsilon_{\mathrm{LJ}}\,\sigma_{\mathrm{LJ}}^3\left[-\frac{4}{45}\left(\frac{\sigma_{\mathrm{LJ}}}{z}\right)^9+\frac{2}{3}\left(\frac{\sigma_{\mathrm{LJ}}}{z}\right)^3\right] & \text{for } z>\sqrt[6]{2}\sigma_{\mathrm{LJ}}, \end{cases} \tag{7.47}$$

from which the liquid–gas interfacial tension follows as

$$\sigma_{\mathrm{lg}}^{\mathrm{WCA-LJ}} \;=\; \frac{9}{16}\,2^{2/3}\,\pi\,(\Delta\varrho)^2\,\varepsilon_{\mathrm{LJ}}\,\sigma_{\mathrm{LJ}}^4 \;>\; 0. \tag{7.48}$$

For a WCA-LJ fluid and an approximated WCA-LJ fluid the coexisting densities ϱ_{l} and ϱ_{g} are the same, since the integrated potential strength is the same and the phase diagram in first-order perturbation theory only depends on this quantity. Even if the effective hard-sphere diameter is taken into account, the phase diagrams do not differ, since this effective diameter is determined by the repulsive part of the interaction alone. Within the sharp-kink approximation the ratio of liquid–gas surface tensions calculated for the analytical approximation of a WCA-LJ fluid and an exactly treated WCA-LJ fluid is

$$\frac{\sigma_{\mathrm{lg}}^{\mathrm{WCA-LJ,app}}}{\sigma_{\mathrm{lg}}^{\mathrm{WCA-LJ}}} \;=\; \left(\frac{16}{9}\right)^2\,\frac{1}{2^{1/6}\,\pi} \;\simeq\; 0.896259. \tag{7.49}$$

Hence the analytical approximation underestimates the liquid–gas surface tension by approximately 10 % in comparison to the exact treatment of the WCA-LJ fluid.

Here the effective interface potential is given by

$$\omega_{\mathrm{WCA-LJ}}(l) = \Delta\varrho \left\{ \varrho_{\mathrm{l}} \left(-\pi\,\varepsilon_{\mathrm{LJ}}\sigma_{\mathrm{LJ}}^4\right) \left[b_1\left(\frac{l-d_{\mathrm{w}}}{\sigma_{\mathrm{LJ}}}\right)\,\Theta\Big(l-d_{\mathrm{w}}-\sqrt[6]{2}\sigma_{\mathrm{LJ}}\Big) + b_2\left(\frac{l-d_{\mathrm{w}}}{\sigma_{\mathrm{LJ}}}\right)\,\Theta\Big(\sqrt[6]{2}\sigma_{\mathrm{LJ}}-(l-d_{\mathrm{w}})\Big)\right] + \sum_{i\geq 2}\frac{1}{i}\,\frac{u_{i+1}}{l^i}\right\} \tag{7.50}$$

with the auxiliary functions

$$b_1(s) := \frac{1}{3}\,s^{-2} - \frac{1}{90}\,s^{-8} \tag{7.51}$$

and

$$b_2(s) := \frac{9}{8}\,2^{2/3} - \frac{16}{9}\,\sqrt{2}\,s + \frac{9}{10}\,2^{1/3}\,s^2 - \frac{1}{12}\,s^4. \tag{7.52}$$

The analytically feasible parts of the line tension can be expressed as

$$(\tau_{a1})_{\mathrm{WCA-LJ}}(\theta) = -\frac{24}{35}\,2^{5/6}\,(\Delta\varrho)^2\,\sigma_{\mathrm{LJ}}^5\,\varepsilon_{\mathrm{LJ}}\,\left(1-\frac{\theta}{\tan\theta}\right) \tag{7.53}$$

and

$$\begin{aligned}(\tau_{a2})_{\mathrm{WCA-LJ}}(l_0,\theta) = \frac{\Delta\varrho}{\tan\theta}\Bigg\{ \varrho_{\mathrm{l}}\left(-\pi\,\varepsilon_{\mathrm{LJ}}\,\sigma_{\mathrm{LJ}}^5\right)\Bigg[&\frac{1}{3}\left(\max\left\{\tfrac{l_0-d_{\mathrm{w}}}{\sigma_{\mathrm{LJ}}},\sqrt[6]{2}\right\}\right)^{-1} \\ -\frac{1}{630}\left(\max\left\{\tfrac{l_0-d_{\mathrm{w}}}{\sigma_{\mathrm{LJ}}},\sqrt[6]{2}\right\}\right)^{-7} &+ \left(\frac{187}{360}\,2^{5/6} - \frac{9}{8}\,2^{2/3}\,\tfrac{l_0-d_{\mathrm{w}}}{\sigma_{\mathrm{LJ}}} + \tfrac{8}{9}\,\sqrt{2}\,\left(\tfrac{l_0-d_{\mathrm{w}}}{\sigma_{\mathrm{LJ}}}\right)^2\right. \\ -\frac{3}{10}\,2^{1/3}\,\left(\tfrac{l_0-d_{\mathrm{w}}}{\sigma_{\mathrm{LJ}}}\right)^3 + \frac{1}{60}\,\left(\tfrac{l_0-d_{\mathrm{w}}}{\sigma_{\mathrm{LJ}}}\right)^5 &\left.\Big)\,\Theta\Big(\sqrt[6]{2}-\tfrac{l_0-d_{\mathrm{w}}}{\sigma_{\mathrm{LJ}}}\Big)\right] \\ &+ \sum_{i\geq 1}\frac{1}{i\,(i+1)}\,\frac{u_{i+2}}{l_0^i}\Bigg\}.\end{aligned} \tag{7.54}$$

7.5 Square-well fluid

The general expressions from Sec. 7.3 are specified here for the case of a square-well (SW) fluid (see Sec. 2.3.5). They read

$$t_{\mathrm{SW}}(z) = \begin{cases} -\pi\,\varepsilon_{\mathrm{SW}}\,\frac{4}{3}\sigma_{\mathrm{SW}}^3 & \text{for } z < -\sigma_{\mathrm{SW}} \\ -\pi\,\varepsilon_{\mathrm{SW}}\,\left(\frac{2}{3}\sigma_{\mathrm{SW}}^3 - \sigma_{\mathrm{SW}}^2\,z + \frac{1}{3}\,z^3\right) & \text{for } -\sigma_{\mathrm{SW}} \leq z \leq \sigma_{\mathrm{SW}} \\ 0 & \text{for } z > \sigma_{\mathrm{SW}}, \end{cases} \tag{7.55}$$

$$\sigma_{\mathrm{lg}}^{\mathrm{SW}} = \frac{\pi}{8}\,(\Delta\varrho)^2\,\varepsilon_{\mathrm{SW}}\sigma_{\mathrm{SW}}^4 > 0, \tag{7.56}$$

$$\omega_{\mathrm{SW}}(l) = \Delta\varrho\left\{\varrho_{\mathrm{l}}\left(-\pi\,\varepsilon_{\mathrm{SW}}\sigma_{\mathrm{SW}}^4\right)\left[\frac{1}{4} - \frac{2}{3}\,\frac{l-d_{\mathrm{w}}}{\sigma_{\mathrm{SW}}} + \frac{1}{2}\,\left(\frac{l-d_{\mathrm{w}}}{\sigma_{\mathrm{SW}}}\right)^2 - \frac{1}{12}\,\left(\frac{l-d_{\mathrm{w}}}{\sigma_{\mathrm{SW}}}\right)^4\right]\Theta\big(\sigma_{\mathrm{SW}}-(l-d_{\mathrm{w}})\big) + \sum_{i\geq 2}\frac{1}{i}\,\frac{u_{i+1}}{l^i}\right\}, \tag{7.57}$$

$$(\tau_{a1})_{\rm sw}(\theta) \;=\; -\frac{1}{15}(\Delta\varrho)^2\,\sigma_{\rm sw}^5\,\varepsilon_{\rm sw}\,\left(1-\frac{\theta}{\tan\theta}\right) \tag{7.58}$$

and

$$\begin{aligned}(\tau_{a2})_{\rm sw}(l_0,\theta) \;=\; & \frac{\Delta\varrho}{\tan\theta}\left\{\varrho_{\rm l}\left(-\pi\,\varepsilon_{\rm sw}\,\sigma_{\rm sw}^5\right)\left[\frac{1}{15}-\frac{1}{4}\frac{l_0-d_{\rm w}}{\sigma_{\rm sw}}+\frac{1}{3}\left(\frac{l_0-d_{\rm w}}{\sigma_{\rm sw}}\right)^2\right.\right.\\ & \left.\left.-\frac{1}{6}\left(\frac{l_0-d_{\rm w}}{\sigma_{\rm sw}}\right)^3+\frac{1}{60}\left(\frac{l_0-d_{\rm w}}{\sigma_{\rm sw}}\right)^5\right]\;+\;\sum_{i\geq 1}\frac{1}{i\,(i+1)}\,\frac{u_{i+2}}{l_0^i}\right\}.\end{aligned} \tag{7.59}$$

7.6 Interface displacement model motivated by the sharp-kink DFT

The interface displacement model (IDM) [44] represents a mesoscopic approach to the line tension of a sessile liquid wedge. Important predictions for the behavior of the line tension and the wedge contour upon approaching the wetting transition were derived from it (see Sec. 1.6). In the IDM the line tension is defined via deviations of the film contour from a constant height according to

$$\tau \;=\; \int_{-\infty}^{\infty}{\rm d}x\;\left[\frac{1}{2}\,\sigma_{\rm lg}\left(\frac{{\rm d}l}{{\rm d}x}\right)^2+\omega\big(l(x)\big)\right]\;+\;\text{constant}, \tag{7.60}$$

where τ is the equilibrium value, if $l(x)$ is the equilibrium contour. Therefore this line tension definition is different from the one in the microscopic approaches, i. e., the sharp-kink DFT or the fully microscopic treatment. If in a DFT picture it is desired to refer to predictions from the IDM, at least a crude connection between both definitions should be established.

Here a motivation of the line tension definition from the IDM is presented, on the basis of the above described sharp-kink DFT. Within the sharp-kink approach the wedge line tension consists of four parts (see the explicit formulae in Sec. 7.3),

$$\tau[l(x)] \;=\; \tau_{a1}(\theta)\;+\;\tau_{a2}(l_0,\theta)\;+\;\tau_{\omega}[l(x)]\;+\;\tau_{\rm i}[l(x)]. \tag{7.61}$$

The first term only depends on the contact angle and even vanishes vor $\theta\to 0$, thus it is neglected here. The second term is

$$\tau_{a2}(l_0,\theta) \;=\; \frac{1}{\tan\theta}\,\int_{l_0}^{\infty}{\rm d}l\;\omega(l). \tag{7.62}$$

If the actual contour looks like the reference wedge (i. e., for $l(x)=a(x)$), it can be expressed as

$$\tau_{a2}(l_0,\theta) \;=\; \int_{x=0}^{\infty}{\rm d}x\;\;\omega\big(l(x)\big). \tag{7.63}$$

The third term vanishes for $l(x)\equiv a(x)$. Note that the predictions of the IDM upon approaching the wetting temperature $T_{\rm w}$ refer to wedge contours which differ relatively strongly from an exact wedge, thus the basic assumption of the above motivation is not fulfilled well. Since the IDM line tension definition also implies the way to determine the equilibrium wedge contour, the wedge shapes according to the IDM and the sharp-kink DFT differ.

The fourth term in the local approximation (apart from a term solely depending on the contact angle) can be approximated by

$$\tau_{\mathrm{i}}[l(x)] \;\simeq\; \sigma_{\mathrm{lg}} \int_{-\infty}^{\infty} \mathrm{d}x\, \frac{1}{2} \left(\frac{\mathrm{d}l}{\mathrm{d}x} \right)^2 \;+\; \text{const.} \tag{7.64}$$

Thus the second and the fourth term essentially resemble the expressions from the IDM line tension definition, Eq. (7.60). Consequently for roughly wedge-shaped contours [i. e., $l(x) \simeq a(x)$] the line tension definition according to the IDM can be related to a sharp-kink DFT. By calculating the remaining, omitted contributions, control over the deviations between the microscopic and the mesoscopic line tension definitions is possible.

Altogether this consideration gives some indication that line tension values from the microscopic and the mesoscopic level of description are of comparable order of magnitude. Indeed Getta and Dietrich [50, 51] as well as Bauer and Dietrich [11, 52] have shown numerically that the asymptotic behavior of the wedge line tension obeys the IDM predictions. For a simple model system of three coexisting phases Koga and Widom [100, 101] recovered the IDM predictions as well. One can conjecture that the IDM predictions are universal, since microscopic details of a model system are expected to be unimportant for the qualitative behavior of the line tension very close to wetting. The quantitative behavior, i. e., the prefactor and the range of validity of the description by the leading order term, certainly depends on microscopic details.

8 Results and discussion

In this chapter quantitative line tension results are presented and discussed. Several model systems are addressed by means of three different line tension theories:
First, line tension values calculated *fully microscopically* for several systems are shown in Sec. 8.1. These systems have been tuned such that they are easily addressable via the fully microscopic approach.
Second, the quality of the *SK line tension theory* is analyzed in Sec. 8.2. This approach is hardly applicable to the systems from Sec. 8.1. Nevertheless a system has been tailored in order to facilitate a quantitative comparison between SK and fully microscopic line tension values.
Third, a *"hybrid theory"* is introduced in Sec. 8.3. It corresponds to the standard SK line tension approach into which an improved effective interface potential $\omega(l)$ is inserted. For the cases studied in Sec. 8.1 this hybrid theory yields semi-quantitative agreement with the corresponding fully microscopic line tension values. It fails, however, for the rather extreme case of the tailored system from Sec. 8.2.

Finally the status of the three line tension theories is appraised in Sec. 8.4. This means that the power of predicting line tension values and the numerical efficiency of the three methods are discussed.

8.1 Fully microscopic results

Indekeu's [44] predictions for the behavior of the line tension upon approaching a wetting transition distinguish between four wetting scenarios (see Sec. 1.6). They correspond to systems comprising long- or short-ranged forces, respectively, undergoing a first-order or critical wetting transition, respectively. Subsections 8.1.1 to 8.1.2 refer to three of these four wetting scenarios.

The fourth wetting scenario, i. e., a system with short-ranged forces undergoing a critical wetting transition, could in principle occur for a SW fluid in the presence of a short-ranged substrate potential. Since mean-field predictions are believed to be not very reliable in this case, this wetting scenario is beyond the scope of this work.

8.1.1 Long-ranged forces, first-order wetting

8.1.1.1 Lennard-Jones fluid on a LJ substrate

In fully microscopic, numerical calculations a cut-off of the LJ potential range has to be introduced. Although its cut-off distance might be large compared to the atomic radius, the cut LJ potential is, strictly speaking, short-ranged compared to the original, infinitely long-ranged LJ potential. This cut-off approximation influences the wetting behavior and the asymptotics of the line tension upon approaching wetting. The truncated interaction acts as long-ranged for a liquid-like film whose thickness is smaller or of the order of the cut-off distance. For a much larger film thickness the presence of the cut-off is revealed, and the character of the wetting transition changes from long-ranged to short-ranged.

Since the external potential is not truncated here, the (partially cut and shifted) LJ fluid under the influence of an LJ (9–4–3) substrate potential belongs to the class of "long-ranged forces". First-order wetting and critical wetting (due to a vanishing Hamaker constant) can be observed.

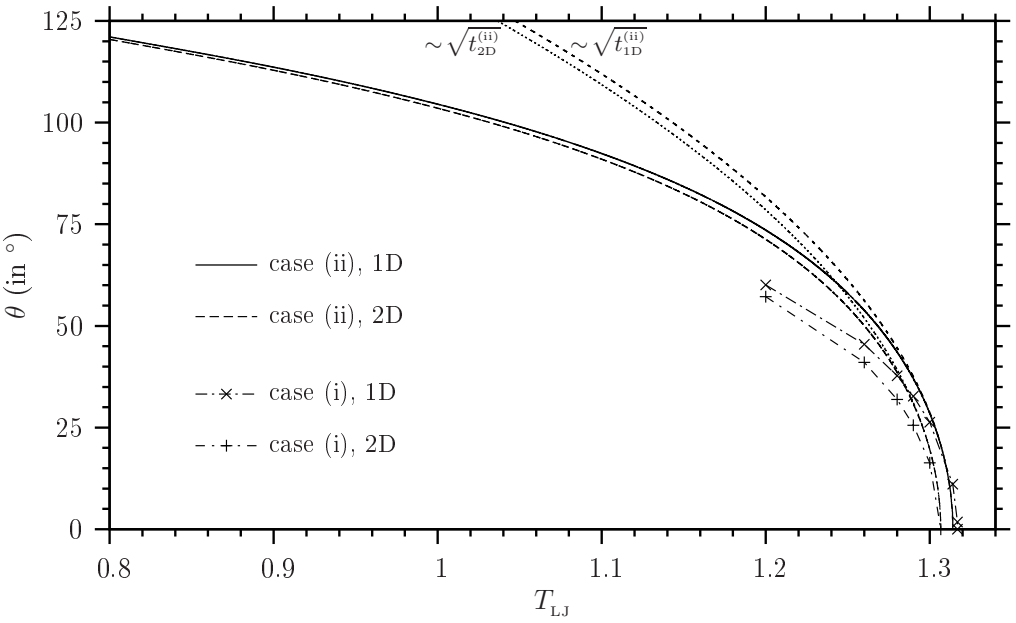

Fig. 8.1: Contact angle of a WCA-LJ fluid on a LJ (9–3) substrate. The LJ fluid–fluid interaction is truncated at an interparticle distance of 10 atomic radii (see Sec. 6.1). The substrate potential strength is characterized by $\beta\varepsilon_{\mathrm{w}}^{(\mathrm{ii})} = 0.6707$, refered to as case (ii). In case (i) the substrate potential depth is fixed and adjusted such that the 2D wetting temperature equals the one in case (ii), i. e., $\varepsilon_{\mathrm{w}}^{(\mathrm{i})} = 1.3066\ \varepsilon_{\mathrm{LJ}} \times 0.6707$. The predicted asymptotic relation $\theta \sim \sqrt{t}$ [Eq. (1.9)] holds for each of the curves and for small contact angles $\theta \lesssim 35°$. t denotes the reduced temperature with $t = \left(T_{\mathrm{LJ,w}} - T_{\mathrm{LJ}}\right)/T_{\mathrm{LJ,w}}$, which is specified for the cases (i) and (ii) in 1D or 2D, respectively. The wetting temperatures in the different cases are $T_{\mathrm{LJ,w}}^{(\mathrm{1D;i})} \simeq 1.3169$, $T_{\mathrm{LJ,w}}^{(\mathrm{1D;ii})} \simeq 1.3140$, and $T_{\mathrm{LJ,w}}^{(\mathrm{2D;i})} = T_{\mathrm{LJ,w}}^{(\mathrm{2D;ii})} \simeq 1.3066$. Hence the 2D wetting temperature in case (i) or (ii) is about 0.78 % or 0.56 %, respectively, smaller than the corresponding 1D wetting temperature.

A first-order wetting transition of a WCA-LJ fluid in contact with a planar LJ (9–3) substrate is analyzed here. The contact angle dependence of the line tension is aimed at. There are basically two simple ways to change the contact angle θ theoretically: Either (i) the potential depth parameters of the fluid–fluid and the substrate–fluid interaction, $\varepsilon_{\mathrm{LJ}}$ and ε_{w}, are fixed and the temperature T (of both the substrate and the fluid) is changed. Hence the effective temperature $T_{\mathrm{LJ}} = 1/(\beta\varepsilon_{\mathrm{LJ}})$ is changed and the dimensionless substrate parameter $\beta\varepsilon_{\mathrm{w}} \sim \beta\varepsilon_{\mathrm{LJ}}$ as well. Or (ii) the temperature T is fixed and the fluid–fluid interaction parameter $\varepsilon_{\mathrm{LJ}}$ is changed, while $\beta\varepsilon_{\mathrm{w}}$ is fixed. Both methods of changing θ are employed here, since this gives an idea to what extend the line tension value solely depends on the value of θ or how important the actual way of establishing such a contact angle is important.

The temperature dependence of the contact angle is shown in Fig. 8.1. The typical behavior for first-order wetting is found, i. e., $\theta \sim \sqrt{t}$ for small contact angles and a reduced temperature t. Effectively one-dimensional (1D) and effectively two-dimensional (2D) calculations exhibit small deviations of the wetting temperature. This small error results from different cut-offs of the LJ fluid–fluid interaction in 1D and 2D (see Sec. 6.1) as well as from slightly different discretization errors in 1D and 2D. Results for a SW fluid (cf. Fig. 8.6), where no cut-off exists and the differences between 1D and 2D data are even smaller, indicate that the small differences between the 1D and 2D data for the LJ fluid are mainly due to the different cut-offs in 1D and 2D. For consistency 2D density profiles are employed as boundary profiles in the — likewise 2D — sessile liquid wedge calculations.

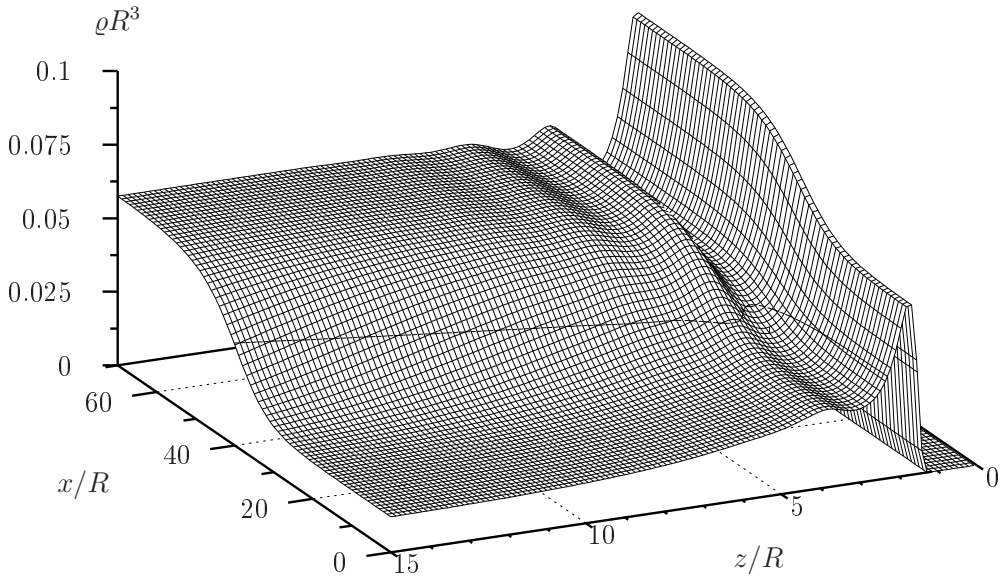

Fig. 8.2: Density $\varrho(x, z)$ in the contact region of a sessile liquid wedge on a LJ substrate. The fluid consists of WCA-LJ particles. The employed parameters are $\mathrm{cut}_{\mathrm{LJ}} = 10$, $T_{\mathrm{LJ}} = 1.295$, and $\beta\varepsilon_{\mathrm{w}} = 0.6707$. This choice leads to $\theta \simeq 25.80°$. Additionally the contour refering to the arithmetic average of bulk liquid and gas densities is indicated.

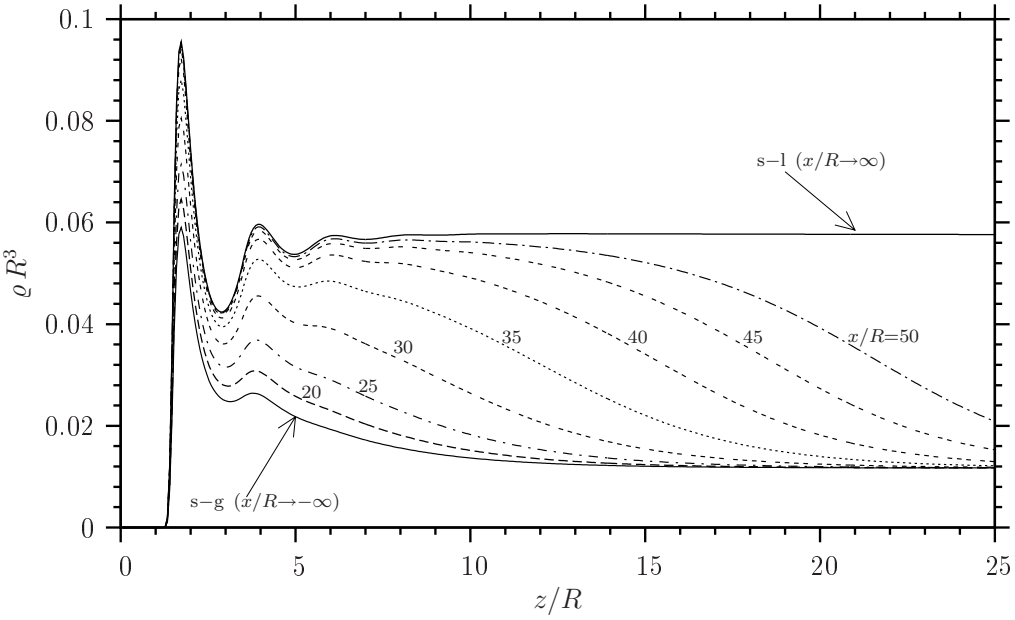

Fig. 8.3: Cuts through $\varrho(x, z)$ from Fig. 8.2. For several fixed values of x the density ϱ as a function of the distance z from the surface is displayed. Hence the density profile of a planar s–g or s–l interfacial is recovered, if x is situated far from the contact line on the gas or liquid side, respectively.

The microscopic structure of a sessile liquid wedge formed by a LJ fluid resting on a LJ (9–3) substrate is illustrated in Fig. 8.2. Cuts/slices through this specific density $\varrho(x, z)$ for certain x values are presented in Fig. 8.3. The contour of this density distribution is contained in Fig. 8.4, which provides fully microscopic contours for several contact angles.

Line tension values of a sessile liquid wedge formed by a LJ fluid on a LJ substrate are obtained from fully microscopicly calculated density distributions $\varrho(x, z)$. The line tension is presented in Fig. 8.5 for both cases (i) and (ii) of varying the contact angle. The line

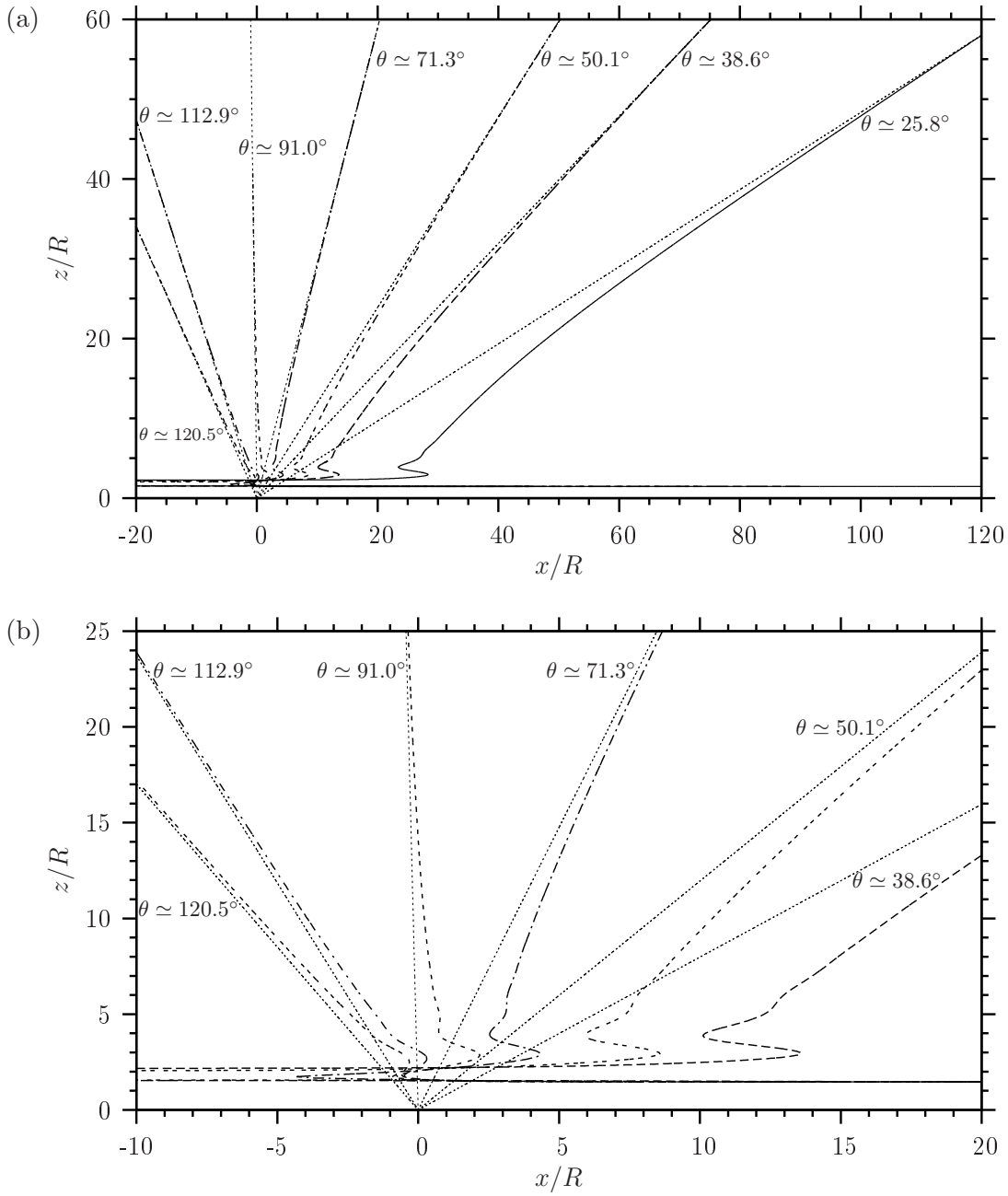

Fig. 8.4: Contour of a sessile liquid wedge comprising a LJ fluid and a LJ (9–3) substrate. The choice of parameters corresponds to case (ii) in Fig. 8.1. The convergence of the contours towards their asymptotes is shown in (a), whereas (b) resolves the contour shapes in the vicinity of the substrate surface. The curve for $\theta \simeq 25.80°$ displayed (a) is left out in (b), since its triple line is situated out of the focus there. Contour oscillations near the surface originate from oscillations in the corresponding planar s–l interface, which decay towards the gas side in the three-phase contact region. Such contour oscillations have been found before in WDA-DFT studies of small sessile droplets [168]. It is characteristic for a first-order wetting transition that far from the contact line the contour reaches its asymptote from below. Even for obtuse contact angles (i. e., $90° \leq \theta < 180°$) the contour attains the inclined reference l–g dividing interface from the liquid side.

tension in the accessible contact angle range is compatible with Indekeu's predictions with respect to the asymptotic behavior. Besides the typical features that τ is negative for large θ and crosses zero for some small value of θ (here for $\theta \simeq 3°$, which depends on the choice of the solid–fluid dividing interface) are recovered as well.

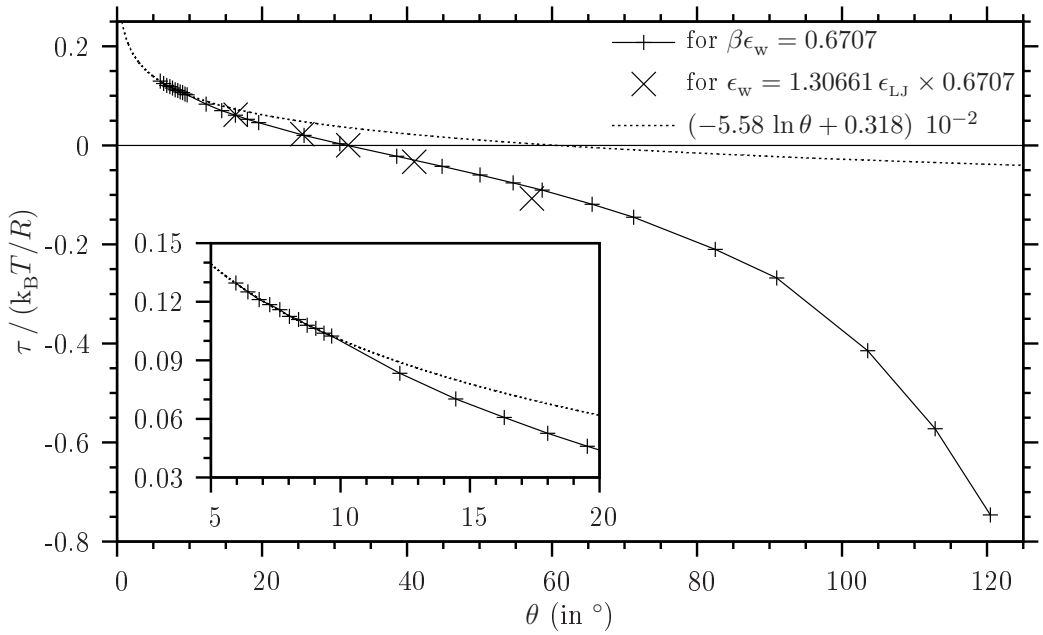

Fig. 8.5: Line tension of a sessile liquid wedge formed by a WCA-LJ fluid on a LJ substrate. The parameters are the same as in Fig. 8.1. The two ways of changing θ give very similar results for small contact angles $\theta \lesssim 40°$. For this scenario a diverging line tension is predicted [Eq. (1.8)], with an asymptotic contact angle dependence $\tau \sim -\ln\theta$. As shown in the inset, the predicted asymptotic law, $\tau \sim -\ln\theta$, fits the data for $\beta\varepsilon_w = 0.6707$ very well up to $\theta \lesssim 9.5°$. The small additive constant in the fit function is unimportant, since one could chose another solid–fluid dividing interface to make it vanish. Between $\theta \simeq 9.5°$ and $\theta \simeq 12°$ the shape of $\tau(\theta)$ rather abruptly changes from the asymptotic behavior (for $\theta \lesssim 9.5°$) to the behavior for intermediate θ (say for $12° \lesssim \theta \lesssim 40°$). This abrupt change most likely originates from the second fluid layer in the substrate–gas interface, whose density peak slightly grows for decreasing θ in this cross-over regime. However, in $\theta(T_{LJ})$ (from 2D calculations) no imprint of this tiny effect could be observed. Note that the contact angle θ is expressed as radian measure in $\ln\theta$ and that the plane $z = 0$ is chosen as the solid–fluid dividing interface.

8.1.1.2 Square-well fluid on a LJ substrate

Even though the square-well fluid–fluid interaction potential is of short range, a long-ranged LJ (9–3) substrate potential leads to a classification of the system as "long-ranged forces". This model system is employed for fully microscopic calculations of the wedge line tension as well. Thereby one can estimate to what extend the quantitative results $\tau(\theta)$ depend on the choice of the fluid.

Like for the LJ fluid discussed in the previous subsubsection, two ways (i) and (ii) of changing the contact angle are compared. The temperature dependence of the contact angle for both cases and caluclated in effectively one or two dimensions, respectively, is displayed in Fig. 8.6. Finy deviations between the 1D and the 2D wetting temperature originate exclusively from slightly different discretization errors, since in this model system the fluid–fluid interaction is not truncated.

The liquid wedge line tension as a function of the contact angle is given for both cases (i) and (ii) in Fig. 8.7. Very small contact angles are not accessible in this fully microscopic approach and hence the leading order term for vanishing θ cannot be extracted. However, around $\theta \simeq 20°$ τ increases more than linearly for decreasing θ, which gives some indication for a possible divergence at vanishing θ. The data are compatible with Indekeu's predictions for the asymptotic line tension behavior.

The line tension value is negative for large contact angles, crosses zero for $\theta \simeq 40°$, and further increases on decreasing θ. Note that the line tension value depends on the choice of the solid–fluid dividing interface, and hence another choice would shift the zero towards another contact angle. Although not confirmable in this approach, the line tension of this system is likely to diverge upon approaching wetting. These results are in agreement with Indekeu's predictions from the interface displacement model.

The shape of $\tau(\theta)$ for the SW fluid is similar to the corresponding curve for the LJ fluid [see Fig. 8.5]. At a certain θ the SW line tension is approximately half as large as the LJ line tension. In the analyzed contact angle range $10° \lesssim \theta \lesssim 120°$ the line tension in dimensionless units attains values in the range $-0.4 \lesssim \tau/(\mathrm{k_B}T/R) \lesssim 0.05$ for the SW fluid and $-0.7 \lesssim \tau/(\mathrm{k_B}T/R) \lesssim +0.1$ for the LJ fluid case. Hence for room temperature ($T = 298$ K) and a hard-sphere radius of $R = 0.1$ nm the line tension in this contact angle range varies continuously between -16 pN and $+2$ pN for the SW fluid or between -28 pN and $+4$ pN for the LJ fluid, respectively.

Freezing:
For $T_{\mathrm{SW}} = 0.8/(\frac{64}{81}\sqrt{2})$ quasi-two-dimensional freezing occurs in this system. The density distribution $\varrho(x, z)$ exhibits peaks ordered on a triangular lattice in the xz plane, as shown in Fig. 8.8. The large density oscillations destabilize the iteration procedure and thus impede a perfect minimization. At least on the observed intermediate stage crystal peaks are exclusively present in the former liquid region of the wedge system, whereas the gas region still contains gas-like densities. Most likely the optimal configuration here corresponds to density peaks on a triangular lattice and spread all over the finite system size except close to the boundary profiles.

In the wedge system translational invariance in the y direction is enforced, so density variations in this direction are excluded. A breakup of this constraint is expected to lead to freezing in all three dimensions, such that one could interpret the density peaks as localized particles on a three-dimensional lattice.

The effectively one-dimensional solid–liquid interface profile $\varrho(z)$ exhibits strong density oscillations, which argue for freezing suppressed through the constraint of translational invariance in the x and y directions. Freezing is not directly observable at the planar solid–gas or solid–liquid interaface density distributions $\varrho(x, z)$ at this temperature, if a planar

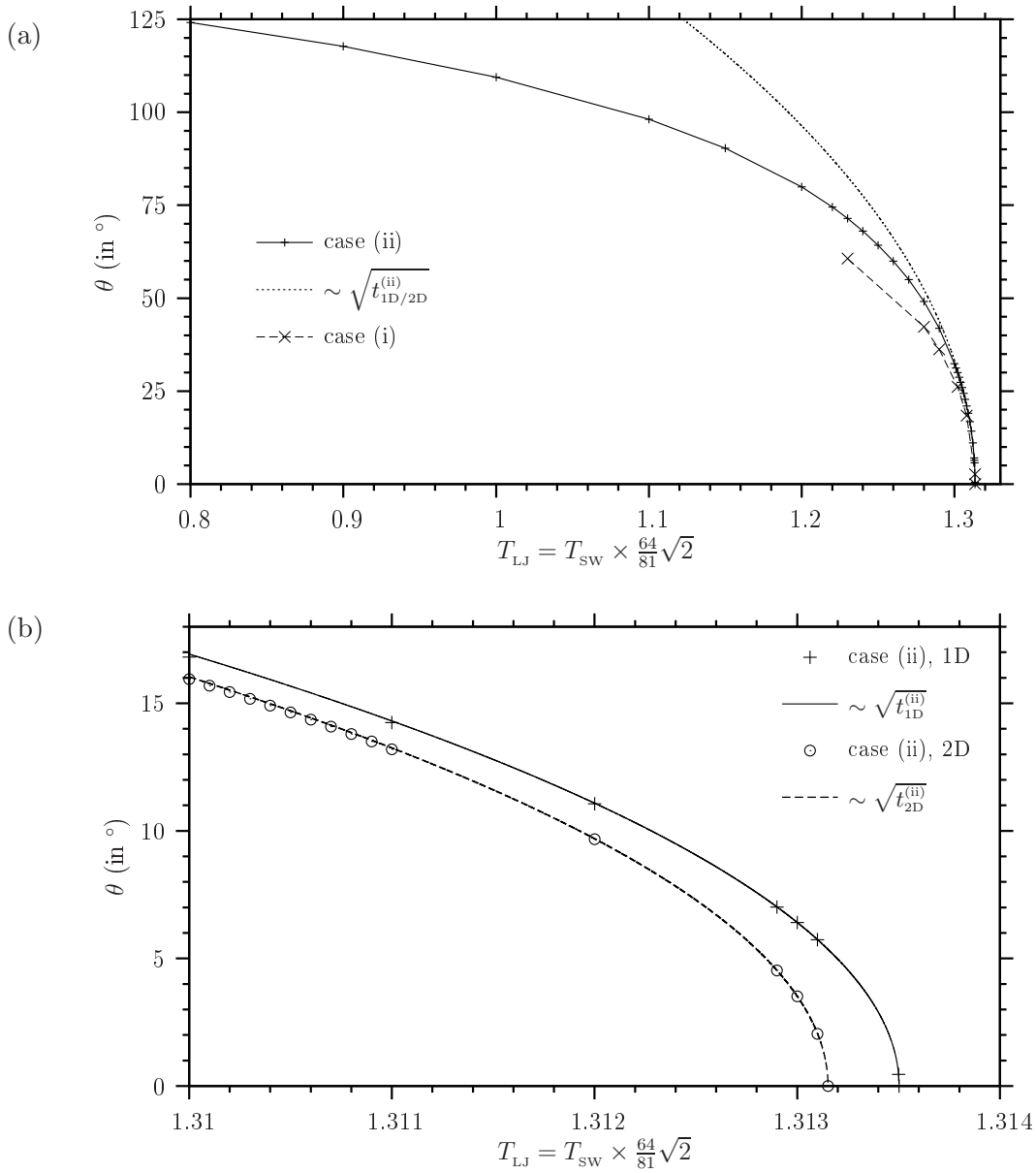

Fig. 8.6: Contact angle of a SW fluid on a LJ (9–3) substrate. Two ways of changing the contact angle are pursued: In case (ii) $\beta\varepsilon_{\rm w}^{\rm (ii)} = 0.45$ and in case (i) $\varepsilon_{\rm SW}^{\rm (ii)}$ is fixed, respectively. The 2D wetting temperatures in both cases are made equal by requiring $\varepsilon_{\rm w}^{\rm (i)} = 1.31315/(\frac{64}{81}\sqrt{2})\ \varepsilon_{\rm SW} \times 0.45$. The contact angle is plotted versus the effective temperature of a LJ fluid with the same integrated strength, $T_{\rm LJ} = T_{\rm SW} \times \frac{64}{81}\sqrt{2}$, in order to facilitate a comparison to results for LJ fluids. The 1D and 2D data are almost indistinguishable on the scale of (a). The predicted asymptotic relation $\theta \sim \sqrt{t}$ is found for $\theta \lesssim 35°$. In (b) the temperature regime close to wetting is resolved for case (ii). Small diferences between 1D and 2D results can be observed. The wetting temperatures in the different cases are $T_{\rm SW,w}^{\rm (1D;i)} \simeq 1.31361/(\frac{64}{81}\sqrt{2})$, $T_{\rm SW,w}^{\rm (1D;ii)} \simeq 1.31350/(\frac{64}{81}\sqrt{2})$, and $T_{\rm SW,w}^{\rm (2D;i)} = T_{\rm SW,w}^{\rm (2D;ii)} \simeq 1.31315/(\frac{64}{81}\sqrt{2})$. Hence the 2D wetting temperature in case (i) or (ii) is about 0.035 % or 0.027 %, respectively, smaller than the corresponding 1D wetting temperature.

initial configuration is used in the iteration procedure. The effectively one-dimensional numerical solutions are metastable states, i. e., they correspond to local, but not global minima in the grand potential density functional. Obviously the initialization profile in the wedge geometry is sufficiently inhomogeneous to initiate freezing.

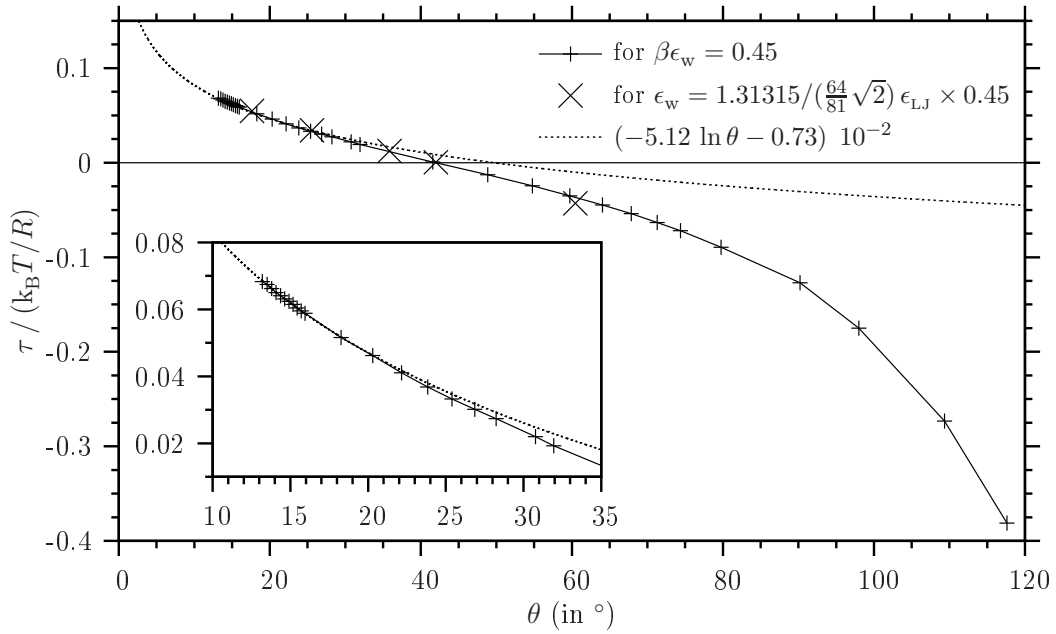

Fig. 8.7: Line tension of a sessile liquid wedge comprising a SW fluid on a LJ (9–3) substrate. The line tension is plotted versus the contact angle θ, which is changed on two different trajectories in parameter space: On varying the effective temperature T_{SW} $\beta\varepsilon_w^{(ii)} = 0.45$ is chosen in case (ii) and $\varepsilon_w^{(i)} = 1.31315/(\frac{64}{81}\sqrt{2})\ \varepsilon_{SW} \times 0.45$ in case (i). The two cases give very similar results for small contact angles $\theta \lesssim 40°$. τ increases more than linearly for small and decreasing θ, thus it is likely to diverge for $\theta \to 0$. As shown in the inset, the predicted asymptotic law, $\tau \sim -\ln\theta$, fits the data for $\beta\varepsilon_w = 0.45$ well up to $\theta \lesssim 20°$. The additive small constant in the fit function is unimportant, since one could chose another solid–fluid dividing interface to make it vanish. Note that the contact angle θ is expressed as radian measure in $\ln\theta$ and that the plane $z = 0$ is chosen as the solid–fluid dividing interface.

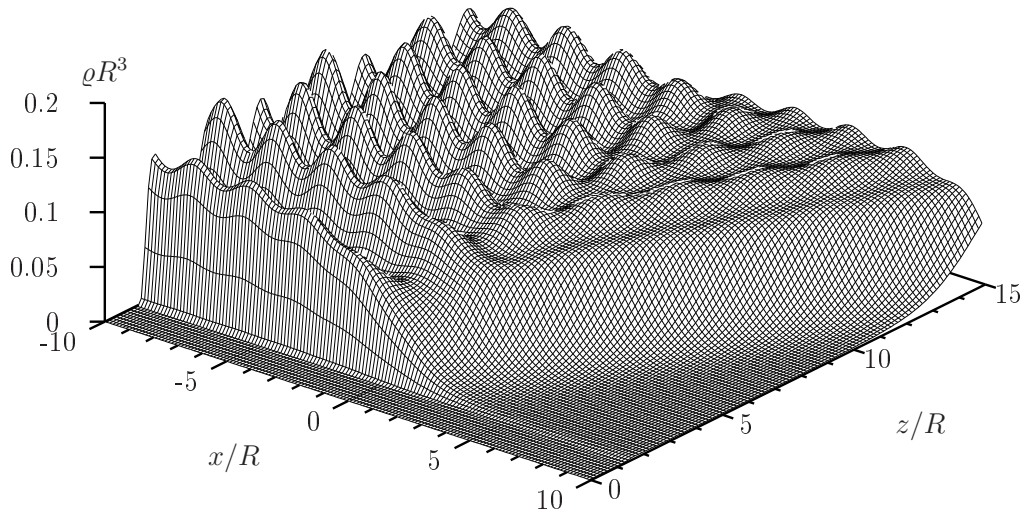

Fig. 8.8: Onset of freezing in a SW liquid wedge residing on a LJ (9–3) substrate. The three-phase contact region is displayed. The effective temperature is $T_{SW} = 0.8/(\frac{64}{81}\sqrt{2})$ here, and the substrate potential is described by $\beta\varepsilon_w = 0.45$. The Picard iteration process is obstructed by high density peaks and therefore has not completely converged.

8.1.2 Long-ranged forces, critical wetting

Critical wetting for long-ranged forces can be analyzed conveniently by means of the effective interface potential $\omega(l)$ and particularly the Hamaker constant a_2, which is the coefficient of the l^{-2} term in $\omega(l)$. A necessary condition for critical wetting involving long-ranged forces is a vanishing Hamaker constant a_2 at the critical wetting temperature This means that the l^{-2} term of the effective interface potential ω vanishes for large film thicknesses l. The l^{-2} contribution stemming from the fluid–fluid interaction has to cancel the contribution generated by the external potential exactly. Furthermore the next-to-leading coefficient of $\omega(l)$ has to be positive, e. g., $a_3 > 0$. If the temperature is slightly below the wetting temperature, the Hamaker constant is not zero any more and a negative l^{-2} term leads to a potential minimum at a certain large film thickness. If this local minimum is the global one, then the system exhibits critical wetting.

The expression for the (vanshing) Hamaker constant is given by [51]

$$a_2 \;=\; \frac{1}{2}\Delta\varrho\left(u_3 - \varrho_\mathrm{l}\, t_3\right) \;\stackrel{!}{=}\; 0. \tag{8.1}$$

t_3 and u_3 are the coefficients of the z^{-3} term of the function $t(z)$ [Eq. (7.11)] and the external potential [Eq. (3.8)], respectively. t_3 exclusively depends on the long-ranged tail of the fluid–fluid interaction.

Critical wetting of a substrate with *short-ranged* fluid–fluid interactions cannot occur, if the substrate–fluid potential is long-ranged. In this case $t_3 = 0$ for a sufficiently thick liquid-like film. Consequently the Hamaker constant a_2 exclusively depends on the long-ranged external potential and thus does not vanish here. Hence critical wettting based on a vanishing Hamaker constant is impossible for a SW fluid.

The scenario of critical wetting in a system governed by long-ranged interactions is addressed here via a Lennard-Jones (LJ) fluid ontop of a LJ (9–4–3) substrate. A LJ (9–3) potential, i. e., without a z^{-4} term, merely can give rise to first-order wetting. However, a sufficiently large value of b_4, the coefficient of the z^{-4} term [Eq. (3.17)], causes a dominant positive l^{-3} term in $\omega(l)$ for large l at the temperature for which the Hamaker constant vanishes. For the case of a *WCA-LJ fluid* on a LJ(9–4–3) substrate the conditional equation for a vanishing Hamaker constant, Eq. (8.1), reads

$$a_2 \;=\; \Delta\varrho\,\sigma_\mathrm{LJ}^3\left(\frac{1}{3}\pi\,\varepsilon_\mathrm{w} \;-\; \frac{1}{3}\pi\,\varrho_\mathrm{l}\,\sigma_\mathrm{LJ}^3\,\varepsilon_\mathrm{LJ}\right) \;\stackrel{!}{=}\; 0. \tag{8.2}$$

Hence the appropriate LJ substrate parameter ε_w [Eq. (3.14)] in order to possibly obtain critical wetting at a certain desired temperature is

$$\varepsilon_\mathrm{w} \;=\; \varrho_\mathrm{l}\,\sigma_\mathrm{LJ}^3\,\varepsilon_\mathrm{LJ}. \tag{8.3}$$

In fully microscopic calculations the attainable range of values of b_4 is limited. For positive b_4 the z^{-4} term adds additional attraction to the substrate potential. In particular the height of the first peak in the density distribution of a solid-liquid interface is increased considerably. For b_4 exceeding 1 considerably the fully microscopic programme becomes instable, since large peaks are precarious for the FFT calculations. Hence systems with $b_4 \gg 1$ cannot be desbribed by means of the actual fully microscopic programme.

The (sharp-kink) effective interface potential $\omega(l)$ predicts first-order wetting for $b_4 \lesssim 2$ and typical values of the other parameters. However, an additional phase transition associated with a sudden increase of the film thickness from very small values (around 3 R) to an intermediate one (around 12 R) occurs for $b_4 \simeq 2$. This prior phase transition

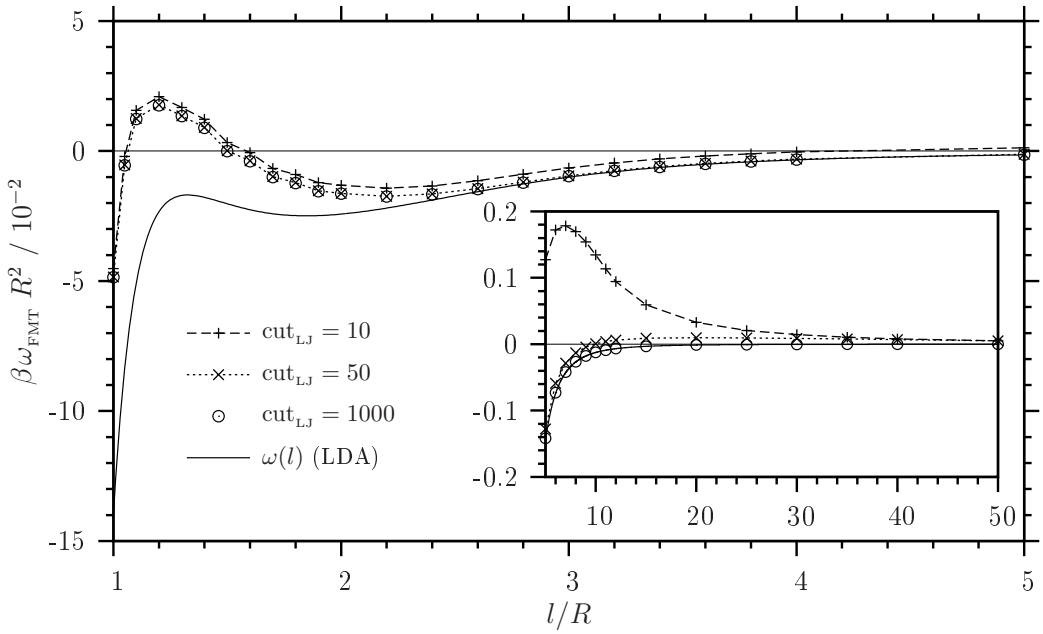

Fig. 8.9: Effective interface potential $\omega_{\rm FMT}(l)$ for sharp-kink (SK) density distributions and a *non-local* hard-sphere excess free energy treated via FMT. This hard-sphere contribution accounts for the repulsive part of the fluid–fluid LJ interaction. The "desired" critical wetting temperature is set to $T_{\rm LJ} = 1.31$, which corresponds to a LJ (9–3) substrate described by $\beta\varepsilon_{\rm w} \simeq 0.34063$. $\omega_{\rm FMT}(l)$ is displayed for $T_{\rm LJ} = 1.31$ and for several cut-off distances. The relative influence of a small cut-off of 10 atomic radii is moderate close to the substrate surface, but quite strong for film thicknesses between 5 and 20 atomic radii. $\omega_{\rm FMT}(l)$ is compared to $\omega(l)$, which is calculated within the SK theory employing the local density approximation (LDA), $d_{\rm w} = R$, and no truncation of the fluid–fluid interaction. The two curves, $\omega_{\rm FMT}(l)$ and $\omega(l)$, deviate considerably for small film thicknesses $l/R \lesssim 3$.

masks the critical wetting transition in a large temperature range. Hence a critical wetting transition unperturbed by such a prior transition requires values of b_4 which are much larger.

On the other hand critical wetting was found by fully microscopic calculations already for $b_4 \simeq 1$. In this regime the sharp-kink theory predicts first-order wetting instead, which moreover takes place at another wetting temperature. Hence predictions based on the sharp-kink effective interface potential for small values of l deviate considerably from the more realistic fully microscopic approach. It is known that for a small film thickness l the effective interface potential is not very reliable.

The discrepancy between the sharp-kink approach and the fully microscopic approach is analyzed further. The hard-sphere contribution to the grand potential is addressed in the local density approximation (LDA) within the SK theory, while the fully microscopic theory uses on the non-local FMT instead. The effect of this difference on the shape of the effective interface potential (within the sharp-kink approximation) can be analyzed by initializing a liquid film between $z = d_{\rm w}$ and the distance l from the substrate. For this density profile the interfacial tension can be calculated numerically very easily. It the interfacial tension for a very large l value (mimicking $l \to \infty$) is substracted, the result equals an effective interface potential within SK but with the non-local FMT. Deviations from the LDA theory are considerable, as can be seen in Fig. 8.9. The LDA-SK model creates much too low values of $\omega(l)$ close to the substrate surface. Both the LDA-SK and the FMT-SK model predict a first-order wetting transition, even though fully microscopic calculations found critical wetting. Consequently $\omega(l)$ is unreliable for small values of l

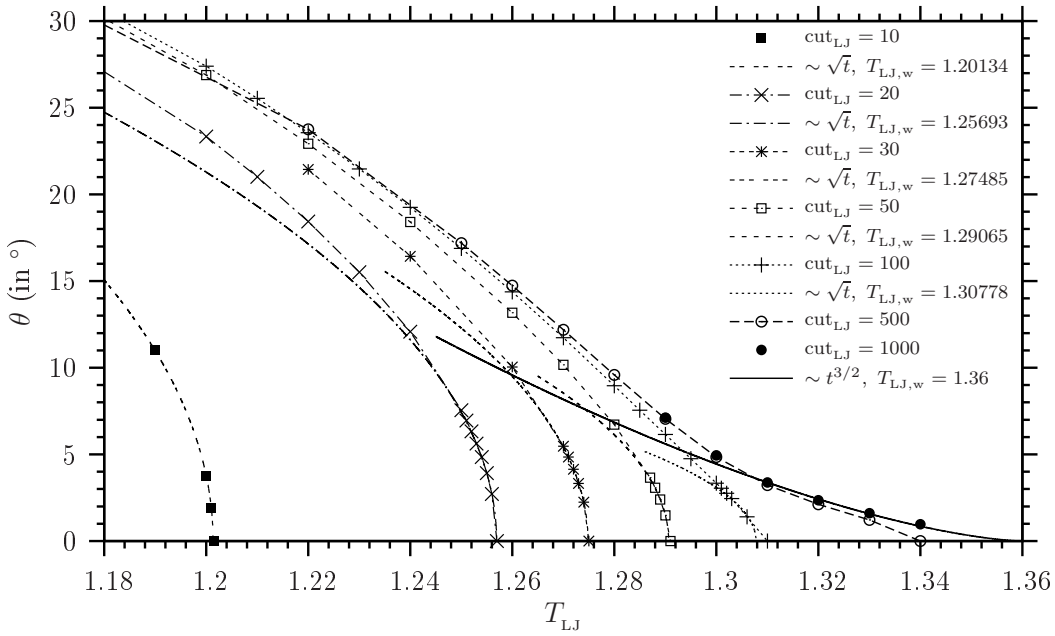

Fig. 8.10: Contact angle for critical wetting and cut-off-induced first-order wetting. A WCA-LJ fluid is exposed to a LJ (9–4–3) substrate. Contact angle curves for several cut-off distances (10, 20, 50, 100, 500, and 1000 hard-sphere radii) are shown. The "desired" critical wetting temperature was set to $T_{LJ} = 1.36$, which corresponds to $\varepsilon_w \simeq 1.36\,\varepsilon_{LJ} \times 0.28798$. In this fully microscopic calculation the choice $b_4 = 1.0$ was — in contrast to SK predictions — sufficient in order to obtain critical wetting. The contact angle is expected to asymptotically depend as $\theta \sim t^{3/2}$ on the reduced temperature $t = (T_{LJ,w} - T_{LJ})/T_{LJ,w}$ with $T_{LJ,w} = 1.36$. This prediction is actually found for very large cut-off distances ($cut_{LJ} \gtrsim 1000$) and very small contact angles ($\theta \lesssim 3°$). Strictly speaking even in this case the wetting transition is still of first-order due to the finite cut-off. For smaller cut-off distances the contact angle exhibits the square-root behavior, $\theta \sim \sqrt{t}$, which is typical for first-order wetting. The size of the contact angle range in which this asymptotic behavior holds decreases with increasing cut-off distance.

mainly due to the constraint of step-shaped density profiles. Additional deviations very close to the surface arise from the LDA. Hence in this critical wetting situation the SK theory fails not only quantitatively but even gives unreliable predictions with respect to the character of the wetting scenario and the wetting temperature. The tendency is that the SK theory might miss a critical wetting transition and might instead predict a first-order wetting at a higher temperature.

Strictly speaking critical wetting due to a vanishing Hamaker constant is only possible for infinitely long-ranged fluid–fluid interactions. Hence the finite LJ cut-off will always prevent a critical wetting character, i. e., a continuously diverging thickness of a liquid-like film in a planar solid–gas interface. However, for still finite film thicknesses the critical wetting signature, i. e., the characteristic temperature dependence of the contact angle and the film thickness [Eqs. (1.12) and (1.13)], is also visible for a finite, large cut-off distance.

Asymptotically the contact angle for critical wetting should behave as $\theta \sim t^{3/2}$ [Eq. (1.12)] instead of $\theta \sim t^{1/2}$ [Eq. (1.9)] for first-order wetting. However, in order to actually observe this behavior the cut-off distance has to be very large. In Fig. 8.10 the influence of the cut-off distance on the contact angle behavior is sketched. In order to observe a contact angle range exhibiting $\theta \sim t^{3/2}$ a very large cut-off distance is necessary.

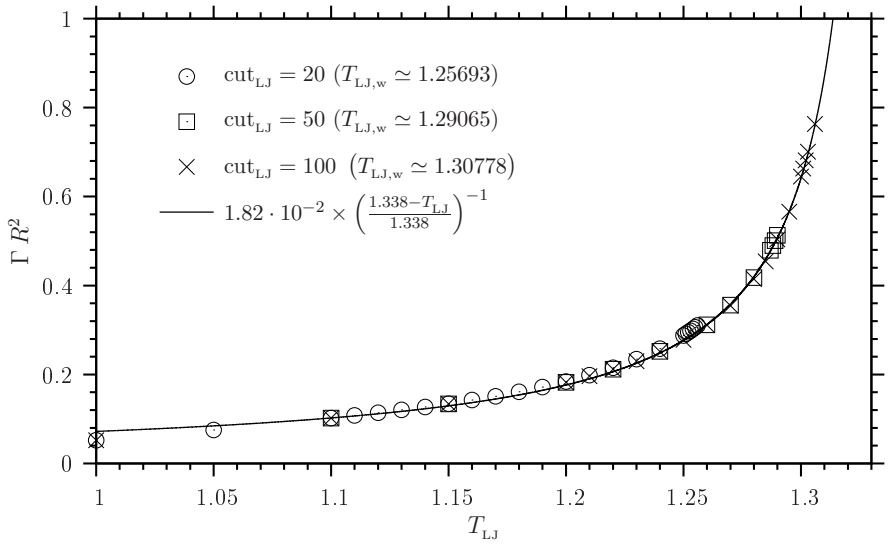

Fig. 8.11: Thickness of the liquid-like film at a substrate–gas interface for systems mimicking critical wetting. The parameters are the same as in Fig. 8.10. The excess adsorption Γ [Eq. (3.25)] is a convenient measure of the film thickness here, since it increases continuously up to the discontinuous divergence. This discontinuous divergence marks a first-order wetting transition, which originates from the truncation of the fluid–fluid interaction. Excess adsorption curves for several cut-off distances (20, 50, and 100 atomic radii) are displayed. The data points are well described by a single curve up to the cut-off dependent wetting temperature. This curve is proportional to the inverse reduced temperature, $\sim t^{-1}$, as expected close to a critical wetting transition [Eq. (1.13)].

Merely from considering these contact angle curves one would not expect critical-wetting-like behavior for a cut-off distance of the order of 20 atomic radii. However, according to Fig. 8.11 the temperature dependence of the thickness of a liquid-like film at a planar substrate–gas interface resembles the behavior typical for critical wetting up to the wetting temperature, where the film thickness diverges discontinuously. The order of the wetting transition is exclusively determined by the diverging behavior of the thickness of the liquid-like film in the planar substrate–gas interface. Here a discontinuous divergence of the film thickness leads undoubtedly to a classification as first-order wetting. Moreover the contact angle behaves as expected for first-order wetting. Critical wetting based on a vanishing Hamaker constant cannot occur in a system comprising a long-ranged external potential and a truncated fluid–fluid interaction. On the other hand the temperature dependence of the film thickness resembles the behavior that is typical for critical wetting. Hence the behavior of this system is ambiguous close to wetting.

Upon approaching critical wetting the thickness of the liquid-like film in the susbstrate–gas interface diverges. Since the microscopic contact region stays in the vicinity of the lateral position $x = 0$ of the macroscopic contact line, the line tension should vanish for critical wetting. This behavior contrasts the first-order wetting scenario, where the lateral position of the three-phase contact region diverges towards $x \to +\infty$. The statement $\tau(\theta = 0) = 0$ holds for every choice of the solid–fluid dividing interface. According to the prediction from the interface displacement model (IDM) in a critical wetting transition τ vanishes with an asymptotic behavior $\tau \sim \theta^{1/3}$ [Eq. (1.11)].

The line tension of a WCA-LJ fluid on the substrate described in Fig. 8.10 is calculated. The fluid–fluid LJ interaction is truncated at a interparticle distance of 20 atomic radii. The contact angle behavior and particularly the wetting temperature is slightly different in effectively one- and two-dimensional calculations (see Fig. 8.12).

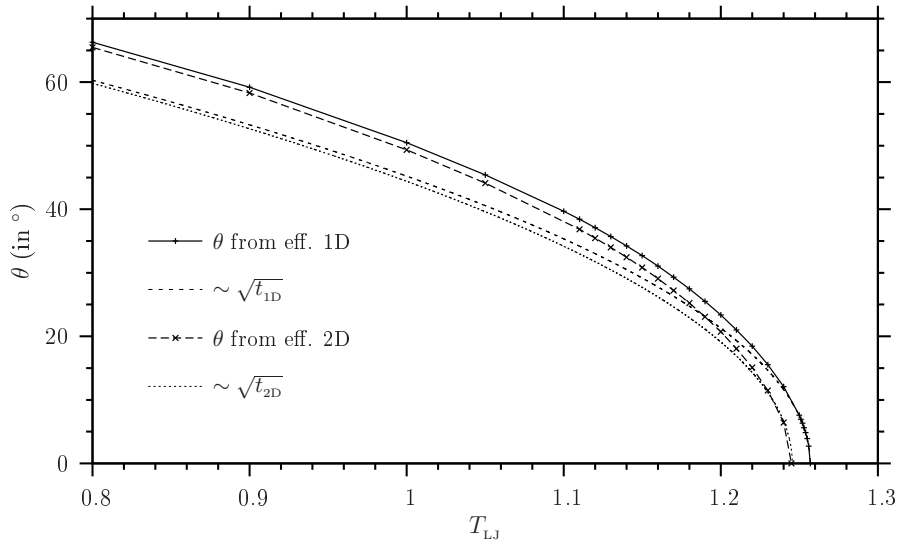

Fig. 8.12: Contact angle for a first-order wetting system due to a truncation of the fluid–fluid LJ interaction. The corresponding system with untruncated interactions would exhibit critical wetting. The calculations are performed both in effectively one and two dimensions, since the 2D profiles are employed as boundary profiles in the wedge line tension calculations. The parameters are $\varepsilon_{\mathrm{w}} = 1.36\ \varepsilon_{\mathrm{LJ}} \times 0.28798$, $b_4 = 1$ and $\mathrm{cut}_{\mathrm{LJ}} = 20$. For small contact angles the temperature dependence can be described by the characteristic square-root law, $\theta \sim \sqrt{t}$. The reduced temperature in 1D or 2D, t_{1D} or t_{2D}, refers to the wetting temperature $T_{\mathrm{LJ,w}}^{(\mathrm{1D})} \simeq 1.2569$ or $T_{\mathrm{LJ,w}}^{(\mathrm{2D})} \simeq 1.2450$, respectively. Hence the 2D wetting temperature is about 0.95 % smaller than in 1D, which is mainly due to different cut-offs in 1D and 2D.

It is an interesting question, how the line tension in this system reacts to both critical-wetting-like and first-order-wetting-like aspects. For vanishing contact angle the line tension is expected to diverge due to first-order wetting. There might be a contact angle range for which the line tension tends towards zero for decreasing θ. However, tiny contact angle values are not addressable fully microscopicly. Furthermore for finite contact angles subleading terms lead to deviations from the asymptotic curve. The system discussed in Ref. [51], for instance, exhibits the leading-order only for extremely small contact angles. Consequently there are several uncertainties in interpreting the results from the fully microscopic calculations.

The contact angle dependence of the liquid wedge line tension τ of this system is presented in Fig. 8.13. The shape of $\tau(\theta)$ is similar to typical curves for first-order wetting. No imprint of the predicted line tension behavior upon approaching critical wetting was found. Consequently, if the untruncated system exhibits the predicted behavior, it is masked by the truncation of the fluid–fluid interaction. Hence only for a very large cut-off distance a regime with $\tau \sim \theta^{1/3}$ is expected to be observable.

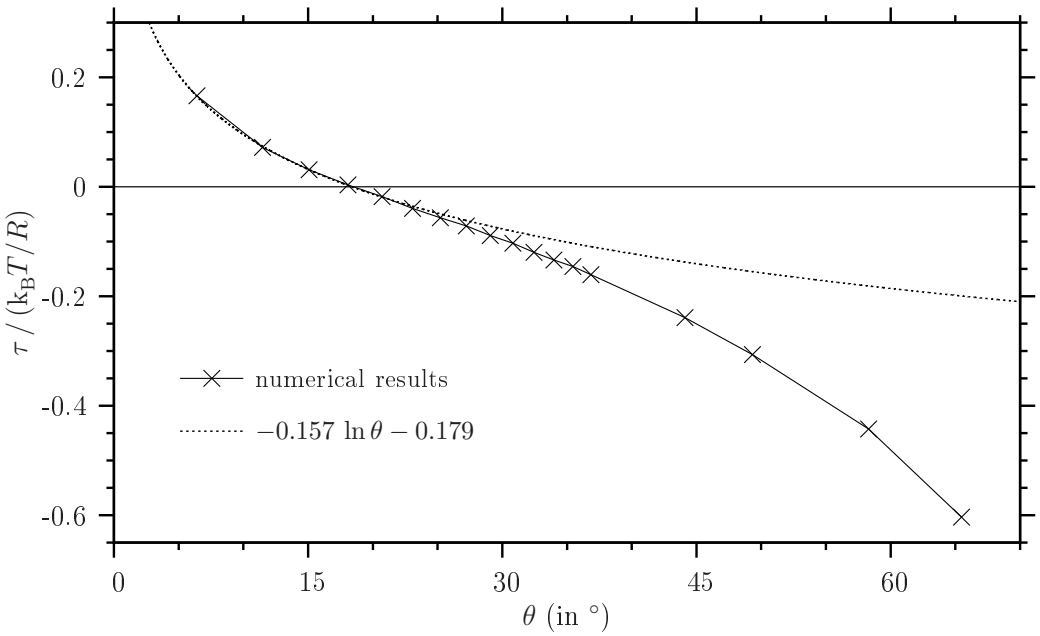

Fig. 8.13: Line tension of a liquid wedge for critical-wetting-like behavior of a WCA-LJ fluid on a LJ (9–4–3) substrate. The system undergoes a first-order wetting transition for $\theta \to 0$, however, for finite contact angle values it exhibits some characteristic features of a system approaching critical wetting. The parameters $\varepsilon_{\mathrm{w}} = 1.36\,\varepsilon_{\mathrm{LJ}} \times 0.28798$ and $b_4 = 1$ were adjusted such that merely the finite cut-off distance of 20 atomic radii prevents the system from exhibiting a critical wetting transition. For a critical wetting transition the prediction from the interface displacement model (IDM) is, that τ vanishes as $\tau \sim \theta^{1/3}$ [Eq. (1.11)]. For this system with a truncated fluid–fluid interaction, however, the line tension resembles the typical behavior near a first-order wetting transition (see Figs. 8.5 and 8.7). Note that the contact angle θ is expressed as radian measure in $\ln\theta$ and that the plane $z = 0$ is chosen as the solid–fluid dividing interface.

8.1.3 Short-ranged forces, first-order wetting

The classification as "short-ranged forces" requires short-ranged fluid–fluid and substrate–fluid interactions. A SW fluid on a cut and shifted LJ substrate potential fulfills these requests. The LJ (9–3) substrate potential is not only truncated at a cut-off distance $\mathrm{cut}_{\mathrm{ext}}$ away from the substrate surface, since the density distribution varies strongly in a small spatial region. If the discretization is chosen as $N = 15$ as usual, the density apparently jumps at a the cut-off position. This unpleasant feature is omitted by additionally shifting the truncated LJ (9–3) potential such that the substrate potential attains zero (at $z = z_{\mathrm{cut}}$) smootly. The shape of the resulting cut and shifted potential only depends on the cut-off distance. For a given cut-off the parameter ε_{w} is merely a prefactor to this potential. The shift corresponds to approximately 6.07 % of the depth of the minimum of the original LJ (9–3) potential.

Here the case of

$$z_{\mathrm{cut}}/R \;:=\; 5 \tag{8.4}$$

is studied. The range of interaction of the SW potential is 3 R throughout this study, so the solid–fluid and the fluid–fluid interaction ranges are of the same order of magnitude.

The cut and shifted LJ (9–3) potential reads

$$V_{\mathrm{ext}}^{\mathrm{cs}}(z) \;:=\; \left[V_{9-3}(z) + V_{\mathrm{shift}}\right]\, \Theta(z_{\mathrm{cut}} - z) \tag{8.5}$$

with

$$V_{\mathrm{shift}} \;:=\; \frac{2}{3}\pi\varepsilon_{\mathrm{w}} \left[\frac{2}{15}\left(\frac{2}{5}\right)^9 - \left(\frac{2}{5}\right)^3\right] \;\simeq\; 0.133968082\ \varepsilon_{\mathrm{w}}. \tag{8.6}$$

The strength of the external potential is described by the LJ energy parameter

$$\varepsilon_{\mathrm{w}} \;:=\; 1.31039/(\tfrac{64}{81}\sqrt{2})\ \varepsilon_{\mathrm{SW}} \times 0.6707. \tag{8.7}$$

The wetting temperature determined in an effectively two-dimensional (2D) calculation, $T_{\mathrm{SW,w}}^{(\mathrm{2D})} \simeq 1.30899/(\tfrac{64}{81}\sqrt{2})$, is about 0.11 % smaller than the 1D result, $T_{\mathrm{SW,w}}^{(\mathrm{1D})} \simeq 1.31039/(\tfrac{64}{81}\sqrt{2})$.

For the present system the temperature dependence of the contact angle determined in 1D and 2D calculations is shown in Fig. 8.14. The corresponding liquid wedge line tension is presented in Fig. 8.15. The calculated line tension curve is compatible with Indekeu's prediction, $\tau \simeq \tau_{\mathrm{wetting}} + c_1\,\theta\ln\theta + c_2\,\theta$, for a system with short-ranged forces close to a first-order wetting transition. For the available data and the inherent numerical errors one could not exclude a different behavior at very small contact angles, namely the predicted behavior for system with long-ranged forces upon approaching first-order wetting, $\tau \sim -\ln\theta$. However, the predicted curve for short-ranged forces fits the data slightly better [see the inset in Fig. 8.15 (b)]. Consequently there is some indication that $\tau(\theta)$ asymptotically resembles the predicted behavior for first-order wetting and short-ranged forces.

Freezing:
For $T_{\mathrm{SW}} = 0.9/(\tfrac{64}{81}\sqrt{2})$ quasi-two-dimensional freezing is observed here. Peaks in the density distribution $\varrho(x, z)$ are distributed on a triangular lattice in the xz plane. As mentioned in the related paragraph in Sec. 8.1.1.2, density peaks localized in the xz plane point to freezing in three dimensions, if the constraint of translational invariance in the y direction is lifted.

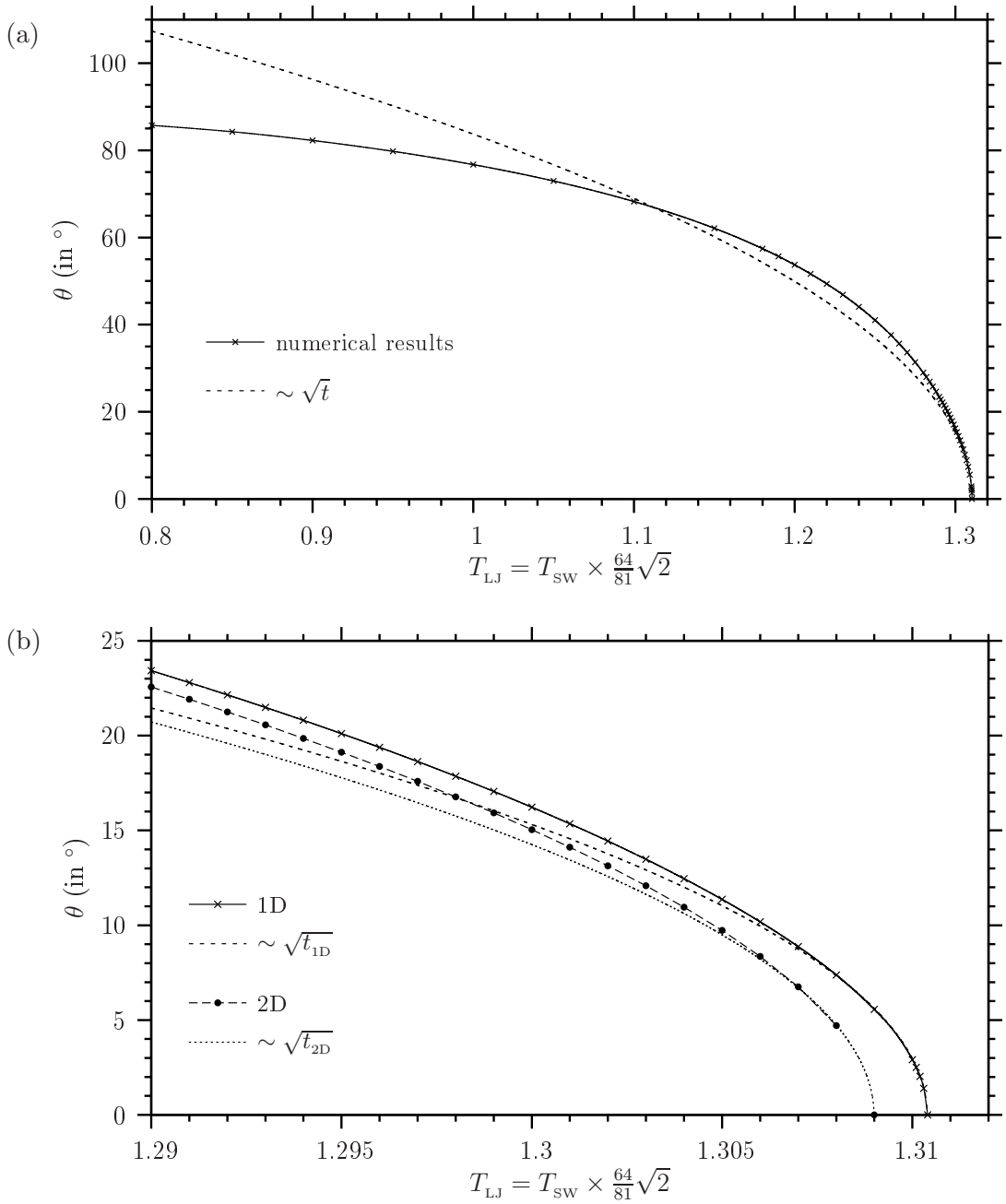

Fig. 8.14: Contact angle of a SW fluid on a cut and shifted LJ (9–3) substrate. On the scale of (a) the data from 1D or 2D calculations are almost indistinguishable. The predicted asymptotic behavior, $\theta \sim \sqrt{t}$, is found for $\theta \lesssim 10°$, and it is still a reasonable approximation up to $\theta \lesssim 75°$. In (b) the temperature regime close to wetting is resolved. The reduced temperature in 1D or 2D, t_{1D} or t_{2D}, refers to the wetting temperature $T_{LJ,w}^{(1D)} \simeq 1.31039$ or $T_{LJ,w}^{(2D)} \simeq 1.30899$, respectively. Hence the 2D wetting temperature is about 0.11 % smaller than in 1D. This tiny error arises from slightly different discretization errors in 1D and 2D.

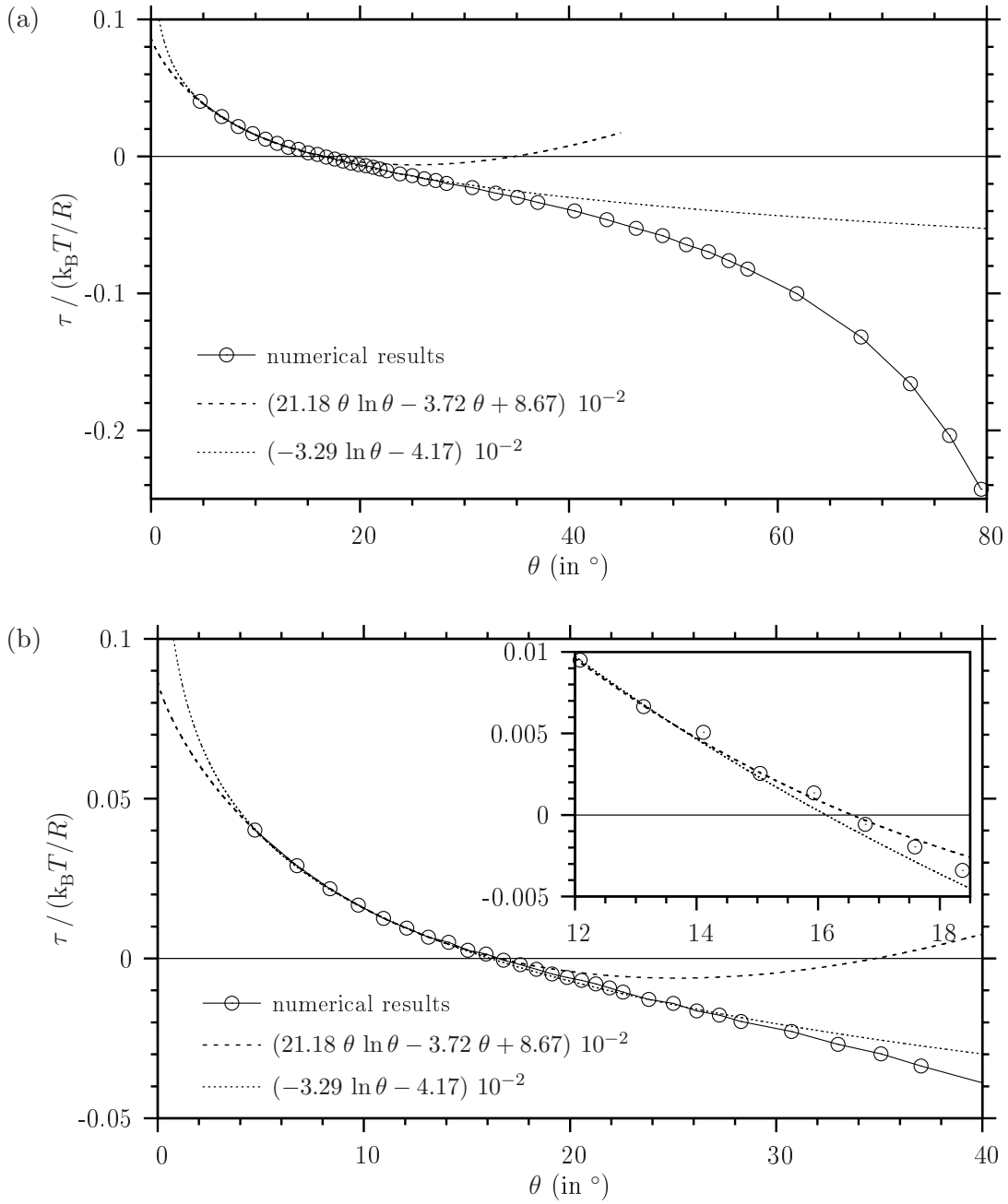

Fig. 8.15: Line tension of a liquid wedge comprising a SW fluid and a short-ranged substrate potential. A cut and shifted LJ (9–3) substrate potential is employed. The potential is defined in the main text [Eqs. (8.4) to (8.7)]. In (a) the whole addressed contact angle range up to almost 80° is displayed, whereas (b) focuses on contact angles up to 40°. The exact asymptotic behavior of the line tension could not be determined in this fully microscopic approach, particularly since the numerical errors for this system are larger than for the other considered cases. The asymptotic law predicted for such a system with short-ranged approaching a first-order wetting transition [Eq. (1.4)], $\tau \simeq \tau_{\mathrm{wetting}} + c_1\,\theta\,\ln\theta + c_2\,\theta$, fits the data in the range $4.7° \leq \theta \leq 13.5°$ as well as the predicted curve for first-order wetting with long-ranged forces, $\tau \sim -\ln\theta$. However, as shown in the inset in (b), the first fit curve describes the data slightly better than the second fit curve in the range $13.5° \leq \theta \leq 18.5°$. Note that the contact angle θ is expressed as radian measure in the fit functions and that the plane $z = 0$ is chosen as the solid–fluid dividing interface.

8.2 Comparison to sharp-kink line tension theory: tailored system

8.2.1 Rare situations accessible by both theories

The model system of a liquid wedge for a certain choice of parameter values should be accessible both by the sharp-kink and the fully microscopic approach, in order to compare the function $\tau(\theta)$ from both theories. To establish such a situation accessible by both theories turns out to be a difficult task. Particularly for the employed LJ substrate potential — including the simple (9–3) version, the (9–4–3) version and the cut and shifted (9–3) potential — no such situation was found. One typically faces the following difficulties:

First, if the parameters are chosen such that the fully microscopic approach registers a wetting transition with convenient features (like a suitable wetting temperature and moderate density oscillations in the s–g interface), then in all the situations discussed in the recent sections of this chapter the effective interface potential exhibits an "edge minimum", i. e., $l_0 = d_\mathrm{w}$. For the systems discussed in the previous sections corresponding sharp-kink contact angles even at much higher temperatures are much higher (mostly larger than 90°) than in the fully microscopic approach. Wetting either does not occur at all or extremely close to the critical point. The sharp-kink theory is out of its valid range here, since an edge minimum $l_0 = d_\mathrm{w}$ corresponds to a vanishing equilibrium film thickness, since d_w denotes the excluded volume. Sharp-kink solutions are obviously not expected to be reliable here.

Second, assume the parameters to be tuned for the sharp-kink theory such that the equilibrium film thickness l_0 is clearly larger than d_w. Thus the LJ (9–4–3) potential is very strong and comprises a rather localized and deep potential minimum near the substrate surface. In this situation the fully microscopic calculation either observes an already wet state (with a much lower wetting temperature) or local crystallization, i. e., crystal-like density peaks near the substrate surface. Even for a substrate attraction strength that is clearly below the parameter values desireable for the sharp-kink theory, the fully microscopic iteration process becomes very delicate or mostly impossible. The high density peaks tend to disable the fast Fourier transforms of the density profile at the employed discretization. The mixing parameter (see Sec. 6.2.4.1) almost vanishes, so that the computational time almost diverges.

8.2.2 Tailored substrate

Still the question remains, how the predictions from both the sharp-kink and the fully microscopic theories compare quantitatively, once a situation accessible by both theories has been established. In order to overcome the difficulties of the sharp-kink approach, namely the tendency to show an edge minimum in the effective interface potential, a substrate potential has been constructed. The system under consideration exhibits a first-order wetting transition. A WCA-LJ fluid is presumed, for which the effective interface potential $\omega_{\mathrm{WCA-LJ}}(l)$ is given by [Eqs. (7.15) and (7.50)]

$$\omega_{\mathrm{WCA-LJ}}(l) \;=\; \omega_{\mathrm{WCA-LJ,ff}}(l) + \omega_{\mathrm{WCA-LJ,ext}}(l) \tag{8.8}$$

with the contribution

$$\omega_{\mathrm{WCA-LJ,ff}}(l) \;:=\; \Delta\varrho\,\varrho_\mathrm{l}\,\left(-\pi\,\varepsilon_\mathrm{LJ}\sigma_\mathrm{LJ}^4\right)\,\left[b_2\left(\frac{l-d_\mathrm{w}}{\sigma_\mathrm{LJ}}\right)\,\Theta\Big(\sqrt[6]{2}\sigma_\mathrm{LJ}-(l-d_\mathrm{w})\Big)\right] \tag{8.9}$$

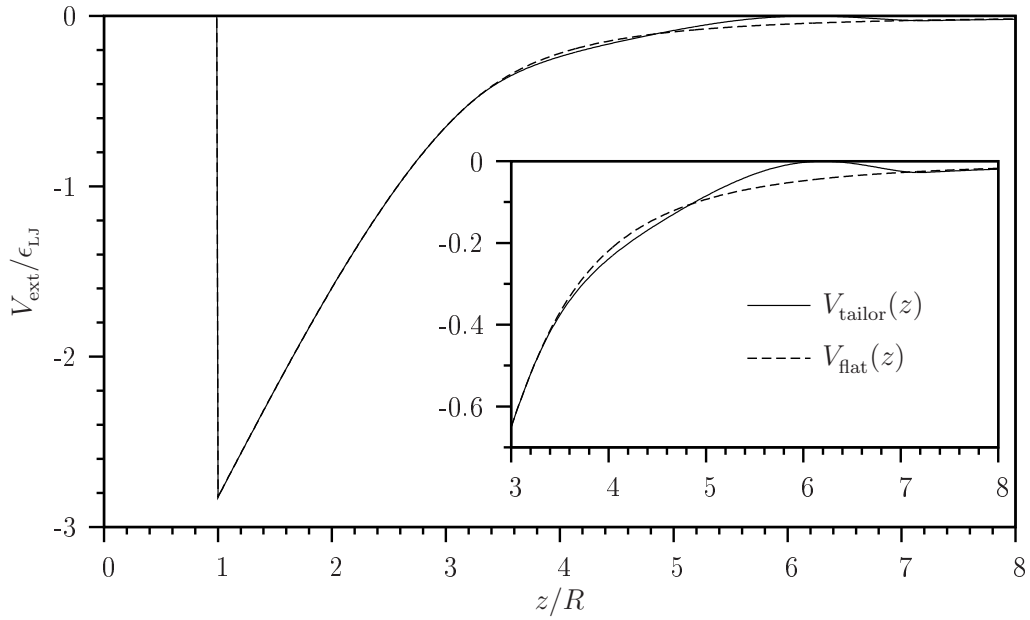

Fig. 8.16: Tailored substrate potential $V_{\rm tailor}(z)$ compared to the flatline potential $V_{\rm flat}(z)$. The main plot provides an overview in a larger spatial region, while the inset zooms into the region between $z_0 = d_{\rm w} + \sqrt[6]{2}\,\sigma_{\rm LJ} \simeq 3.245\ R$ and $z_0 + \Delta \simeq 7.245\ R$, where the modulation takes place For $z > z_0 + \Delta$ the tailored potential is $m = 1.12$ times stronger than the flatline potential. For a modulation coefficient $v = 0$ and an amplification factor $m = 1$ the tailored potential would recover the flatline potential. The tailored potential is negative for $z > R$ and almost vanishes around $z/R \simeq 6.2$.

from the fluid–fluid interaction and the contribution

$$\omega_{\rm WCA-LJ,ext}(l) \;:=\; -\,\Delta\varrho \int\limits_{z=l}^{\infty} {\rm d}z\; V_{\rm ext}(z) \tag{8.10}$$

from the substrate–fluid interaction. The auxiliary functions $b_1(s)$ and $b_2(s)$ are defined in Eqs. (7.51) and (7.52), respectively.

The constructed substrate potential $V_{\rm ext}(z) = V_{\rm tailor}(z)$ is defined as follows:

$$V_{\rm tailor}(z) \;:=\; \begin{cases} \infty & \text{for } z < d_{\rm w} \\ V_{\rm flat}(z) & \text{for } d_{\rm w} \le z \le z_0 \\ V_{\rm ref}(z) + V_{\rm mod}(z) & \text{for } z_0 < z < z_0 + \Delta \\ m \times V_{\rm flat}(z) & \text{for } z \ge z_0 + \Delta \end{cases} \tag{8.11}$$

with the abbreviation $z_0 := d_{\rm w} + \sqrt[6]{2}\,\sigma_{\rm LJ}$, an amplification factor $m := 1.12$, and a width $\Delta := 4\ R$ of the modulation region. The "flatline potential" is given as

$$V_{\rm flat}(z) \;:=\; \begin{cases} \infty & \text{for } z < d_{\rm w} \\ \pi\,\sigma_{\rm LJ}^3 \varrho_{\rm l}\big|_{T_{\rm LJ,comp}}\; b_2'\left(\frac{z-d_{\rm w}}{\sigma_{\rm LJ}}\right) & \text{for } d_{\rm w} \le z \le z_0 \\ \pi\,\sigma_{\rm LJ}^3 \varrho_{\rm l}\big|_{T_{\rm LJ,comp}}\; b_1'\left(\frac{z-d_{\rm w}}{\sigma_{\rm LJ}}\right) & \text{for } z > z_0 \end{cases} \tag{8.12}$$

with

$$b_2'(s) \;=\; -\,\frac{16}{9}\sqrt{2} + \frac{9}{5}\,2^{1/3}\;s - \frac{1}{3}\;s^3 \tag{8.13}$$

and

$$b_1'(s) \;=\; -\frac{2}{3}\,s^{-3} + \frac{4}{45}\,s^{-9}. \tag{8.14}$$

The tailored external potential $V_{\text{tailor}}(z)$ is displayed and compared to the flatline potential $V_{\text{flat}}(z)$ in Fig. 8.16. If this flatline potential was chosen as external potential, the effective interface potential would be zero for all $l \in [R, \infty)$ at the compensation temperature $T_{\text{LJ}} = T_{\text{LJ,comp}}$. Here

$$T_{\text{LJ,comp}} \;:=\; 1.385 \tag{8.15}$$

was chosen. $\varrho_{\text{l}}\big|_{T_{\text{LJ,comp}}}$ is the liquid density of a coexisting WCA-LJ liquid and gas at the compensation temperature. The reference potential

$$V_{\text{ref}}(z) \;:=\; V_{\text{flat}}(z) \times \left[\frac{m-1}{\Delta}\,(z - z_0) + 1\right] \tag{8.16}$$

interpolates smoothly between $V_{\text{flat}}(z)$ (at $z = z_0$) and $v \times V_{\text{flat}}(z)$ (at $z = z_0 + \Delta$). The flatline potential is amplified for $z \geq z_0 + \Delta$, so that the effective interface potential reaches zero for $z \to \infty$ from above at the compensation temperature (in order to create a first-order wetting scenario). The modulation potential

$$V_{\text{mod}}(z) \;:=\; v \times (z - z_0)^2\,[z - (z_0 + \Delta_1)]\,[z - (z_0 + \Delta\,)]^2 \tag{8.17}$$

with a modulation coefficient

$$v \;:=\; 3.315588 \cdot 10^{-3}\;\varepsilon_{\text{LJ}} \tag{8.18}$$

and a parameter

$$\Delta_1 \;:=\; 1.5\;R \tag{8.19}$$

is added to the reference potential in order to tune the shape of the effective interface potential. Since it is a polynomial of fifth order it remains continuously differentiable at the connection points $z = z_0$ and $z = z_0 + \Delta$. The external potential is continuous as well, however, its derivative is not perfectly continuous, since $m \neq 1$, but the effect is very small here, since $m = 1.12$ is approximately 1.

The value of the excluded zone width d_{w} can be chosen in an optimal way [Eqs. (7.2) and (7.3)]. Acccording to the obtained fully microscopic density profiles for the tailored substrate potential with $d_{\text{w}} := R$ one finds a posteriori $d_{\text{w}}/R \simeq 0.7 < 1$ as optimal choice. Since the substrate contains a hard wall contribution, only values $d_{\text{w}}/R \geq 1$ are sensible. Hence in the SK as well as the fully microscopic calculations $d_{\text{w}} = R$ was chosen.

8.2.3 Wetting behavior within the SK theory

For the tailored system the effective interface potential $\omega(l) = \omega_{\text{WCA-LJ}}(l)$ is continuously differentiable and can be calculated analytically. It exhibits a thin–thick transition and is displayed for several temperatures in Fig. 8.17.

From the effective interface potential $\omega(l)$ and the Eqs. (7.17) and (7.48) the contact angle θ is obtained as shown in Fig. 8.18. The thin–thick transition observed by means of the effective interface potential (see Fig. 8.17) is reflected in the shape of the function $\theta(T_{\text{LJ}})$: For large contact angles $\theta \gg 17.39°$ the function is similar to what one would expect for a first-order wetting transition at $T_{\text{LJ}} \simeq 1.38714$. However, at $\theta \simeq 17.39°$ the curve changes abruptly and exhibits a "cantilever-like" shape for smaller contact angles. Finally a first-order wetting transition occurs at $T_{\text{LJ,w}}^{(\text{SK})} \;\simeq\; 1.42274$.

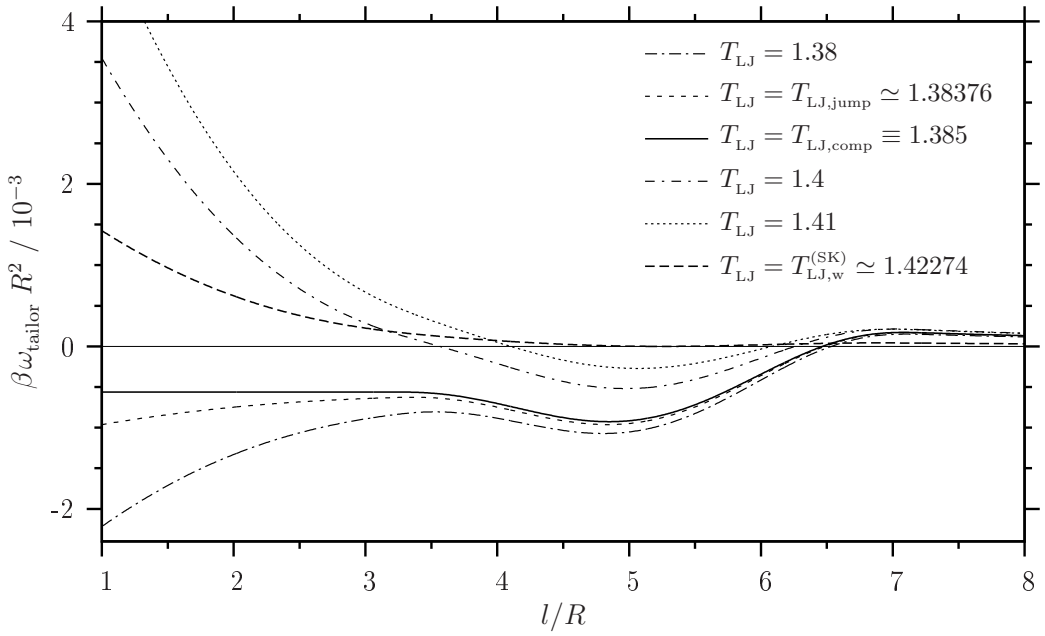

Fig. 8.17: Effective interface potential $\omega(l)$ for a WCA-LJ fluid on the tailored substrate with the solid–fluid potential $V_{\text{tailor}}(z)$. At the compensation temperature $T_{\text{LJ}} = T_{\text{LJ,comp}} \equiv 1.385$ the function $\omega(l)$ exhibits a constant value for a small film thickness l and a local and global minimum at the equilibrium film thickness $l_0^{(\text{SK})} \simeq 4.8371\ R$. On further increasing l it obtains a maximum and finally converges to zero from above. The contact angle at this temperature is $\theta(T_{\text{LJ}} = 1.385) \simeq 17.36°$. At the wetting temperature $T_{\text{LJ,w}}^{(\text{SK})} \simeq 1.42274$ the equilibrium film thickness diverges discontinuously, i. e., a first-order wetting transition occurs. A thin–thick transition occurs at $T_{\text{LJ}} = T_{\text{LJ,jump}}^{(\text{SK})} \simeq 1.38376$, since the global minimum converts discontinuously from an edge minimum at $l_0^{(\text{SK})} = d_{\text{w}}$ to a local minimum at a larger film thickness $l_0^{(\text{SK})} \simeq 4.8371\ R$. The corresponding contact angle is $\theta = \theta_{\text{jump}}^{(\text{SK})} \simeq 17.39°$.

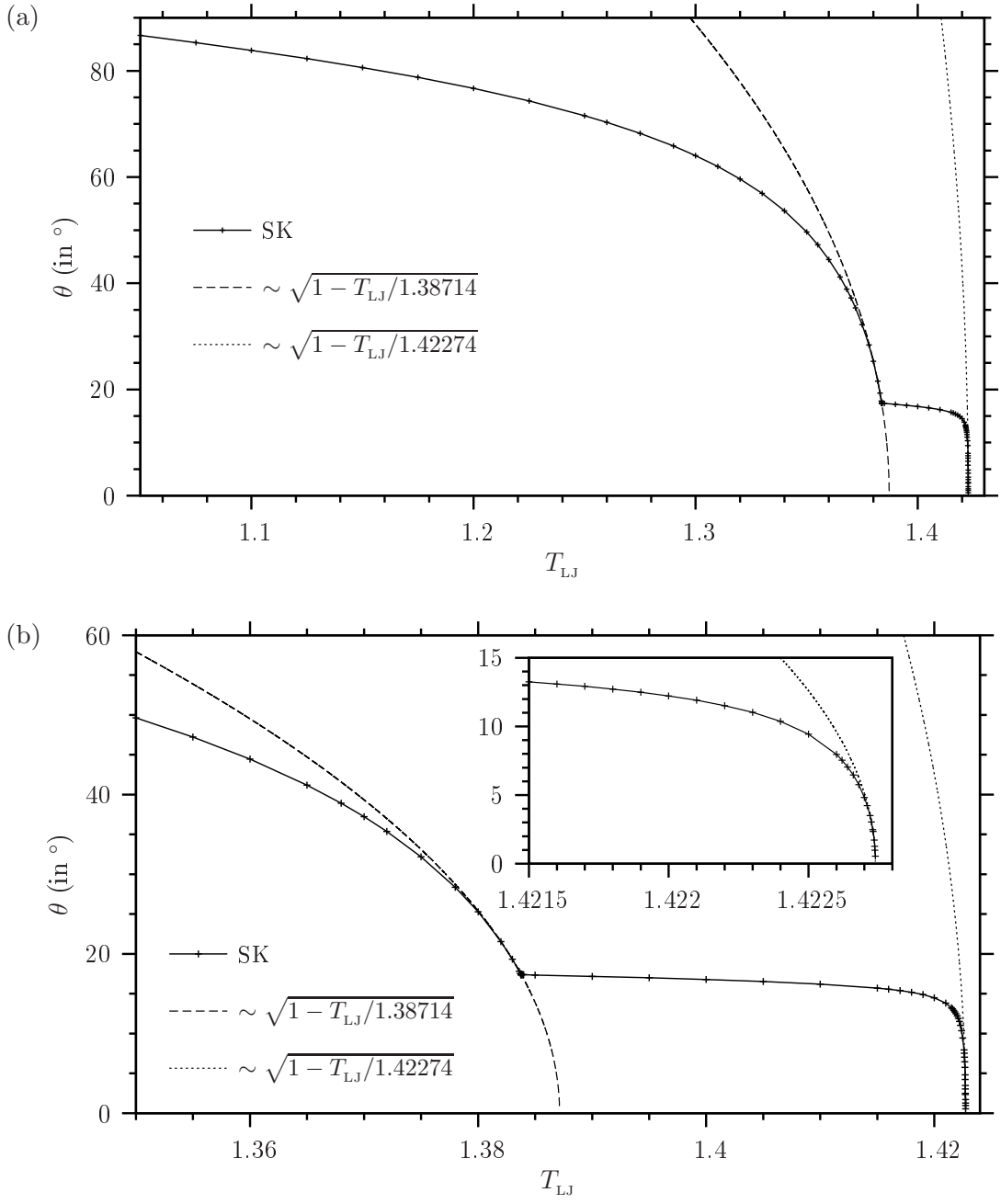

Fig. 8.18: Contact angle of a wedge formed by the liquid and gas phases of a WCA-LJ fluid in contact with the tailored substrate. In (a) an overview over a large contact angle range (up to almost 90°) is given. In (b) the thin–thick transition at $T_{\rm LJ} = T_{\rm LJ,jump}^{\rm (SK)} \simeq 1.38376$ and $\theta = \theta_{\rm jump}^{\rm (SK)} \simeq 17.39°$ is pointed out. The inset in (b) highlights the vicinity of the wetting transition at $T_{\rm LJ} = T_{\rm LJ,w}^{\rm (SK)} \simeq 1.42274$.

8.2.4 Line tension within the SK theory

The liquid wedge line tension can be obtained within the SK approach in a large contact angle range. In the local approximation $\tau_{\mathrm{i}}^{(\mathrm{loc})}$ of the line tension component τ_{i} [Eq. (7.26)] this accessible range includes very small contact angles as well [11, 51]. The line tension of a liquid wedge comprising a LJ fluid and the tailored substrate is illustrated in Fig. 8.19.

The substrate potential was tuned such that $\omega(l)$ possesses a shallow minimum and also a low maximum for $\theta < \theta_{\mathrm{jump}} \simeq 17.39°$. Hence the SK line tension attains low absolute values of the line tension for $5° \lesssim \theta \lesssim 17.39°$. For larger contact angles, $\theta_{\mathrm{jump}} < \theta \lesssim 80°$, the SK line tension is of an order of magnitude larger, $\tau \simeq -0.1 \mathrm{k_B} T/R$. This value is of the order of magnitude obtained for the other studied systems for similar contact angles (see Figs. 8.5, 8.7, 8.13, and 8.15).

The SK line tension contains four terms (see Sec. 7.3 and Sec. 7.4.2). Fig. 8.20 shows the contact angle dependence of these line tension components, whose behavior is discussed in the figure caption. The asymptotic behavior of the line tension components and the total line tension is very similar to what has been observed in a related system [51]. For $\theta > \theta_{\mathrm{jump}}$ the individual line tension components play a qualitatively different role than for small contact angles.

8.2.5 Jump of the wedge line tension at a surface phase transition

As demonstrated in the previous subsection, for the tailored system the SK wedge line tension exhibits a jump at $\theta = \theta_{\mathrm{jump}} \simeq 17.39°$ ($T_{\mathrm{LJ}} = T_{\mathrm{LJ,jump}}^{(\mathrm{SK})} \simeq 1.383756$). This jump occurs simultaneously with a surface phase transition: The equilibrium thickness of a liquid-like film in the planar substrate–gas interface discontinuously increases from $l_0/R = 1$ to approximately 4.84.

In the following it is explained why a surface phase transition in the solid–gas interface is always accompanied by a jump of the line tension of a sessile liquid wedge (cf. Sec. 8.2.5.1). Special attention is payed to the influence of the local approximation within the SK line tension theory (cf. Sec. 8.2.5.2).

8.2.5.1 Non-local theory: Jump heigth determined solely by the boundary tension

Even though the line tension jump was detected within the local theory, here at first the general case *without* the local approximation is analyzed. Hence the consideration in this subsubsection applies to the non-local SK theory, the fully microscopic theory, and the interface displacement model.

The mentioned surface phase transition from a thin to a thick liquid-like film occurs at a point in the phase diagram which is corresponding to bulk coexistence of gas and liquid below the wetting temperature. This means that it is not a prewetting scenario, where a point in the phase diagram situated off liquid–gas bulk coexistence and above the wetting temperature of a first-order wetting transition is considered.

The shape of the *contour* $l(x)$ upon approaching the surface phase transition *separates* into a thin–thick region and a thick–wedge region. This phenomenon is called *contact line wetting* [46, 169]. The distance between the thin–thick contact line and the wedge contact line diverges. This happens analogously to the divergence of the thickness of a liquid-like film in wetting. The contour $l(x)$ within the local theory and close to the surface phase transition is depicted in Fig. 8.21.

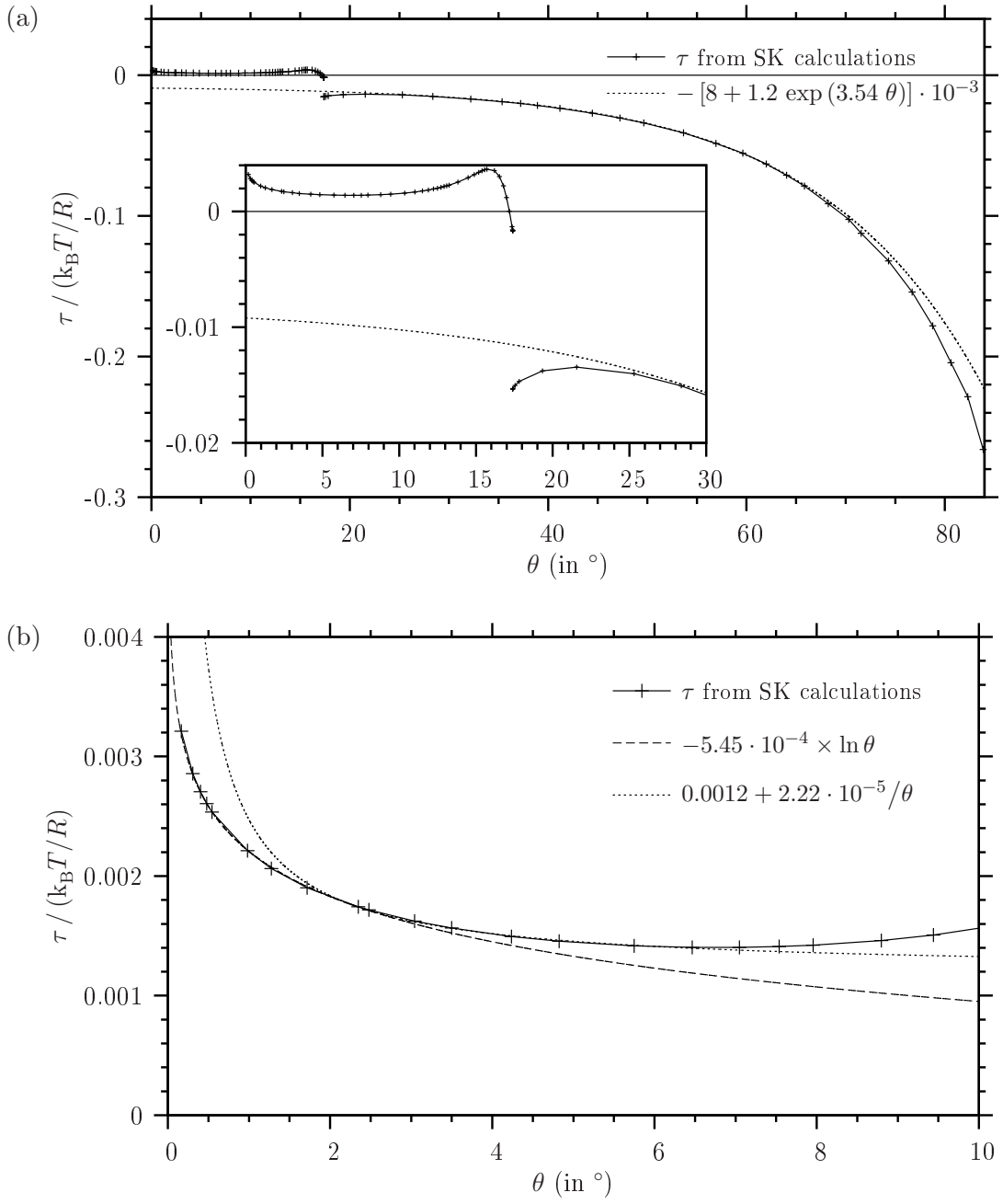

Fig. 8.19: Line tension within the SK theory. The system contains a WCA-LJ fluid (forming a liquid wedge and the coexisting gas phase) and the tailored substrate. (a) contains the whole contact angle range considered here. The jump of τ at $\theta = \theta_{\text{jump}}^{(\text{SK})} \simeq 17.39°$ reflects the qualitative change of $\omega(l)$ there, whose global minimum changes discontinuously from an edge minimum to a local minimum [see Fig. 8.17]. The upper branch of τ and the jump are highlighted in the inset. The end points of the two branches of the line tension curve correspond to physical situations which cannot coexist. Hence the grand potential and the line tension do not have to be continuous there. The line tension jump is analyzed in more detail in Sec. 8.2.5. τ can be approximated by an empirical exponential function for large θ. (b) focuses on the line tension behavior for small contact angles. In the range $2° \lesssim \theta \lesssim 6°$ the line tension behaves as $\tau \sim 1/\theta$. Such a regime has been found before in a different system [51]. For $\theta \lesssim 2.4°$ the predicted asymptotic behavior, $\tau \sim -\ln\theta$, emerges. Note that θ is expressed as radian measure in the fit functions and that the plane $z = 0$ is chosen as the solid–fluid dividing interface.

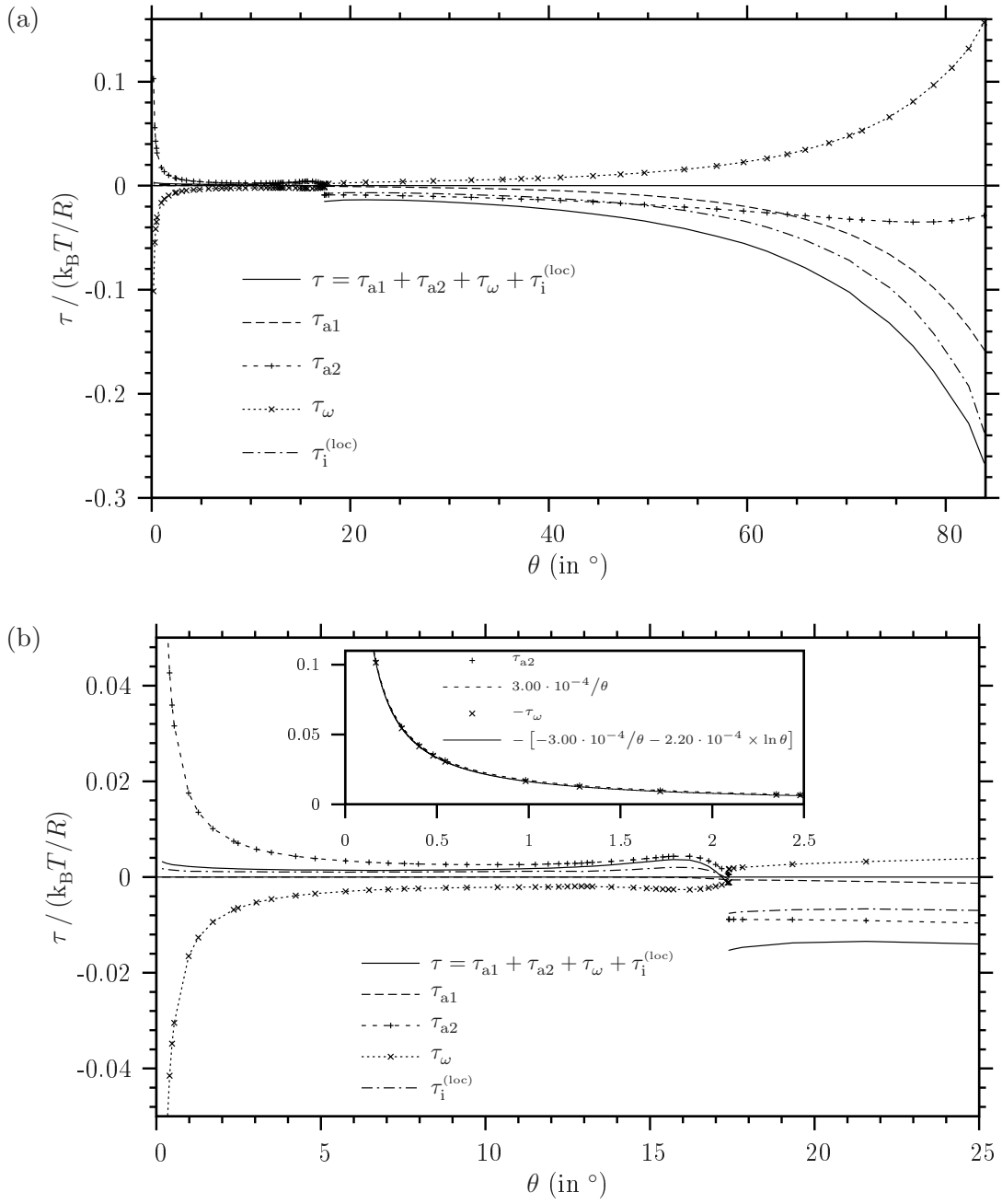

Fig. 8.20: Components of the line tension within the SK theory. The line tension from Fig. 8.19 is decomposed into its four contributions, $\tau = \tau_{a1}(\theta) + \tau_{a2}(l_0, \theta) + \tau_\omega[l(x)] + \tau_{\mathrm{i}}^{(\mathrm{loc})}[l(x)]$. (a) covers the whole addressed contact angle range, (b) magnifies the small angle regime, and the inset in (b) depicts the behavior of the two dominating terms for $\theta \to 0$. For $\theta < \theta_{\mathrm{jump}} \simeq 17.39°$ the term τ_{a1} is negligibly small. $\tau_{\mathrm{i}}^{(\mathrm{loc})}$ is positive and small, but still of the order of τ, since τ_{a2} and τ_ω almost cancel each other for $\theta \gtrsim 2°$. For very small contact angles the leading $1/\theta$-term in $\tau_{a2} + \tau_\omega$ cancels and leaves $-\ln\theta$ as leading order. At $\theta = \theta_{\mathrm{jump}}$ every component except $\tau_{\mathrm{i}}^{(\mathrm{loc})}$ changes it sign. All four terms are quantitatively important in the range $\theta > \theta_{\mathrm{jump}}$. Here τ_ω and $\tau_{\mathrm{i}}^{(\mathrm{loc})}$ possess the largest absolute values and almost cancel each other. Hence the previously neglected τ_{a1} strongly influences the line tension for large contact angles, since its prefactor $-(1 - \theta/\tan\theta) \simeq -\frac{1}{3}\,\theta^2 - \frac{1}{45}\,\theta^4$ becomes very large here. Conversely the previously important τ_{a2} is the one which contributes the least for large contact angles.

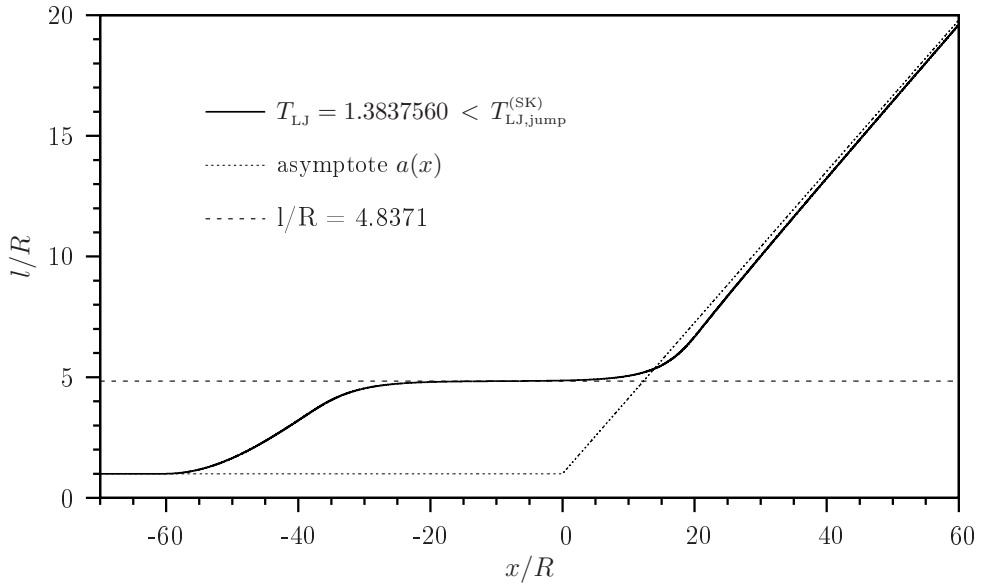

Fig. 8.21: Contact line wetting in the tailored system oberserved by the local SK line tension theory. The contour $l(x)$ of a sessile liquid wedge is displayed for a temperature slightly below the temperature of a surface phase transition, $T < T^{(\mathrm{SK})}_{\mathrm{LJ,jump}}$. In this surface phase transition the thickness of a liquid-like film in a planar substrate–gas interface jumps. For $T_{\mathrm{LJ}} \nearrow T^{(\mathrm{SK})}_{\mathrm{LJ,jump}}$ the contour separates into an interface between the two surface phases (thin–thick contact region) and a wedge involving the thick surface phase and the liquid phase (thick–wedge contact region). Hence the two surface phases and the liquid phase coexist. For a temperature above $T^{(\mathrm{SK})}_{\mathrm{LJ,jump}}$ the thin surface phase is absent, hence the thin–thick contact line is absent as well. Therefore the boundary line tension related to the thin–thick contact line does not contribute to the wedge line tension in this case. Consequently the wedge line tension values $\tau^{(\mathrm{thin})}$ and $\tau^{(\mathrm{thick})}$, which correspond to the limiting cases $T_{\mathrm{LJ}} \nearrow T^{(\mathrm{SK})}_{\mathrm{LJ,jump}}$ and $T_{\mathrm{LJ}} \searrow T^{(\mathrm{SK})}_{\mathrm{LJ,jump}}$, respectively, differ in general. Since the two situations (i. e., the thin–thick–wedge situation and the thick–wedge situation cannot exist simultaneously, the grand potential does not have to be continuous at the surface phase transition. In the present case the height of the line tension jump is given by the boundary tension and an extra term due to the local approximation [cf. Eq. (8.22)].

There are two possible conceptions of a discontinuous line tension curve, e. g., $\tau(\theta)$ or $\tau(T_{\mathrm{LJ}})$: (i) One can either consider *different* wedge line tensions, one for each surface phase in the gas part of the sessile liquid wedge. Then each line tension is continuous up to a surface phase transtion. (ii) Or one can combine these different line tensions to a *single* wedge line tension, which at a surface phase transtion exhibits a jump. Since the physical situations corresponding to the end points of the two branches of the line tension curve cannot coexist, the line tension jump is no contradiction to the requirement that different phases must have the same grand potential value in order to coexist in thermodynamic equilibrium (see Sec. 2.3.3).

The difference between the different line tension values approaching a surface phase transition is given by the boundary line tension [46, 169]:

$$\tau^{(\mathrm{thin})} = \tau^{(\mathrm{thick})} + \tau_{\mathrm{b}}^{(\mathrm{thin-thick})}. \tag{8.20}$$

Hence the line tension jump height (for decreasing contact angle, i. e., increasing temperature) reads

$$\tau^{(\mathrm{thick})} - \tau^{(\mathrm{thin})} = -\tau_{\mathrm{b}}^{(\mathrm{thin-thick})}, \tag{8.21}$$

which is negative, since the boundary tension has to be positive for stability reasons.

8.2.5.2 Local theory: Artefacts from the local approximation

Equation (8.20) should hold for a fully microscopical approach, a non-local SK approach and the interface displacement model. The *local approximation*, however, which is inherent in the performed calculations of the SK wedge line tension and the SK boundary tension, leads to an additional term in the relation between $\tau^{(\mathrm{thin})}$, $\tau^{(\mathrm{thick})}$, and $\tau_{\mathrm{b}}^{(\mathrm{thin-thick})}$:

$$\boxed{\tau^{(\mathrm{thin})} \;=\; \tau^{(\mathrm{thick})} \;+\; \tau_{\mathrm{b}}^{(\mathrm{thin-thick})} \;-\; (l_2 - l_1)\,\sigma_{\mathrm{lg}}\,\sin\theta.} \tag{8.22}$$

The boundary tension within the local theory is given as [154]

$$\tau_{\mathrm{b}}^{(\mathrm{thin-thick})} = \int_{-\infty}^{\infty} \mathrm{d}x\, \Big\{\omega\big(l(x)\big) - \omega\big(l_\infty(x)\big)\Big\} + \sigma_{\mathrm{lg}} \int_{-\infty}^{\infty} \mathrm{d}x\, \Big\{\sqrt{1+[l'(x)]^2} - 1\Big\}. \tag{8.23}$$

$l_\infty(x)$ is a step-like reference contour with $l_\infty(x) = l_1\Theta(-x) + l_2\Theta(x)$ (without loss of generality). In the local theory for the reference contour $l_\infty(x)$ the boundary tension value vanishes, $\tau_{\mathrm{b}}^{(\mathrm{thin-thick})}[l(x) = l_\infty(x)] = 0$, while it is positive within the non-local theory.

The validity of Eq. (8.22) has been checked numerically by calculating all involved quantities separately using the local approximation.

There are basically two reasons for the extra term in Eq. (8.22):
(i) the SK line tension contains the term $\tau_{a2}(l_0,\theta) \equiv \frac{1}{\tan\theta}\int_{l=l_0}^{\infty}\mathrm{d}l\;\omega(l)$, where the starting point of the integration depends on the film thickness. In general the integral value is different for different equilibrium film thicknesses l_1 and l_2. Hence $\tau_{a2}(l_0,\theta)$ for the thin and the thick surface phase differ by $\frac{1}{\tan\theta}\int_{l=l_1}^{l_2}\mathrm{d}l\;\omega(l)$. The other contribution related to the asymptote $a(x)$, $\tau_{a1}(\theta)$, remains unchanged undergoing the surface phase transition.
(ii) The wedge asymptote $a(x)$ possesses a part inclined by the contact angle θ with respect to the substrate surface, while the boundary tension within the local theory refers to deviations from a step-like asymptote $l_\infty(x)$. This gives another extra contribution to the jump heigth. These two extra terms from (i) and (ii) can be combined to the single expression $-(l_2 - l_1)\,\sigma_{\mathrm{lg}}\,\sin\theta$.

It might be possible to find a situation in which the two last terms in Eq. (8.22) cancel each other. In this case the line tension would not exhibit a jump within the local theory.

8.2.6 Wetting behavior within the fully microscopic approach

For the fully microscopic calculations a cut-off of the fluid–fluid LJ interaction is necessary, and here a cut-off of 20 atomic radii was introduced for the effectively one- and two-dimensional calculations in the way discussed in Sec. 6.1. The temperature dependence of the contact angle within the fully microscopic approach (in effectively one and two dimensions) is displayed in Fig. 8.22. Like in the SK approach a qualitative change of the function $\theta(T_{\mathrm{LJ}})$ in the vicinity of the contact angle θ_{jump} is registered. However, here an extended cross-over between the two branches occurs. In other words, the discontinuous transition predicted by the SK theory is smoothed out in the fully microscopic treatment.

Here wetting occurs at a much lower temperature than predicted by the SK theory (see Figs. 8.18 and 8.22). To some extent this difference may be due to the cut-off in the fully microscopic theory, although a cut-off of 20 atomic radii is already relatively large and the obtained results are expected to agree well with the untruncated case.

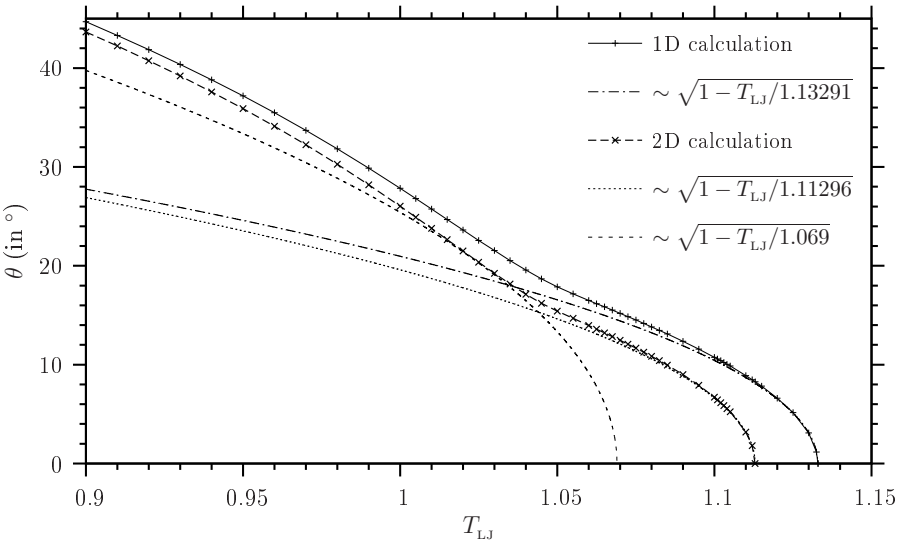

Fig. 8.22: Contact angle θ from effectively 1D and 2D fully microscopic calculations. A LJ fluid is exposed to the tailored substrate. The LJ fluid is described by means of the WCA-LJ scheme, and the fluid–fluid interaction is truncated at an interparticle distance of 20 atomic radii. The wetting temperature in 1D, $T_{\rm LJ,w}^{\rm (fm,2D)} \simeq 1.11296$, is about 1.77 % lower than in 2D, $T_{\rm LJ,w}^{\rm (fm,1D)} \simeq 1.13291$. For large contact angles, $\theta \gg 17°$, the function seems to approach a first-order wetting transition (at $T_{\rm LJ} \simeq 1.07$ for the 2D data). However, betweeen $\theta \simeq 15°$ and $\theta \simeq 20°$ the contact angle curve (for both 1D and 2D data) changes smoothly to a cantilever-like shape for smaller contact angles. In contrast to the SK results in Fig. 8.18 the transition between the two branches takes place in a cross-over region, and the cantilever-like branch is less pronounced here.

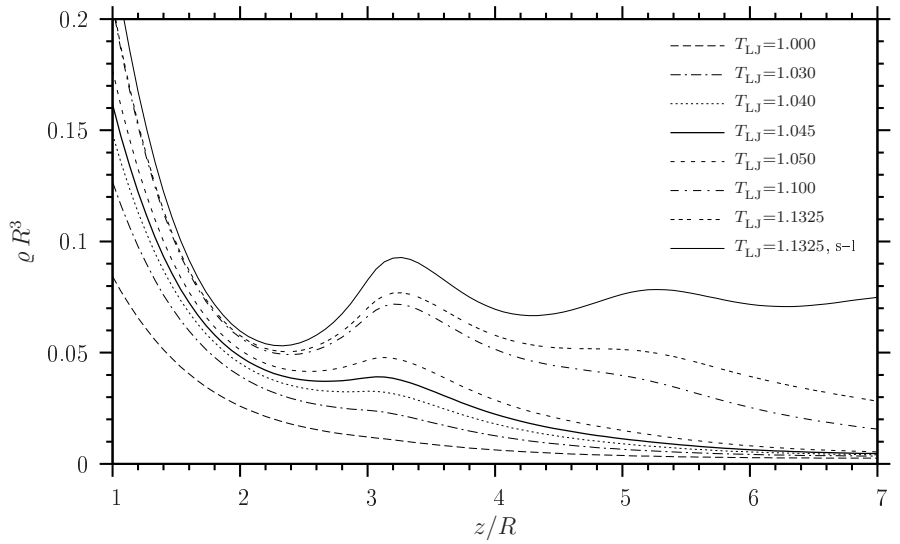

Fig. 8.23: Density profiles $\varrho(z)$ of planar interfaces between a LJ gas and the tailored substrate. Effectively one-dimensional calculations with a LJ cut-off of 20 atomic radii were performed. The last two curves correspond to a temperature slightly below the wetting temperature; the last curve represents a solid–liquid density profile. The temperature around $T_{\rm LJ} \simeq 1.045$ corresponds to the cross-over in the contact angle around $\theta \simeq 17°$ (see Fig. 8.22). In this temperature or contact angle range the particle density around $z/R \simeq 3.2$ of corresponding solid–gas interfaces increases and forms a second fluid layer (in addition to the first layer around $z = R$).

In the cross-over region of the contact angle (i. e., around $\theta \simeq 17°$) the s–g interfacial density profile $\varrho(z)$ forms a second hump near the substrate surface. In Fig. 8.23 several solid–gas interfacial profiles are plotted.

Since the solid–gas interfacial tension is rather sensitive to changes of the density profile, it is plausible that the value of σ_{sg} (and consequently the contact angle) changes considerably there. In contrast to the SK results the film thickness changes continuously here. Still it is notable that the phenomenon occurs for very similar contact angles in both approaches. That the wetting behavior is similar for both theories is very convenient for a meaningful comparison between the respective line tension behavior.

8.2.7 Line tension within the fully microscopic approach

The fully microscopic calculation of the line tension for this tailored system is presented in Fig. 8.24. At first glance the behavior of the line tension is quite anomalous compared to the SK results and the other fully microscopic results in this section: The maximum of the absolute value here is more than one order of magnitude larger than the largest value obtained in the other fully microscopic calculations. Furthermore $\tau(\theta)$ reaches a constant value for large θ and for small θ apparently tends towards a divergence to $-\infty$. The underlying substrate potential, however, is rather anomalous as well, compared to a standard LJ (9–3) or (9–4–3) potential. Moreover only a finite contact angle range is accessible: Smaller θ are numerically too demanding for the provided computational power and already for $\theta \simeq 45^\circ$ the fluid is very likely to crystallize. Thus the typical negative values for "large" values of θ (around 80 or 120°) in the other systems are not addressable here. Likewise the regime of very small contact angles is not accessible either. It is known from other systems [51] that the asymptotic behavior may become visible only for very small contact angles. Hence the line tension is nevertheless likely to diverge to $+\infty$ for $\theta \to 0$ here.

The behavior of the fully microscopic line tension is qualitatively completely different from the SK predictions. For $17^\circ \lesssim \theta \lesssim 45^\circ$ the absolute values of τ are an order of magnitude larger than for the SK approach. For $4^\circ \lesssim \theta \lesssim 17^\circ$ the absolute values of τ are roughly three orders of magnitude larger than for the SK approach. Note that these values depend on the choice of the solid–fluid dividing interface, and another choice may reduce the relative deviations. The line tension seems to reach a constant value for large contact angles, i. e., $\tau(\theta \simeq 40^\circ) \simeq -2.08\ \mathrm{k_B}T/R$. This result is in contrast to the SK prediction that the absolute value of the line tension increases in this contact angle regime.

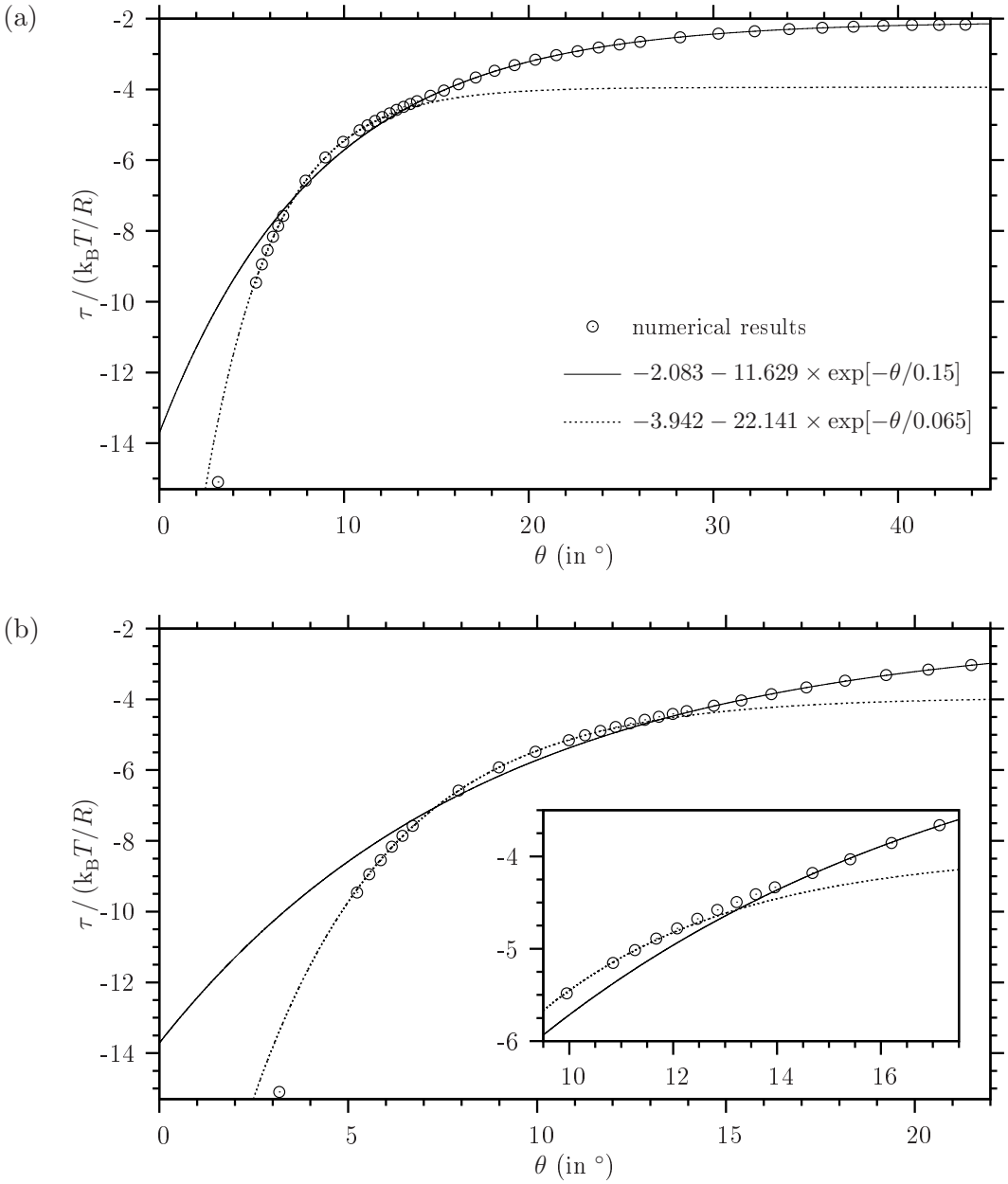

Fig. 8.24: Line tension within the fully microscopic approach for the tailored system. In (a), (b), and the inset in (b) the same three curves are displayed in different contact angle ranges. In the accessible contact angle range $4^\circ \lesssim \theta \lesssim 45^\circ$ the line tension follows two exponential functions with a cross-over at $8^\circ \lesssim \theta \lesssim 15^\circ$. It is plausible that this cross-over occurs around that contact angle where the curve $\theta\big(T_{\text{LJ}}\big)$ exhibits a cross-over as well. The data point for $\theta \simeq 3.18^\circ$ comprises a relatively large numerical error, particularly since here τ is evaluated at a stage of the iteration process which is far from convergence. Note that θ is expressed as radian measure in the fit functions and that the plane $z = 0$ is chosen as the solid–fluid dividing interface.

8.3 Hybrid theory: Sharp-kink line tension theory with an improved $\omega(l)$

As shown in the previous section, the SK line tension theory suffers already from an unreliable description of the wetting behavior through the effective interface potential $\omega(l)$. This section is dedicated to the question, whether the (local) SK line tension theory describes the fully microscopic results (i. e., the values obtained without the local density approximation, the sharp-kink approximation and the local approximation) in a better way, if an improved effective interface potential is inserted into the calculation. The details of this hybrid theory are described in Sec. 8.3.1. Thereafter in Sec. 8.3.2 this novel approach is applied to the systems from Sec. 8.1 with smooth substrate potential and moderate spatial density variations. Finally the tailored system (featuring a strongly varying substrate potential and strong density oscillations) is addressed within the hybrid method in Sec. 8.3.3.

8.3.1 Specifications of the hybrid theory

8.3.1.1 Hybrid wetting theory

The wetting behavior has to be determined first. A key quantity to describe the wetting behavior is the effective interface potential $\omega(l)$. The SK version of $\omega(l)$ is not very reliable in the region near the substrate surface, hence the wetting behavior predicted by the SK theory is not very reliable either. A fully microscopic effective interface potential can be defined as well (cf. Sec. 8.4.1). An efficient compromise between these two methods, a "hybrid theory" is proposed in the following.

In general an effective interface potential $\omega(l)$ is defined via

$$\sigma_{\mathrm{sg}}(l) \equiv \sigma_{\mathrm{sl}} + \sigma_{\mathrm{lg}} + \omega(l). \tag{8.24}$$

Since $\omega(l \to \infty) = 0$, it can be expressed as

$$\omega(l) = \sigma_{\mathrm{sg}}(l) - \sigma_{\mathrm{sg}}(l \to \infty). \tag{8.25}$$

Here a *hybrid effective interface potential* $\omega_{\mathrm{hybrid}}(l)$ is calculated with the help of hybrid solid–gas interfacial density profiles. They are established by the fully microscopic solid–liquid interfacial profile for the given parameters which is then truncated at a distance l from the substrate surface. From thereon the bulk gas density ϱ_{g} is employed.

The systematic variation of the parameter l, which corresponds to the thickness of a liquid-like layer, yields $\omega_{\mathrm{hybrid}}(l)$. The discrete values of l are chosen to be non-equidistant, since for small values of l a smaller distance between neighboring points is needed than for very large values of l. An equidistant grid of l values would unnecessarily increase the computational time enormously. At a certain temperature the fully microscopic solid–gas interfacial structure has more degrees of freedom to optimize its free energy than the hybrid density profiles. Hence for this hybrid method the solid–gas interfacial tension at a certain temperature and therefore the wetting temperature are higher than within the fully microscopic approach.

8.3.1.2 Hybrid line tension theory

A hybrid line tension τ_{hybrid} is defined here as the SK line tension value, if instead of the standard SK effective interface potential the hybrid one is employed. The above described quantity $\omega_{\text{hybrid}}(l)$ enters the hybrid line tension calculation in twofold manner: First, it is used to determine the wedge contour $l(x)$ within the hybrid approach according to Eq. (7.29). Second, the line tension components $\tau_{a2}(l_0, \theta)$ [Eq. (7.23)] and $\tau_{\omega}[l(x)]$ [Eq. (7.24)] depend on it.

In comparison to the standard SK theory the contour and the line tension integrals have to be calculated for a discrete, non-equidistant function $\omega_{\text{hybrid}}(l)$.

Note that the line tension contribution $\tau_{a1}(\theta)$ [Eq. (7.22)] refers to a SK wedge profile. If one has a "hybrid wedge profile" — consisting of a fully microscopic solid–liquid interfacial profile up to the contour $l(x)$ and bulk gas density beyond — in mind, to adopt this contribution represents an approximation.

8.3.2 Application to the potentials from Section 8.1

For each of the systems studied in Sec. 8.1 the SK theory predicts a wetting behavior which is completely different from the fully microscopic results. Therefore the SK effective interface potential, which determines the wetting behavior, is unreliable. This aspect is analyzed in more detail in Sec. 8.3.3.2

The SK wedge line tension theory suffers from this unreliable SK effective interface potential. Hence the question arises how well the hybrid line tension values describe the corresponding fully microscopic data, i. e., if an improved effective interface potential is inserted into the standard SK line tension calculation. The hybrid effective interface potential $\omega_{\text{hybrid}}(l)$ and the wedge contour $l(x)$ are obtained as described in the previous subsection.

The hybrid method is applied to the four systems (related to three wetting scenarios) studied before fully microscopically in Sec. 8.1:

8.3.2.1 Long-ranged forces, first-order wetting: (i) LJ fluid

A model system consisting of a (WCA-)LJ fluid and a LJ (9–3) substrate has been analyzed in Sec. 8.1.1.1. Both the fluid–fluid and the substrate–fluid interactions are of long range in this system, and it exhibits first-order wetting. The hybrid method applied to this system yields the wetting behavior and the line tension values illustrated in Fig. 8.25.

The *"net line tension"* $\tau/\Delta\varrho$ is considered here in order to try to subtract the effect of different wetting temperatures within the two approaches. At a certain contact angle or at a certain value of the reduced temperature t different wetting temperatures imply different gas and liquid bulk densities, ϱ_{g} and ϱ_{l}. The bulk density difference $\Delta\varrho \equiv \varrho_{\text{l}} - \varrho_{\text{g}}$ acts as a prefactor in the SK expression for the line tension [Eqs. (7.22), (7.23), (7.24), and (7.26)], since $\omega(l)$ and σ_{lg} comprise this prefactor as well [Eqs. (7.15) and (7.13)].

Indekeu's prediction $\tau \sim -\ln\theta$ for the line tension behavior on approaching a first-order wetting transition comprising long-ranged forces is recovered by the hybrid method. Note that the line tension value depends on the choice of the solid–fluid dividing interface [Eq. (6.4)]. Herefore $z = 0$ is employed throughout this work (for all three considered line tension theories).

8.3.2.2 Long-ranged forces, first-order wetting: (ii) SW fluid

A model system of a SW fluid under the influence of a LJ (9–3) substrate potential can be categorized as a system comprising long-ranged forces as well, since herefore merely one kind of interaction (here the substrate–fluid interaction) needs to be of long range. The studied system in Sec. 8.1.1.2 undergoes a first-order wettting transition.

The wetting behavior and the line tension values obtained for this system by means of the hybrid theory are displayed in Fig. 8.26.

8.3.2.3 Long-ranged forces, (almost) critical wetting

Only the finite cut-off distance required by the numerical calculation hindered the model system analyzed in Sec. 8.1.2 — a LJ fluid and a carefully tuned LJ (9–4–3) substrate potential — from exhibiting critical wetting. The temperature dependence of the excess adsorption resembles the typical behavior expected for critical wetting up to the wetting temperature, where the excess adsorption discontinuously diverges. In the contact angle dependence of the line tension the leading-order behavior expected for critical wetting could not be observed.

The hybrid wetting behavior and the hybrid line tension values for this system are shown in Fig. 8.27. Despite the small line tension jump due to a surface phase transition the hybrid line tension curve $\tau_{\mathrm{hybrid}}(\theta)$ approximates the corresponding fully microscopic curve very well. One could conjecture that the critical-wetting-like behavior is responsible for this almost quantitative agreement here: For increasing temperature the contact angle decrease (i. e., a shift of the value of the global minimum in the effective interface potential) is accompagnied by a growing film thickness (i. e., a shift of the position l_0 of the global minimum in the effective interface potential). The equilibrium film thickness l_0 strongly influences the SK/hybrid line tension value [Eq. (7.23)]. Since this film thickness growth happens very regularly also within the fully microscopic approach (see Fig. 8.11), a high degree of agreement (which is superior to the already good agreement in the other cases studied in Sec. 8.3.2) is plausible.

8.3.2.4 Short-ranged forces, first-order wetting

The wetting scenario of a system comprising solely short-ranged interactions and exhibiting a first-order wetting transtion has been addressed by a SW fluid and a cut and shifted LJ substrate potential in Sec. 8.1.3.

The temperature dependence of the contact angle and the contact angle and temperature dependence of the line tension calculated via the hybrid method for this system are depicted in Fig. 8.28.

The present system is the only analyzed case where first-order wetting comprising short-ranged forces occurs. A fit function based on Indekeu's prediction for this scenario [Eq. (1.4) and the key in Fig. 8.28 (b)] yields a better description of the hybrid line tension results than a fit based on the prediction $\tau \sim -\ln\theta$ for long-ranged forces. Even though the employed discretization of the hybrid effective interface potential creates relatively large numerical errors for small contact angles, the results support Indekeu's prediction for this short-ranged first-order wetting scenario.

8.3.2.5 Conclusion: semi-quantitative agreement

In these four cases of the previous subsubsections the hybrid method is capable to describe the fully microscopic line tension results from relatively well. The temperature dependence of the contact angle within the hybrid theory exhibits a shape that is roughly similar to the fully microscopic curve. However, the wetting temperature predicted by the hybrid approach is higher than the fully microscopic wetting temperature. In the four cases the relative deviations from the 2D fully microscopic wetting temperature are approximately $3-5\,\%$. Compared to the SK wetting temperatures, which in these cases are either absent due to drying or situated very close to the critical temperature, these deviations appear rather small. Hence the fully microscopic wetting behavior is reasonably approximated by the hybrid theory.

The deviations of the hybrid and fully microscopic curves for $\tau(\theta)$ can be described by a factor of the order of 1 for not too small contact angles and line tension values. This means that the order of magnitude of the line tension and its qualitative behavior as a function of the contact angle is predicted correctly. The typical deviations are relatively small, such that one can speak at least about a *semi-quantitative* description.

In the representation of the line tension as net line tension, $\tau/\Delta\varrho$, the shapes of the hybrid and the fully microscopic curves are very similar for not too small contact angles. The hybrid net line tension curve is situated slightly above the fully microscopic one in most cases (exception: the almost critical wetting case). This offset might be due to the approximation of the wedge asymptote line tension value by the original SK expression $\tau_{a1}(\theta)$ [Eq. (7.22)].

However, one cannot control the error of the hybrid approach for an arbitrary system with lacking fully microscopic line tension data. It is shown in the following subsection that the hybrid method fails for the tailored system, where exclusively the fully microscopic approach yields reliable results.

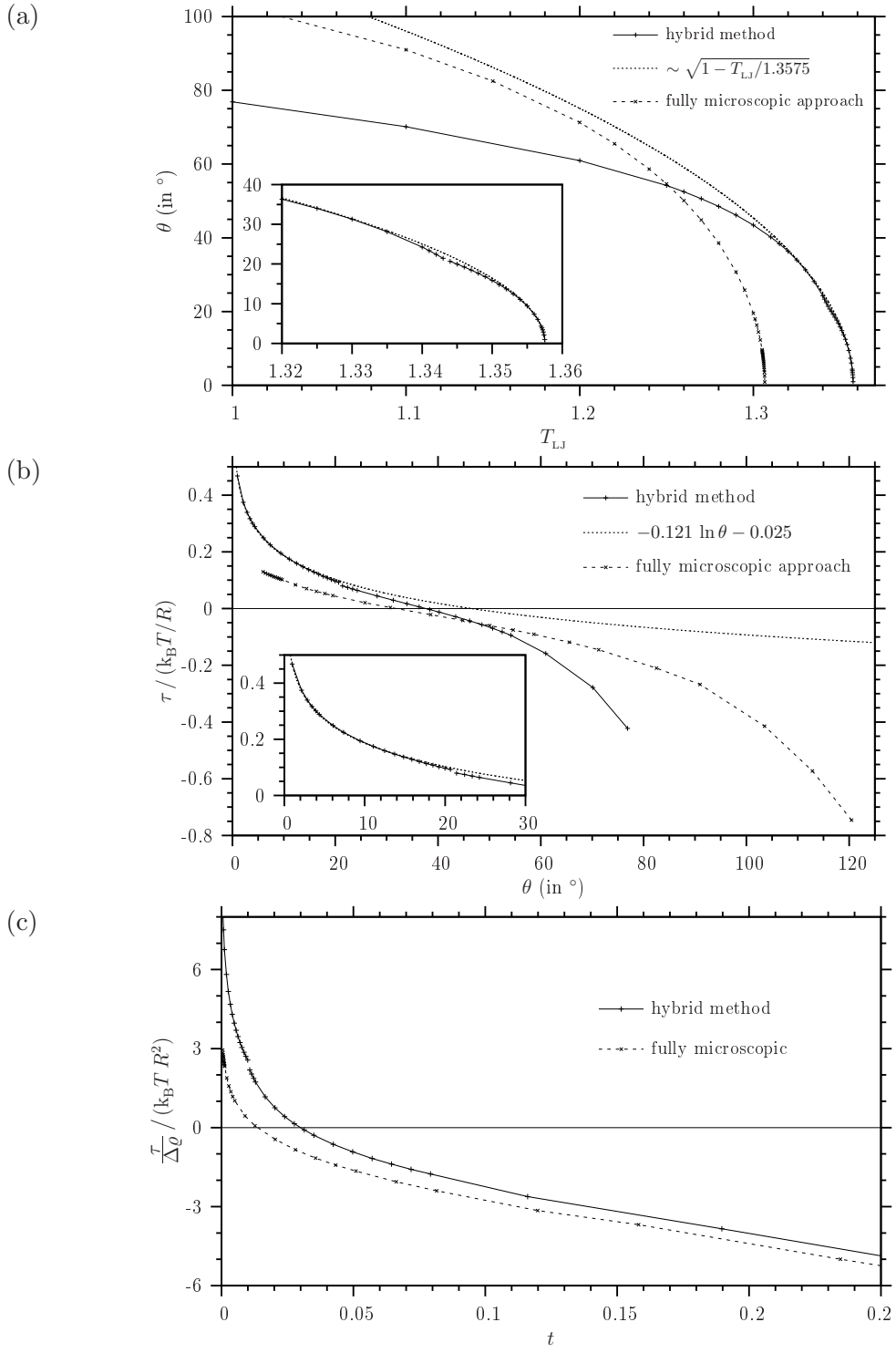

Fig. 8.25: Application of the hybrid theory to a WCA-LJ fluid on a LJ (9–3) substrate (see Sec. 8.1.1.1). In (a) the function $\theta(T_{\mathrm{LJ}})$ is shown for the hybrid and the fully microscopic theory. Within the hybrid approach the system exhibits a surface phase transtion at $\theta \simeq 21.0°$ ($T_{\mathrm{LJ}} \simeq 1.3435$), where the thickness of a liquid-like film in a planar substrate–gas interface jumps from $l_0/R \simeq 1.4$ to 2.2. According to Eq. (8.22) this transition induces a jump of the line tension value. It is accompagnied by a kink in the continuous curve $\theta(T_{\mathrm{LJ}})$. In (b) the hybrid line tension as a function of the contact angle, $\tau_{\mathrm{hybrid}}(\theta)$, is compared to the corresponding fully microscopic result. In (c) the "net line tension" $\tau/\Delta\varrho$ is plotted versus the reduced temperature $t \equiv 1 - T_{\mathrm{LJ}}/T_{\mathrm{LJ,w}}$ for the two approaches. This representation attempts to remove the effect of different wetting temperatures (see the main text). Note that the contact angle θ is expressed as radian measure in $\ln\theta$ and that the plane $z = 0$ is chosen as the solid–fluid dividing interface.

(a)

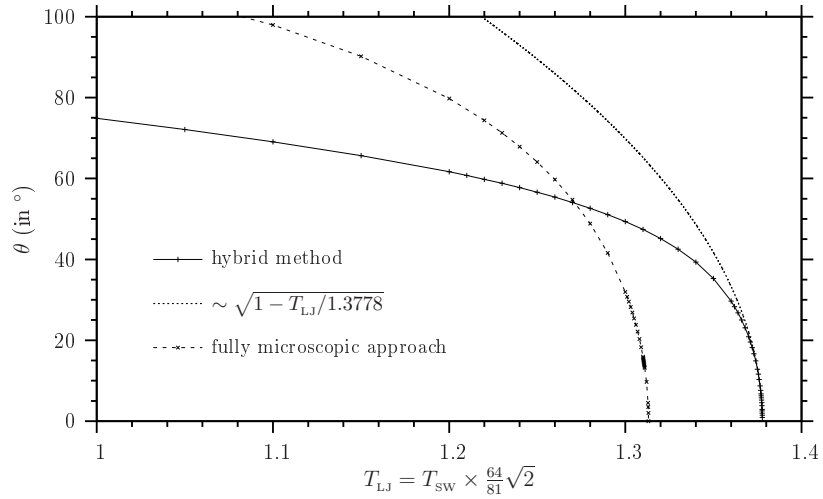

(b)

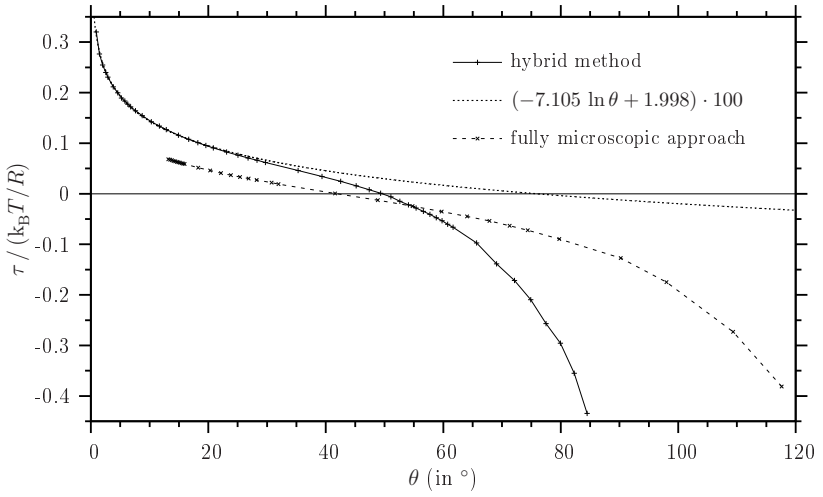

(c)

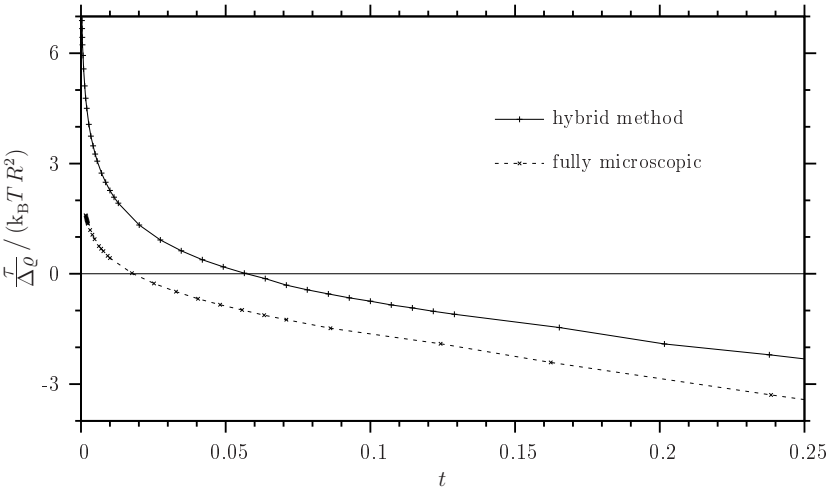

Fig. 8.26: Application of the hybrid theory to a SW fluid on a LJ (9–3) substrate (see Sec. 8.1.1.2). Analogously to Fig. 8.25 in (a), (b), and (c) the curves $\theta(T_{SW})$, $\tau(\theta)$, and $\tau/\Delta\varrho$ as a function of $t \equiv 1 - T_{SW}/T_{SW,w}$, respectively, are shown for the hybrid method and the fully microscopic approach. Note that the contact angle θ is expressed as radian measure in $\ln\theta$ and that the plane $z = 0$ is chosen as the solid–fluid dividing interface.

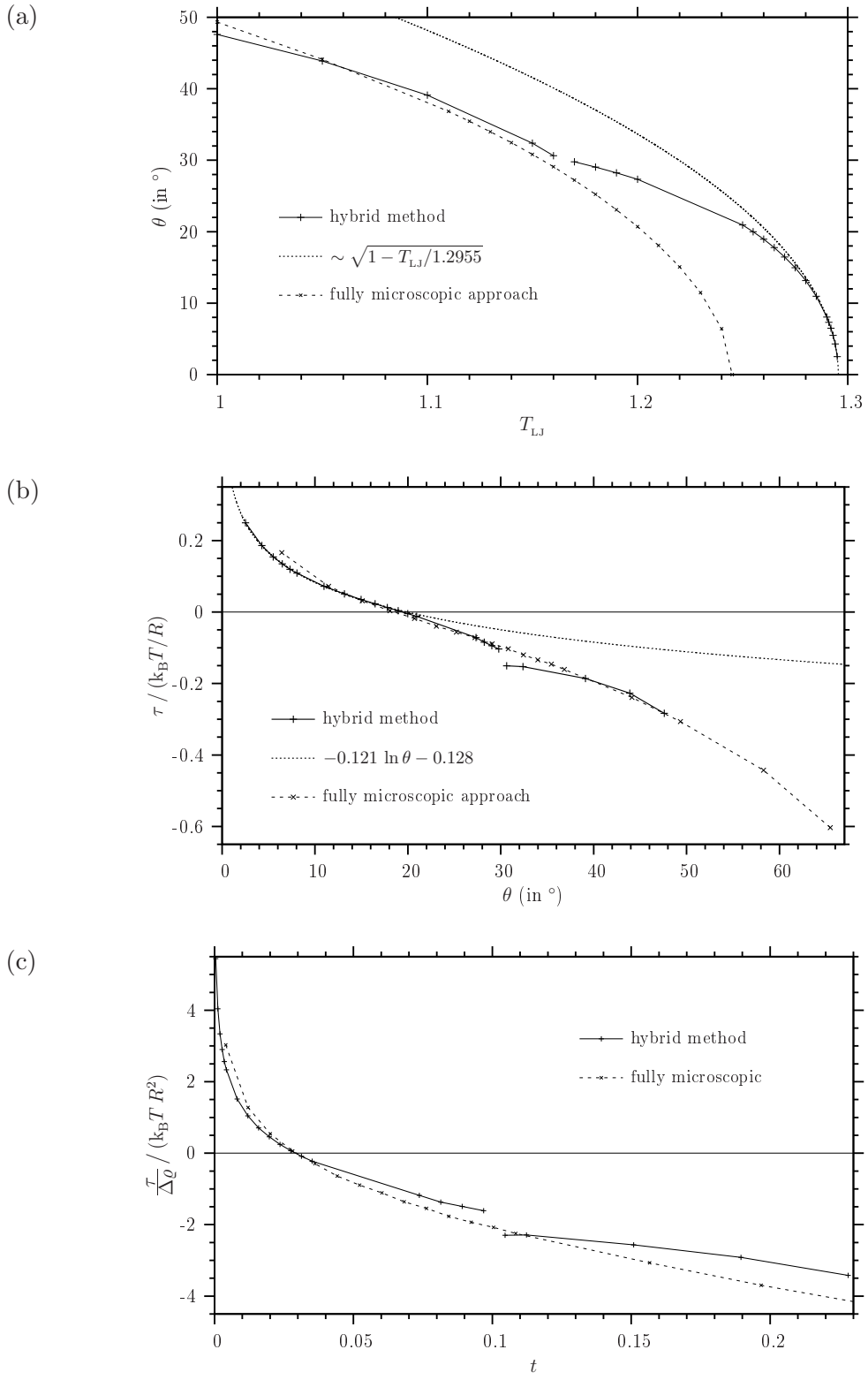

Fig. 8.27: Application of the hybrid theory to a LJ fluid on a LJ (9–4–3) substrate (see Sec. 8.1.2). Analogously to Fig. 8.25 in (a), (b), and (c) the curves $\theta(T_{\mathrm{LJ}})$, $\tau(\theta)$, and $\tau/\Delta\varrho$ as a function of $t \equiv 1 - T_{\mathrm{LJ}}/T_{\mathrm{LJ,w}}$, respectively, are shown for the hybrid method and the fully microscopic approach. Within the hybrid approach the system exhibits a surface phase transtion at $\theta \simeq 30.2°$ ($T_{\mathrm{LJ}} \simeq 1.165$), where the film thickness of a liquid-like film in a planar substrate–gas interface jumps from $l_0/R \simeq 1.2$ to 1.9. The surface phase transition induces a jump of the line tension and a kink in the continuous curve $\theta(T_{\mathrm{LJ}})$. Note that the contact angle θ is expressed as radian measure in $\ln\theta$ and that the plane $z = 0$ is chosen as the solid–fluid dividing interface.

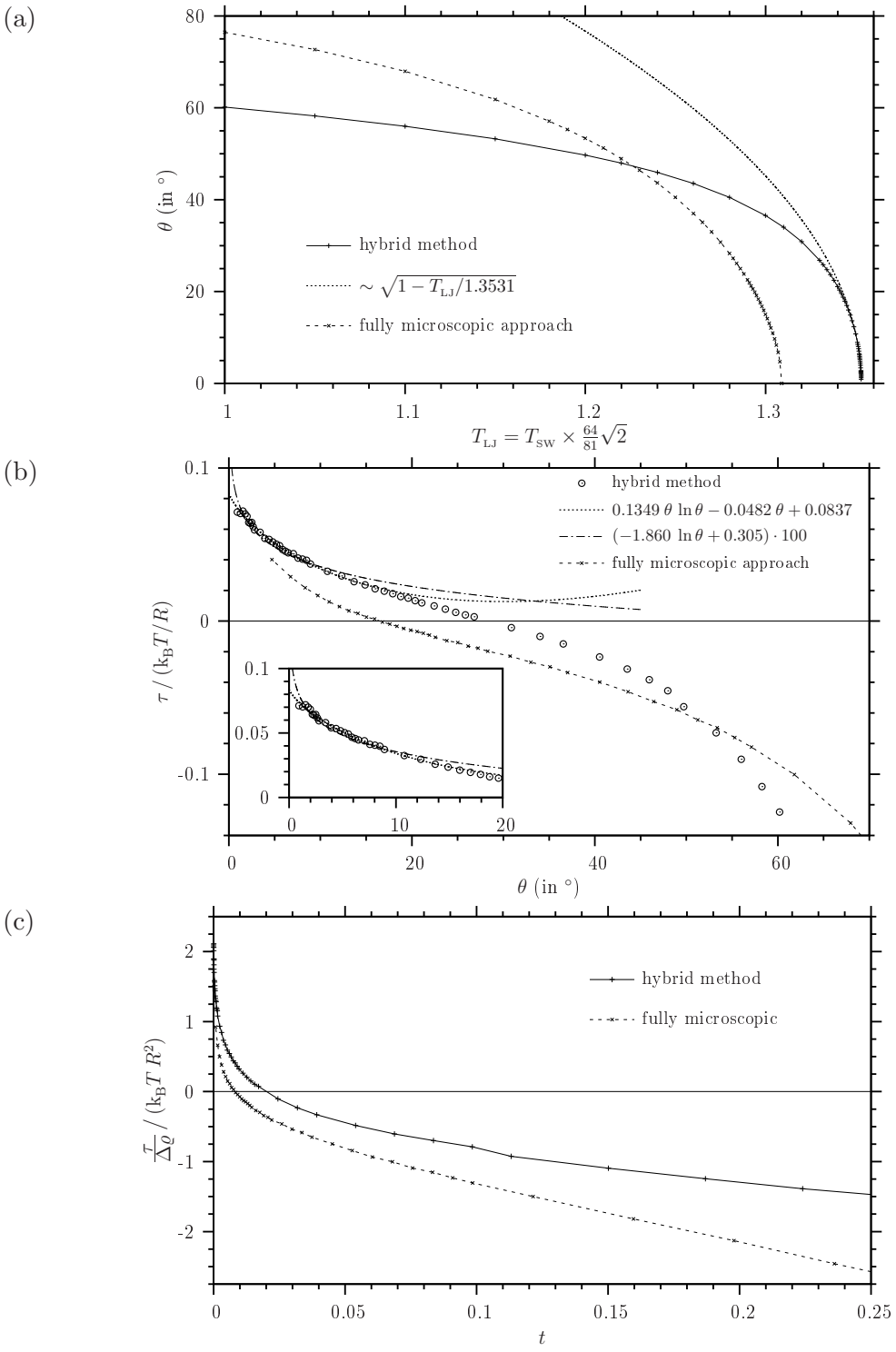

Fig. 8.28: Application of the hybrid theory to a SW fluid on a cut and shifted LJ (9–3) substrate (see Sec. 8.1.3). Analogously to Fig. 8.25 in (a), (b), and (c) the curves $\theta(T_{\rm SW})$, $\tau(\theta)$, and $\tau/\Delta\varrho$ as a function of $t \equiv 1 - T_{\rm SW}/T_{\rm SW,w}$, respectively, are shown for the hybrid method and the fully microscopic approach. At $t \simeq 0.1$ a tiny jump of the thickness of the liquid-like film in a planar solid–gas interface occurs. This film thickness jump is at the order of the grid spacing of the discretized hybrid effective interface potential. Hence the tiny line tension jump at $t \simeq 0.1$ is merely a discretization artefact. Note that θ is expressed as radian measure in the fit functions and that the plane $z = 0$ is chosen as the solid–fluid dividing interface.

8.3.3 Application to the tailored system from Section 8.2

The hybrid line tension theory is applied to the tailored system described in Sec. 8.2, i. e., a WCA-LJ fluid and the tailored substrate. The hybrid line tension values are presented in Sec. 8.3.3.1. The hybrid method helps to understand shortcomings of the SK theory in comparison to the fully microscopic approach. This is the reason why the large differences between the SK and the fully microscopic line tension values are discussed in this subsection as well, namely in Sec. 8.3.3.2. Moreover the mismatch between the hybrid and the fully microscopic line tension values is analyzed in Sec. 8.3.3.3.

8.3.3.1 Discrepancy between sharp-kink/hybrid and fully microscopic line tension values

The mismatch between the SK and the fully microscopic line tension values for the tailored system has been described in Sec. 8.2.7. This quantitative disagreement calls for a comparison to line tension results from the hybrid theory. The wetting behavior of the tailored system addressed by means of the hybrid method is described in Fig. 8.29.

The hybrid line tension as a function of the contact angle, $\tau_{\text{hybrid}}(\theta)$, is displayed in Fig. 8.30 (a) together with the corresponding SK and fully microscopic results. The hybrid line tension values are at the order of magnitude of the SK data for $\theta > \theta_{\text{jump}}^{(\text{SK})} \simeq 17.39°$.

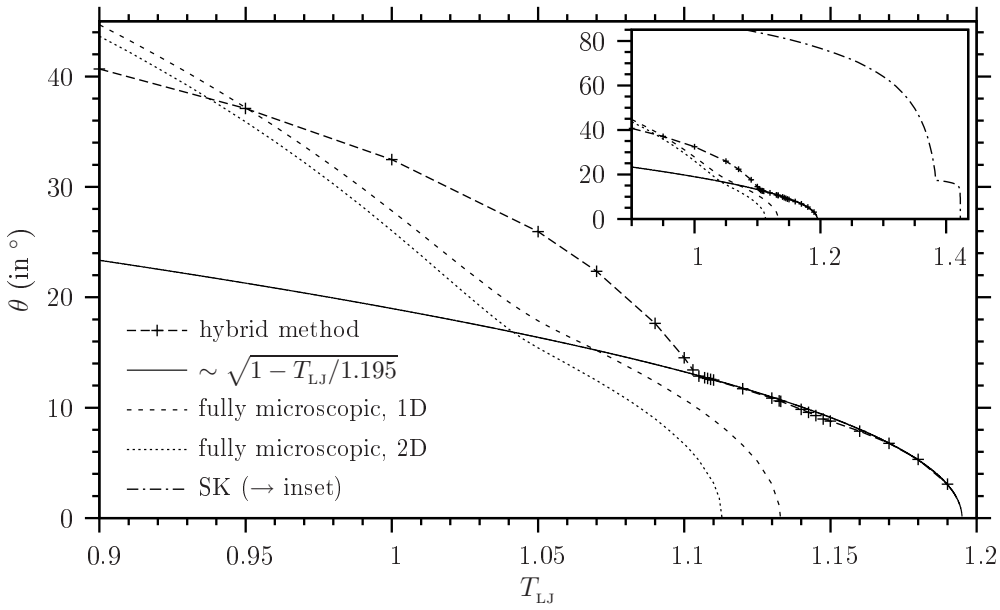

Fig. 8.29: Application of the hybrid theory to the tailored system consisting of a WCA-LJ fluid and a tailored long-ranged substrate potential (see Sec. 8.2.2). The temperature dependence of the contact angle is illustrated for the hybrid method, the fully microscopic calculations in 1D and 2D, and the SK theory. At $\theta \simeq 13.1°$ ($T_{\text{LJ}} \simeq 1.104$) and $\theta \simeq 9.1°$ ($T_{\text{LJ}} \simeq 1.146$) the thickness of the liquid-like film in a planar solid–gas interface jumps from $l_0/R \simeq 1$ to 4.2 and from $l_0/R \simeq 4.4$ to 5.6, respectively, within the hybrid theory. According to Sec. 8.2.5 each of these two surface phase transitions leads to a kink in the continuous function $\theta(T_{\text{LJ}})$ and a discontinuity of the line tension (cf. Fig. 8.30). Qualitatively the shape of the hybrid contact angle curve resembles the fully microscopic behavior. The wetting temperature $T_{\text{LJ,w}}$ within the SK approach, the hybrid method, and the fully microscopic calculation in 1D or 2D is approximately 1.4227, 1.195, 1.1329, or 1.1130, respectively. Hence the fully microscopic wetting behavior is approximated by the hybrid theory much better than by the SK theory.

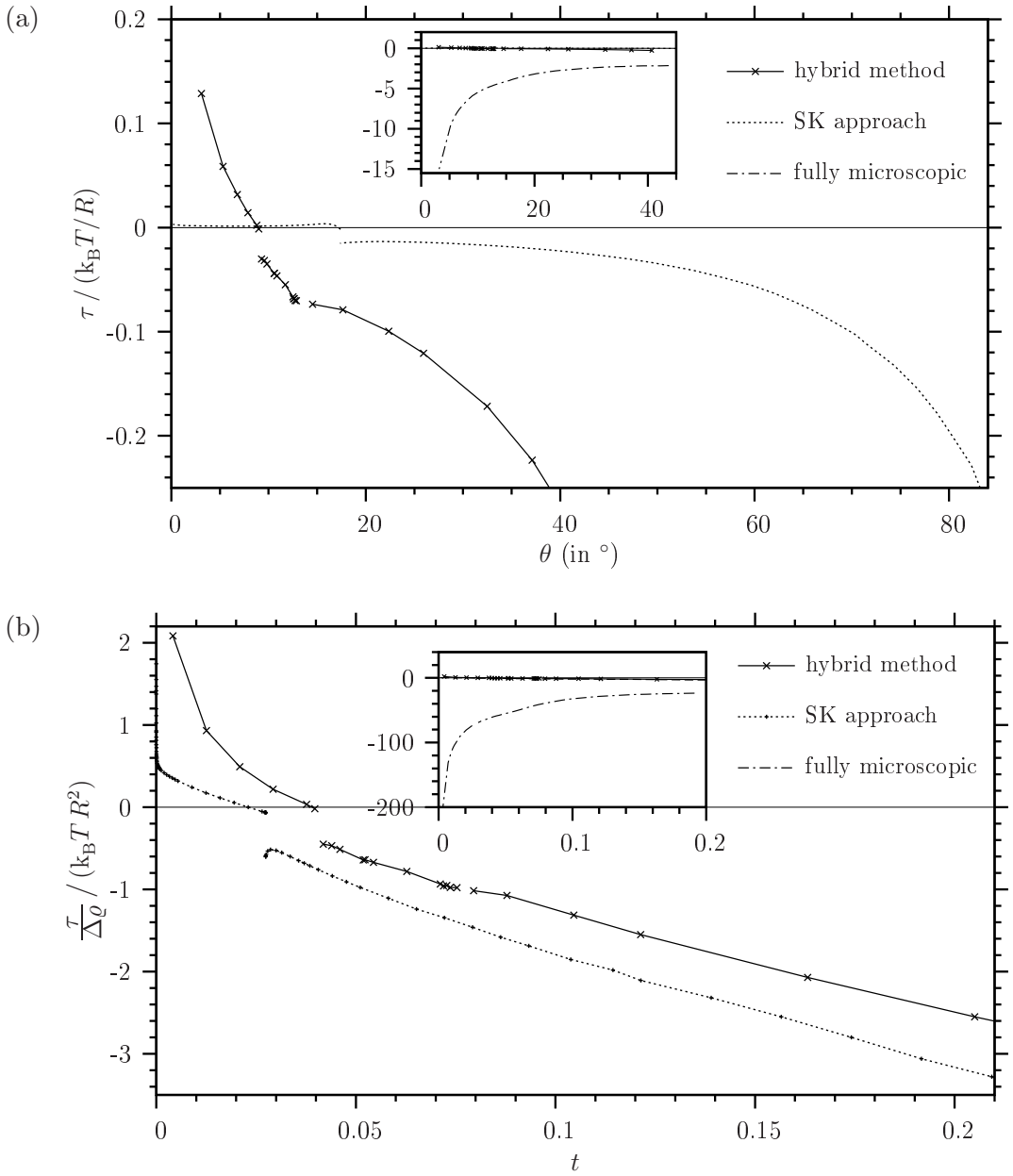

Fig. 8.30: Application of the hybrid theory to the tailored system. In (a) the contact angle dependence of the line tension, $\tau(\theta)$, within the hybrid method is compared to the results from the SK and the fully microscopic calculations. In (b) the same line tension data are presented as net line tension $\tau/\Delta\varrho$ in order to account for the different bulk liquid and gas densities at the different wetting temperatures (see Fig. 8.29). The two discontinuities of the hybrid line tension curves occur due to surface phase transitions. Note that the plane $z = 0$ is chosen as the solid–fluid dividing interface.

For smaller but not too small contact angles, i. e., for $1° \lesssim \theta \lesssim 17.39°$, the hybrid line tension grows rapidly, while the SK line tension is extremely small (by construction). For not too small contact angales the absolute values of the line tension obtained by means of the hybrid theory or the SK theory are up to two orders of magnitude smaller than the fully microscopic values. Consequently in the present case the SK theory and the hybrid method both fail to describe the order of magnitude of the fully microscopic line tension correctly.

The *net line tension* $\tau/\Delta\varrho$ as a function of the reduced temperature $t \equiv 1 - T_{\mathrm{LJ}}/T_{\mathrm{LJ,w}}$ is displayed in Fig. 8.30 (b) for the three approaches. This representation helps to extract a trivial effect of the different wetting temperatures, namely that the bulk density difference $\Delta\varrho \equiv \varrho_{\mathrm{l}} - \varrho_{\mathrm{g}}$ decreases with increasing temperature and thus leads to smaller line tension values (see the explanation in Sec. 8.3.2.1). For $t \gtrsim 1\ \%\ \theta > \theta_{\mathrm{jump}}^{(\mathrm{SK})} \simeq 17.39°$ the hybrid net line tension curve is similar to the SK net line tension curve. For the tailored system the SK wetting temperature is situated rather close to the critical point, where the bulk density difference $\Delta\varrho$ vanishes. Consequently here the effect of the prefactor $\Delta\varrho$ in the SK/hybrid line tension expressions is very strong in comparison to the cases studied in Sec. 8.3.2. Hence it is plausible that the hybrid and SK curves for the net line tension $\tau/\Delta\varrho$ are similar, even though the two curves for $\tau(\theta)$ possess rather different shapes. However, even in this net line tension representation the hybrid results are far way off from the corresponding fully microscopic curve.

8.3.3.2 Explanation of the discrepancy between SK and fully microscopic line tension values

The discrepancy between the SK and the fully microscopic line tension results for the tailored system are analyzed here, whereas the discrepancy between the hybrid and the fully microscopic line tension results are investigated in Sec. 8.3.3.3.

The SK line tension behavior is very different from the fully microscopic line tension behavior. Severe differences arise already on the level of the wetting behavior.

Explanation for the differences in wetting behavior:
The wetting temperatures within the two theories, the SK and the fully microscopic approach, are extremely different: A substrate potential has been designed carefully such that both wetting temperatures lie in the numerically accessible range. The SK wetting temperature is situated little below the critical temperature, and the fully microscopic wetting temperature lies not far above the melting temperature.

In order to pinpoint the reason for these strong deviations in the wetting behavaior, a bridge between the SK and the fully microscopic model system is built. The influence of the different approximations contained in the SK theory compared to the fully microscopic theory have to be revealed. For this purpose the hybrid model (see Sec. 8.3) is used, and furthermore a non-local SK theory is introduced.

A convenient tool to study wetting phenomena within the SK theory is the effective interface potential $\omega(l)$. It describes the grand canonical free energy per unit area which is necessary to establish a liquid-like film in a substrate–gas interface at a thickness l instead at an infinitely large distance from the substrate surface. The SK density profile used for this solid–gas interface contains the bulk liquid density for $d_{\mathrm{w}} \leq z \leq l$ and the bulk gas density for $z > l$. In the semi-microscopic SK wetting theory a local density approximation (LDA) is assumed in addition to the constraint to sharp-kink-like density distributions. This means that the non-local excess free energy density is approximated by the bulk excess free energy density for the particle density at the considered position. The LDA-SK theory represents the usual SK theory. The influence of the LDA and of the restriction to SK density distrubitions have to be dissected in order to gain more insight into the reason for the deviations described above.

1. **LDA-SK theory:**
   A first step is to include the LDA into the fully microscopic programme. This offers a helpful tool to test the lenghty analytical calculation of the effective interface potential that is related to the tailored substrate potential. The effective interface potential can be calculated by means of the fully microscopic programme by initializing a liquid-like film at a solid–gas interface and iterating zero times. The effective interface potential $\omega(l) \equiv \omega_{\mathrm{LDA-SK}}(l)$ is calcualted numerically via

   $$\omega_{\mathrm{LDA-SK}}(l) \;=\; \sigma_{\mathrm{sg}}(l) - \sigma_{\mathrm{sg}}(l \to \infty) \tag{8.26}$$

   [for details see the explanation around Eq. (8.25)].

   Clearly, the fully microscopic system is discretized (here on an effectively one-dimensional grid with N grid points per hard sphere radius R) and subject to a truncation of the fluid–fluid interaction (at a cut-off distance $\mathrm{cut}_{\mathrm{LJ}}$ in units of R). For infinitely fine grid spacing and infinitely large cut-off distance, however, the resulting effective interface potentials have to be identical. This equality is recovered numerically, as demonstrated in Fig. 8.31. Consequently the analytically obtained effective interface potential $\omega(l)$ indeed corresponds to the tailored substrate potential.

2. **FMT-SK theory:**
   A second step is to calculate the effective interface potential for a *non-local SK theory*. In order to describe the excess free energy of the hard cores of the WCA-LJ particles the FMT (see Sec. 2.2) is employed here instead of the LDA. The SK theory refered to in this work makes use of the CS EOS for the hard spheres, hence the non-local SK theory introduced here employs the White Bear version of FMT. The numerical calculation of the effective interface potential within the non-local SK theory, $\omega_{\mathrm{FMT-SK}}(l)$, is performed analogously to the calculation of $\omega_{\mathrm{LDA-SK}}(l)$. Signs that the LDA can be unreliable have been found before (see Fig. 8.9).

   As shown in Fig. 8.31, the values of $\omega_{\mathrm{LDA-SK}}(l)$ and $\omega_{\mathrm{FMT-SK}}(l)$ collapse for $l/R \geq 3$. This behavior originates from the range R of the hard-sphere weight functions: With respect to the hard-sphere free energy contribution the two steps at $z/R = 1$ and $z/R = 3$ forming the SK interfacial profile are energetically uncoupled within FMT for a distance $\geq 2\,R$ between them. However, in the region near the surface (i. e., for $l/R < 3$) there are strong deviations between the LDA-SK and the FMT-SK results. These strong deviations become meaningful, since at a certain temperature they may give rise to a different equilibrium film thickness and a different contact angle, which is related to the depth of ω at the minimum l_0. $\omega(l) = \omega_{\mathrm{LDA-SK}}(l)$ yields much smaller values than $\omega_{\mathrm{FMT-SK}}(l)$ for small l. There is a large temperature range, $1.3838 \simeq T_{\mathrm{LJ,jump}}^{(\mathrm{SK})} > T_{\mathrm{LJ}} \gtrsim 1.13$, where LDA-SK predicts an edge minimum and FMT-SK does not. For temperatures below this range also FMT-SK changes (continuously) to an edge minimum, however, the depth of the minimum is still very different for LDA-SK and FMT-SK. Altogether this finding tells that the quantities and properties based on the part of $\omega(l)$ with $l/R \lesssim 3$ are subject to artefacts from the LDA.

3. **Hybrid model:**
   The third step is to generalize the concept of an effective interface potential from SK-like density profiles to more realistic ones (i. e., similar to fully microscopic ones). In comparison to the fully microscopic treatment, which for the same functional is regarded as the correct reference, the SK approximation is relatively good for a liquid–gas interface, however, it is less purposeful for solid–fluid interfaces. Packing effects are especially important for this tailored subsrate, since it comprises a steep and narrow

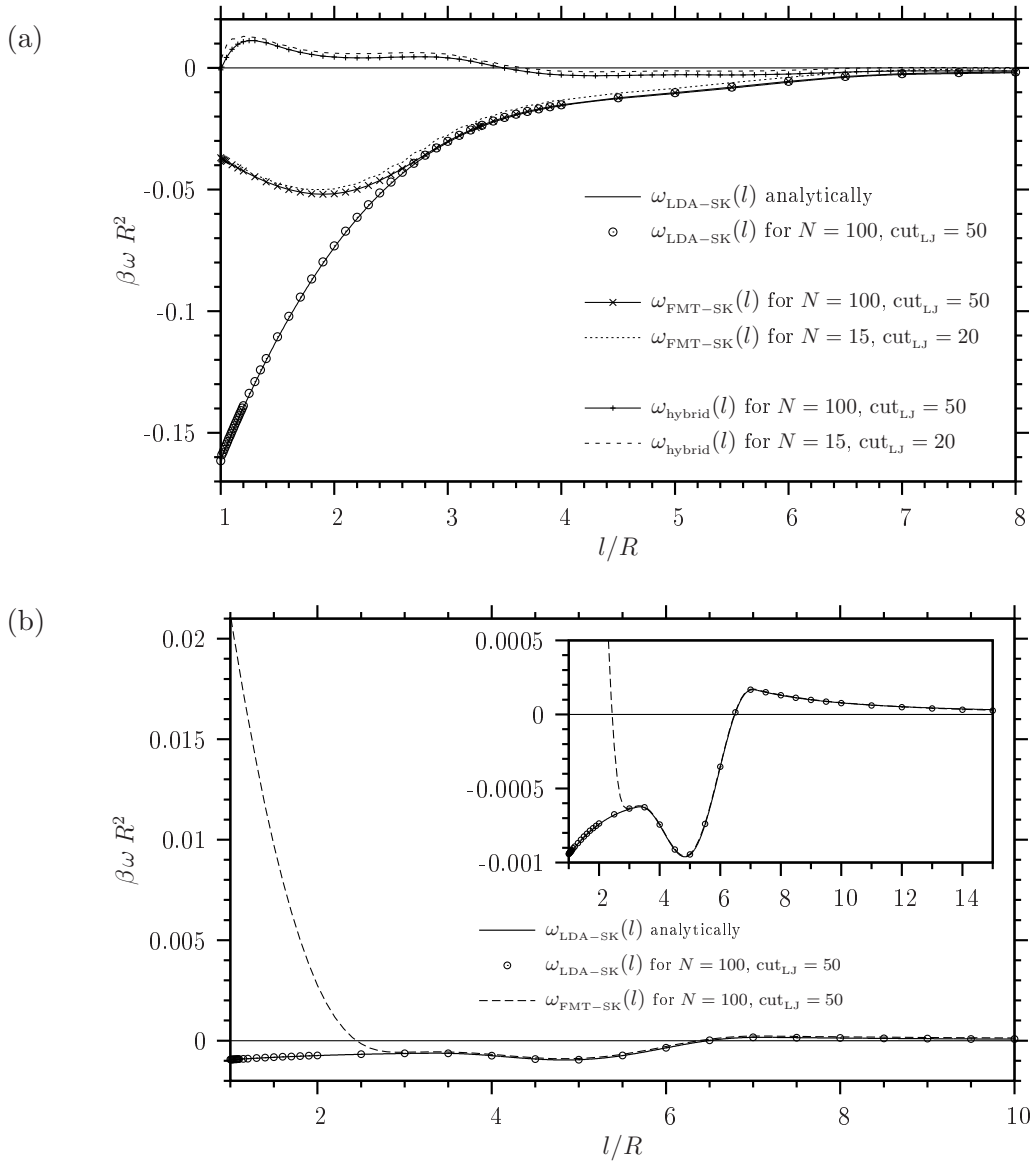

Fig. 8.31: Effective interface potentials for the tailored system within several approaches. The temperature in (a), $T_{\mathrm{LJ}} = 1.1325$, is very close to the fully microscopic wetting temperature, $T_{\mathrm{LJ,w}}^{(\mathrm{fm,1D})} \simeq 1.13291$. In (b) the temperature is $T_{\mathrm{LJ}} = 1.3838$, at which in $\omega_{\mathrm{LDA-SK}}(l)$ a jump from an edge minimum $l_0 = d_{\mathrm{w}} = R$ to a finite film thickness $l_0 \simeq 4.8371\ R$ occurs. The numerical data for the LDA-SK model match the analytically obtained function $\omega_{\mathrm{LDA-SK}}(l)$ very well. Therewith the analytical result for $\omega_{\mathrm{LDA-SK}}(l)$ is verified. $\omega_{\mathrm{FMT-SK}}(l)$ recovers $\omega_{\mathrm{LDA-SK}}(l)$ for $l/R \geq 3$. For smaller l, however, the LDA leads to large deviations from the FMT-SK curve. (b) illustrates, that these deviations may lead to different orders of magnitude of the amplitudes at a certain contact angle. The inset in (b) magnifies the minima in $\omega_{\mathrm{LDA-SK}}(l)$ and $\omega_{\mathrm{FMT-SK}}(l)$. The edge minimum in $\omega_{\mathrm{LDA-SK}}(l)$ is an artefact of the LDA. The hybrid model curve, $\omega_{\mathrm{hybrid}}(l)$, resembles the shape of the two SK curves for $l/R \gtrsim 13$. For smaller l, however, deviations between them are severe and lead to qualitatively different wetting behavior. Consequently both $\omega_{\mathrm{LDA-SK}}(l)$ and $\omega_{\mathrm{FMT-SK}}(l)$ are unreliable here for $l/R \lesssim 13$. In (a) the contact angles within the different approaches are 1.2° (fully microscopic), 9.1° (hybrid model), 53.5° (FMT-SK), and 81.8° (LDA-SK).

minimum at $z = R$, thus variations of the density near the surface should be taken into account. Hence a hybrid ansatz (see Sec. 8.3.1.1) for the employed density distribution describing the substrate–gas interface is set up: Taking the idea of a liquid-like film on

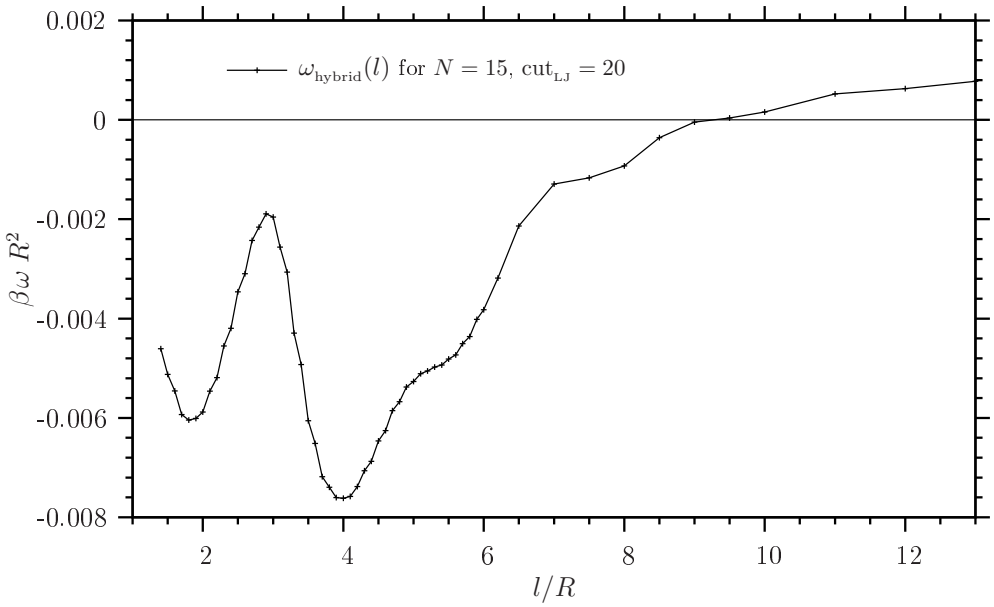

Fig. 8.32: Hybrid effective interface potential for $T_{\text{LJ}} = 1.05$, where the cross-over regime in $\theta(T_{\text{LJ}})$ within the fully microscopic approach is situated. The hybrid model illustrates the behavior of the system within the fully microscopic approach, for which an effective interface potential has not been established here. The hybrid model detects a discontinuous increase of the equilibrium film thickness, whereas the film grows continuously according to the fully microscopic calculations. Here the depth of the minimum is an order of magnitude larger than for the LDA-SK or FMT-SK model with $\theta \simeq \theta_{\text{jump}}$ [see the inset in Fig. 8.31 (b)]. These different energy scales make different orders of magnitude of the line tension results plausible.

a solid surface literally, the fully microscopic solid–liquid interfacial profile is employed up to a film thickness l, from where on the bulk gas density is used. For not too small values of l this gives a more realistic density distribution than the one from the local or non-local SK theory. In this hybrid model also the non-local treatment of the hard cores is applied. Results for the hybrid effective interface potential, $\omega_{\text{hybrid}}(l)$, are displayed and compared to corresponding LDA-SK and FMT-SK curves in Fig. 8.31.

For $l/R \gtrsim 13$ and for a certain discretization and cut-off the curves $\omega(l)$ are the same for all three models. This means that the SK approximation is reasonable for large film thicknesses, if one takes the hybrid model as the reference. However, very strong differences between the effective interface potentials of the hybrid model and the two SK theories occur in the region close to the substrate surface. Errors due to a finite grid spacing and a truncation of the fluid–fluid interaction are relatively small and do not change the curves qualitiatively. The wetting temperatures within LDA-SK and FMT-SK are equal here and very different from the wetting temperature of the hybrid model, which lies slightly above the fully microscopic wetting temperature.

Figure 8.32 contains the hybrid effective interface potential for the temperature $T_{\text{LJ}} = 1.05$, at which $\theta(T_{\text{LJ}})$ exhibits a cross-over. Also the hybrid model exhibits a double trough potential. Thus there is evidence for a transition from a very small liquid-like film to a small liquid-like film in the LDA-SK, the FMT-SK, and the hybrid model.

4. **Fully microscopic approach:**
   Compared to the hybrid ansatz the fully microscopic solid–gas interface at a certain temperature possesses further opportunities to reduce its grand canonical free energy and hence its solid–gas surface tension, which in turn decreases the contact angle. Consequently it is plausible that wetting within the fully microscopic approach occurs at slightly smaller temperature than predicted by the hybrid model.

   In the LDA-SK, FMT-SK, and hybrid approaches the transition from a very small film thickness to a small one takes place discontinuously, however, the fully microscopic results show a smooth/continuous growth of the film thickness. Hence the hybrid method is a helpful tool to understand the fully microscopic behavior, but there are still differences between results of the two approaches. Especially for a small film thickness l the hybrid ansatz is a crude approximation, so that a fully microscopic calculation is inevitable.

Consequences on the interpretation of the line tension behavior:
The SK line tension calculation performed in this study rests on liquid-like films in the solid–gas interface, whose thickness l is situated in the regime of the effective interface potential that is sensitive to both the LDA and the SK approximation. Hence differences in the wetting behavior reflect themselves in a different line tension behavior.

The SK line tension for $\theta > \theta_{\text{jump}} \simeq 17.39°$ suffers from the LDA in comparison to a non-local SK theory. This in turn exhibits a different wetting behavior than the hybrid model and the fully microscopic approach. Consequently in this regime of contact angles the discrepancy between the SK line tension values and the fully microscopic ones is (to some extent) due to *artefacts from both the LDA and the SK approximation*.

In the small contact angle regime $3° \lesssim \theta < \theta_{\text{jump}} \simeq 17.39°$ the line tension results are different as well: Here the SK line tension exhibits tiny absolute values, while the fully microscopic ones are much larger. The system was designed such that the effective interface potential for small θ exhibits *tiny amplitudes*, i. e., a shallow minimum and a low maximum. Already the effective interface potential within the non-local SK theory comprises amplitudes which are larger by an order of magnitude in this contact angle range. The whole shape of the effective interface potential enters expressions for important components of the SK line tension [Eqs. (7.23) and (7.24)]. Therefore it is plausible that also the absolute line tension values are much smaller than the fully microscopic ones.

To some extent the different orders of magnitude of the line tension within the SK or the fully microscopic approach, respectively, go back to the very *different wetting temperatures*. The wetting temperature within the SK theory is situated almost at the critical temperature, in order to leave room at lower temperatures such that the fully microscopic approach is applicable as well. For the high SK wetting temperature in this system the bulk liquid and bulk gas densities in the addressed contact angle range differ only slightly, hence the SK expressions related to $\Delta\varrho$ are relatively small. This effect contributes to the small absolute values of the SK line tension. The bulk liquid densities employed in the fully microscopic calculations are clearly larger than in the SK calculations, thus $\Delta\varrho$ is larger here as well. Moreover packing effects at the substrate surface are more pronounced for the large bulk liquid densities and contribute to the deviations from the SK results. The *"net line tension"* $\tau/\Delta\varrho$ tries to subtract the effect of different bulk liquid and gas densities (see Sec. 8.3.2). According to Fig. 8.30 (b), however, even in this representation the discrepancy between the SK and the fully microscopic line tension values persists.

The wetting behavior on a planar, homogeneous substrate refers to an effectively one-dimensional system. The fully microscopic calculation of the line tension of a sessile liquid wedge, however, forms an effectively *two-dimensional* system. Since the density in the three-phase contact region changes considerably in both the vertical and the lateral direction, it is intuitively clear that the LDA and the SK approximation affects the line tension value even to larger extent than they influence the wetting behavior.

Line tension behavior for large contact angles:
The line tension $\tau(\theta)$ for large θ decreases rapidly within the SK appraoch and tends to a constant value within the fully microscopic approach.

For $\theta > \theta_{\mathrm{jump}}$ the contour $l(x)$ from the SK theory is qualitatively different from the regime of smaller contact angle values, since the global minimum of the effective interface potential jumps discontinuously from a local minimum to an edge minimum. The typical contour near first-order wetting exhibits a contact line shifted towards the liquid region (i. e., towards larger x values). This expected behavior is indeed observed for $\theta < \theta_{\mathrm{jump}}$. However, for $\theta > \theta_{\mathrm{jump}}$ the contour changes to a smoother shape with $\delta l(x) \equiv l(x) - a(x) > 0$ for all x. Such a contour is characteristic for a system near critical wetting. For this reason and due to the reasons described in the analysis of the wetting behavior above this outcome can be regarded as an *artefact from the edge minimum*, for which the SK theory is not valid.

$\tau_{\mathrm{i}}^{(\mathrm{loc})}$ is very small and positive for $\theta < \theta_{\mathrm{jump}}$, however, it jumps to a negative value at $\theta < \theta_{\mathrm{jump}}$ and is responsible for the large negative values of the SK line tension for large contact angles. Since the magnitude (and the sign) of this term are regarded as an artefact of the edge minimum as well, one could tentatively neglect it. Then the SK line tension approximated that way varies only little (down to $\tau \simeq -0.036\ \mathrm{k_B}T/R$ instead of $\tau \simeq -0.2\ \mathrm{k_B}T/R$ for $\theta = 80°$). In the range $17° \lesssim \theta \lesssim 45°$ this curve is almost constant and hence can be reconciled with the qualitative behavior of the fully microscopic line tension there.

Asymptotic line tension behavior:
The SK line tension exhibits unusual behavior in the regime of small contact angles: Starting at a contact angle $\theta = 17°$ and decreasing it, the SK line tension decreases, attains a minimum at $\theta \simeq 6°$ and rises again until it finally diverges to $+\infty$ according to the general prediction. Very small contact angle values are necessary in order to observe a considerable increase of the SK line tension, i. e., its asymptotic behavior. Since the SK line tension forms the positive trend only for very small contact angle values, it is possible that for $\theta \lesssim 4°$ the fully microscopic line tension exhibits such a *reversal* towards $+\infty$ as well.

8.3.3.3 Explanation of the discrepancy between hybrid and fully microscopic line tension values

The hybrid wetting and line tension theory describes the fully microscopic wetting and line tension behavior for the potentials from Sec. 8.3.2 semi-quantitatively. While the wetting behavior of the tailored system is described fairly well by the hybrid method, this approach fails to predict the line tension values for this system by orders of magnitude.

Within the hybrid method the effective interface potential is calculated by introducing a step-like cross-over from a fully microscopic solid–liquid interfacial structure to bulk gas density. "Hybrid line tension theory" then means to insert this hybrid effective interface potential into the standard SK line tension theory. If one takes the idea of the hybrid method serious, the "hybrid density profile" corresponding to the wedge contour $l(x)$ consists of a fully microscopic, planar solid–liquid interfacial profile which is cut at $a(x)$ and a bulk gas density beyond this asymptote, i. e., $\varrho\big(x, z > a(x)\big) = \varrho_{\mathrm{g}}$. The line tension contribution τ_{a1} is small for not too small contact angles and is adopted (as an approximation) from the standard SK theory. For not too small contact angles the SK line tension (and at least its order of magnitude) can be approximated well by the SK line tension for the wedge asymptote. Hence only the hybrid wedge asymptote line tension $\tau[a(x)]$ is addressed in the following.

One can compare the hybrid asymptote line tension values (calculated by means of the SK line tension theory and the hybrid effective interface potential) to the fully microscopic line tension values of hybrid asymptote density profiles. This means that the density array is initialized with the hybrid asymptote profile and then (without any iterations) the asymptote line tension can be extracted. In the fully microscopic calculation relatively large discretization errors occur. The origin of these are the strong density variations at $a(x)$, where the density profile $\varrho(x, z)$ resembles a cliff line. Fortunately an analysis of the discretization effect allows to estimate the limit of perfect discretization, i. e., $N \to \infty$. Furthermore errors due to the cut-off of the fluid–fluid interaction occur, which are small here compared to the discretization errors. As illustrated in Fig. 8.33, for a certain temperature, $T_{\mathrm{LJ}} = 1.0$, a factor of approximately three was found between the hybrid asymptote line tension value and the corresponding fully microscopic value. This shows that for the asymptote the hybrid method is not a very good description. However, at least the order of magnitude is predicted correctly.

Another question is, whether the above asumption $\tau[l(x)] \simeq \tau[a(x)]$ also holds fully microscopically. In order to answer this, the Picard iteration process is started for the hybrid asymptote density profile as the initial configuration. With a small mixing parameter $\alpha = 0.1$ the line tension value decreases dramatically within the first few iteration steps, see Fig. 8.34. Already after 10 iteration steps the final order of magnitude is reached. This order of magnitude is the order of magnitude of the fully microscopic line tension values (which were calculated at the identical temperature for a slightly different contact angle). This procedure shows that lifting the constraint to optimize the density profile is responsible for the final order of magnitude of the fully microscopic line tension values. Since the SK liquid–gas interfacial tension is not very different from the corresponding fully microscopic value, the gain in energy through this optimization is most likely due to *lateral smoothing* in the very vicinity of the contact line.

Hence for the tailored system the hybrid line tension theory — no matter whether merely for the asymptote $a(x)$ or for the full contour profile $l(x)$ — represents an insufficient description of the corresponding fully microscopic results.

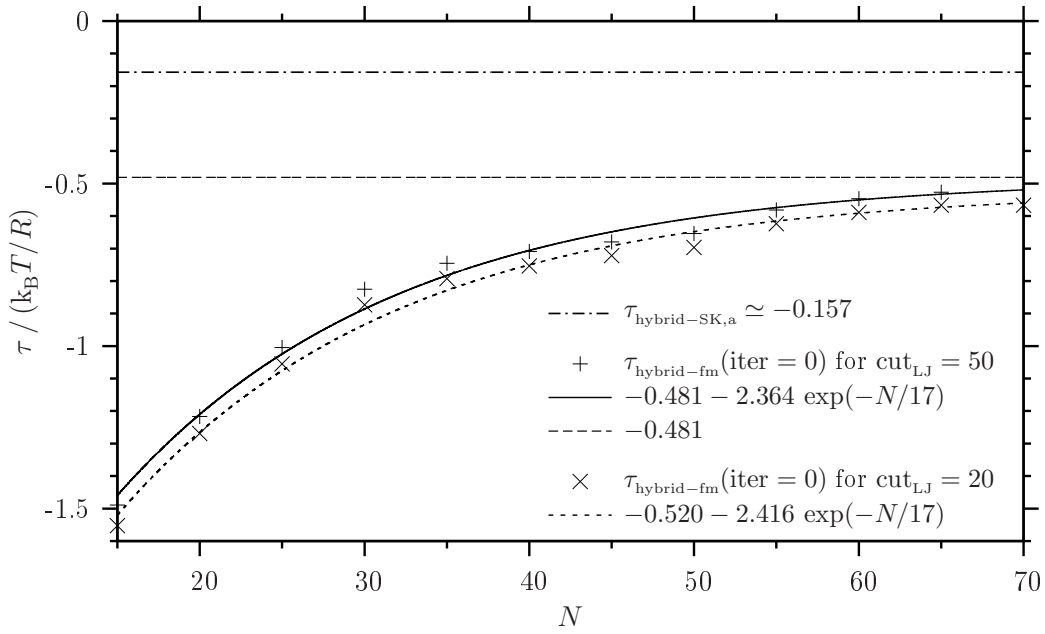

Fig. 8.33: The line tension of the wedge contour asymptote $a(x)$ is studied within the hybrid method and by inserting a hybrid density profile into the fully microscopic program and calculating the line tension without any iterations. Due to the sharp liquid–gas interface of the hybrid approach the discretization errors are large, whereas the errors due to a finite cut-off distance are comparably small. The "hybrid-fm" line tension is plotted versus the discretization parameter N for two cut-off distances ($\mathrm{cut_{LJ}} = 20$ and 50). An exponential fit allows to read off the limiting value for $N \to \infty$ and $\mathrm{cut_{LJ}} \to \infty$ as namely $\tau_{\mathrm{hybrid-fm}}(\mathrm{iter}=0) \simeq -0.48$, which is approximately three times as large as the prediction from the hybrid(-SK) theory. Note that the plane $z = 0$ is chosen as the solid–fluid dividing interface.

As a thumb rule for the quality of the hybrid method one could propose that this approach is able to describe the behavior of the line tension semi-quantitatively, if the substrate potential is slowly varying with one distinct minimum and does not cause very large spatial oscillations in the effectively one-dimensional solid–liquid density profiles. In this sense the tailored system is an extreme case, since (i) the potential represents a double-well tailored potential with strong variations and two local minima and since (ii) the density oscillations exceed the ones of the studied "harmless" potentials.

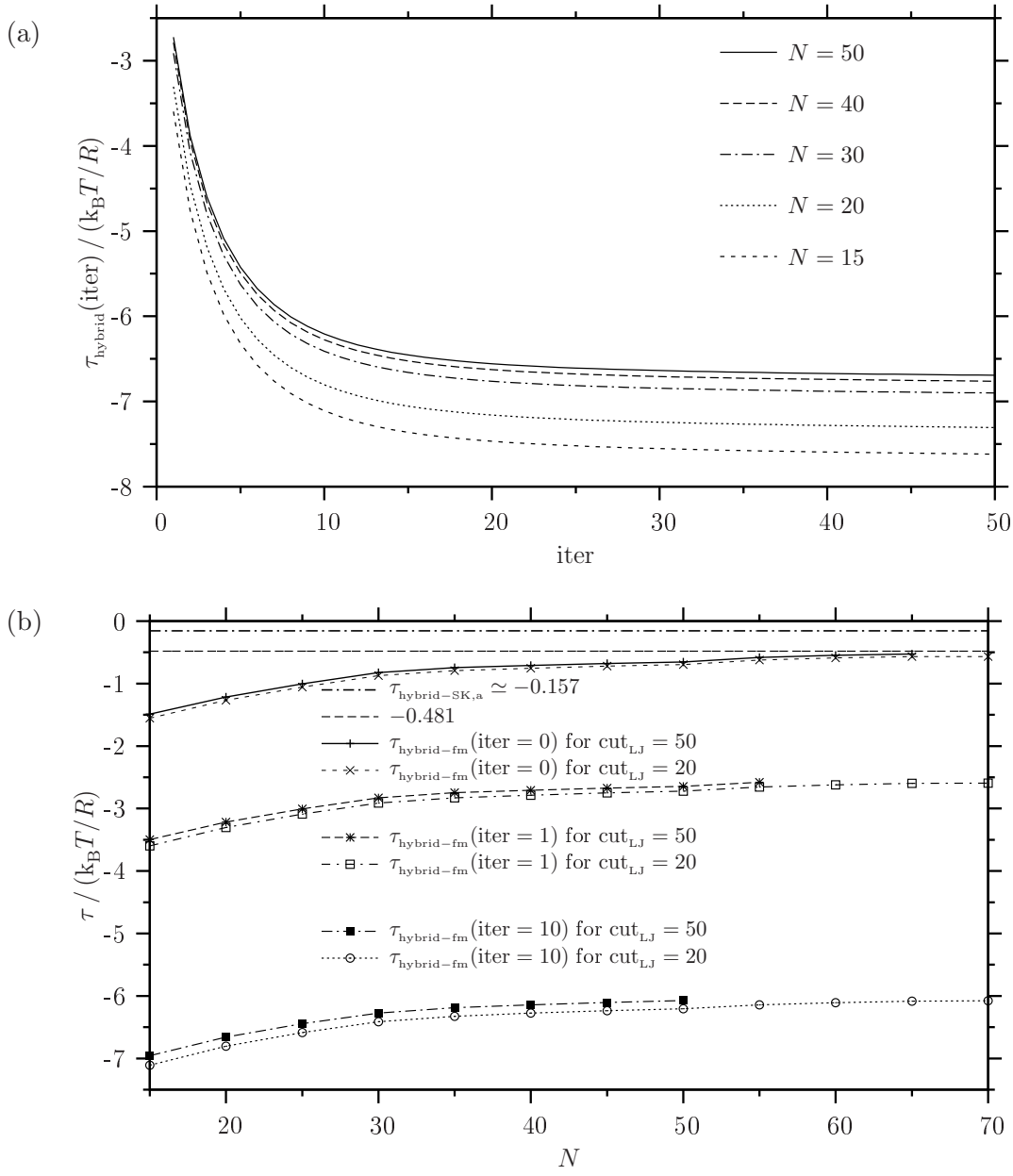

Fig. 8.34: Rapid decrease of the line tension value during the iteration. The hybrid density profile is employed as a starting configuration. In (a) a cut-off parameter of $\mathrm{cut_{LJ}} = 20$ is used, and the line tension is plotted versus the number of iterations (with a mixing parameter $\alpha = 0.1$). In (b) the line tension value after 0, 1, and 10 iteration steps is plotted versus the discretization parameter N for $\mathrm{cut_{LJ}} = 20$ and 50. The drastic decrease of $\tau_{\mathrm{hybrid-fm}}$ during the iteration demonstrates that the optimization of the density profile may not be neglected for this tailored system. Especially the lateral relaxations of the density peaks very close to the substrate surface are believed to represent the source of the quantitative discrepancy. The hybrid method fails to approximate this optimized fluid structure in the three-phase contact region well enough.

8.4 Classification of the SK, hybrid, and fully microscopic line tension theories

After the individual analysis of the SK, the hybrid, and the fully microscopic line tension theory in the previous sections a comparison of the three methods is performed here. The three approaches are compared with respect to several aspects, e. g., the degree of quantitative reliability, the ability to study systems close to a wetting transition, and the numerical efficiency.

All three line tension theories represent useful approaches to address certain aspects of the wide topic of the line tension of a sessile liquid wedge. They are based on classical DFT calculations. The underlying "original" functional is the same, however, different approximations are made within the different theories. As far as numerical results can tell, all three approaches recover Indekeu's predictions for the line tension behavior upon approaching a wetting transition.

8.4.1 Quantitative reliability

The original functional in Eq. (2.17) is the starting point of all three methods. The properties of this original functional (without further approximations) is regarded as the benchmark, which the different approaches featuring different approximations try to reproduce.

SK line tension theory:
Situations are rare where both the SK line tension theory and the fully microscopic approach are applicable. For the tailored system a comparison between these two methods is possible. The results for the tailored system deviate by even two orders of magnitude. The SK theory of wetting yields effective interface potentials which are unreliable in the region near the substrate surface, i. e., for small film thicknesses l. This large error is carried forward to the SK line tension theory and makes its results quantitatively unreliable.

Hybrid line tension theory:
The hybrid theory is a way to mimic a fully microscopic effective interface potential. Here for simplicity sharply cut fully microscopic solid–liquid profiles are used as approximative solid–gas interfacial structures. These hybrid density profiles serve to determine the hybrid effective interface potential. The wetting behavior of the fully microscopic approach is reproduced relatively well by the hybrid theory. This improved effective interface potential is inserted into the formulae of the SK line tension theory.

For the potentials from Sec. 8.1 a semi-quantitative agreement with the fully microscopic line tension data has been observed. For the tailored system, however, the methods fails and the discrepancy between the SK and the fully microscopic line tension values cannot be overcome by the hybrid method. One may conjecture that the hybrid theory works well for smoothly varying substrate potentials and moderate density variations. Unfortunately one can only tell a posteriori how well the hybrid model works for a certain considered system. Once the validity has been checked for one contact angle, the calculation of the whole $\tau(\theta)$ curve via the hybrid method represents a good and efficient description.

The hybrid theory could be improved by refering to fully microscopic, non-equilibrium solid–gas interfacial profiles in order to recover the fully microscopic wetting behavior (i. e., the $\theta(T)$ curve). One could, for instance, start the Picard iteration process for a very large liquid-like film in the solid–gas interface and calculate the hybrid effective interface potential on the fly during the iteration, where l decreases. There are infinitely many possibilities to define this film thickness l, however, at the wetting transition all

these degrees of freedom in defining l should collapse, since the equilibrium film thickness should be obtained there. Clearly, for temperatures below the wetting temperature such a fully microscopic effective interface potential depends on the definition of l. Within this approach only the part $\omega(l > l_0)$ is accessible, which causes no problems, since only this part is needed for the further calculation of the contour and the line tension value. Anyway, the benefit of an improvement of the hybrid theory is questionable, since it would most likely still fail in describing the fully microscopic line tension values of the tailored system, where lateral spatial density relaxations are supposed to be the origin of the quantitative discrepancy.

In summary the hybrid theory represents a useful way to cure the SK line tension theory from its deficiencies with respect to $\omega(l)$ for many systems. In order to obtain quantitatively reliable line tension results for an arbitrary model system, however, fully microscopic calculations are required.

Fully microscopic line tension theory:
The fully microscopic approach comprises three approximations: (i) the discretization error due to a finite (and not vanishing) grid spacing, (ii) the finite size error due to limited computer memory (and computational time), and (iii) the error due to the finite cut-off distance of a possibly long-ranged fluid–fluid interaction (e. g., in the case of a LJ fluid). Nevertheless the numerical errors are found to be relatively small, below 5 %, for not too small contact angles. Hence the numerical results of the fully microscopic calculations are regarded as a very good approximation of the inaccessible perfect solution the original functional.

8.4.2 Numerical costs and benefits

The three line tension theories considered here require different amounts of programming effort and computational resources. Which of the three methods represents the optimal choice depends on the actual purpose of the calculation.

SK line tension theory:
Sharp-kink line tension calculations of the studied systems can be performed typically within a few seconds (for $\theta \gtrsim 20°$) or a few minutes (for $\theta \gtrsim 1°$). Solving the Euler-Lagrange equation for the contour $l(x)$ of the liquid wegde requires merely a shooting algorithm for the solution of the boundary value problem.

The SK line tension theory can address situations close to a wetting transition rather easily. However, its results are quantitatively unreliable. Hence this method in its standard form (i. e., not modified by means of an improved effective interface potential) is merely useful to study the qualitative behavior of the line tension close to wetting.

Hybrid line tension theory:
Hybrid line tension calculations consist of several stages and require a period of time at the order of an hour. The hybrid effective interface potential $\omega_{\text{hybrid}}(l)$ is available only in descretized form. The spacings of the l grid have been chosen to be non-equidistant here, in order to have a fine description near the substrate surface and to efficiently calculate large ranges of l clearly away from the surface. Certainly the non-equidistant grid has to be accounted for in the numerical integrations. Furthermore a one-dimensional FMT-DFT routine is required to determine the fully microscopic solid–liquid interfacial density profile, which is underlying $\omega_{\text{hybrid}}(l)$.

The larger programming and computational effort of the hybrid method pays off and is recommended for any SK-like calculation of wetting behavior and line tensions. On the other hand side, without a check with a fully microscopic calculation one is not definitely sure about the quality of the data.

Fully microscopic line tension theory:
Fully microscopic calculations typically take at least weeks (for small system sizes, small cut-off lengths and contact angles around 90° or usually several months. A two-dimensional FMT-DFT apparatus has to be available and (costly in terms of time) adapted to the trapezoidal shape of the finite computer system.

The huge programming and computational costs of fully microscopic line tension calculations are necessary, if one is interested in a high quantitative reliability of the obtained line tension values or/and if one desires to control the validity of the hybrid method for the considered system.

9 Perspectives

The present work opens the way for further studies. First, the liquid wedge system can be enriched (cf. Sec. 9.1). Second, the method of two-dimensional, microscopicly oriented DFT applied in this work is applicable to other model systems as well (cf. Sec. 9.2). Third, an efficient way to treat axisymmetric sessile droplets is outlined in Sec. 9.3.

9.1 Extensions of the liquid wedge model

9.1.1 Mixtures of spherical fluid particles

The considered model system of a sessile liquid wedge could be generalized from a one-component fluid to a binary (or even ternary) liquid mixture. A binary liquid mixture allows for the (unconstrained) thermodynamic coexistence of three phases feasible, i. e., a substrate is not required. Consequently one could study the binary liquid mixture in a sessile wedge geometry (on a substrate) or in the Neumann triangle geometry. Since experimentally the scenario of unconstrained three-phase coexistence is expected to render the line tension more precisely than for a potentially imperfect substrate, some characteristic aspects of binary fluid mixtures are depicted in the following.

FMT for hard-sphere mixtures:
Fundamental measure theory (FMT) was designed for a fluid containing a mixture of hard-spheres [113, 170, 171]. Therefore the repulsive parts of the fluid–fluid interactions in a mixture cause no problems. For each of the n species (with radii R_i, $i \in \{1, 2, \dots n\}$) one has to keep track of the corresponding density $\varrho_i(\mathbf{r})$. With the radius dependent weight functions the weighted densities follow according to Eq. (2.31). This method was applied to a binary hard-sphere fluid in contact with a hard substrate [172]. The first-order perturbation theory (RPA, see Sec. 2.3.1) can readily be applied to a mixture [66]. Then the attractive excess free energy functional contains $1/2\, n\, (n+1)$ different terms instead of one term in Eq. (2.52),

$$\mathcal{F}_{\mathrm{ex}}^{\mathrm{att}} \;=\; \frac{1}{2} \sum_{i=1}^{n} \sum_{j=1}^{n} \int_{\mathbb{R}^3} \mathrm{d}\mathbf{r} \int_{\mathbb{R}^3} \mathrm{d}\mathbf{r}\; \varrho_i(\mathbf{r})\, \varrho_j(\mathbf{r}')\, \phi_{ij}^{\mathrm{att}}(|\mathbf{r}-\mathbf{r}'|), \tag{9.1}$$

with the interaction potential $\phi_{ij}^{\mathrm{att}}(r)$ between particles of species i and j at distance r.

9.1.2 Second-order perturbation theory

The quantitative accuracy of predicting the properties of Lennard-Jones fluids could be increased by improving the way of treating the attractive part of the interaction. Instead of the first-order perturbation theory (see Sec. 2.3) a kind of "second-order" perturbation theory could be employed.

In 2003 Tang and Wu [173] constructed a functional for an inhomogeneous Lennard-Jones fluid from the so-called "energy route", which employs the radial distribution function. In 2004 Tang and Wu [174] presented an alternative, numerically more convenient way to construct a functional for an inhomogeneous Lennard-Jones fluid. Rosenfeld's perturbative method [175], which is based on the bulk direct correlation function as an input, was applied for this construction. The direct correlation function of a sum of two Yukawa potentials, which approximates the Lennard-Jones (12–9) potential, was determined analytically within the first-order mean-spherical approximation (FMSA) [176]. The FMSA

is an approximation of the mean-spherical approximation (MSA), employing only the first term in an inverse temperature expansion of the radial distribution function. The MSA is a closure relation for the Ornstein-Zernike integral equation, which relates the direct correlation function $c(\mathbf{R})$ to the radial distribution function $g(\mathbf{R})$ or, equivalently, to the total correlation function $h(\mathbf{R})$.

The Tang/Wu approach introduced in 2004 is valid for a clearly defined bulk packing fraction η, since the formulae need this quantity as input. Consequently a system exhibiting liquid–gase coexistence cannot be addressed directly with this method, since this involves two bulk densities and choosing merely one of them would not lead to the desired solution for the second bulk-like region.

A way to generalize the Tang/Wu approach to situations *with liquid–gas coexistence* is to replace the packing fraction η by the weighted density $n_3(\mathbf{r})$, which can be regarded as a local packing fraction. In liquid regions far away from the liquid–gas interface n_3 equals the bulk liquid packing fraction, while in gaseous regions far away from the interface the bulk gas packing fraction is recovered. So both bulk fluids are described consistently, and n_3 performs a reasonable interpolation between the two bulk-like regions.

Very recently, in 2007, Tang applied the method of finding the direct correlation function within FMSA to the case of a *square-well* fluid [177]. Consequently the Tang/Wu method introduced in 2004 could be extended towards a SW fluid. Likewise the above proposed generalization for a liquid–gas interface could be applied. This procedure points towards a more accurate treatment of a SW fluid involving the wedge line tension. However, since the SW model fluid does not capture the dispersion forces of actual fluids the benefit from quantitatively improved predictions is limited.

9.2 Effectively two-dimensional Cartesian models

The method of FMT-DFT plus perturbation theory in two effective Cartesian dimensions can be applied to other model systems as well.

9.2.1 Parallel cylinders

Parallel cylinders (or, in general, objects that are translationally invariant in one direction) surrounded by a fluid could be approached with the Cartesian program, which provides $\varrho(x, z)$. The cylinders would have to be discretized on the Cartesian grid. Furthermore a liquid–gas interface could be established in the system. The cylinders could be positioned, e. g., at the liquid–gas interface, so that they are partially immersed in the liquid.

9.2.2 Confined geometries

Various geometries confining the fluid could be addressed, e. g., irregularly shaped slits or pores. If the fluid system is translationally invariant in one direction, it could in principle be tackled with the program developed here. E. g., capillary condensation in a capped capillary [178], which consists of a slit and an additional wall perpendicular to the slit walls, could be studied. Here deviations from the behavior for an infinitely deep slit occur. A periodic arrangement of such capped capillaries (i. e., rectangular grooves) could be addressed fully microscopicly as well and thereby serve as a comparison to a mesoscopic theory (using an effective interface Hamiltonian) [179, 180].

9.2.3 Geometrically and chemically structured substrates

The method of calculation applied to a homogeneous, planar substrate in this work also allows for the description of a chemically or/and geometrically structured substrate, which remains translationally invariant in one direction. The ongoing nanotechnological advances in substrate patterning require theoretical studies of such systems. Fluids interacting with nanostructured systems are relevant for biological and biomimetic systems, e. g., it is believed that air humidity contributes to the strong adhesion force of geckos at various kinds of substrate [181]. One distinguishes between a structured substrate, if there is a fluid bulk region unperturbed by the substrate, and a confined system, if the fluid is influenced by the substrate everywhere.

Substrate wedge or edge:
The system of a hard-sphere fluid in a right-angled wedge or at a right-angled edge [182], for instance, could be extended readily towards a Lennard-Jones or square-well fluid and arbitrary angles of the substrate wedge or edge [183].

A liquid-like film eventually forms in the corner of the solid wedge and grows (and finally diverges) upon approaching the filling temperature below the wetting temperature for a planar substrate. This phenomenon, the filling of a wedge, can be studied with the method presented in this work. Thereby a fully microscopic foundation for a corresponding mesoscopic theory [184, 185] (using an effective interface Hamiltonian) and a semi-microscopic DFT [186] (using the sharp-kink approximation) can be achieved. The influence of a line tension (attributed to the wedge bottom line) on the wedge filling has already been pointed out on the level of an effective interface Hamiltonian and a transfer matrix analysis [187].

If the two solid plates establishing the wedge are made up from different materials, the shape of the interface between a liquid-like film and the gas phase (i. e., the meniscus) in this chemically asymmetric wedge becomes asymmetric as well [188].

Liquid wedge in a solid edge:
The liquid wedge investigated in this work (i. e., a planar liquid–gas interface approaching a planar, homogeneous substrate) could be generalized and brought into contact with a geometrically or chemically structured substrate. E. g., a liquid wedge placed in a solid edge such that the planar macroscopic liquid–gas reference interface meets the solid surface near or at the edge, would lead to an interplay of the edge region with the liquid and gas phases. In an experiment such a situation could be approximately obtained, if the contact line of a large sessile droplet is moved [e. g., by an atomic force microscope (AFM) tip] towards a second substrate region, which is inclined with respect to the substrate ground level. In this way the morphology of the three-phase contact region can be influenced by a geometric obstacle. The force acting on a droplet near an obstacle could be calculated by comparing grand potential values for slightly shifted positions of the liquid–gas boundary profile.

Chemical step or stripe:
A single chemical step and the associated line tension, the substrate boundary line tension, was already mentioned in Sec. 5.2.2. The sharp-kink DFT approach dealing with this issue [11] could be compared to a fully microscopic calculation.

Another example for possible applications is a (more or less) hemicylindrical droplet on a planar substrate with a *chemical stripe*. A chemical stripe is equivalent to two neighboring chemical steps where two substrate regions are composed of the same material. Typically a water-like fluid and a hydrophilic chemical stripe with hydrophobic embedding substrates

is considered. A fluid in contact with such a strip was studied before by means of an effective interface Hamiltonian (i. e., an interface displacement model) [189].

A chemical stripe favoring a *thinner* wetting layer than the outer region has been treated in a sharp-kink DFT approach (comparable to the approach to the wedge system in Chapter 7) [190, 191, 192]. For small stripe widths or/and small amounts of liquid a fully microscopic treatment is desirable.

Among several structures, a single chemical stripe and a periodic grid of chemical stripes were investigated via a minimization of the total interfacial free energy of a sessile droplet on a mesoscopic level [193, 194, 195, 196, 197]. Such chemical stripes can serve as channels for liquid transport in open [194] or closed [198] micro-/nanofluidic devices. Even vesicles (i. e., closed lipid bilayers) can adhere to these striped surface domains [199, 200].

In view of these applications the question of *stability* of a liquid hemicylindrical droplet (liquid ridge) [201] against pearling (i. e., the formation of single droplets instead of one connected amount of liquid) [202, 203, 204] and against leaking/overflow (i. e., liquid leaves the typically hydrophilic chemical pathway and spreads into the hydrophobic outer zone) arises. Pearling cannot be represented in an effectively two-dimensional description. An interface displacement model predicts this instability on a mesoscopic level [205]. MD simulations, for instance, allow one to study the dynamics of these small amounts of liquid [206]. Flowing nanodroplets near geometrical [207] or chemical [208] structures can be investigated in terms of hydrodynamics, e. g., by solving the Stokes equation (i. e., the Navier-Stokes equation in the limit of slow flow) for effectively two-dimensional liquid ridges numerically.

A straight *nanowire*, i. e., a very fine molecular chain lying on the solid surface (or embedded in it), can be regarded as the limiting case of a chemical stripe for very small stripe width. For this special case the additional external potential can be obtained easily for a square-well or Lennard-Jones interaction between the nanowire particles and the fluid particles: It is proportional to the integrated potential w_{ff} [Eqs. (2.109) and (2.110)] for the actual interaction parameters.

Fluids near semipermeable walls:
Semipermeable (non-fluid) membranes are technologically important. Within a DFT approach a semipermeable wall can be modelled by an external potential barrier [209, 210]. Generalizations towards polydisperse fluids [211], ionic fluids [212] and a semipermeable spherical wall [213] (mimicking a vesicle; here treated within an integral equation approach) are possible.

What the described computer program can accomplish:
The fluid structure and the line tension related to chemical inhomogeneities (e. g., a chemical step or stripe) are feasible on the fully microscopic level as well. Only minor modifications of the existing code would be necessary. Clearly, within the described method such a system could be extended towards an arbitrary (i. e., a geometrically and chemically rough) substrate, as long as the system remains effectively two-dimensional.

Morphometric thermodynamics to address very complicated structures:
More complicated, fully three-dimensional geometries (i. e., without simplifying symmetries) can be tackled within DFT only for very small system sizes or by using tremendous computer power and computation times. However, many important biophysical systems, e. g., protein folding taking into account the solvent [214, 215, 216, 217], should be treated in a three-dimensional fashion in order to obtain realistic results. *Morphometric thermodynamics* is a method, which can be applied to a large variety of fluid systems with a complicated morphology (i. e., shape of the fluid region) [218, 219, 220, 221]. This

approach uses Hadwiger's theorem [222] of integral geometry. It states, that any (i) motion-invariant, (ii) additive, and (iii) continuous functional can be written as a linear combination of the fundamental measures of the fluid region S with suitable expansion coefficients. These coefficients do not depend on the shape of the S. (For an illustrative explanation of the three conditions see, e. g., Ref. [220].) The fundamental measures are the volume V, the surface area A, the integrated mean curvature

$$C \;=\; \frac{1}{4\,\pi} \int_{\partial S} \mathrm{d}A \; H, \tag{9.2}$$

and the integrated Gaussian curvature or Euler characteristic

$$X \;=\; \frac{1}{4\,\pi} \int_{\partial S} \mathrm{d}A \; K. \tag{9.3}$$

Here H and K denote the local mean curvature

$$H(\mathbf{r}) = \frac{1}{2} \left(\frac{1}{R_1(\mathbf{r})} + \frac{1}{R_2(\mathbf{r})} \right) \tag{9.4}$$

and the local Gaussian curvature

$$K(\mathbf{r}) = \frac{1}{R_1(\mathbf{r})\; R_2(\mathbf{r})}, \tag{9.5}$$

respectively, with the two principal radii of curvature, $R_2(\mathbf{r})$ and $R_2(\mathbf{r})$, at a point $\mathbf{r}$. σ denotes the surface tension at a planar wall; κ and $\bar{\kappa}$ are two bending rigidities. Thus the grand potential of a fluid system, which satisfies the three premises mentioned above, can be written as

$$\Omega \;=\; -\,p\,V \;+\; \sigma\,A \;+\; \kappa\,C \;+\; \bar{\kappa}\,X. \tag{9.6}$$

This means that the grand potential can be approximated by a linear combination of the fundamental measures. The thermodynamic coefficients σ, κ, and $\bar{\kappa}$ can be calculated separately in simple geometries, e. g., for a spherical or cylindrical substrate using the same kind of substrate–fluid and fluid–fluid interactions and the same definitions of the dividing interfaces.

9.2.4 Bridge formation between a solid wedge and a substrate

If a solid wedge immersed in a gas approaches a planar substrate, a so-called "liquid bridge" may form between the wedge and the substrate. This means that there is a region of high, liquid-like density between the two solid objects. This system has been analyzed in a macroscopic theory [223]. A (fully) microscopic theory for this system is desirable, especially in order to analyze small liquid bridges, their microscopic structure and the onset of bridge formation. The shapes of large liquid bridges (i. e., their liquid–gas dividing interfaces) are expected to resemble the results from the macroscopic theory.

9.3 Axisymmetric model systems

9.3.1 Axisymmetric sessile droplets

The line tension of a sessile liquid wedge is related to the line tension of a sessile droplet (see Sec. 4.6). However, the wedge line tension is not sufficient to predict the contact angle of small sessile droplets. Rather the line tension for a finite droplet, the Tolman length and two derivates of the line tension (including subleading terms) with respect to droplet size parameters are required. Axisymmetric sessile droplets are also effectively two-dimensional, since the density solely depends on the distance from the axis and on the distance from the planar substrate surface. This cylindrical coordinate system is not Euklidian, hence the convolution integrals for the calculation of weighted densities n_α and n_{ff} cannot be calculated by Fourier transforms directly. Numerical real-space integrations are too time-consuming for reasonable droplet sizes. In order to calculate the convolutions efficiently, the Fourier transform can be applied in an indirect way. The general method to treat axisymmetric fluid systems within FMT-DFT is presented in the following section.

Once this method is implemented into the computer code, further qualitative differences to the wedge system have to be taken into account: First, the increased pressure inside the droplet (i. e., the Laplace pressure) leads to the fact that the binodals in the bulk phase diagram are not valid to describe liquid–gas coexistence for a small droplet. For each droplet size the densities of the coexisting liquid and gas phases have to be calculated separately.

Second, the iteration process might become instable, so that the droplet either disappears or grows too much. Suitable boundary conditions and careful control of the iteration process are essential. As boundary conditions a solid–gas interfacial profile can be used near the substrate far away from the droplet. One might split the iteration process in main steps, in which the density in the spatial region of the droplet top is fixed, and intermediate steps, in which this constraint is removed and the density in the top region is allowed to adapt to its neighborhood. This "soft constraint" is expected to overcome the possible problem of metastability.

9.3.2 Method to treat convolutions in cylindrical coordinates

Three-dimensional convolution integrals have to be calculated in order to obtain weighted densities n_α and n_{ff}. The idea to evaluate real-space convolutions efficiently by products in Fourier space is extended to an axisymmetric system, for which cylindrical coordinates are appropriate. In Sec. 9.3.2.1 the Hankel transform, the Fourier transform of a two-dimensional, radially symmetric function, is described. In Sec. 9.3.2.2 the full three-dimensional case of an axisymmetric system is considered.

9.3.2.1 (Fast) Hankel transform

The *Hankel transform* (HT) (of order zero) of a radially symmetric function $f(x, y) = f(r)$ is defined as

$$F_{\mathrm{H}}(k) \;:=\; \mathcal{H}\left(f(r)\right) \;:=\; \int_{r=0}^{\infty} \mathrm{d}r \; f(r)\, r\, J_0(kr), \tag{9.7}$$

where $J_0(kr)$ is the Bessel Function of order zero of the first kind. The HT of another order ν is defined analogously to a Bessel function of order ν of the first kind, $J_\nu(kr)$. In

the following HT means the HT of order zero. Due to the integral kernel the HT is also known as Fourier-Bessel transform. The HT is related to the two-dimensional Fourier transform $\widehat{f}(k_x, k_y) = \widehat{f}(k)$ (with $k := \sqrt{k_x^2+k_y^2}$) of a radially symmetric function $f(r)$ via $\widehat{f}(k) = 2\pi\, F_{\mathrm{H}}(k)$. The *inverse* Hankel transform reads

$$f(r) \;=\; \mathcal{H}^{-1}\left(F_{\mathrm{H}}(k)\right) \;:=\; \int\limits_{k=0}^{\infty} \mathrm{d}k\; F_{\mathrm{H}}(k)\; k\, J_0(kr). \tag{9.8}$$

The *discrete* Hankel transform adapts the HT to a discrete lattice. Analogously to the FFT there is a number of *fast Hankel transform* (FHT) algorithms (Siegman 1977 [224], Sheng and Siegman 1980 [225], Candel 1981 [226], Anderson 1982 [227], and Hansen 1985 [228]). They share Siegman's idea to express the product $k\,r$ as $e^{\ln k + \ln r}$ and the transform as a convolution in the variables $\ln r$ and $\ln k$: If the variables r and k are substituted by the variables

$$s \;:=\; \ln r \quad \text{and} \quad t \;:=\; \ln k, \tag{9.9}$$

the HT reads

$$\begin{aligned} F_{\mathrm{H}}^{(\log)}(t) \;&:=\; F_{\mathrm{H}}(k) \;\equiv\; \int\limits_{s=-\infty}^{\infty} \mathrm{d}s\; f\big(r(s)\big)\,\big[r(s)\big]^2\, J_0(e^{s+t}) \\ &=:\; \int\limits_{s=-\infty}^{\infty} \mathrm{d}s\; a(-s)\, b(s+t) \;=\; \int\limits_{s=-\infty}^{\infty} \mathrm{d}s\; a(s)\, b(t-s) \\ &=\; (a \otimes b)\,(t) \;=\; \mathcal{F}^{-1}\left\{\mathcal{F}\left(a(s)\right) \cdot \mathcal{F}\left(b(s)\right)\right\}. \end{aligned} \tag{9.10}$$

Hence a HT can be calculated by the sequence of two FT, a multiplication, and an inverse FT. Likewise a FHT can be replaced by two FFT, a multiplication, and an inverse FFT. The FHT takes a factor of approximately 3–4 longer than single one-dimensional FFT and is therefore much more efficient than the corresponding full two-dimensional FFT. The inverse transform of the FHT can be accomplished by a similar FFT sequence as well.

If convolutions are evaluated discretely using FFT, the grid of the integration variable has to be equidistant. Contrarily a FHT requires a sequence of exponentially spaced r-points and k-points, so that the logarithms of r or k are equidistant [Eq. (9.10)].

9.3.2.2 Three-dimensional Fourier transform in cylindrical coordinates

In this section $r := \sqrt{x^2+y^2}$ denotes the radial part of the vector $\mathbf{r}$ projected onto the xy plane. Similarly $k := \sqrt{k_x^2+k_y^2}$ describes the radial part of the vector $\mathbf{k}$ projected to the $k_x k_y$ plane. As an example the convolution of a weighted density n_α is discussed. This method can be applied analogously to the convolution of n_{ff}.

The quantity to be evaluated is [Eqs. (2.31) and (6.6)]

$$n_\alpha(\mathbf{r}) \;=\; n_\alpha(r,z) \;=\; (\varrho \otimes w_\alpha)\,(r,z) \;=\; \mathcal{F}^{-1}\left\{\mathcal{F}\left(\varrho(r,z)\right) \cdot \mathcal{F}\left(w_\alpha(r,z)\right)\right\}. \tag{9.11}$$

Therefore the Fourier transforms (see Sec. 6.1) of $\varrho(r,z)$ and $w_\alpha(r,z)$ have to be determined. Given a function $f(r,z)$, the Fourier transform $\widehat{f}(\mathbf{k}) = \widehat{f}(k,k_z)$ reads

$$\widehat{f}(k,k_z) \;=\; 2\pi \int\limits_{z=-\infty}^{\infty} \mathrm{d}z\; e^{-ik_z z} \int\limits_{r=0}^{\infty} \mathrm{d}r\; f(r,z)\; r\, J_0(kr). \tag{9.12}$$

The second integral corresponds to a Hankel transform (HT). Thus the whole three-dimensional Fourier transform consists of a (one-dimensional) Hankel transform for the radial part and a one-dimensional FT for the z component. Indicating the variables on which the respective transform acts under the transformation operator symbol, the three-dimensional Fourier transform can be described as

$$\widehat{f}(k,k_z) \;=\; 2\pi \underset{z\mapsto k_z}{\mathcal{F}}\Big(\underset{r\mapsto k}{\mathcal{H}}\big(f(r,z)\big)\Big). \tag{9.13}$$

The discrete lattice for $\mathbf{r}$ and $\mathbf{k}$ requires equidistant spacings in the z- and k_z-direction, respectively. However, in the radial direction, r or k, an *exponential grid*, which is equidistant in the logarithmic space of $\ln r$ or $\ln k$, is inevitable.

The product of the two three-dimensional Fourier transforms is transformed back to real-space by an inverse Fourier transform, which here consists of an inverse FT for the k_z component and an inverse HT for the radial part k.

9.3.3 Other axisymmetric model systems

As soon as a numerical code for an axisymmetric problem is available, many systems can be addressed.

9.3.3.1 Finite solid cylinder

An infinitely long cylinder with radius R_{cyl} surrounded by a fluid can be treated as an effectively one-dimensional system. The wetting behavior of a fluid at an infinitely extended cylinder has been studied already [229] via an effective interface potential, which had been constructed from a density functional inserting a sharp-kink approximation, analogously to the sharp-kink theory discussed in Chapter 7.

However, a fluid-surrounded *finite* cylinder (i. e., a cylinder with a finite heigth h) is an effectively two-dimensional system in cylindrical coordinates, which could be treated with the axisymmetric program. The *line tension* $\tau(R_{\mathrm{cyl}},h)$ associated to the two circular edges of the cylinder could be determined. The grand potential can be separated into

$$\begin{aligned}\Omega_{\mathrm{cyl,fin}} \;&=\; -\,p\,V \;+\; \sigma_{\mathrm{sf}}^{\mathrm{clyl,inf}}(R_{\mathrm{cyl}})\;2\pi R_{\mathrm{cyl}}\,h \\ &\quad +\,2\,\sigma_{\mathrm{sf}}\;\pi R_{\mathrm{cyl}}^2 \;+\; 2\,\tau(R_{\mathrm{cyl}},h)\;2\pi R_{\mathrm{cyl}},\end{aligned} \tag{9.14}$$

where $\sigma_{\mathrm{sf}}^{\mathrm{clyl,inf}}(R_{\mathrm{cyl}})$ denotes the solid–fluid surface tension for an infinite cylinder and σ_{sf} the surface tension for a planar solid–fluid interface. Here the contribution related to the interaction between the two cylinder caps is included in $\tau(R_{\mathrm{cyl}},h)$. For $h\to\infty$ this line tension recovers the line tension of the circular cap of a semi-infinite cylinder. This system could be extended readily such that the solid cylinder contains a stripe-like chemical inhomogeneity giving rise to a line tension at a curved chemical boundary [230].

9.3.3.2 Cylindrical pores

Pores connect a reservoir to an otherwise isolated bassin. Pores play an important role in biological systems, e. g., as ion channels in cell membranes. An infinitely long cylinder coupled (virtually) to a bath consisting of a binary mixture (mimicking, e. g., an ion species and water) or even a ternary mixture (mimicking, e. g., two ion species and water) is an interesting model system of a pore, which explains some basic, entropy-driven selective filtering phenomena [231]. A cylindrical hole with *finite* length in a solid-like layer separating two fluid regions might be a helpful model system of a membrane pore, since

actual pores are only a few nanometers long. The fluid structure in the vicinity of the pore openings could be considered, and the behavior in the pore center could be compared to results for an infinite cylinder.

The cylindrical pore could be generalized to a region filled with fluid which has the shape of a frustum (of a cone). A frustum corresponds to a cone the tip of which has been cut off parallel to the basal plane. Capillary evaporation (or condensation) in this complex geometry is an interesting phenomenon and could be analyzed fully microscopicly, not least in order to compare it with the morphometric approach applied for this system [232]. Measurements on capillary rise in a conical pore permit to determine the line tension in an alternative geometry than for a planar substrate [233, 234]. Furthermore a fluid confined between two coaxial cylinders is feasible [235].

9.3.3.3 Frustum

Similarly a solid frustum (of a cone) could be considered. (In contrast to the frustum-shaped fluid region mentioned in Sec. 9.3.3.2 now the frustum is solid and surrounded by fluid.) Let R_1 and $R_2 < R_1$ be the radii of the two confining circles. Although the grand potential could be calculated relatively easily with the axisymmetric program, it is difficult to identify excess quantities. The curved cone shell leads to the fact that the excess free energy (in comparison to a pure bulk fluid) related to the surface does not simply scale with the surface area. From my point of view there are mainly two options to define a reference system:

First, the surface tension $\sigma_{\mathrm{sf}}^{(\mathrm{cyl})}(R_{\mathrm{cyl}})$ for a solid cylinder with radius R_{cyl} surrounded by a fluid is calculated. Then the reference system is a frustum described *locally* by the surface tension of an infinitely large cylinder, so that the corresponding decomposition of the grand potential reads

$$\begin{aligned}\Omega_{\mathrm{frustum}}^{(1)} &= -p\,V_{\mathrm{f}}^{(1)} + \int_{\mathcal{A}} \mathrm{d}A_{\mathrm{sf}}^{(\mathrm{cone})}\ \sigma_{\mathrm{sf}}^{(\mathrm{cyl})}(R_{\mathrm{cyl}}) \\ &\quad + \sigma_{\mathrm{sf}}\ \pi\big(R_1^2 + R_2^2\big) + \tau(R_{\mathrm{cyl}}, h)\ 2\pi\big(R_1 + R_2\big). \end{aligned} \tag{9.15}$$

Second, the reference system could be a fluid-surrounded finite cylinder with a radius R_{cyl} and a length that equals the cone height. The grand potential can be expressed as

$$\begin{aligned}\Omega_{\mathrm{frustum}}^{(2)} &= -p\,V_{\mathrm{f}}^{(2)} + \sigma_{\mathrm{sf}}^{(\mathrm{cyl})}(R_{\mathrm{cyl}})\ 2\pi R_{\mathrm{cyl}} h \\ &\quad + 2\,\sigma_{\mathrm{sf}}\ \pi R_{\mathrm{cyl}}^2 + 2\,\tau(R_{\mathrm{cyl}}, h)\ 2\pi R_{\mathrm{cyl}}. \end{aligned} \tag{9.16}$$

There are several possibilities to choose the radius R_{cyl}, e. g., as R_1, so that the cylinder encloses the whole frustum. Or the radius R_{cyl} is chosen by a more complicated condition, e. g., such that the volume or the surface area of the frustum and the cylinder are equal. However, the combined condition (equal volume and surface area) does not possess a solution for all values of the paramters (R_1, R_2, and h), so this approach is limited to some configurations. This combined condition represents the "fairest" choice, since no additional or missing volume or surface elements are assigned to the line tension of the frustum.

9.3.3.4 Point tension of a cone

The concept of excess quantities can also be extended beyond the line tension. A contribution to the grand potential that is related to a point-like structure and does not scale with a length, area, or volume is called *point tension*. Since following σ (sigma), used for

the surface tension, and τ (tau), used for the line tension, the next letter in the Greek alphabet is υ (upsilon/wye), this letter is used for the point tension here.

The frustum of the previous section, Sec. 9.3.3.3, resembles a cone for $R_2 \to 0$. In this limiting case the length of the smaller confining circle vanishes. The cone can be finite (i. e., with a finite value of the height h) or infinitely large, depending on the boundary conditions. The calculation of the grand potential for this system should be feasible, however, the definition of a reference system is as difficult as in the case of a frustum.

For each of the two definitions suggested there, the decomposition of the grand potential involves a point tension υ. For the first definition of a reference system the point tension for a finite cone is defined via

$$\begin{aligned}\Omega^{(1)}_{\text{finite cone}} &= -p\,V_{\text{f}}^{(1)} + \int_{\mathcal{A}} \mathrm{d}A_{\text{sf}}^{(\text{cone})}\ \sigma_{\text{sf}}^{(\text{cyl})}(R_{\text{cyl}}) \\ &\quad + \sigma_{\text{sf}}\ \pi R_1^2 + \tau(R_{\text{cyl}}, h)\ 2\pi R_1 + \upsilon^{(1)}_{(\text{finite})}(R_1, h). \end{aligned} \tag{9.17}$$

For an infinite cone (which is mimicked by suitable boundary conditions) the decomposition reads

$$\Omega^{(1)}_{\text{infinite cone}} = -p\,V_{\text{f}}^{(1)} + \int_{\mathcal{A}} \mathrm{d}A_{\text{sf}}^{(\text{cone})}\ \sigma_{\text{sf}}^{(\text{cyl})}(R_{\text{cyl}}) + \upsilon^{(1)}_{(\text{infinite})}. \tag{9.18}$$

Analogously for the second reference system and a finite cone one has

$$\begin{aligned}\Omega^{(2)}_{\text{finite cone}} &= -p\,V_{\text{f}}^{(2)} + \sigma_{\text{sf}}^{(\text{cyl})}(R_{\text{cyl}})\ 2\pi R_{\text{cyl}} h \\ &\quad + \sigma_{\text{sf}}\ \pi R_{\text{cyl}}^2 + \tau(R_{\text{cyl}}, h)\ 2\pi R_{\text{cyl}} + \upsilon^{(2)}_{(\text{finite})}(R_1, h). \end{aligned} \tag{9.19}$$

For the LJ interaction (and other long-ranged fluid–fluid interactions with van der Waals tails), however, the point tension is ill defined: The surface tension, line tension, and point tension can be expressed by moments of the interaction potential. For a LJ fluid these three quantities contain integrals over $1/r^3$, $1/r^2$, or $1/r$, respectively. Therefore for a LJ fluid the point tension diverges. For a SW fluid (and other short-ranged interaction potentials which are exactly zero beyond a certain interparticle distance) the point tension is well defined.

In this context it is worth mentioning that experimentally even drops resting on a solid cone (at or below the tip) can be studied [236], which clearly is an even more difficult system to be analyzed in terms of line and point tensions.

The situation of a fluid outside a solid cone could also be inverted, such that a cone is filled with fluid. The filling of a cone has been analyzed macroscopicly [237], and a fully microscopic treatment is desirable. A mesoscopic theory for cone filling (involving an effective interface Hamiltonian) is in preparation [238].

9.3.3.5 Bridge formation between a solid cone or sphere and a substrate

For atomic force microscopy (AFM) it is essential to understand the formation of a liquid bridge between the AFM tip and the substrate. This situation could be theoretically mimicked by a solid cone near a planar substrate. Analogously to the similar case of a solid wedge instead of a solid cone (see Sec. 9.2.4) microscopic insight into the formation of a liquid bridge could be compared to the macroscopic theory [239].

A similar, axisymmetric system is a solid sphere resting on a substrate. Capillary condensed liquid can form around the contact point of both solids. At the contact line of the surface of the liquid-like ring and the sphere or the substrate the line tension (for curved

interfaces and a curved contact line) comes into play. This system and the associated line tension was addressed theoretically already in 1997 [240]. (This macroscopic analysis is based on the modified Young equation and the Kelvin equation for the curved surface of the liquid-like ring.) The above described method to treat axisymmetric model systems within FMT-DFT is suitable to calculate the corresponding fluid structure and the line tension rather precisely.

9.3.3.6 Wetting of circular or ring-shaped surface domains

Chemically heterogeneous substrates permit a large variety of experimental implementations. Translationally invariant chemical heterogeneities on planar surfaces have been discussed in Sec. 9.2.3 as a possible field of application of the computer program developed here. Axisymmetric chemical (or geometrical) substrate structures could be investigated with the described program as well. Surface domains formed by two concentric rings [241] or by circles [242, 243, 244] were analyzed both experimentally and theoretically (namely by minimizing the free energy of the wetting layer on a macroscopic level). For small extensions (on the nanometer scale) the fully microscopic FMT-DFT approach could contribute to these subjects.

9.3.3.7 Stationary colloids

The radially symmetric system of a colloid completely immersed in a fluid could be addressed in an effectively one-dimensional calculation efficiently. The wetting of a Lennard-Jones fluid at a spherical colloid has already been addressed in a sharp-kink DFT approach [229] and a FMT-DFT approach [245].

If the system is generalized towards cylindrical symmetry, the effectively two-dimensional system could be treated with the axisymmetric program described above. An example of such a cylindrical symmetric system is a single, large colloid partially immersed in a thin liquid film [246]. For small particle radii the line tension becomes important and changes the equilibrium wetting configuration. At a critical line tension value the particle is expelled from the film undergoing a dewetting transition.

A single colloid at a liquid–gas interface:
The system of a colloid situated at a liquid–gas interface could be addressed with the axisymmetric program. It could provide the equilibrium density distribution for a spatially fixed colloid, i. e., one could imagine an optical tweezer keeping the colloid fixed. The level of the planar liquid–gas interface far away from the colloid defines the depth of immersion of the colloid. By subsequent calculations for different depths the equilibrium depth of immersion could be determined. The chemical structure of the colloid surface may be mimicked by a specific external potential. A FMT-DFT analysis of the wetting behavior takes into account packing effects near the colloid. Thus small colloids could be treated as well, which are too small for mesoscopic approaches based on the effective interface potential or capillary waves.

The *line tension* of the three-phase contact region, where the colloid meets the liquid–gas interface, could be calculated. An obvious choice of the reference system is a colloid with a spherical solid–fluid dividing interface and bulk liquid and gas density in the liquid and gas region, respectively. A decomposition of the grand potential then defines the line tension,

$$\Omega \;=\; -\,p\,V \;+\; A_{\mathrm{sl}}\,\sigma_{\mathrm{sl}} \;+\; A_{\mathrm{sg}}\,\sigma_{\mathrm{sg}} \;+\; A_{\mathrm{lg}}\,\sigma_{\mathrm{lg}} \;+\; \tau\;2\pi R_{\mathrm{coll}}. \tag{9.20}$$

The surface tension of the curved colloid–gas or colloid–liquid interface, respectively, depends on the radius of curvature and has to be calculated separately. For small colloids this line tension represents an important ingredient for the analysis of the capillary- and fluction-induced interactions between two partially immersed colloids [247, 248, 249, 250, 251]. For particle sizes in the submicrometer range the preferred orientation of a ellipsoidal particle that is partially immersed in a liquid (at a planar liquid–gas interface) depends on the line tension [252]. The penetration depth of such a particle into a liquid droplet is influenced by the line tension as well [253].

The line tension for this system depends on the choice of the dividing interfaces. Besides the solid–fluid interface position also the liquid–gas dividing interface position is crucial, since a parallel shift of it would change the length of the three-phase contact line and the surface areas A_{sl} and A_{sg}.

Two colloids surrounded by a fluid:
The problem of two colloids fixed in a solvent (or even several colloids aligned in a line) could be tackled as well. The force between the colloids could be analyzed by slight variations of their distance D. Even the case that the colloids touch each other is accessible.

For small colloid distances the fluid structure in the region in between changes in comparison to the case of two colloids far apart. The excess grand canonical free energy associated with this effect could be interpreted as an effective interaction $v(D)$ between the two colloids. The grand potential can be decomposed in

$$\Omega \;=\; -\,p\,V \;+\; 2\,A_{\mathrm{sf}}\,\sigma_{\mathrm{sf}} \;+\; \phi_{\mathrm{cc}}^{\mathrm{eff}}(D), \tag{9.21}$$

so that the reference system is given by the bulk fluid density around the colloids. Alternatively this free energy contribution $v(D)$ could be perceived as a distance dependent point tension. For a single colloid deviations of the density in comparison to the bulk density are reflected in the curvature dependence of the colloid/solid–fluid surface tension σ_{sf}. Clearly, for macroscopicly separated colloids the effective colloid–colloid interaction vanishes,

$$\lim_{D\to\infty} \phi_{\mathrm{cc}}^{\mathrm{eff}}(D) \;=\; 0. \tag{9.22}$$

The formation of bridges between liquid-like layers between two spheres has been addressed already in a mesoscopic theory [254], namely an interface displacement model which is based on DFT. The fully microscopic DFT approach could yield the finely resolved liquid structure and thereby a rather accurate description of the bridge morphology, which serves as comparison to the mesoscopic theory. Moreover a liquid–gas interface could occur between the two colloids.

10 Summary

A liquid wedge residing on a substrate has been investigated theoretically. Corresponding line tension values have been calculated within a fully microscopical, non-local classical density functional theory (DFT) approach. A Lennard-Jones (LJ) fluid and a square-well (SW) fluid served as model fluids, i. e., the fluid is composed of particles interacting either via a long-ranged LJ (12–6) potential or via a short-ranged SW potential. The shape of the SW potential suggests, how to separate the potential into repulsive and attractive parts. The LJ interaction was decomposed into repulsive and attractive parts via the Weeks-Chandler-Andersen (WCA) scheme such that the LJ fluid is approximated by a WCA-LJ fluid. The repulsive part of the fluid–fluid interaction was accounted for by fundamental measure theory (FMT), whereas the attractive part was addressed by means of the random phase approximation (RPA), a kind of mean-field perturbation theory. The substrate was taken to be homogeneous, planar, and chemically inert. Its interaction with a single fluid particle was described by several substrate potentials, namely a LJ (9–3) potential, a LJ (9–4–3) potential, a cut and shifted LJ (9–3) potential, and a tailored potential. Within the sharp-kink (SK) approximation (see Fig. 7.1) used in related previous works the particle density distributions are piecewise constant. By contrast the fully microscopic calculations presented here employed continuous density profiles. Hence packing effects (i. e., density oscillations near the substrate surface) have been taken into account. The model system of a sessile liquid wedge is effectively two-dimensional, which is reflected by a two-dimensional spatial dependence of the particle density distribution $\varrho = \varrho(x, z)$. Several precaution measures have been taken in order to achieve a sufficiently high precision of the calculated line tensions.

Different wetting scenarios have been addressed, namely first-order wetting involving short-ranged and long-ranged forces as well as critical wetting involving long-ranged forces. The comparison to the predictions by Indekeu [44] for the line tension behavior upon approaching wetting transitions is possible with available computational resources for contact angles larger than $5^\circ - 10^\circ$. The results are compatible with Indekeu's predictions (see Figs. 8.5, 8.7, 8.13, and 8.15). This finding supports the conjecture that structural details are unimportant for the qualitative behavior of the line tension close to a wetting transition.

In order to clarify how important packing effects are for line tension values a comparison was made with results from a SK line tension theory. For this purpose the SK line tension theory has been extended to incorporate the fluid–fluid interaction potentials under consideration, i. e., the WCA-LJ potential and the SW potential. A quantitative comparison between the fully microscopic approach and the semi-microscopic SK approach is very difficult, since one typically faces the following phenomenon: For parameters well suited for SK calculations the fluid within the fully microscopic approach exhibits (i) wetting at a much lower temperature or/and (ii) local crystallization near the substrate surface, which makes a fully microscopic calculation very difficult or in most cases impossible. On the other hand convenient parameters for the fully microscopic programme lead to an edge minimum in the effective interface potential, i. e., the global minimum of $\omega(l)$ occurs near the substrate surface. In this case the SK predictions are completely different from fully microscopic results.

A substrate potential has been designed (see Fig. 8.16) to overcome this incompatibility and to permit a quantitative comparison. For this tailored system and for contact angles up to approximately 17° the global minimum of $\omega(l)$ is a bona fide local minimum and not an edge minimum, hence the SK theory is applicable. Already known features of the SK line tension have been recovered. This means that the asymptotic behavior of the line tension (see Fig. 8.19) follows Indekeu's predictions and the various contributions of the line tension (see Fig. 8.20) behave similarly as described by Getta and Dietrich [51] and confirmed by Bauer and Dietrich [11]. The fully micriscopic approach reveals a very different wetting temperature, but a similar behavior of the contact angle as a function of the reduced temperature describing the relative deviation from the wetting temperature. Around $\theta \simeq 17°$ the contact angle changes its behavior like in the SK case. Consequently a quantitative comparison of the results in the contact angle range between 10° and 17° should be relatively meaningful. Nevertheless, the quantitative agreement of the results from the SK theory and the fully microscopic theory is very poor. The fully microscopic line tension values are about ten to a hundred times as large as the corresponding SK line tension values for the employed position ($z = 0$) of the substrate–fluid dividing interface.

This discrepancy between the SK and the fully microscopic results was traced back to fundamental differences in the wetting behavior. In order to distinguish between the influences of the two approximations from the SK theory, namely the SK approximation of the density profiles and the local density approximation (LDA) for the hard-sphere energy contributions, two model systems have been introduced. First, the LDA-SK theory was upgraded to a non-local treatment of the hard-sphere part; this approach is called FMT-SK theory. Second, a hybrid model serves to approximately describe wetting within the fully microscopic theory in terms of an effective interface potential, $\omega_{\mathrm{hybrid}}(l)$. This hybrid theory is based on substrate–gas interfacial profiles which consist of the fully microscopic substrate–liquid interfacial structure up to the distance l from the substrate and bulk gas density beyond. For small film thicknesses, $l/R \lesssim 13$, the deviations between $\omega_{\mathrm{hybrid}}(l)$ and the LDA-SK and FMT-SK theories are severe (see Fig. 8.31). For very small film thicknesses, $l/R \lesssim 3$, the LDA leads additionally to deviations from the FMT-SK theory.

The line tension values within the LDA-SK theory, which represents the standard SK theory, are rather small, since the tailored substrate potential was designed such that the effective interface potential $\omega(l) = \omega_{\mathrm{LDA-SK}}(l)$ exhibits very small amplitudes for $\theta \lesssim 17°$ (see Fig. 8.17). At the same time the tailored substrate potential is strongest near the substrate surface (see Fig. 8.16). This is the spatial region where packing effects (density variations) are most pronounced. Hence in the considered situation the influence of packing effects is relatively strong. In the wetting studies the density $\varrho = \varrho(z)$ varies solely in one direction, perpendicular to the substrate surface, and already there the influence of the two approximations inherent in the SK theory are severe. However, the wedge scenario gives rise to density variations in two directions, $\varrho = \varrho(x, z)$, thus the effect of the two approximations is certainly even stronger. For all these reasons the discrepancy between the line tension values from SK theory and the fully microscopic calculation is plausible.

The hybrid model for the wetting behavior was applied to the SK line tension theory. This *hybrid line tension theory* corresponds to the standard SK line tension expressions, in which the improved effective interface potential $\omega_{\mathrm{hybrid}}(l)$ from the hybrid model is inserted. While the wetting behavior of the tailored system is described well by the hybrid

approach (see Fig. 8.29), the hybrid line tension values are at the order of magnitude of the SK results. Therefore the hybrid line tension theory fails to predict the order of magnitude of the fully microscopic results correctly (see Fig. 8.30). The origin of this discrepancy is most likely the lateral smoothing of the effectively two-dimensional density profile $\varrho(x, z)$ in the very vicinity of the three-phase contact line.

For the other four considered systems the hybrid theory describes the fully microscopic line tension values at least semi-quantitatively (see Figs. 8.25 to 8.28). The hybrid line tension theory is expected to be valid, if the spatial variations of the substrate potential and the solid–liquid interfacial density are comparably small. For a control of the qualitity of the hybrid approach, however, a comparison to results from fully microscopical line tension calculations is inevitable.

To conclude, in this work the line tension has been determinded with molecular resolution, which in this context marks the forefront of research. A semi-microscopic line tension theory based on the sharp-kink approximation has been further developed. The sharp-kink results concerning wetting and line tension behavior deviate considerably from the fully microscopic results. A hybrid line tension theory has been introduced, which employs an improved effective interface potential for the SK line tension calculation. For most of the studied cases the results from this hybrid method describe the fully microscopic line tension values semi-quantitatively. However, for a tailored system with relatively strong spatial variations of the substrate potential and of the solid–liquid interfacial density the hybrid method fails and does not predict the correct order of magnitude of the line tension values. Hence in general the fully microscopic approach is required, if one is interested in quantitatively reliable line tension values or/and if the validity of the hybrid method for the considered system has not been checked. The calculation of the line tension of a liquid wedge is an important contribution for understanding the shape of very small droplets (below the micrometer range). Furthermore a proposal is given, how axisymmetric sessile droplets can be addressed efficiently within DFT.

Appendix

A: Expansion of the weight function $w_{\mathrm{LJ}}(x,z)$

The attractive part of an intermolecular potential is accounted for in first-order perturbation theory by a weight function. In a three-dimensional system with translational invariance in one Cartesian direction the weight function $w_{\mathrm{LJ}}(x,z)$ for a Lennard-Jones (9–3) potential for a separation into repulsive and attractive parts following Weeks, Chandler, and Andersen (WCA) is given by Eq. (2.110) on page 36. At the origin the value is known analytically [Eq. (2.112)]. However, in a numerical implementation this expression is difficult to evaluate near the origin. Thus an expansion of $w_{\mathrm{LJ}}(x,z)$ around the origin, i. e., for small values of $c \equiv \sqrt{x^2+z^2}$ and for $0 < c < \sqrt[6]{2}\sigma_{\mathrm{LJ}}$, is displayed here:

$$\begin{aligned} w_{\mathrm{LJ}}(x,z) &\equiv w_{\mathrm{LJ}}\big(c/\sigma_{\mathrm{LJ}} =: s\big) \\ &= \beta\varepsilon_{\mathrm{LJ}}\sigma_{\mathrm{LJ}}\Big\{ -\frac{144}{55}\sqrt[6]{2} + \frac{36}{91}\,2^{5/6}\,s^2 + \frac{1}{15}\sqrt{2}\,s^4 + \frac{9}{374}\sqrt[6]{2}\,s^6 \\ &\qquad + \frac{45}{7904}\,2^{5/6}\,s^8 + \frac{1}{320}\sqrt{2}\,s^{10} + \frac{189}{100096}\sqrt[6]{2}\,s^{12} \\ &\qquad + \frac{297}{486400}\,2^{5/6}\,s^{14} + \frac{143}{344064}\sqrt{2}\,s^{16} + \frac{6435}{21856256}\sqrt[6]{2}\,s^{18} \\ &\qquad + \frac{21879}{203161600}\,2^{5/6}\,s^{20} + \mathcal{O}\left(s^{22}\right)\Big\}. \end{aligned} \tag{A.1}$$

B: Transformation of the wedge line tension

In Sec. 6.1 the topic is addressed, how the value of the liquid wedge line tension changes, if the solid–fluid dividing interface is shifted by δh in the positive z direction.

The grand potential of the whole system [Eq. (6.1)], including the substrate, is the starting point for this consideration. While the grand potential of the whole system stays the same, the line tension changes during the shift as

$$\begin{aligned} \tau^{(2)} - \tau^{(1)} &= \frac{1}{L}\Big\{ -\big(V_{\mathrm{s}}^{(2)} - V_{\mathrm{s}}^{(1)}\big)\,\omega_{\mathrm{s}} - \big(V_{\mathrm{f}}^{(2)} - V_{\mathrm{f}}^{(1)}\big)\,\omega_{\mathrm{f}} \\ &\qquad - \big(A_{\mathrm{sg}}^{(2)}\,\sigma_{\mathrm{sg}}^{(2)} - A_{\mathrm{sg}}^{(1)}\,\sigma_{\mathrm{sg}}^{(1)}\big) - \big(A_{\mathrm{sl}}^{(2)}\,\sigma_{\mathrm{sl}}^{(2)} - A_{\mathrm{sl}}^{(1)}\,\sigma_{\mathrm{sl}}^{(1)}\big) \\ &\qquad - \big(A_{\mathrm{lg}}^{(2)}\,\sigma_{\mathrm{lg}}^{(2)} - A_{\mathrm{lg}}^{(1)}\,\sigma_{\mathrm{lg}}^{(1)}\big)\Big\}. \end{aligned} \tag{B.2}$$

The grand canonical free energy density is the same for the liquid and gas phase,

$$\omega_{\mathrm{f}} = \omega_{\mathrm{l}} = \omega_{\mathrm{g}} = -p. \tag{B.3}$$

The changes of the surface areas are abbreviated as $\Delta A_i := A_i^{(2)} - A_i^{(1)}$ for $i \in \{\mathrm{sg}, \mathrm{sl}, \mathrm{lg}\}$. The volume change of the substrate,

$$\Delta V := V_{\mathrm{s}}^{(2)} - V_{\mathrm{s}}^{(1)} = \big(A_{\mathrm{sg}}^{(2)} + A_{\mathrm{sl}}^{(2)}\big)\,\delta h = \big(A_{\mathrm{sg}}^{(1)} + A_{\mathrm{sl}}^{(1)}\big)\,\delta h, \tag{B.4}$$

equals the negative value of the volume change of the fluid,

$$-\Delta V = V_{\mathrm{f}}^{(2)} - V_{\mathrm{f}}^{(1)}. \tag{B.5}$$

Furthermore the s–g and s–l surface tensions transform via Eq. (3.19), while the l–g surface tension is independent of the choice of the dividing interface (see Sec. 3.2.1):

$$\sigma_{\mathrm{sg}}^{(2)} = \sigma_{\mathrm{sg}}^{(1)} + (\omega_{\mathrm{g}} - \omega_{\mathrm{s}})\,\delta h \quad , \tag{B.6}$$

$$\sigma_{\mathrm{sl}}^{(2)} = \sigma_{\mathrm{sl}}^{(1)} + (\omega_{\mathrm{l}} - \omega_{\mathrm{s}})\,\delta h \quad , \tag{B.7}$$

$$\sigma_{\mathrm{lg}}^{(2)} = \sigma_{\mathrm{lg}}^{(1)} =: \sigma_{\mathrm{lg}}. \tag{B.8}$$

Hence the difference $\sigma_{\mathrm{sg}} - \sigma_{\mathrm{sl}}$ is independent of the choice of the dividing interface,

$$\sigma_{\mathrm{sg}}^{(2)} - \sigma_{\mathrm{sl}}^{(2)} = \sigma_{\mathrm{sg}}^{(1)} - \sigma_{\mathrm{sl}}^{(1)}. \tag{B.9}$$

For a macroscopic contact angle θ and an (infinitely large) length of the contact line, L, the area changes can be expressed as

$$A_{\mathrm{sg}}^{(2)} - A_{\mathrm{sg}}^{(1)} \equiv \Delta A_{\mathrm{sg}} = \frac{\delta h}{\tan\theta}\, L \quad , \tag{B.10}$$

$$A_{\mathrm{sl}}^{(2)} - A_{\mathrm{sl}}^{(1)} \equiv \Delta A_{\mathrm{sl}} = -\Delta A_{\mathrm{sg}} \quad , \tag{B.11}$$

$$A_{\mathrm{lg}}^{(2)} - A_{\mathrm{lg}}^{(1)} \equiv \Delta A_{\mathrm{lg}} = -\frac{\delta h}{\sin\theta}\, L. \tag{B.12}$$

With all these ingredients inserted Eq. (B.2) can be written as

$$\begin{aligned}
\tau^{(2)} - \tau^{(1)} &= \frac{1}{L}\Big\{\Delta V\left(\omega_{\mathrm{f}} - \omega_{\mathrm{s}}\right) - A_{\mathrm{sg}}^{(1)}\left(\sigma_{\mathrm{sg}}^{(2)} - \sigma_{\mathrm{sg}}^{(1)}\right) - A_{\mathrm{sl}}^{(1)}\left(\sigma_{\mathrm{sl}}^{(2)} - \sigma_{\mathrm{sl}}^{(1)}\right) \\
&\qquad - \Delta A_{\mathrm{sg}}\left(\sigma_{\mathrm{sg}}^{(2)} - \sigma_{\mathrm{sl}}^{(2)}\right) - \Delta A_{\mathrm{lg}}\,\sigma_{\mathrm{lg}}\Big\} && \text{(B.13)} \\
&= \frac{1}{L}\Big\{\left(A_{\mathrm{sg}}^{(1)} + A_{\mathrm{sl}}^{(1)}\right)\delta h\left(\omega_{\mathrm{f}} - \omega_{\mathrm{s}}\right) - A_{\mathrm{sg}}^{(1)}\left(\omega_{\mathrm{g}} - \omega_{\mathrm{s}}\right)\delta h \\
&\qquad - A_{\mathrm{sl}}^{(1)}\left(\omega_{\mathrm{l}} - \omega_{\mathrm{s}}\right)\delta h - \Delta A_{\mathrm{sg}}\left(\sigma_{\mathrm{sg}}^{(1)} - \sigma_{\mathrm{sl}}^{(1)}\right) \\
&\qquad - \Delta A_{\mathrm{lg}}\,\sigma_{\mathrm{lg}}\Big\} && \text{(B.14)} \\
&= \frac{1}{L}\left\{-\Delta A_{\mathrm{sg}}\left(\sigma_{\mathrm{sg}}^{(1)} - \sigma_{\mathrm{sl}}^{(1)}\right) - \Delta A_{\mathrm{lg}}\,\sigma_{\mathrm{lg}}\right\} && \text{(B.15)} \\
&= \frac{1}{L}\left\{-\frac{\delta h}{\tan\theta}\, L\left(\sigma_{\mathrm{sg}}^{(1)} - \sigma_{\mathrm{sl}}^{(1)}\right) - \left(-\frac{\delta h}{\sin\theta}\, L\right)\sigma_{\mathrm{lg}}\right\} && \text{(B.16)} \\
&= \frac{\sigma_{\mathrm{lg}} + \left(\sigma_{\mathrm{sl}}^{(1)} - \sigma_{\mathrm{sg}}^{(1)}\right)\cos\theta}{\sin\theta}\,\delta h. && \text{(B.17)}
\end{aligned}$$

Applying Young's law finally yields

$$\tau^{(2)} - \tau^{(1)} = \sigma_{\mathrm{lg}}\,\sin\theta\;\delta h. \tag{B.18}$$

Hence the liquid wedge line tension strongly depends on the definition of the solid–fluid dividing interface.

C: Wetting as a phase transition

Here a summary of the argumentation [142] is presented, why wetting represents a phase transition in a strict sense (see Sec. 3.3.5). Furthermore it is illustrated that complete and critical wetting correspond to second-order or continuous phase transitions and that first-order wetting justly carries its name.

For *complete wetting* the excess adsorption diverges as

$$-\frac{\partial\sigma_{\mathrm{sg}}}{\partial\mu} \overset{(3.26)}{=} \Gamma = |\mu-\mu_{\mathrm{coex}}|^{\beta_{\mathrm{complete}}}. \tag{C.19}$$

At complete wetting the surface solid–gas surface tension approaches the sum of the other two surface tensions,

$$\sigma_{\mathrm{sg}}-(\sigma_{\mathrm{sl}}+\sigma_{\mathrm{lg}}) \sim -|\mu-\mu_{\mathrm{coex}}|^{2-\alpha_{\mathrm{complete}}}, \tag{C.20}$$

where the critical exponents are related via $\beta_{\mathrm{complete}} = 1-\alpha_{\mathrm{complete}}$. Hence the second derivative of σ_{sg} (with respect to μ) diverges as

$$-\frac{\partial^2\sigma_{\mathrm{sg}}}{\partial\mu^2} \sim |\mu-\mu_{\mathrm{coex}}|^{-\alpha_{\mathrm{complete}}}. \tag{C.21}$$

For *critical wetting* the excess adsorption diverges as

$$-\frac{\partial\sigma_{\mathrm{sg}}}{\partial\mu} \overset{(3.26)}{=} \Gamma = |t|^{\beta_{\mathrm{crit}}} \tag{C.22}$$

with t as a reduced temperature, that indicates the relative deviation from the wetting temperature,

$$t := \frac{T_{\mathrm{w}}-T}{T_{\mathrm{w}}}. \tag{C.23}$$

The solid–gas surface tension approaches its limiting value as

$$\sigma_{\mathrm{sg}}-(\sigma_{\mathrm{sl}}+\sigma_{\mathrm{lg}}) \sim -|t|^{2-\alpha_{\mathrm{critical}}}, \tag{C.24}$$

so that the second derivative of σ_{sg} (with respect to t) diverges as

$$-\frac{\partial^2\sigma_{\mathrm{sg}}}{\partial t^2} \sim |t|^{-\alpha_{\mathrm{critical}}}. \tag{C.25}$$

Consequently critical and complete wetting transitions are second-order or continuous phase transitions,

For *first-order wetting* the solid–gas surface tension behaves as

$$\sigma_{\mathrm{sg}}-(\sigma_{\mathrm{sl}}+\sigma_{\mathrm{lg}}) \sim \begin{cases} -|t| & \text{for } t<0 \quad (\text{i.e., } T<T_{\mathrm{w}}) \\ 0 & \text{for } t>0 \quad (\text{i.e., } T>T_{\mathrm{w}}). \end{cases} \tag{C.26}$$

Thus the surface entropy

$$s_{\mathrm{surface}} = -\frac{\partial\sigma_{\mathrm{sg}}}{\partial T}, \tag{C.27}$$

that is involved in the differential relation [Eq. (1.12) in Ref. [142]]

$$\mathrm{d}\sigma = -s_{\mathrm{surface}}\,\mathrm{d}T - \Gamma\,\mathrm{d}\mu, \tag{C.28}$$

makes a jump at the wetting temperature; this is associated with a latent heat. Since a first partial derivative of the surface entropy exhibits a jump, a first-order wetting transition truely fulfills the definition of a first-order phase transition.

Zusammenfassung

Ein flüssiger Keil, der auf einem Substrat ruht, wurde theoretisch untersucht. Zugehörige Linienspannungswerte wurden in einem vollmikroskopischen, nicht-lokalen Zugang auf Grundlage klassischer Dichtefunktionaltheorie (DFT) berechnet. Eine Lennard-Jones-Flüssigkeit (LJ) und eine Square-Well-Flüssigkeit (SW) dienten als Modellflüssigkeiten, d. h. das Fluidum besteht aus Teilchen, die mittels eines langreichweitigen LJ-(12–6)-Potentials oder eines kurzreichweitigen SW-Potentials wechselwirken. Die Form des SW-Potentials legt nahe, wie man das Potential in abstoßende und anziehende Teile zerlegen kann. Die LJ-Wechselwirkung wurde gemäß des Weeks-Chandler-Andersen-Schemas (WCA) in abstoßende und anziehende Teile zerlegt, so dass das LJ-Fluid durch ein WCA-LJ-Fluid angenähert wird. Der abstoßende Teil der Fluid–Fluid-Wechselwirkung wurde durch die Fundamental Measure Theory (FMT) berücksichtigt, während der anziehende Teil mit Hilfe der Random Phase Approximation (RPA), einer Mean-Field-artigen Störungstheorie, behandelt wurde. Das Substrat wurde als homogen, flach und chemisch inert vorausgesetzt. Seine Wechselwirkung mit einem einzelnen Fluidteilchen wurde durch diverse Substratpotentiale beschrieben, nämlich einem LJ-(9–3)-Potential, einem LJ-(9–4–3)-Potential, einem abgeschnittenen und verschobenen LJ-(9–3)-Potential und einem maßgeschneiderten Potential. Bei der Sharp-Kink-Näherung (SK-Näherung, s. Abb. 7.1), welche in vorangegangenen, verwandten Arbeiten benutzt wurde, sind die Teilchendichteverteilungen stückweise konstant. Im Gegensatz dazu verwendete die hier vorgestellte vollmikroskopische Rechnung kontinuierliche Dichteprofile. Daher wurden Packungseffekte (d. h., Dichteschwankungen nahe der Substratoberfläche) berücksichtigt. Das Modellsystem eines aufsitzenden flüssigen Keils ist effektiv zweidimensional, was sich in einer zweidimensionalen räumlichen Abhängigkeit der Teilchendichteverteilung, $\varrho = \varrho(x, z)$, widerspiegelt. Verschiedene Vorsichtsmaßnahmen wurden ergriffen, um eine hinreichend große Genauigkeit der berechneten Linienspannungen zu erreichen.

Auf verschiedene Benetzungsszenarien wurde eingegangen, nämlich sowohl auf Benetzung erster Ordnung unter Einfluss kurz- und langreichweitiger Kräfte als auch auf kritische Benetzung unter Einfluss langreichweitiger Kräfte. Der Vergleich mit Indekeus Vorhersagen für das Linienspannungsverhalten beim Annähern an Benetzungsphasenübergänge [44] ist mit den zur Verfügung stehenden Computerresourcen für Kontaktwinkel ab ca. 5 bis 10° möglich. Die Ergebnisse sind mit Indekeus Vorhersagen vereinbar (s. Abb. 8.5, 8.7, 8.13 und 8.15). Dieser Befund stützt die Vermutung, dass strukturelle Details für das qualitative Verhalten der Linienspannung nahe eines Benetzungsübergangs unwichtig sind.

Um zu klären, wie wichtig Packungseffekte für Linienspannungswerte sind, wurde ein Vergleich mit Ergebnissen einer SK-Linienspannungstheorie angestellt. Zu diesem Zweck wurde die SK-Linienspannungstheorie erweitert, so dass sie die betrachteten Fluid–Fluid-Wechselwirkungspotentiale, d. h., das WCA-LJ-Potential und das SW-Potential, enthält. Ein quantitativer Vergleich zwischen dem vollmikroskopischen Zugang und dem semi-mikroskopischen SK-Zugang is sehr schwierig, weil man typischerweise folgendem Phänomen gegenübersteht: Für Parameter, die für SK-Rechnungen gut geeignet sind weist das Fluidum gemäß der vollmikroskopischen Theorie (i) Benetzung bei einer viel niedrigeren Temperatur oder/und (ii) lokale Kristallisation nahe der Substratoberfläche auf, welche einen vollmikroskopischen Zugang sehr schwierig oder in den meisten Fällen unmöglich macht. Auf der anderen Seite führen für das vollmikroskopische Programm

günstige Parameter zu einem Randminimum im effektiven Grenzflächenpotential, d. h., das globale Minimum von $\omega(l)$ erscheint nahe der Substratoberfläche. In diesem Fall sind die SK-Vorhersagen von den vollmikroskopischen Ergebnissen völlig verschieden.

Ein Substratpotential wurde entworfen (s. Abb. 8.16), um diese Inkompatibilität zu überwinden und einen quantitativen Vergleich zu erlauben. Für dieses maßgeschneiderte System und für Kontatkwinkel bis ca. 17° ist das globale Minimum von $\omega(l)$ ein echtes lokales Minimum und kein Randminimum, folglich ist die SK-Theorie anwendbar. Bereits bekannte Aspekte der SK-Linienspannung wurden wiedergefunden. Das heißt, das asymptotische Verhalten der Linienspannung (s. Abb. 8.19) gehorcht Indekeus Vorhersagen und die einzelnen Beiträge der Linienspannung (s. Abb. 8.20) verhalten sich ähnlich wie von Getta und Dietrich [51] beschrieben und von Bauer und Dietrich [11] bestätigt. Der vollmikroskopische Zugang offenbart eine ganz andere Benetzungstemperatur, weist aber ein ähnliches Verhalten des Kontaktwinkels als Funktion der reduzierten Temperatur auf, welche die relative Abweichung von der Benetzungstemperatur beschreibt. Um $\theta \simeq 17°$ ändert der Kontaktwinkel sein Verhalten wie im SK-Fall. Folglich sollte ein quantitativer Vergleich der Ergebnisse im Kontaktwinkelbereich zwischen 10° und 17° aussagekräftig sein. Nichtsdestotrotz weichen die Ergebnisse der SK-Theorie und der vollmikroskopischen Theorie quantitativ stark ab. Die vollmikroskopischen Linienspannungswerte sind ungefähr zehnmal so groß wie die zugehörigen SK-Linienspannungswerte für die verwendete Position der Substrat–Fluid-Grenzfläche.

Diese Diskrepanz wurde auf grundlegende Unterschiede des Benetzungsverhaltens zurückgeführt. Um zwischen den Einflüssen der beiden Näherungen der SK-Theorie zu unterscheiden, nämlich der SK-Näherung der Dichteprofile und der lokalen Dichtenäherung (LDA) für den Hartkugel-Energiebeitrag, wurden zwei Modellsysteme eingeführt. Erstens wurde die LDA-SK-Theorie durch eine nicht-lokale Behandlung des Hartkugelanteils erweitert; dieser Zugang wird FMT-SK-Theorie genannt. Zweitens dient ein Hybridmodell dazu, Benetzung gemäß der vollmikroskopischen Theorie näherungsweise in Form eines effektiven Grenzflächenpotentials, $\omega_{\text{hybrid}}(l)$, zu beschreiben. Diese Hybridtheorie basiert auf Substrat–Gas-Grenzflächenprofieln, die bis zum Abstand l vom Substrat aus der vollmikroskopischen Substrat–Flüssigkeits-Grenzflächenstruktur und ab dort aus der "Bulk"-Gasdichte bestehen. Für kleine Filmdicken, $l/R \lesssim 13$, sind die Abweichungen zwischen $\omega_{\text{hybrid}}(l)$ und der LDA-SK- und FMT-SK-Theorie schwerwiegend (s. Abb. 8.31). Für sehr kleine Filmdicken, $l/R \lesssim 3$, führt die LDA zusätzlich zu Abweichungen von der FMT-SK-Theorie.

Die Linienspannungswerte gemäß der LDA-SK-Theorie, die die standardmäßige SK-Theorie darstellt, sind ziemlich klein, da das maßgeschneiderte Potential so entworfen worden ist, dass das effektive Grenzflächenpotential $\omega(l) = \omega_{\text{LDA-SK}}(l)$ für $\theta \lesssim 17°$ sehr kleine Amplituden aufweist(s. Abb. 8.17). Gleichzeitig ist das maßgeschneiderte Potential am stärksten nahe der Substratoberfläche (s. Abb. 8.16). Dies ist das räumliche Gebiet, wo Packungseffekte (Dichteschwankungen) am ausgeprägtesten sind. Daher ist in der untersuchten Situation der Einfluss von Packungseffekten relativ stark. In Benetzungsuntersuchungen ändert sich die Dichte $\varrho = \varrho(z)$ lediglich in einer Richtung, senkrecht zur Substratoberfläche, und bereits da ist die Wirkung der zwei der SK-Theorie innewohnenden Näherungen schwerwiegend. Allerdings führt das Keil-Szenario zu Dichteänderungen in zwei Richtungen, $\varrho = \varrho(x, z)$, somit ist der Effekt der zwei Näherungen gewiss noch stärker. Aus diesen Gründen ist die Diskrepanz zwischen den Linienspannungswerten der SK-Theorie und der vollmikroskopischen Theorie plausibel.

Das Hybridmodell für das Benetzungsverhalten wurde auf die SK-Linienspannungstheorie angewandt. Diese *Hybrid-Linienspannungstheorie* entspricht den gewöhnlichen Ausdrücken für die Sharp-Kink-Linienspannung, in die das verbesserte effektive Grenzflächenpotential $\omega_{\mathrm{hybrid}}(l)$ des Hybridmodells eingesetzt worden ist. Während das Benetzungsverhalten des maßgeschneiderten Systems durch den Hybridzugang gut beschrieben wird (s. Abb. 8.29), sind die Hybrid-Linienspannungswerte in der Größenordnung der SK-Ergebnisse. Daher versagt die Hybrid-Linienspannungstheorie, die Größenordnung der vollmikroskopischen Linienspannungsergebnisse korrekt vorherzusagen (s. Abb. 8.30). Der Ursprung dieser Diskrepanz ist höchstwahrscheinlich die laterale Glättung des effektiv zweidimensionalen Dichteprofils $\varrho(x, z)$ im engen Umfeld der Dreiphasen-Kontaktlinie.

Bei den anderen vier betrachteten System beschreibt die Hybridtheorie die vollmikroskopischen Linienspannungswerte mindestens semi-quantitativ (s. Abb. 8.25 bis 8.28). Von der Hybrid-Linienspannungstheorie wird erwartet, dass sie gültig ist, falls die räumlichen Schwankungen des Substratpotentials und der Substrat–Flüssigkeits-Grenzflächendichte vergleichsweise klein sind. Für eine Kontrolle der Qualität des Hybridzugangs ist jedoch ein Vergleich mit vollmikroskopischen Linienspannungswerten unvermeidlich.

Zusammenfassend wurde in dieser Arbeit die Linienspannung mit molekularer Auflösung bestimmt, was in diesem Kontext die Forschungsfront darstellt. Eine auf der Sharp-Kink-Näherung basierende semi-mikroskopische Linienspannungstheorie wurde weiterentwickelt. Die Sharp-Kink-Ergebnisse bezüglich Benetzung und Linienspannungsverhalten weichen beträchtlich von den vollmikroskopischen Ergebnissen ab. Eine Hybrid-Linienspannungstheorie wurde eingeführt, welche ein verbessertes effektives Grenzflächenpotential für die Sharp-Kink-Linienspannungsberechnung verwendet. In den meisten der untersuchten Fälle beschriben Ergebnisse dieser Hybridtheorie die vollmikroskopischen Linienspannungswerte semi-quantitativ. Jedoch beim maßgeschneiderten System mit relativ starken räumlichen Schwankungen des Substratpotentials und der Substrat–Flüssigkeits-Grenzflächendichte versagt die Hybridmethode und beschreibt die Größenordnung der Linienspannungswerte nicht richtig. Folglich ist im Allgemeinen der vollmikroskopische Zugang erforderlich, falls man an quantitativ verlässlichen Linienspannungswerten interessiert ist oder/und falls die Gültigkeit der Hybridmethode für das betrachtete System nicht überprüft worden ist. Die Berechung der Linienspannung eines flüssigen Keils ist ein wichtiger Beitrag zum Verständnis der Form sehr kleiner Tröpfchen (unterhalb des Mikrometerbereichs). Ferner wird ein Vorschlag gemacht, wie axialsymmetrische, aufsitzende Tröpfchen mittels DFT effizient behandelt werden können.

Bibliography

[1] Picture taken from http://researchnews.osu.edu/archive/nanocrptpix.htm and used by courtesy of the originator, the Ohio State University.

[2] T. Young, *An essay on the cohesion of fluids*, Philos. Trans. R. Soc. London **95**, 65 (1805).

[3] J. W. Gibbs, *On the equilibrium of heterogeneous substances*, Connecticut Academy Transactions **3**, 108-248 and 343-524 (1878). Also in *The scientific papers of J. Willard Gibbs*, (OxBow Press, Woodbridge, 1993), Vol. 1, p. 288.

[4] L. Schimmele, M. Napiórkowski, and S. Dietrich, *Conceptual aspects of line tensions*, J. Chem. Phys. **127**, 164715 (2007).

[5] A. I. Rusanov, *Thermodynamics of solid surfaces*, Surf. Sci. Rep. **23**, 173 (1996); *Surface thermodynamics rvisited*, Surf. Sci. Rep. **58**, 111 (2005);

[6] A. I. Rusanov, *Classification of line tension*, Colloids Surf. A **156**, 315 (1999).

[7] P. G. de Gennes, *Wetting: statics and dynamics*, Rev. Mod. Phys. **57**, 827 (1985).

[8] H. Fan, *Liquid droplet spreading with line tension effect*, J. Phys.: Condens. Matter **18**, 4481 (2006).

[9] G. Navascués and P. Tarazona, *Line tension effects in heterogeneous nucleation theory*, J. Chem. Phys. **75**, 2441 (1981).

[10] S. Perković, E. M. Blokhuis, E. Tessler, and B. Widom, *Boundary tension: from wetting transition to prewetting critical point*, J. Chem. Phys. **102**, 7584 (1995).

[11] C. Bauer and S. Dietrich, *Quantitative study of laterally inhomogeneous wetting films*, Eur. Phys. J. B **10**, 767 (1999).

[12] J. Drelich, J. D. Miller, A. Kumar, and G. M. Whitesides, *Wetting characteristics of liquid drops at heterogeneous surfaces*, Colloids Surf. A **93**, 1 (1994). J. Drelich, J. L. Wilbur, J. D. Miller, and G. M. Whitesides, *Contact angles for liquid drops at a model heterogeneous surface consisting of alternating and parallel hydrophobil/hydrophilic strips*, Langmuir **12**, 1913 (1996); C. Fang and J. Drelich, *Theoretical contact angles on a nano-heterogeneous surface composed of parallel apolar and polar strips*, Langmuir **20**, 6679 (2004).

[13] A. Marmur and B. Krasovitski, *Line tension on curved surfaces: liquid drops on solid micro- and nanospheres*, Langmuir **18**, 8919 (2002).

[14] L. Guzzardi and R. Rosso, *Sessile droplets on a curved substrate: effects of line tension*, J. Phys. A: Math. Theor. **40**, 19 (2007).

[15] A. I. Hienola, P. M. Winkler, P. E. Wagner, H. Vehkamäki, A. Lauri, I. Napari, and M. Kulmala, *Estimation of line tension and contact angle from heterogeneous nucleation experimental data*, J. Chem. Phys. **126**, 094705 (2007).

[16] C. Bauer and S. Dietrich, *Shapes, contact angles, and line tensions of droplets on cylinders*, Phys. Rev. E **62**, 2428 (2000).

[17] V. W. A. de Villeneuve, R. P. A. Dullens, D. G. A. L. Aarts, E. Groeneveld, J. H. Scherff, W. K. Kegel, and H. N. W. Lekkerkerker, *Colloidal hard-sphere crystal growth frustrated by large spherical impurities*, Science **309**, 1231 (2005).

[18] V. W. A. de Villeneuve, D. Verboekend, R. P. A. Dullens, D. G. A. L. Aarts, W. K. Kegel, and H. N. W. Lekkerkerker, *Hard sphere crystal nucleation and growth near large spherical impurities*, J. Phys.: Condens. Matter **17**, S3371 (2005).

[19] U. Retter, K. Siegler, and D. Vollhardt, *Determination of the nucleus-to-surroundings interfacial tensions and the line tension of lenticular nuclei formed from insoluble monolayers at the air–water interface*, Langmuir **12**, 3976 (1996).

[20] E. Mendez-Villuendas, and R. K. Bowles, *Surface nucleation in the freezing of gold nanoparticles*, Phys. Rev. Lett. **98**, 185503 (2007).

[21] S. Suzuki, A. Nakajima, N. Yoshida, M. Sakai, A. Hashimoto, Y. Kameshima, and K. Okada, *Freezing of water droplets on silicon surfaces coated with various silanes*, Chem. Phys. Lett. **445**, 37 (2007).

[22] E. M. Blokhuis, *Boundary tension between amphiphilic layers*, Int. J. Thermophysics **16**, 53 (1995); *Structure and tension of the boundary line between amphiphilic layers*, Physica A **214**, 169 (1995).

[23] L. Zou, J. Wang, P. Basnet, and E. K. Mann, *Line tension and structure of smectic liquid-crystal multilayers at the air-water interface*, Phys. Rev. E **76**, 031602 (2007).

[24] M. Schick, K. Katsov, and M. Müller, *The central role of line tension in the fusion of biological membrane*, Phys. Rev. Lett. **95**, 226107 (2005).

[25] T. Baumgart, S. T. Hess, and W. W. Webb, *Imaging coexisting fluid domains in biomembrane models coupling curvature and line tension*, Nature **425**, 821 (2003).

[26] S. A. Akimov, P. I. Kuzmin, J. Zimmerberg, and F. S. Cohen, *Lateral tension increases the line tension between two domains in a lipid bilayer membrane*, Phys. Rev. E **75**, 011919 (2007).

[27] A. Tian, C. Johnson, W. Wang, and T. Baumgart, *Line tension at fluid membrane domain boundaries measured by micropipette aspiration*, Phys. Rev. Lett. **98**, 208102 (2007).

[28] K. B. Towles, and N. Dan, *Line tension and coalescence in heterogeneous membranes*, Langmuir **23**, 13053 (2007).

[29] A. Naydenov, P. A. Pincus, and S. A. Safran, *Equilibrium domains on heterogeneously charged surfaces*, Langmuir **23**, 12016 (2007).

[30] C. Esposito, A. Tian, S. Melamed, C. Johnson, S.-Y. Tee, and T. Baumgart, *Flicker spectroscopy of thermal lipid bilayer domain boundary fluctuations*, Biophys. J. **93**, 3169 (2007).

[31] B.-L. Stottrup, A. M. Heussler, and T. A. Bibelnieks, *Determination of line tension in lipid monolayers by Fourier analysis of capillary waves*, J. Phys. Chem. Lett. B **111**, 11091 (2007).

[32] S. Trabelsi, S. Zhang, T. R. Lee, and D. K. Schwartz, *Linactants: surfactant analogues in two dimensions*, Phys. Rev. Lett. **100**, 037802 (2008).

[33] J. A. de Feijter, and A. Vrij, *I. Transition regions, line tensions, and contact angles in soap films*, J. Electroanal. Chem. **37**, 9 (1972).

[34] B. V. Toshev, and D. Platikanov, *Disjoining pressure, contact angles, and line tension in free thin liquid films*, Adv. Coll. Interf. Sci. **40**, 157 (1992).

[35] J. R. Wintersmith, L. Zou, A. J. Bernoff, J. C. Alexander, J. A. Mann, Jr., E. E. Kooijman, and E. K. Mann, *Determination of interphase line tension in Langmuir films*, Phys. Rev. E **75**, 061605 (2007).

[36] L. Zhang and S. Taniguchi, *Fundamentals of inclusion removal from liquid steel by bubble flotation*, Int. Mater. Rev. **45**, 59 (2000).

[37] A. Amirfazli and A. W. Neumann, *Status of the three-phase line tension*, Adv. Coll. Interf. Sci. **110**, 121 (2004).

[38] J. Y. Wang, S. Betelu, and B. M. Law, *Line tension approaching a first-order wetting transition: experimental results from contact angle measurements*, Phys. Rev. E **63**, 031601 (2001).

[39] L. R. White, *The contact angle on an elastic substrate. 1. The role of disjoining pressure in the surface mechanics*, J. Colloid Interface Sci. **258**, 82 (2003).

[40] E. M. Blokhuis, Y. Shilkrot, and B. Widom, *Young's law with gravity*, Mol. Phys. **86**, 891 (1995).

[41] E. M. Blokhuis, *Comment on "Effect of gravity on contact angle: a theoretical investigation" [J. Chem. Phys. 109, 3651 (1998)]*, J. Chem. Phys. **112**, 5511 (2000).

[42] S. Vafaei and M. Z. Podowski, *Theoretical analysis on the effect of liquid droplet geometry on contact angle*, Nucl. Eng. Des. **235**, 1293 (2005). *Analysis of the relationship between liquid droplet size and contact angle*, Adv. Coll. Interf. Sci. **113**, 133 (2005).

[43] P. Tarazona and G. Navascués, *A statistical mechanical theory for line tension*, J. Chem. Phys. **75**, 3114 (1981).

[44] J. O. Indekeu, *Line tension near the wetting transition: results from an interface displacement model*, Physica A **183**, 439 (1992).

[45] J. O. Indekeu, *Line tension at wetting*, Int. J. Mod. Phys. B **3**, 309 (1994).

[46] H. T. Dobbs and J. O. Indekeu, *Line tension at wetting: interface displacement model beyond the gradient-squared approximation*, Physica A **201**, 457 (1993).

[47] J. O. Indekeu and H. T. Dobbs, *Line tension at wetting: finite-size effects and scaling functions*, J. Phys. I France **4**, 77 (1994).

[48] S. Perkovic, E. M. Blokhuis, and G. Han, *Line and boundary tensions at the wetting transition: two fluid phases on a substrate*, J. Chem. Phys. **102**, 400 (1995).

[49] E. M. Blokhuis, *Line tension between two surface phases on a substrate*, Physica A **202**, 402 (1994).

[50] T. Getta, *Oberflächen- und Linienspannungen bei Benetzungsphasenübergängen*, thesis, Bergische Universität Wuppertal (1996).

[51] T. Getta and S. Dietrich, *Line tension between fluid phase and a substrate*, Phys. Rev. E **57**, 655 (1998).

[52] C. Bauer, *Benetzung chemisch strukturierter Substrate*, thesis, Bergische Universität Wuppertal (1999).

[53] H. T. Dobbs, *Line tension of n-alkanes on water from a Cahn-type theory*, Langmuir **15**, 2586 (1999).

[54] A. S. Clarke, *Thermal fluctuations of a three phase contact line. I. Two fluid phases and one solid phase*, J. Chem. Phys. **96**, 9073 (1992).

[55] L. Boruvka and A. W. Neumann, *Generalization of the classical theory of capillary*, J. Chem. Phys. **66**, 5464 (1976).

[56] A. Marmur, *Line tension and the intrinsic vontact angle in solid–liquid–fluid systems*, J. Colloid Interface Sci. **186**, 462 (1997).

[57] A. I. Rusanov, A. K. Shchekin, and D. V. Tatyanenko, *The line tension and the generalized Young equation: the choice of dividing surface*, Colloids Surf. A **250**, 263 (2004).

[58] J. A. Nieminen, D. B. Abraham, M. Karttunen, and K. Kaski, *Molecular dynamics of a microscopic droplet on solid surface*, Phys. Rev. Lett. **69**, 124 (1992).

[59] T. Werder, J. H. Walther, R. L. Laffe, T. Halicioglu, and P. Koumoutsakos, *On the water–carbon interaction for use in molecular dynamics simulations of graphite and carbon nanotubes*, J. Phys. Chem. B **107**, 1345 (2003); R. L. Laffe, P. Gonnet, T. Werder, J. H. Walther, and P. Koumoutsakos, *Water–carbon interactions 2: calibration of potentials using contact angle data for different interaction models*, Molecular Simulation **30**, 205 (2004).

[60] T. Ingebrigsten and S. Toxvaerd, *Contact angles of Lennard-Jones liquids and droplets on planar surfaces*, J. Phys. Chem. C **111**, 8518 (2007).

[61] H.-K. Guo and H.-P. Fang, *Drop size dependence of the contact angle of nanodroplets*, Chin. Phys. Lett. **22**, 787 (2005).

[62] J. T. Hirvi and T. A. Pakkanen, *Molecular dynamics simulations of water droplets on polymer surfaces*, J. Chem. Phys. **125**, 144712 (2006).

[63] E. R. Cruz-Chu, A. Aksimentiev, and K. Schulten, *Water–silica force field for simulating nanodevices*, J. Phys. Chem. B **110**, 21497 (2006).

[64] A. I. Milchev and A. A. Milchev, *Wetting behavior of nanodroplets: the limits of Young's rule validity*, Europhys. Lett. **56**, 695 (2001).

[65] D. Gandolfo, L. Laanait, S. Miracle-Sole, and J. Ruiz, *A lattice model for the line tension of a sessile drop*, J. Stat. Phys. **126**, 133 (2007).

[66] For an introduction see J.-P. Hansen and I. R. McDonald, *Theory of simple liquids*, (Academic Press, London, 1986), second edition.

[67] A. Checco and P. Guenoun, *Nonlinear dependence of the contact angle of nanodroplets on contact line curvature*, Phys. Rev. Lett. **91**, 186101 (2003).

[68] T. Pompe and S. Herminghaus, *Three-phase contact line energetics from nanoscale liquid surface topographies*, Phys. Rev. Lett. **85**, 1930 (2000).

[69] T. Pompe, *Line tension behavior of a first-order wetting system*, Phys. Rev. Lett. **89**, 076102 (2002).

[70] A. Checco, H. Schollmeyer, J. Daillant, P. Guenoun, and R. Boukherroub, *Nanoscale wettability of self-assembled monolayers investigated by noncontact atomic force microscopy*, Langmuir **22**, 116 (2006).

[71] K. W. Stöckelhuber, B. Radoev, and H. J. Schulze, *Some new observations on line tension of microscopic droplets*, Colloids Surf. A **156**, 323 (1999).

[72] M. Sundberg, A. Månsson, and S. Tågerud, *Contact angle measurements by confocal microscopy for non-destructive microscale surface characerization*, J. Colloid Interf. Sci. **313**, 454 (2007).

[73] D. Aronov, G. Rosenman, and Z. Barkay, *Wettability study of modified silicon dioxide surface using environmental scanning electron microscopy*, J. Applied Phys. **101**, 084901 (2007).

[74] Y. Rotenberg, L. Boruvka, and A. W. Neumann, *Determination of surface tension and contact angle from the shapes of axisymmetric fluid interfaces*; J. Colloid Interface Sci. **93**, 169 (1982).

[75] P. Cheng, D. Li, L. Boruvka, Y. Rotenberg, and A. W. Neumann, *Automation of axisymmetric drop shape analysis for measurements of interfacial tensions and contact angles*; Colloids Surf. **43**, 151 (1990).

[76] J. Lee, K. Morita, and T. Tanaka, *Determination of macro-contact angle and line tension at high temperatures for Au/Al_2O_3 system at 1373 K using a micro-scale wetting method*, Mater. Trans. **44**, 2659 (2003).

[77] J. Lee, M. Nakamoto, and T. Tanaka, *Thermodynamic study on the melting of nanometer-sized gold particles on graphite substrate*, J. Mater. Sci. **40**, 2167 (2005).

[78] F. Mugele and J.-C. Baret, *Electrowetting: from basics to applications*, J. Phys.: Condens. Matter **17**, R705 (2005).

[79] B. Shapiro, H. Moon, R. L. Garrell, and C.-J. Kim, *Equilibrium behavior of sessile dropls under surface tension, applied external fields and material variations*, J. Applied Phys. **93**, 5794 (2003).

[80] J. Buehrle, S. Herminghaus, and F. Mugele, *Interface profiles near three-phase contact lines in electric fields*, Phys. Rev. Lett. **91**, 086101 (2003).

[81] F. Mugele, A. Klingner, J. Buehrle, D. Steinhauser, and S. Herminghaus, *Electrowetting: a convenient way to switchable wettability patterns*, J. Phys.: Condens. Matter **17**, S559 (2005).

[82] F. Mugele and J. Buehrle, *Equilibrium drop surface profiles in electric fields*, J. Phys.: Condens. Matter **19**, 375112 (2007).

[83] H. Ren, R. B. Fair, M. G. Pollack, and E. J. Shaughnessy, *Dynamics of electrowetting droplet transport*, Sens. Act. B **87**, 201 (2002).

[84] S. Walker and B. Shapiro, *A control method for steering individual particles inside liquid droplets actuated by electrowetting*, Lab Chip **5**, 1404 (2005).

[85] R. Digilov, *Charge-induced modification of contact angle: the secondary electrocapillary effect*, Langmuir **16**, 6719 (2000).

[86] K. H. Kang, I. S. Kang, and C. M. Lee, *Electrostatic contribution to line tension in a wedge-shaped contact region*, Langmuir **19**, 9334 (2003).

[87] J. Drelich and D. Chibowska, *Spreading kinetics of water drops on self-assembled monolayers of thiols: Significance of Intertial Effects*, Langmuir **21**, 7733 (2005).

[88] J. Drelich, *Instability of the three-phase contact region and its effect on contact angle relaxation*, J. Adhesion Sci. Technol. **13**, 1437 (1999).

[89] U. Frisch, B. Hasslacher, and Y. Pomeau, *Lattice-gas automata for the Navier-Stokes equation*, Phys. Rev. Lett. **56**, 1505 (1986).

[90] D. Raabe, *Overview of the lattice Boltzmann method for nano- and microscale fluid dynamics in materials science and engineering*, Modelling Simul. Mater. Sci. Eng. **12**, R13 (2004).

[91] J. Hyväluoma, A. Koponen, P. Raiskinmäki, and J. Timonen, *Droplets on inclined rough surfaces*, Eur. Phys. J. E **23**, 289 (2007).

[92] L. Guzzardi, R. Rosso, and E. G. Virga, *Residual stability of sessile droplets with negative line tension*, Phys. Rev. E **73**, 021602 (2006) and references therein.

[93] X. Noblin, A. Buguin, and F. Brochard-Wyart, *Triplon modes of puddles*, Phys. Rev. Lett. **94**, 166102 (2005).

[94] D. Bartolo, F. Bouamrirene, É. Verneuil, A. Buguin, P. Silberzan, and S. Moulinet, *Bouncing or sticky droplets: impalement transitions on superhydrophobic micropatterned surfaces*, Europhys. Lett. **74**, 299 (2006).

[95] S. Wurlitzer, P. Steffen, M. Wurlitzer, Z. Khattari, and Th. M. Fischer, *Line tension in Langmuir monolayers probed by point forces*, J. Chem. Phys. **113**, 3822 (2000).

[96] H. Dobbs, *The elasticity of a contact line*, Physica A **271**, 36 (1999).

[97] J. R. Errington and D. W. Wilbert, *Prewetting boundary tensions from Monte Carlo simulations*, Phys. Rev. Lett. **95**, 226107 (2005).

[98] H. Ibach, M. Giesen, and W. Schmickler, *Potential dependence of the step line tension on surfaces in contact with an electrolyte*, J. Electroanalytical Chem. **544**, 13 (2003).

[99] I. Szleifer and B. Widom, *Surface tension, line tension and wetting*, Mol. Phys. **75**, 925 (1992).

[100] K. Koga and B. Widom, *Line and boundary tensions on approach to the wetting transition*, J. Chem. Phys. **127**, 064704 (2007).

[101] K. Koga and B. Widom, *Mean-field density-functional model of a second-order wetting transition*, J. Chem. Phys. **128**, 114716 (2008).

[102] Y. Djikaev, *Histogram analysis as a method for determining the line tension of a three-phase contact region by Monte Carlo simulations*, J. Chem. Phys. **123**, 184704 (2005).

[103] Y. Takata, H. Matsubara, Y. Kikuchi, N. Ikeda, T. Matsuda, T. Takiue, and M. Aratono, *Line tension and wetting behavior of an air/hexadecane/aqueous surfactant system*, Langmuir **21**, 8594 (2005).

[104] A. S. Clarke, *Thermal fluctuations of a three phase contact line. II. Three fluid phases*, J. Chem. Phys. **96**, 9078 (1992).

[105] P. Hohenberg and W. Kohn, *Inhomogeneous electron gas*, Phys. Rev. **136**, B864 (1964).

[106] W. Kohn and L. J. Sham, *Self-consistent equations including exchange and correlation effects*, Phys. Rev. **140**, A1133 (1965).

[107] N. D. Mermin, *Properties of the inhomogeneous electron gas*, Phys. Rev. **137**, B1441 (1964).

[108] R. Evans, *The nature of the liquid-vapour interface and other topics in the statistical mechanics of non-uniform, classical fluids*, Advances in Physics **28**, 143 (1979).

[109] R. Evans, *Density functionals in nonuniform fluids*, in *Fundamentals of inhomogeneous fluids*, edited by D. Henderson (Marcel Dekker, New York, 1992).

[110] J. Wu, *Density functional theory for chemical engineering: from capillarity to soft materials*, AIChE J. **52**, 1169 (2006).

[111] A. Robledo and J. S. Rowlinson, *The distribution of hard rods on a line of finite length*, Mol. Phys. **58**, 711 (1986).

[112] P. Tarazona, *A density functional theory of melting*, Mol. Phys. **52**, 81 (1984); P. Tarazona and R. Evans, *A simple density functional theory for inhomogeneous liquids — wetting by gas at a solid–liquid interface*, Mol. Phys. **52**, 847 (1984); P. Tarazona, *Free-energy density functional for hard spheres*, Phys. Rev. A **31**, 2672 (1985); P. Tarazona, *Erratum*, Phys. Rev. A **32**, 3148 (1985).

[113] Y. Rosenfeld, *Free-energy model for the inhomogeneous hard-sphere fluid mixture and density-functional theory of freezing*, Phys. Rev. Lett. **63**, 980 (1989).

[114] R. Roth, R. Evans, A. Lang, and G. Kahl, *Fundamental measure theory for hard-sphere mixtures revisited: the White Bear version*, J. Phys.: Condens. Matter **14**, 12063 (2002).

[115] H. Hansen-Goos and R. Roth, *Density functional theory for hard-sphere mixtures: the White Bear version mark II*, J. Phys.: Condens. Matter **18**, 8413 (2006).

[116] E. Helfand, H. Reiss, H. L. Frisch, and J. L. Lebowitz, *Scaled particle theory of fluids*, J. Chem. Phys. **33**, 1379 (1960).

[117] S. M. Oversteegen and R. Roth, *General methods for free-volume theory*, J. Chem. Phys. **122**, 214502 (2005).

[118] J. K. Percus and G. J. Yevick, *Analysis of classical statistical mechanics by means of collective coordinates*, Phys. Rev. **110**, 1 (1958).

[119] E. Thiele, *Equation of state for hard spheres*, J. Chem. Phys. **39**, 474 (1963).

[120] M. S. Wertheim, *Exact solution of the Percus-Yevick integral equation for hard spheres*, Phys. Rev. Lett. **10**, 321 (1963).

[121] E. Kierlik and M. L. Rosinberg, *Free-energy density functional for the inhomogeneous hard-sphere fluid: application to interfacial adsorption*, Phys. Rev. A **42**, 3382 (1990).

[122] S. Phan, E. Kierlik, M. L. Rosinberg, B. Bildstein, and G. Kahl, *Equivalence of two free-energy models for the inhomogeneous hard-sphere fluid*, Phys. Rev. E **48**, 618 (1993).

[123] N. F. Carnahan and K. E. Starling, *Equation of state for nonattracting rigid spheres*, J. Chem. Phys. **51**, 635 (1969).

[124] T. Boublík, *Hard-sphere equation of state*, J. Chem. Phys. **53**, 471 (1970).

[125] G. A., Mansoori, N. F. Carnahan, K. E. Starling, and T. W. Leland, Jr., *Equilibrium thermodynamic properties of the mixture of hard spheres*, J. Chem. Phys. **54**, 1523 (1971).

[126] H. Hansen-Goos and R. Roth, *A new generalization of the Carnahan-Starling equation of state to additive mixtures of hard spheres*, J. Chem. Phys. **124**, 154506 (2006).

[127] J. D. Weeks, D. Chandler, and H. C. Andersen, *Role of repulsive forces in determining the equilibrium structure of simple liquids*, J. Chem. Phys. **54**, 5237 (1971); H. C. Andersen, J. D. Weeks, and D. Chandler, *Relationship between the hard-sphere fluid and fluids with realistic repulsive forces*, Phys. Rev. A **4**, 1597 (1971).

[128] J. A. Barker and D. Henderson, *Perturbation theory and equation of state for fluids. II. A successful theory of liquids*, J. Chem. Phys. **47**, 4714 (1967).

[129] R. Ohnesorge, H. Löwen, and H. Wagner, *Density functional theory of crystal–fluid interfaces and surface melting*, Phys. Rev. E **50**, 4801 (1994).

[130] G. Kahl and J. Hafner, *Optimized cluster theory, optimized random phase approximation and mean spherical model for the square-well fluid with variable range*, Phys. Chem. Liq. **12**, 109 (1982).

[131] L. Vega, E. de Miguel, L. F. Rull, G. Jackson, and I. A. McLure, *Phase equilibria and critical behavior of square-well fluids of variable width by Gibbs ensemble Monte Carlo simulation*, J. Chem. Phys. **96**, 2296 (1992).

[132] A. Lang, G. Kahl, C. N. Likos, H. Löwen, and M. Watzlawek, *Structure and thermodynamics of square-well and square-shoulder fluids*, J. Phys.: Condens. Matter **11**, 10143 (1999).

[133] J. S. Rowlinson, *A drop of liquid*, J. Phys.: Condens. Matter **6**, A1 (1994).

[134] C. A. Galán, A. Mulero, and F. Cuadros, *Calculation of the surface tension and the surface energy of Lennard-Jones fluids from the radial distribution function in the interface zone*, Mol. Phys. **104**, 2457 (2006).

[135] R. Evans and R. J. F. Leote de Carvalho, *Decay of correlations in bulk fluids and at interfaces: a density-functional perspective*, in *Chemical applications of density-functional theory*, edited by B. B. Laird, R. B. Ross, and T. Ziegler, ACS Symposium Series 629 (American Chemical Society, Washington, DC, 1996), p. 166.

[136] J. A. Barker and J. R. Henderson, *Generalized van der Waals theories and the asymptotic form of the density profile of a liquid–vapor interface*, J. Chem. Phys. **76**, 6303 (1982).

[137] J. A. Støvneng, T. Aukrust, and E. H. Hauge, *Asymptotics of a free liquid–gas interface according to the non-local van der Waals theory*, Physica A **143**, 40 (1987).

[138] S. Dietrich and M. Napiórkowski, *Analytic results for wetting transitions in the presence of van der Waals tails*, Phys. Rev. A **43**, 1861 (1991).

[139] M. E. Fisher and B. Widom, *Decay of correlations in linear systems*, J. Chem. Phys. **50**, 3756 (1969).

[140] D. Henderson, L. Blum, and J. L. Lebowitz, *An exact formula for the contact value of the density profile of a system of charged hard spheres near a charged wall*, J. Electroanal. Chem. **102**, 315 (1979).

[141] S. Dietrich, *Wetting phenomena*, in *Phase transitions and critical phenomena*, edited by C. Domb and J. L. Lebowitz (Academic Press, London, 1988), Vol. 12, p. 1.

[142] M. Schick, *Introduction to wetting phenomena*, in *Liquids at interfaces*, Les Houches Summer School Proceedings 48, 1988, edited by J. Charvolin, J. F. Joanny, and J. Zinn-Justin (Elsevier, Amsterdam, 1990), p. 415.

[143] J. W. Cahn, *Critical point wetting*, J. Chem. Phys. **66**, 3667 (1977).

[144] G. Langie and J. O. Indekeu, *Wetting, dewetting, and reentrant wetting in Landau theory and lattice mean-field theory*, Phys. Rev. B **40**, 417 (1989).

[145] H. Dobbs, *The modified Young's equation for the contact angle of a small sessile drop from an interface displacement model*, Int. J. Mod. Phys. B **13**, 3255 (1999).

[146] R. Tsekov, K. W. Stöckelhuber, and B. V. Toshev, *Disjoining pressure and surface tension of a small drop*, Langmuir **16**, 3502 (2000).

[147] R. C. Tolman, *The effect of droplet size on surface tension*, J. Chem. Phys. **17**, 333 (1949).

[148] A. E. van Giessen, E. M. Blokhuis, and D. J. Bukman, *Mean field curvature corrections to the surface tension*, J. Chem. Phys. **108**, 1148 (1998).

[149] E. M. Blokhuis and J. Kuipers, *On the determination of the structure and tension of the interface between a fluid and a curved hard wall*, J. Chem. Phys. **126**, 054702 (2007).

[150] M. Deserno, M. M. Müller, and J. Guven, *Contact lines for fluid surface adhesion*, Phys. Rev. E **76**, 011605 (2007).

[151] U. Seifert and R. Lipowsky, *Adhesion of vesicles*, Phys. Rev. A **42**, 4768 (1990).

[152] U. Seifert, *Configurations of fluid membranes and vesicles*, Adv. Phys. **46**, 13 (1997).

[153] Y. Djikaev and B. Widom, *Geometric view of the thermodynamics of adsorption at a line of three-phase contact*, J. Chem. Phys. **121**, 5602 (2004); C. M. Taylor and B. Widom, *Adsorption equation for the line of three-phase contact*, Mol. Phys. **103**, 647 (2005); B. Widom, *New views of the Gibbs adsorption equation*, Physica A **372**, 169 (2006); B. Widom, *Models of adsorption at a line of three-phase contact*, J. Phys. Chem. B **110**, 22125 (2006); K. Koga and B. Widom, *Line adsorption in a mean-field density-functional model*, Mol. Phys. **104**, 3469 (2006).

[154] W. Koch, S. Dietrich, and M. Napiórkowski, *Morphology and line tension of liquid films adsorbed on chemically structured substrates*, Phys. Rev. E **51**, 3300 (1995).

[155] A. B. D. Cassie and S. Baxter, *Wettability of porous surfaces*, Trans. Faraday Soc. **40**, 546 (1944).

[156] A. B. D. Cassie, *Contact angles*, Discuss. Faraday Soc. **3**, 11 (1948).

[157] P. S. Swain and R. Lipowsky, *Contact angles on heterogeneous surfaces: a new look at Cassies's and Wenzel's laws*, Langmuir **14**, 6772 (1998).

[158] J. Drelich and J. D. Miller, *Modification of the Cassie equation*, Langmuir **9**, 619 (1993).

[159] J. Drelich, *The significance and magnitude of the line tension in three-phase (solid–liquid–fluid) systems*, Colloids Surf. A **116**, 43 (1996).

[160] L. Gao and T. J. McCarthy, *How Wenzel and Cassie were wrong*, Langmuir **23**, 3762 (2007).

[161] R. N. Wenzel, *Resistance of solid surfaces to wetting by water*, Ind. Eng. Chem. **28**, 988 (1936).

[162] P. Bryk, O. Pizio, and S. Sokołowski, *Adsorption of a hard-sphere fluid in a slitlike pore with molecularly rough walls*, J. Chem. Phys. **109**, 2310 (1998).

[163] Y. Duda, S. Sokołowski, P. Bryk, and O. Pizio, *Structure and adsorption of a hard sphere fluid in a cylindrical and spherical pore filled by a disordered matrix: a Monte Carlo study*, J. Phys. Chem. B **102**, 5490 (1998).

[164] P. Bryk, D. Henderson, and S. Sokołowski, *The wetting transition associated with the adsorption of a gas on a rough surface*, Langmuir **15**, 6026 (1999).

[165] P. Bryk, W. Rżysko, A. Malijevsky, and S. Sokołowski, *Capillary condensation in pores with rough walls: a density functional approach*, J. Colloid Interf. Sci. **313**, 41 (2007).

[166] The utilized FFT routine was taken from http://www.fftw.org, version 3.

[167] *Numerical recipes: the art of scientific computing*, third edition, (Cambridge University Press, New York, 2007), sections 17.1 and 18.1.

[168] G. O. Berim and E. Ruckenstein, *Nanodrop on a nanorough solid surface: density functional theory considerations*, J. Chem. Phys. **129**, 014708 (2008).

[169] A. Robledo, C. Varea, and J. O. Indekeu, *Wetting transition for the contact line and Antonov's rule for the line tension*, Phys. Rev. A **45**, 2423 (1992).

[170] C. Grodon, *Structure and solvation forces in binary hard-sphere mixtures*, thesis, Universität Stuttgart (2003).

[171] C. Grodon, *Phase behavior and effective interactions in colloidal suspensions*, thesis, Universität Stuttgart (2007); also (Cuvillier, Göttingen, 2007).

[172] R. Roth and S. Dietrich, *Binary hard-sphere fluids near a hard wall*, Phys. Rev. E **62**, 6926 (2000).

[173] Y. Tang and J. Wu, *A density-functional theory for bulk and inhomogeneous Lennard-Jones fluids from the energy route*, J. Chem. Phys. **119**, 7388 (2003).

[174] Y. Tang and J. Wu, *Modeling inhomogeneous van der Waals fluids using an analytical direct correlation function*, Phys. Rev. E **70**, 011201 (2004).

[175] Y. Rosenfeld, *Free energy model for inhomogeneous fluid mixtures: Yukawa-charged hard spheres, general interactions and plasmas*, J. Chem. Phys. **98**, 8126 (1993).

[176] Y. Tang, *On the first-order mean spherical approximation*, J. Chem. Phys. **118**, 4140 (2003).

[177] Y. Tang, *Direct correlation function for the square-well potential*, J. Chem. Phys. **127**, 164504 (2007).

[178] A. O. Parry, C. Rascón, N. B. Wilding, and R. Evans, *Condensation in a capped capillary is a continuous critical phenomenon*, Phys. Rev. Lett. **98**, 226101 (2007).

[179] M. Tasinkevych and S. Dietrich, *Complete wetting of nanosculptured substrates*, Phys. Rev. Lett. **97**, 106102 (2006).

[180] M. Tasinkevych and S. Dietrich, *Complete wetting of pits and grooves*, Eur. Phys. J. E **23**, 117 (2007).

[181] G. Huber, H. Mantz, R. Spolenak, K. Mecke, K. Jacobs, S. N. Gorb, and E. Arzt, *Evidence for capillary contributions to gecko adhesion from single spatula nanomechanical measurements*, Proc. Nat. Acad. Sci. **102**, 16293 (2005).

[182] P. Bryk, R. Roth, M. Schoen, and S. Dietrich, *Depletion potentials near geometrically structured substrates*, Europhys. Lett. **63**, 233 (2003).

[183] J. R. Henderson, *Statistical mechanics of fluids adsorbed in wedges and edges*, Molec. Sim. **31**, 435 (2005) and references therein.

[184] K. Rejmer, S. Dietrich, and M. Napiórkowski, *Filling transition for a wedge*, Phys. Rev. E **60**, 4027 (1999).

[185] A. Bednorz and M. Napiórkowski, *Interfacial fluctuations near the critical filling transition*, Phys. Rev. E **63**, 031602 (2001).

[186] M. Napiórkowski, W. Koch, and S. Dietrich, *Wedge wetting by van der Waals fluids*, Phys. Rev. A **45**, 5760 (1992).

[187] J. M. Romero-Enrique and A. O. Parry, *Controlling the order of wedge filling transitions: the role of line tension*, New J. Phys. **9**, 167 (2007).

[188] P. Jakubczyk and M. Napiórkowski, *Adsorption in a nonsymmetric wedge*, Phys. Rev. E **66**, 041107 (2002).

[189] P. Jakubczyk and M. Napiórkowski, *The influence of droplet size on line tension*, J. Phys.: Condens. Matter **16**, 6917 (2004); *Erratum*, J. Phys.: Condens. Matter **18**, 2107 (2006),

[190] C. Bauer, S. Dietrich, and A. O. Parry, *Morphological phase transitions of thin fluid films on chemically structured substrates*, Eur. Phys. Lett. **47**, 474 (1999).

[191] C. Bauer and S. Dietrich, *Wetting films on chemically heterogeneous substrates*, Phys. Rev. E **60**, 6919 (1999).

[192] C. Bauer and S. Dietrich, *Phase diagram for morphological transitions of wetting films on chemically structured substrates*, Phys. Rev. E **61**, 1664 (2000).

[193] P. Lenz and R. Lipowsky, *Morphological transitions of wetting layers on structured surfaces*, Phys. Rev. Lett. **80**, 1920 (1998).

[194] H. Gau, S. Herminghaus, P. Lenz, and R. Lipowsky, *Liquid morphologies on structured surfaces: from microchannels to microchips*, Science **283**, 46 (1999).

[195] R. Lipowsky, P. Lenz and P. S. Swain, *Wetting and dewetting of structured and imprinted surfaces*, Colloids Surf. A **161**, 3 (2000).

[196] R. Lipowsky, *Morphological wetting transitions at chemically structured surfaces*, Curr. Opin. Colloid Interface Sci. **6**, 40 (2001).

[197] R. Lipowsky, *Structured surfaces and morphological wetting transitions*, Interface Sci. **9**, 105 (2001).

[198] B. Zhao, J. S. Moore, and D. J. Beebe, *Surface-directed liquid flow inside microchannels*, Science **291**, 1023 (2001).

[199] R. Lipowsky, M. Brinkmann, R. Dimova, T. Franke, J. Kierfeld, and X. Zhang, *Droplets, bubbles and vesicles at chemically structured surfaces*, J. Phys.: Condens. Matter **17**, S537 (2005).

[200] G. T. Linke, R. Lipowsky, and T. Gruhn, *Adhesion of fluid vesicles at chemically structured substrates*, Eur. Phys. J. E **24**, 217 (2007).

[201] A. Checco, Y. Cai, O. Gang, and B. M. Ocko, *High resolution non-contact AFM imaging of liquids condensed onto chemically nanopatterned surfaces*, Ultramicroscopy **106**, 703 (2006).

[202] P. Lenz and R. Lipowsky, *Stability of droplets and channels on homogeneous and structured surfaces*, Eur. Phys. J. E **1**, 249 (2000).

[203] M. Brinkmann, J. Kierfeld, and R. Lipowsky, *A general stability criterion for droplets on structured substrates*, J. Phys. A: Math. Gen. **37**, 11547 (2004).

[204] M. Brinkmann, J. Kierfeld, and R. Lipowsky, *Stability of liquid channels or filaments in the presence of line tension*, J. Phys.: Condens. Matter **17**, 2349 (2005).

[205] S. Mechkov, G. Oshanin, M. Rauscher, M. Brinkmann, A. M. Cazabat, and S. Dietrich, *Contact line stability of ridges and drops*, Europhys. Lett. **80**, 66002 (2007).

[206] J. Koplik, T. S. Lo, M. Rauscher, and S. Dietrich, *Pearling instability of nanoscale fluid flow confined to a chemical channel*, Phys. Fluids **18**, 032104 (2006).

[207] A. Moosavi, M. Rauscher, and S. Dietrich, *Motion of nanodroplets near edges and wedges*, Phys. Rev. Lett. **97**, 236101 (2006).

[208] A. Moosavi, M. Rauscher, and S. Dietrich, *Motion of nanodroplets near chemical heterogeneities*, Langmuir **24**, 734 (2008).

[209] P. Bryk, A. Patrykiejew, J. Reszko-Zygmunt, and S. Sokołowski, *Phase behaviour of a Lennard-Jones fluid in a pore with permeable walls of a finite thickness: a density functional approach*, Mol. Phys. **96**, 1509 (1999).

[210] P. Bryk, A. Patrykiejew, and S. Sokołowski, *Surface phase transitions of a Lennard-Jones fluid in contact with a permeable wall of finite thickness: a density functional approach*, Phys. Chem. Chem. Phys. **2**, 3227 (2000).

[211] P. Bryk, A. Patrykiejew, and S. Sokołowski, *Polydisperse fluid in contact with a semipermeable membrane*, Mol. Phys. **99**, 1709 (2001).

[212] P. Bryk, A. Patrykiejew, S. Sokołowski, D. Boda, and D. Henderson, *Ions at membranes: a density functional approach*, Phys. Chem. Chem. Phys. **2**, 269 (2000).

[213] P. Bryk, *Fluid in contact with semipermeable vesicle: second-order integral equation approach*, Mol. Phys. **98**, 1479 (2000).

[214] R. Roth, Y. Harano, and M. Kinoshita, *Morphometric approach to the solvation free energy of complex molecules*, Phys. Rev. Lett. **97**, 078101 (2006).

[215] Y. Harano, R. Roth, and M. Kinoshita, *On the energetics of protein folding in aqueous solution*, Chem. Phys. Lett. **432**, 275 (2006).

[216] Y. Harano, R. Roth, Y. Sugita, M. Ikeguchi, and M. Kinoshita, *Physical basis for characterizing native structures of proteins*, Chem. Phys. Lett. **437**, 112 (2007).

[217] H. Hansen-Goos, R. Roth, K. Mecke, and S. Dietrich, *Solvation of proteins: linking thermodynamics to geometry*, Phys. Rev. Lett. **99**, 128101 (2007).

[218] P.-M. König, R. Roth, and K. R. Mecke, *Morphological thermodynamics of fluids: shape dependence of free energies*, Phys. Rev. Lett. **93**, 160601 (2004).

[219] P.-M. König, P. Bryk, K. Mecke, and R. Roth, *Curvature expansion of density profiles*, Europhys. Lett. **69**, 832 (2005).

[220] R. Roth, *Fluid mixtures at curved walls*, J. Phys.: Condens. Matter **17**, S3463 (2005).

[221] P.-M. König, *Interplay between geometry and fluid properties*, thesis, Universität Stuttgart (2005).

[222] H. Hadwiger, *Vorlesungen über Inhalt, Oberfläche und Isoperimetrie*, (Springer, Berlin, 1957).

[223] F. Dutka and M. Napiórkowski, *Formation of capillary bridges in two-dimensional atomic force microscope-like geometry*, J. Chem. Phys. **124**, 121101 (2006).

[224] A. E. Siegman, *Quasi fast Hankel transform*, Opt. Lett. **1**, 13 (1977).

[225] S.-C. Sheng and A. E. Siegman, *Nonlinear-optical calculations using fast-transform methods: second-harmonic generation with depletion and diffraction*, Phys. Rev. A **21**, 599 (1980).

[226] S. M. Candel, *Dual algorithms for fast calculation of the Fourier-Bessel transform*, IEEE Trans. Acoust. Speech Signal Process. **29**, 963 (1981).

[227] W. L. Anderson, *Fast Hankel transforms using related and lagged convolutions*, ACM Trans. Math. Software **8**, 344 (1982).

[228] E. W. Hansen, *Fast Hankel transform algorithm*, IEEE Trans. Acoust. Speech Signal Process. **33**, 666 (1985).

[229] T. Bieker and S. Dietrich, *Wetting of curved surfaces*, Physica A **252**, 85 (1998); *Erratum*, Physica A **259**, 466 (1998).

[230] P. Jakubczyk and M. Napiórkowski, *Influence of inhomogeneous substrate curvature on line tension*, Phys. Rev. E **72**, 011603 (2005).

[231] R. Roth and D. Gillespie, *Physics of size selectivity*, Phys. Rev. Lett. **95**, 247801 (2005).

[232] R. Roth and K. M. Kroll, *Capillary evaporation in pores*, J. Phys.: Condens. Matter **18**, 6517 (2006).

[233] W. C. Jensen and D. Li, *Determination of line tensions from the capillary rise in a conical tube*, Colloids Surf. A **156**, 519 (1999).

[234] S. O. Asekomhe and J. A. W. Elliott, *The effect of interface deformation due to gravity on line tension measurement by the capillary rise in a conical tube*, Colloids Surf. A **220**, 271 (2003).

[235] P. Bryk, L. Łajtar, O. Pizio, Z. Sokołowska, and S. Sokołowski, *Adsorption of fluids in pores formed between two hard cylinders*, J. Colloid Interf. Sci. **229**, 526 (2000).

[236] R. Hanumanthu and K. J. Stebe, *Equilibrium shapes and locations of axisymmetric, liquid drops on conical, solid surfaces*, Colloids Surf. A **282-283**, 227 (2006).

[237] G. P. Kubalski and M. Napiórkowski, *A liquid drop in a cone — line tension effects*, J. Phys.: Condens. Matter **12**, 9221 (2000).

[238] M. Napiórkowski, private communication.

[239] F. Dutka and M. Napiórkowski, *The influence of line tension on the formation of liquid bridges in atomic force microscope-like geometry*, J. Phys.: Condens. Matter **19**, 466104 (2007).

[240] R. Aveyard, J. H. Clint, and D. Nees, *Theory for the determination of line tension from capillary condensation*, J. Chem. Soc., Faraday Trans. **93**, 4409 (1997).

[241] P. Lenz, W. Fenzl, and R. Lipowsky, *Wetting of ring-shaped surface domains*, Eur. Phys. Lett. **53**, 618 (2001).

[242] P. Lenz, C. Bechinger, C. Schäfle, P. Leiderer, and R. Lipowsky, *Perforated wetting layers from periodic patterns of lyophobic surface domains*, Langmuir **17**, 7814 (2001).

[243] C. Schäfle, *Morphologie, Verdampfung und Kondensation von Flüssigkeiten auf benetzungsstrukturierten Oberflächen*, thesis, Universität Konstanz (2002).

[244] P. Blecua, R. Lipowsky, and J. Kierfeld, *Line tension effects for liquid droplets on circular surface domains*, Langmuir **22**, 11041 (2006).

[245] M. C. Stewart and R. Evans, *Wetting and drying at a curved substrate: long-ranged forces*, Phys. Rev. E **71**, 011602 (2005).

[246] J. Fiegel, F. J. Jin, J. Hanes, and K. Stebe, *Wetting of a particle in a thin film*, J. Colloid Interface Sci. **291**, 507 (2005).

[247] M. Oettel, A. Domínguez, and S. Dietrich, *Effective capillary interaction of spherical particles at fluid interfaces*, Phys. Rev. E **71**, 051401 (2005); *Erratum*, Phys. Rev. E **73**, 039902(E) (2006).

[248] H. Lehle, M. Oettel, and S. Dietrich, *Eective forces between colloids at interfaces induced by capillary wavelike fluctuations*, Europhys. Lett. **75**, 174 (2006).

[249] H. Lehle and M. Oettel, *Importance of boundary conditions for fluctuation-induced forces between colloids at interfaces*, Phys. Rev. E **75**, 011602 (2007).

[250] H. Lehle, *Fluktuations -und Kapillarkräfte zwischen Kolloiden an fluiden Grenzflächen*, thesis, Universität Stuttgart (2008).

[251] F. Bresme and M. Oettel, *Nanoparticles at fluid interfaces*, J. Phys.: Condens. Matter **19**, 413101 (2007).

[252] L. Dong and D. T. Johnson, *Adsoprtion of acicular particles at liquid–fluid interfaces and the influence of the line tension*, Langmuir **21**, 3838 (2005).

[253] B. Krasovitski and A. Marmur, *Particle adhesion to drops*, J. Adhesion **81**, 869 (2005).

[254] C. Bauer, T. Bieker, and S. Dietrich, *Wetting-induced effective interaction potential between spherical particles*, Phys. Rev. E **62**, 5324 (2000).